Experimental investigation of turbulent transport at the edge of a tokamak plasma

Nicolas Fedorczak

▶ **To cite this version:**

Nicolas Fedorczak. Experimental investigation of turbulent transport at the edge of a tokamak plasma. Fluid Dynamics [physics.flu-dyn]. Université de Provence - Aix-Marseille I, 2010. English. NNT : . tel-00627522

HAL Id: tel-00627522

https://theses.hal.science/tel-00627522

Submitted on 28 Sep 2011

HAL is a multi-disciplinary open access archive for the deposit and dissemination of scientific research documents, whether they are published or not. The documents may come from teaching and research institutions in France or abroad, or from public or private research centers.

L'archive ouverte pluridisciplinaire **HAL**, est destinée au dépôt et à la diffusion de documents scientifiques de niveau recherche, publiés ou non, émanant des établissements d'enseignement et de recherche français ou étrangers, des laboratoires publics ou privés.

Thèse de doctorat de l'Université de Provence

Spécialité : **Physique des plasmas**

Présentée par :

Nicolas FEDORCZAK

Etude Expérimentale du Transport Turbulent au Bord d'un Plasma de Tokamak

Soutenue publiquement le 24 Septembre 2010 devant le jury composé de :

Jean-Marc LAYET	Président du jury	Professeur des universités
Pascale HENNEQUIN	Rapporteur du jury	Professeur des universités
George TYNAN	Rapporteur du jury	Professeur des universités
Alain POCHEAU	Directeur de thèse	Professeur des universités
Pascale-MONIER-GARBET	Responsable CEA	Expert au niveau
Gabriel MARBACH	Membre du jury	Directeur de recherche IRFM
Gérard BONHOMME	Membre du jury	Professeur des universités
James GUNN	Membre du jury	Ingenieur de recherche

Laboratoire d'accueil:

Service Intégration Plasma Paroi
Institut de Recherche pour la Fusion Magnétique
CEA Cadarache
13108 Saint Paul-lez-Durance

energie atomique • energies alternatives

Avant-propos

"Faisons au mieux aujourd'hui pour que nos enfants et les leurs vivent dans un monde sain, et par la même occasion nous en serons sûrement nous-même satisfaits." P.

Entre autres, la technologie, qui fait indiscutablement partie de notre identité, nous impose la consommation d'une quantité d'énergie monumentale, que nous produisons principalement en brûlant des réserves fossiles puisées du sol de la Terre. Dans notre frénésie de consommation, nous commençons néanmoins à percevoir et à nous alarmer des contrecoups présents et futurs: Les réserves fossiles sont-elles suffisantes pour la *croissance* que nous voulons maintenir ? Et pour les autres pays qui se développent ? Quel est l'impact des rejets de combustion sur notre environnement? Comment gérer la distribution des ressources entre les différents pays ? Que pouvons-nous faire ? En vue de ces questions, nous pourrions tout d'abord réfléchir à repenser notre utilisation inconditionnelle de la technologie. Mais indéniablement, nous ne pouvons nous en passer totalement et il s'agit donc de réfléchir aussi sur les vecteurs d'énergie qui nous accorderaient une certaine pérennité.

La production d'énergie via la fusion nucléaire offre à notre monde de technologie un challenge à tous points de vue. Si en finalité ce projet doit potentiellement mener à une tranquillité en matière de ressources et production énergétiques mondiales, de nombreux obstacles scientifiques et technologiques restent encore à surmonter: développement de matériaux supportant de hauts flux de chaleur, matériaux supraconducteurs, accélérateurs de particules neutres pour ne citer qu'eux font partis des principales problématiques en recherche et développement. La physique liée au plasma magnétisé est autrement aussi riche en diversité : de la physique atomique à la magnétohydrodynamique en passant par les phénomènes de turbulence hors équilibres, un riche réseau de problèmes fondamentalement liés au confinement de l'énergie apparaît.

Pouvoir allier un projet énergétique à ce panel scientifique a en quelque sorte motivé mon choix d'orienter mon activité professionnelle dans le domaine de la recherche en physique des plasmas. Outre la richesse de l'ensemble des sujets de recherche, l'aspect international du projet m'est apparu comme un facteur d'épanouissement réel tant du point de vue professionnel que personnel au travers des échanges lors de conférences et collaborations. Il m'est ainsi apparu opportun de rédiger ce manuscrit en anglais afin de lui garantir une visibilité adéquate.

Pour m'avoir permis de mener des études en sciences dans les meilleurs conditions, je tiens tout d'abord à remercier et rendre considérations au ministère de l'éducation et à l'école normale supérieure de Paris, qui a financé et proposé un cursus universitaire de grande qualité. Pour m'avoir accueilli et avoir en grande partie financé cette formation et ces travaux de recherche en physique des plasmas, je tiens à remercier et rendre considérations à l'institut de recherche sur la fusion magnétique contrôlée du centre d'étude atomique de Cadarache.

Nicolas Fedorczak

Résumé élargi

Le contexte énergétique mondial est sans appel : une crise profonde en termes de ressources premières est à venir, à proche ou moyenne échéance, et nous nous devons de préparer immédiatement des solutions viables afin de modérer sa portée humanitaire et économique. Sans détours, la fusion nucléaire offre potentiellement le triple avantage de garantir des ressources abondantes, un très faible impact écologique et une réduction accrue des risques de prolifération nucléaire, souvent critiqués dans la mise en oeuvre à grande échelle de la fission nucléaire. Néanmoins, la preuve de faisabilité de production électrique par principe de fusion nécessite à l'heure actuelle des avancées technologiques et scientifiques importantes. C'est dans ce cadre de compréhension scientifique que s'insère ce travail de thèse, que nous résumerons après une brève revue des principes technologiques et physiques mis en oeuvre dans un réacteur à fusion.

La fusion nucléaire

La fusion de deux noyaux atomiques légers en un noyau plus lourd fait intervenir un défaut de masse dans le bilan de réaction : une partie de l'énergie de liaison interne est transférée en énergie cinétique sur les produits de réaction. Ainsi, pour la réaction Deutérium-Tritium (D-T) retenue pour la première génération de réacteurs à fusion, un noyau d'Hélium et un neutron sont produits avec des énergies cinétiques respectives de 3.5MeV et 14.1MeV (Le neutron est le vecteur d'énergie thermique pour une centrale électrique à vapeur). Si le produit énergétique est réellement grand, la réaction nécessite cependant, pour que les taux de réactions soient maximum, des conditions thermiques initiales extrêmes : les réactifs doivent être portés à des températures avoisinant les 10keV (100 millions de degrés). A cette température, les atomes sont totalement ionisés et nous parlerons désormais d'un milieu en phase *plasma*.
Pour que les conditions de réaction se maintiennent et soient économiquement viables, un bilan de puissance positif doit être respecté: c'est le *critère de Lawson*, qui porte sur le produit de la pression du plasma par le *temps de confinement de l'énergie*, qui décrit le taux avec lequel l'énergie est perdue du système : $nT\tau_E > 2,7.10^{21}\mathrm{m}^{-3}.\mathrm{keV.s}$.
Il existe plusieurs procédés permettant de potentiellement atteindre les conditions de densité (la température étant fixée pour un taux de réaction maximal) et de confinement requises. Nous n'introduirons ici que le principe de *confinement par champ magnétique*, qui permet de confiner l'énergie sur des temps de l'ordre de plusieurs secondes dans un plasma de faible densité (5 ordres de grandeurs en dessous de la densité atmosphérique). Le procédé technologique mis en oeuvre pour confiner le plasma s'appelle un *tokamak*.

A l'heure actuelle, les tokamaks existant n'ont pas pour vocation à produire des réactions de fusion nucléaire, mais plutôt à étudier les processus physiques mis en jeu dans le plasma et à tester spécifiquement des scénarios et technologies. Tore Supra a par exemple vocation à tester les systèmes magnétiques supraconducteurs, permettant la réalisation de décharges longues aux

moyens de systèmes de génération de courant non inductifs. Le projet ITER [1]correspond à la nouvelle génération de tokamaks de très grandes tailles qui permettront de valider tous les concepts developpés ces dernières decennies en vue de produire des réactions de fusion à un rendement quasi-économique.

Le confinement magnétique dans un tokamak

Le principe du confinement magnétique repose sur le fait qu'une particule chargée suit un mouvement de précession cyclotronique autour des lignes de champs. Dans un champ rectiligne uniforme de l'ordre du Tesla, Le rayon de Larmor des ions est de l'ordre du millimètre dans un plasma à 10keV : les particules sont effectivement confinées dans le plan transverse au champ magnétique. Afin de confiner la trajectoire libre selon la direction parallèle au champ, l'idée est de refermer les lignes sur elles mêmes pour former un champ magnétique *torique*. Cette courbure spatiale se répercute néanmoins par une inhomogénéité de l'amplitude du champ magnétique, plus forte côté intérieur du tore. Il s'ensuit un phénomène de dérive séculaire due à la précession des particules dans un champ inhomogène qui conduit à une perte des particules du côté extérieur du tore. Afin de compenser cette dérive qui impose une très faible capacité de confinement, une composante poloïdale (selon le petit rayon du tore) est ajoutée à la composante toroïdale : les lignes de champs s'enroulent hélicoïdalement autour du tore. Ce champ magnétique est généré par un courant toroïdal qui est induit dans le plasma. L'équilibre du plasma avec le champ magnétique est décrit par la magnétohydrodynamique (MHD) : nous montrons que les lignes de champs s'organisent sur des surfaces toriques emboîtées le long desquelles la pression plasma est uniforme. Les surfaces centrales ont une pression plus fortes que les surfaces externes : la configuration tokamak génère un système à l'équilibre macroscopique qui hors équilibre thermodynamique due aux forts gradients de pressions et températures.

Transport et turbulence

Cet état hors équilibre thermodynamique est la cause de processus de transport entre les surfaces de flux. Historiquement, l'approche dite classique n'a tenu compte que des phénomènes de transport par collisions, qui peuvent s'enrichir dans la description dite néoclassique d'une variété de phénomènes propres à la géométrie tokamak. Mais ces théories sous-estiment par plusieurs ordres de grandeurs l'amplitude du transport révélée par l'expérience. La cause en est aujourd'hui claire : des phénomènes de turbulence dominent le transport de particules et d'énergie depuis le centre du plasma vers le bord. La nature de cette turbulence est propre aux plasmas magnétisés puisqu'elle met principalement en jeu des phénomènes de dérives transverses qui sont causés par les champs électrostatiques [2]. Mais au final, nous retrouvons des

[1]International Thermonuclear Experimental Reactor

[2]Les fluctuations du champ magnétiques sont alors négligeables. Un autre aspect du transport dans les plasmas de tokamak est en effet propre à la MHD: le plasma qui est conducteur peut rétroagir sur les champs magnétiques qui le confinent et former des systèmes de lignes de champs complexes qui détériorent le confinement.

caractéristiques qui sont universelles à la turbulence fluide : cellules de convection, avalanches, cascade d'échelles, etc.
Cette turbulence a le double désavantage de réduire la pression du centre en accroissant les pertes vers le bord et d'être très mal connue car il est très difficile de diagnostiquer un plasma thermonucléaire avec la précision microscopique requise. Par exemple le plasma peut être sujet à une transition du régime de turbulence, qui correspond à l'instauration d'une barrière de transport locale (autour d'une surface de flux). Si cette transition est bénéfique car elle augmente la pression interne en raidissant les gradients locaux, elle n'est pour l'heure pas expliquée, outre le constat qu'elle fait intervenir un cisaillement en vitesses qui décorrèle la turbulence. Lorsque cette barrière apparaît au bord, le plasma est dit en *mode H* (High confinement mode).

Le plasma de bord et problématiques du transport associées

Le plasma en équilibre sur ces surfaces de flux est nécessairement contenu dans une enceinte matérielle, dite enceinte *à vide* (car en phase pré plasma la pression de neutres est 5 ordres de grandeur inférieure à la pression atmosphérique) . Ainsi en partant du centre des surfaces concentriques *fermées*, il existe une première surface qui rencontre un élément matériel : il s'agit de la *dernière surface magnétique fermée* (DSMF). A l'extérieur de cette surface les lignes de champs magnétiques rencontrent un élément de paroi : il s'agit des lignes de champ *ouvertes*. Suivant ces lignes de champ, les particules qui sont perdues de la région confinée vont venir en collision avec la paroi. Les conséquences sont un échauffement des parois (les flux de chaleur mis en jeu sont de l'ordre du $MW.m^{-2}$), ainsi qu'une érosion des surfaces sous le bombardement ionique. Afin de contrôler au mieux ces contraintes matérielles, des éléments de parois spécifiques sont placées dans la chambre, spécialement conçus pour évacuer le flux de chaleur et résister à l'érosion : ceux sont les limiteurs. La DSMF est définie à leur contact et sépare le plasma en deux régions distinctes topologiquement : le plasma confiné où les lignes de champs sont fermées, et la *scrape-off layer* (SOL) où les lignes de champs sont ouvertes sur les limiteurs.

Les processus de transport à travers la DSMF et dans la SOL sont directement et indirectement impliqués dans l'efficacité de confinement : directement en contrôlant les gradients au bord et l'amplitude des pertes depuis la région confinée ; et indirectement en contrôlant d'une part l'étendue spatiale des dépôts de chaleur sur les limiteurs, et d'autre part en influençant la migration des impuretés détachées des parois vers la région confinée où elles nuisent aux performances de confinement.

Les objectifs de la thèse

Depuis des décennies, les expériences visent à caractériser (entre autres) les processus de transport qui interviennent au bord. Si le constat est sans ambiguïté que la turbulence y est pleinement développée, il n'est pas encore possible de se faire une idée à la fois précise et globale de l'interrelation des phénomènes qui s'y produisent. Entre autres des écoulements à grande

échelle sont souvent observés dans la SOL, qui ont une conséquence directe sur la migration des impuretés ; et ont été récemment considérés avec intérêt pour leur rôle potentiel dans l'instauration de la barrière de transport du mode H. Pourtant, les mécanismes à l'origine de ces écoulements ne sont pas encore clarifiés avec certitude, non plus que les mécanismes qui les couplent avec la rotation du plasma confiné.

La principale difficulté d'une démarche expérimentale sur un tokamak est la nature pleinement développée et corrélée des processus mis en jeu, qu'il n'est pas possible d'étudier pas à pas comme pour les expériences fluides de laboratoire. Une analogie pourrait être d'élucider les différents termes des équations de Navier Stokes avec pour seul laboratoire d'expérience un torrent.
Nous nous sommes donc attachés durant la thèse à élargir au maximum la gamme d'informations diagnostiquées sur les plasmas de Tore Supra et à construire notre compréhension des phénomènes observés sur cette vue d'ensemble. La ligne directrice qui est apparue d'elle-même en vue des problématiques actuelles et des premières confrontations de résultats est la suivante : élucider la nature du transport au bord des plasma de Tore Supra, élucider ses propriétés spatiales (asymétries) et son lien avec les écoulements à grande échelle.
Après un bref aperçu des éléments de physiques relatifs au plasma de bord, nous décrirons les diagnostics utilisés ainsi que les résultats obtenus avec chacun d'eux, pour ensuite les rassembler dans un modèle global.

Physique des lignes de champs ouvertes

Dans toute la suite, il est supposé que le plasma est un milieu localement neutre car soumis à des forces de rappel électrostatiques.
La description du plasma magnétisé peut suivre plusieurs étapes de simplifications. La description statistique en est le premier ordre : l'évolution temporelle des distributions en vitesse et en espace des particules est exprimée à travers l'équation de Boltzmann, faisant intervenir les champs de forces locaux et les échanges par collisions. Si cette approche offre le maximum de richesses en termes de phénomènes décrits, et est à la base des nouvelles générations de simulations numériques, elle n'offre pas la simplicité requise à une approche expérimentale puisque les diagnostics mesurent des champs *moyens*. En moyennant l'équation de Boltzmann sur l'espace des vitesses, nous obtenons les équations fluides portant sur les différents moments de la distribution en vitesse: densité, vitesse, température. Pour que le système obtenu porte sur un nombre réduit de moments, il est nécessaire que les distributions en vitesse soient régulières : l'approximation maxwellienne est faite. Pour le plasma de bord, nous vérifions que le taux de collisions justifie cette approche.

Au premier ordre, ces moyennes se font sous l'hypothèse de champs moyens : en négligeant les inhomogénéités des champs de forces vis-à-vis du rayon de Larmor. Cependant, nous omettons alors les effets de dérives séculaires. Ces termes de dérives peuvent être soit reconstruits

à partir des équations fluides ainsi obtenues, soit rigoureusement construits en élargissant le modèle de champ moyen aux inhomogénéités spatiales. Finalement, nous ne retenons que les composantes dominantes des vitesses de dérives :

$$v_{\perp}^{s} = \frac{\vec{E} \times \vec{B}}{B^2} + \frac{-\vec{\nabla} P_s \times \vec{B}}{n_s q_s B^2}$$

Où E est le champ électrostatique local, B le champ magnétique P_s la pression de l'espèce s et n_s et q_s la densité et la charge atomique de cette espèce. La dérive électrique est ambipolaire (ne fait pas intervenir de séparation de charges) et génère transport transverse de particules et d'énergie. La dérive diamagnétique (de pression) est non ambipolaire et à divergence nulle (au premier ordre): elle ne génère que des courants transverses qui sont à la base des mécanismes d'instabilité.

Les équations fluides sont alors simplifiées suivant plusieurs approximations :
Tout d'abord au niveau géométrique : les lignes de champs offrent un système de coordonnées privilégiées car le plasma est quasi-homogène selon cette direction (convection libre). Cependant, l'enroulement hélicoïdal des lignes de champs implique que ce référentiel n'est pas galiléen. Dans l'approximation d'un tokamak au grand rapport d'aspect (rapport de son grand rayon sur son petit rayon), nous négligeons les termes de courbure de lignes de champs et traduisons les équations fluides dans un repère cartésien aligné aux lignes de champ (//,r,$\perp$) où r dénote la coordonnée de petit rayon en travers des lignes de champs et $\perp$ est quasiment égal à la direction poloïdale.
En second lieu, nous supposons que les températures sont uniformes le long des lignes de champs (forte conductivité thermique parallèle), et que les transferts d'impulsions orthogonaux aux lignes de champs sont négligeables (termes non diagonaux du tenseur de Reynolds et viscosité).
Ces approximations mènent premièrement à l'approximation des électrons maxwelliens : leurs inertie est négligeable, ce qui relie directement le gradient de densité parallèle au champ électrostatique parallèle. Finalement, les équations fluides que nous retiendrons pour l'étude du bord sont :

$$\begin{aligned} \nabla_{||}(n v_{||}) + \nabla_{\perp}\Gamma_{\perp} + \nabla_r \Gamma_r &= S \\ \nabla_{||}\left(n c_S^2 + n v_{||}^2\right) &= 0 \end{aligned} \tag{1}$$

Où $c_S = \sqrt{\frac{ZT_e + T_i}{m_i}}$ est la vitesse acoustique ionique qui nous permet d'adimensionné la vitesse sous la forme d'un nombre de Mach. S est la source locale de particules par ionisations.

La physique du plasma de bord est soumise à l'interaction plasma-paroi : pour respecter l'ambipolarité des flux de charges des lignes de champ à la paroi, une *gaine* de potentiel apparait à la surface de celle-ci, d'une épaisseur caractéristique la longueur de Debye. A l'entrée de cette gaine, la vitesse de l'écoulement ionique est imposé égal à la vitesse acoustique ionique : c'est le critère de *Bohm*. Ce critère fixe les conditions aux limites d'une ligne de champ, en vitesse et aussi en densité par du fait de la conservation de la pression parallèle. Ce constat

servira de fil directeur à notre analyse des écoulements parallèles dans la SOL.

Nous développons ensuite le principe des sondes de Langmuir. Une électrode placée dans le plasma collecte un flux de charges en fonction de son potentiel de polarisation. La *caractéristique* obtenue permet d'évaluer densité plasma, température, potentiel plasma. La physique d'interaction plasma-sonde est plus spécifique que le modèle précédent et doit prendre en compte les échanges d'impulsions par viscosité : c'est le modèle d'*Hutchinson*, que nous revisitons ici avec un autre formalisme de transport. Au final, nous vérifions que les approximations suivies par ce modèle sont valables à la lumière de quelques évidences expérimentales.
Entre autres, nous vérifions que la sonde *Tunnel* utilisée sur Tore Supra donne une assez bonne estimation de la densité plasma, mais que la mesure de température est sujette à précautions. Pour cette raison nous baserons notre analyse des mesures de sondes sur des données ne dépendant pas directement de la mesure de température.
Nous montrons de plus que si les collecteurs de sondes sont de trop faibles dimensions, le nombre de Mach de l'écoulement parallèle est fortement sous-estimé par rapport à une mesure de référence (sonde tunnel): nous remettons partiellement en cause les mesures effectuées sur d'autres tokamaks.

Transport et sondes de Langmuir : mesures stationnaires

Nous débutons l'étude du transport dans la SOL par les mesures stationnaires d'écoulement parallèle, qui sont diagnostiquée par une sonde mobile situées en haut du plasma. A la lumière de notre modèle d'équilibre du plasma dans la région des lignes de champs ouvertes, les écoulements parallèles sont potentiellement la cause de trois contributions : Nous montrons que la source d'ionisation, évaluée à partir d'une simulation type Monte-Carlo du phénomène de recyclage sur le limiteur, est négligeable dans la SOL. Enfin, nous estimons la contribution des flux transverses (poloïdaux) à partir de mesures expérimentales et concluons qu'elle peut être négligée. Finalement, les écoulements parallèles *dans la SOL de Tore Supra* sont une conséquence de la *distribution spatiale du flux radial de particules.*

A la lumière de ces résultats, il apparait que le plasma de SOL est géré par un équilibre entre les flux parallèles et les flux dans la direction radiale. Nous montrons en particulier que les profils de densité locaux sont une conséquence moyenne du transport radial : la longueur de décroissance des profils peut s'interpréter comme la valeur d'un coefficient de transport moyenné le long des lignes de champ. Ce coefficient de transport dépasse de plusieurs ordres de grandeurs les prévisions néoclassiques. Nous proposons ensuite une réinterprétation des mesures d'écoulements parallèles locaux en termes de flux radial intégré le long des lignes de champ. Malgré le caractère intégré de la donnée, nous pouvons néanmoins quantifier une première asymétrie : Malgré le caractère intégré de la donnée, nous pouvons néanmoins quantifier une première asymétrie : environ 85% du flux radial de particules est localisé côté faible champ du tore.

Dans le but de préciser d'avantage l'asymétrie du flux de particules, nous avons mis au point une démarche expérimentale s'appuyant sur la grande variabilité de la configuration limiteur de Tore Supra : en insérant des limiteurs secondaires dans la SOL, nous pouvons fractionner la distribution de ce flux le long des lignes de champ. En évaluant les changements consécutifs sur les écoulements parallèles, il est possible de remonter aux fractions de flux entrant de part et d'autre de ce second limiteur. En variant la position de ce second limiteur, nous obtenons une cartographie plus détaillée du flux de particule autour de l'équateur côté faible champ.
Le résultat de cette expérience est que le flux est centré autour de l'équateur, dans une région s'étalant poloïdalement sur moins de 50^o de part et d'autres de l'équateur. La distribution obtenue permet d'expliquer l'amplitude écoulements parallèles mesurés dans la SOL de Tore Supra, même lors de configurations limiteurs exotiques durant lesquelles nous observons des transitions dans les écoulements.
Nous avons donc un premier résultat fort sur le transport dans la SOL : le flux radial de particules, bien que de nature inconnue, est fortement localisé côté faible champ, et nous proposons une quantification de cette asymétrie. Cette asymétrie est le principal moteur des écoulements parallèles quasi-soniques mesurés dans la SOL.

Transport et sondes de Langmuir : fluctuations

Les fluctuations dans la SOL sont également mesurées par une sonde mobile située en haut du plasma. Cette fois, le type de sonde ainsi que l'électronique de mesures sont dédiés aux mesures de fluctuations électrostatiques : un peigne fin d'électrodes réparties poloïdalement permet la mesure des fluctuations de densité ou potentiel plasma et d'étudier leur couplage.
Les particularités premières des fluctuations de densité dans la région de bord d'un tokamak sont leurs fortes amplitudes (20-50%) et leur nature intermittente et cohérente : les signaux temporels sont composées de bouffées rares, positives et puissantes, dont les fréquences sont de l'ordre de 10kHz. Ces fluctuations temporelles de densité correspondent à la convection de structures dont la taille transverse au champ magnétique est de l'ordre de 5 mm à quelques cm. Il apparaît de plus que le champ électrostatique poloïdal, déduit d'une différence de potentiel, fluctue en phase avec la densité : ces bouffées sont convectées radialement par dérive électrostatique. La moyenne temporelle du flux résultant est positive, bien que l'écart type de ses fluctuations soit un ordre de grandeurs au dessus : le flux se décompose en une succession de bouffées positives et négatives (analogie du ressac des vagues lors de la marée montante).
Cette description du flux de particules local est comparable à ce qui est observé sur d'autres tokamaks, où ils utilisent des configurations de sonde similaires. Néanmoins nous avons voulu soulever un problème crucial qui est rarement abordé : quel est l'impact d'une sous-discrétisation de champ électrique sur l'amplitude du flux ? Pour répondre à cette question, nous avons eu recours à une sortie de simulation numérique fluide de turbulence de bord (code TOKAM2D) qui offre des caractéristiques de transport qualitativement similaires aux observations. Il apparait que le flux est en effet sous-estimé (jusqu'à un facteur 3) dès lors que la

taille d'échantillonnage du champ électrostatique excède la taille caractéristique des structures de potentiel. Pour les mesures effectuées sur Tore Supra, nous vérifions donc que la taille caractéristique des structures de potentiel, évaluées le long du peigne, est en accord avec ce critère.

L'estimation locale du flux turbulent par dérive électrostatique est ensuite comparée à la cartographie spatiale du flux stationnaire. Localement, les deux mesures coïncident dans une barre d'erreur acceptable en regard des tentatives de comparaisons effectuées sur d'autres tokamaks. Sur ces machines, les mesures de turbulence sont faites dans le plan équatorial côté faible champ, où l'amplitude du flux turbulent est trop importante pour rendre compte des profils de densité. Puisqu'il s'agit précisément de la localisation où nous plaçons le piquage du flux, nous émettons l'hypothèse déjà proposée que le flux par dérive électrostatique est asymétrique spatialement. Cette hypothèse est confrontée aux mesures d'un troisième diagnostic : l'imagerie rapide.

L'imagerie visible rapide

Les conditions du plasma de bord se prêtent à l'imagerie visible car température et densité plasma y sont respectivement de l'ordre de 10eV et $10^{18}\mathrm{m}^{-3}$: des atomes d'hydrogène neutres traversant le plasma peuvent émettre des photons visibles à un taux élevé avant d'être ionisés. L'émissivité plasma étant proportionnelle à la densité électronique locale, ses fluctuations se répercute par des fluctuations de l'émission de photons (le temps de relaxation des atomes neutres excités est largement inférieur à la dynamique de la turbulence).
L'imagerie visible sur Tore Supra consiste en une camera rapide filmant l'intérieur du Tore à travers un système optique dédié. Le diagnostic permet de visualiser l'intégralité de la section du plasma, avec des fréquences d'acquisitions probantes comprises entre 1kHz et 50kHz. Le diagnostic est principalement limité par le flux de photons qui est naturellement faible autour de la section du plasma. Néanmoins, certains protocoles expérimentaux permettent d'augmenter localement la quantité de photons émise : soit en plaçant un limiteur dans la région d'intérêt qui permet d'instaurer un nuage de recyclage à sa surface, soit en injectant du gaz dans la ligne de visée de la caméra, soit en forçant le plasma à se maintenir dans un état de rayonnement fort (le plasma détaché). Aux vues des différentes approches expérimentales, une synthèse robuste des observations est proposée :

les fluctuations dans le bord du plasma sont composées de structures localement alignées aux lignes de champ magnétiques. Ces *filaments* ont une taille transverse de l'ordre du centimètre, en accord qualitatif avec les mesures de sondes. Ces filaments sont observés et dans la SOL et dans la région confinée, même à des positions très centrales (en plasma détaché).
Ils sont très clairement observés côté faible champ du plasma, où ils suivent un mouvement de rotation global et se propagent vers l'extérieur à travers la DSMF. Les vitesses mises en jeu sont en bon accord avec des mesures Doppler effectuées avec un diagnostic radar. La vitesse radiale est de l'ordre de 500 $\mathrm{m.s}^{-1}$.

Ces filaments sont aussi observés dans la partie basse du plasma, mais ne sont pas observés côté fort champ (intérieur) du tore, que ce soit dans la région confinée ou dans la SOL.
Nous avons ici mis en évidence des propriétés essentielles de ces fameux filaments impliqués dans le transport au bord : Leur existence ne dépend pas de la nature ouverte des lignes de champs, remettant en cause un paradigme très repandu que ces filaments n'existent que dans la SOL. Ensuite, ces filaments sont essentiellement *localisés côté faible champ* et possèdent une *extension parallèle finie* qui les déconnectent du côté fort champ.

Mise en cohérence des résultat : vers modèle global de transport au bord

Le flux radial stationnaire a été cartographié dans la SOL et présente une forte asymétrie caractérisé par un piquage à l'équateur côté faible champ. L'amplitude locale de cette cartographie est en accord avec le flux turbulent de dérive électrostatique, qui est mesuré dans la région haute du plasma. Finalement, des filaments plasma sont observés principalement autour de l'équateur côté faible champ, où ils se propagent radialement. Tenant compte du fait que les mesures locales de turbulence électrostatiques correspondent effectivement à la signature d'une convection de filaments de densité, il apparait censé d'affirmer que ces fluctuations électrostatiques sont la signature de la dynamique des filaments observés par camera. Ainsi, *le flux de particule est largement dominé par la convection électrostatique de la densité* et le *fort piquage du flux radial dans le région équatoriale faible champ est une conséquence de l'extension finie des filaments plasmas.*
Nous venons d'énoncer ici un résultat majeur de la thèse. Pour la première fois un accord quantitatif est trouvé entre les mesures de fluctuations et l'amplitude des écoulements stationnaires.

Le processus de génération des filaments est reconsidéré en vue de ses résultats. L'instabilité d' *interchange* est le mieux à même de concilier et le couplage de phase entre champ électrostatique et densité et le fort pique du flux dans la région instable vis-à-vis des processus d'interchange. Lorsqu'une surdensité apparait dans le plasma, le gradient de pression centripète génère un courant plasma autour de la surdensité par dérive diamagnétique. Due à l'inhomogénéité du champ magnétique, ces dérives sont à divergences non nulles et entrainent la polarisation de la surdensité. La polarisation générée localement entraine une dérive électrostatique opposée au gradient de champ magnétique : une surdensité apparaissant côté fort champ est stabilisée et une côté faible champ est au contraire advectée vers l'extérieur du plasma. Considérant la géométrie magnétique de Tore Supra, le critère d'instabilité local s'applique dans une région s'étalant poloïdalement entre $\pm 45^o$ autour de l'équateur côté faible champ.
Cependant, il est nécessaire de prendre en compte les courants parallèles qui tendent à réguler l'instabilité. Un calcul d'ordre de grandeur montre que le plasma ne s'étend que sur une très faible distance parallèle avant que les courants parallèles n'aient bridés la formation des structures électrostatiques, de sorte que le filament plasma garde une extension parallèle confinée

à la zone d'instabilité durant son excursion radiale. Cette extension parallèle ou poloïdale résultant d'un travail d'ordre de grandeur sur les mécanismes d'interchange est comparable à l'extension poloïdale du flux mesurée sur Tore Supra.

En conséquence, expériences et théorie se rejoignent sur le fait que ces filaments plasma naissent dans une région localisée autour de l'équateur côté faible champ, et s'étendent parallèlement depuis cette région. Les mesures relatives aux fluctuations effectuées dans la partie haute du plasma de Tore Supra rejoignent aussi cette hypothèse : l'orientation locale du champ de vitesse transverse propre aux filaments est en accord avec l'idée que le cisaillement magnétique déforme et oriente des structures initialement animées d'un mouvement purement radial à l'équateur.

Conclusion

Les résultats qui viennent d'être résumés sont en partie le fruit de nombreuses journées dédiées à la mise au point du diagnostic d'acquisition rapide pour les sondes. L'environnement tokamak est extrêmement contraignant pour un diagnosticien, car les systèmes sont soumis à des conditions rudes et le temps d'accès à l'installation est très restreint pendant les expériences. Mais le labeur paye par la satisfaction d'avoir pu utiliser ces diagnostics avec confiance et en toutes circonstances .

Ce travail expérimental mené sur Tore Supra a visé à caractériser de manière globale et locale le transport prenant place au bord du plasma. En se basant principalement sur trois diagnostics, nous sommes parvenus à concilier les différentes observations dans un modèle liant la turbulence électrostatique et les écoulements stationnaires. Les filaments plasmas sont des structures relativement allongées le long des lignes de champ et transversalement localisées. Ces filaments apparaissent côté faible champ et se propagent radialement, véhiculant la majorité des pertes en particules depuis la région confinée. Leur extension parallèle finie se répercute par une forte localisation du transport radial autour de l'équateur côté faible champ. Afin de maintenir en moyenne une pression constante le long des lignes de champ, de forts écoulements parallèles sont générés depuis cet équateur vers les limiteurs.
Ce modèle est à même de concilier une large gamme d'observations faites sur Tore Supra, et supporte aussi les observations faites sur d'autres tokamaks dont la géométrie est différente. Nous apportons ici une évidence expérimentale robuste de phénomènes qui sont de plus en plus considères pour leurs impacts en termes de cohérence des observations et de pertinence des modèle numériques développés comme outils de prédictions pour ITER.
La dynamique locale des ces filaments doit maintenant être étudiée plus en détail afin de révéler leur potentialité dans le rétro-couplage entre la SOL et le plasma confiné : le cisaillement magnétique et la localisation parallèle des filaments créent des écoulements transverses et parallèles qui peuvent se propager au plasma confiné et influencer la génération des barrières de transport.

Contents

Chapter 1

Introduction

Along this chapter, we present the general context of the experimental investigation conducted during the thesis. Starting with the motivations of developing the nuclear fusion as a reliable source of energy in a global context, we describe the fusion principle and the tokamak configuration. Then we focus on the crucial physical issues related to edge plasma and plasma-wall interaction, to finally present the motivations and content of the thesis.

1.1 Energy context

By changing our system of references, we appreciate the magnitudes differently : the global energy consumption is currently equivalent of 3 cubic miles of oil every year, having in mind that one half corresponds effectively to oil consumption. It would fill three thousand sport arenas and is equivalent to the volume of water carried by the French Seine river over a year. In fact, it corresponds more or less to 2.5 cubic meters of oil per human per year, but the consumption depends strongly on the country we consider - see figure 1.1. For instance, an

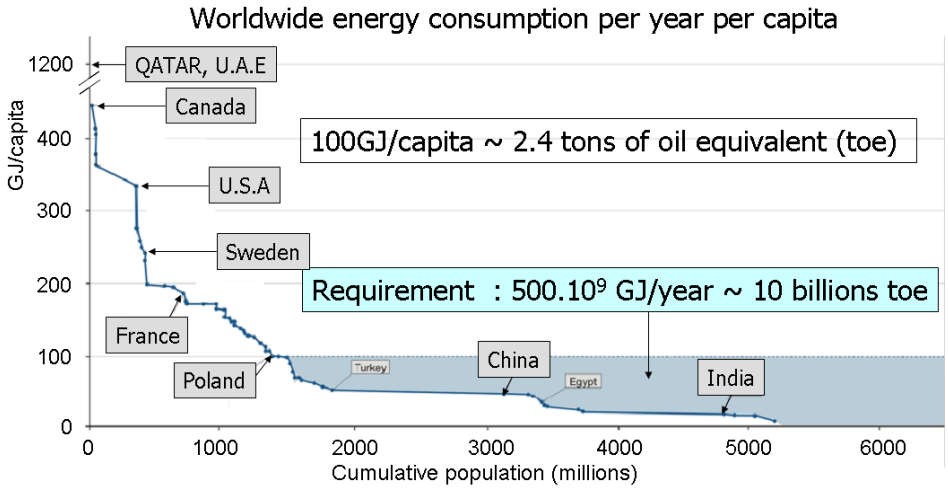

Figure 1.1: *Energy consumption per human over a year , function of the cumulative population. The blue area represent an assessment of the global energy production requirement if the global reference would be the Poland consumption.*

American uses to consume about seven times more energy than a Chinese, and we have to

count with the further development of this country. As an attempt to assess the future energy production requirement related to a global development, we can set a minimum standard of energy consumption, for instance the Poland standard [Caillé 07]. Observing that three quarter of the mankind lives under this standard and assuming that higher standard countries do not change their habits, the additional energy request would be *twice* the current global energy consumption.

From that assessment, we face mainly two critical issues : How long can we burn limited fossil resources, that currently counts for about 80% of the global energy production - see figure 1.2? Can we accept the environmental consequences of mass burning for energy ?

The first issue already gives the answer : According to some estimates, the years of productions left in the ground is about 150 years for coal, 50 years for oil and 60 years for natural gas. Furthermore, that estimate is based on our current consumption rate and does not take into account the possible access of mankind to a minimal standard of living, that seems anyhow unrealistic with these resource conditions. Thus without considering the critical issue of pollution and greenhouse effect, the conclusion is drawn that mankind cannot continue burning fossils for ever : we currently can, but our children should find something else to avoid a global energetic and economical crisis.

Therefore we definitely have to change our way of producing energy than burning fossil re-

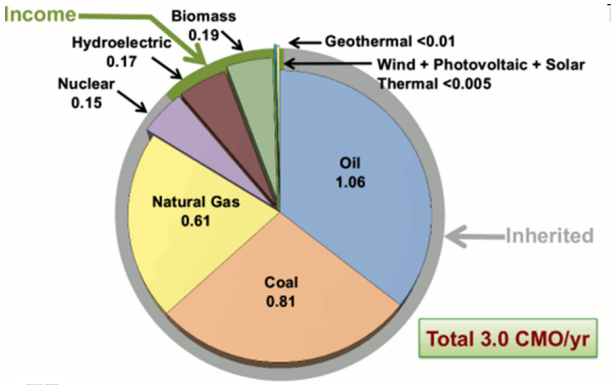

	Consumption Mtoe (2006)	balance
transportation	2180	27%
industry	2226	28%
Residendial	1958	24%
Tertiary	643	8%
Agriculture	181	2%
Other	156	2%
Non-energy	740	9%
Tolal	8084	100%

***Figure 1.2**: Left : Illustration of the different energy sources and their contribution in the global balance; expressed in cubic miles of oil. Right : Balance of the energy consumption between the different needs.*

sources, in accordance with what we do with that energy. Looking in more details, the energy consumption is more or less equality distributed between different needs [Agency 09] : 25 % for either transports or indutry or residential needs. Only 2 % belongs to agriculture - to feed the world, and the rest is shared between services and *non energetic* needs 1.2. Having in mind that rough balance of energy demands, some specific changes could be followed : residentials needs could be provided by local and renewable systems including solar cells and windweels. Transport is a more crucial issue since it is currently totally dependent on oil. Cars are in fact potentially less affected since electrical propulsion is possible - generally said, including all new types of engines indirectly supplied by electricity, but the issue is critical for planes : we are not yet able to design eletrical planes.

Considering industry, the energetic demand cannot be satisfied by renewable energy sources, due to the high powers needed. Combined with the energy demand of the global car fleet, a non burning power plant network is required to supply at least half of the global energy demand. Conventional and future nuclear energy production based on *fission* of heavy atoms may provide the demand at least locally [de l'energie nucléaire 05], but the project faces the realistic argument that nuclear wastes are something we do not really know what to do with. That said, the nuclear energy is generally speaking incomparably efficient compared to burning processes and the nuclear *fusion* appears as a reliable candidate to conciliate all energy production requirements . The following parts are dedicated to the principle of a nuclear fusion reactor and related issues we have to overcome in order to build a fusion power plant.

1.2 The controlled nuclear fusion

1.2.1 The fusion reaction

The basics of nuclear energy production stand in the amount of internal energy stored in an atomic nucleus 1.3. When a heavy nucleus is fissioned into lighter elements the gap in the balance of internal energy is transfered as a kinetic energy to fission products. Similarly, the fusion of light elements produces kinetic energy since the negative binding energy is more important in the fusion product than in the initial nuclei. The efficiency of nuclear reaction to produce energy depends on the binding energy and thus the atomic number of the products and reactants 1.3. Iron nucleus is the most stable element, Uranium is the more reliable natural

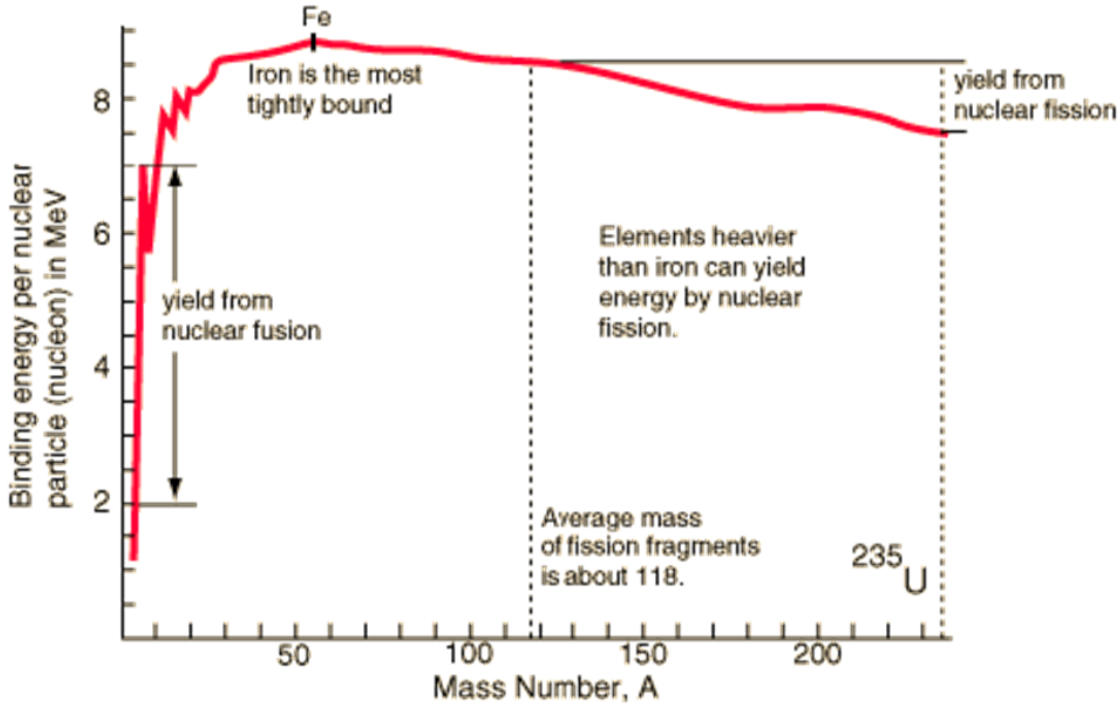

***Figure 1.3**: Binding energy per nucleon function of the atomic number.*

element to produce energy from fission but the reaction is less efficient than fusion: the fusion

of the lightest nuclei - Hydrogen to Boron - is the more reliable source of kinetic energy from a nuclear reaction since the binding energy gap between reactant and products is of the highest amplitude - see figure 1.3. A variety of fusion reactions take place for instance in the Sun, but a few are seriously considered as potential candidates for energy productions 1.1. The main issue encountered in a fusion reaction is the necessity of breaking through the electrostatic repulsion between positive nuclei. Although the tunnel effect helps in the reaction, the kinetic energy of reactants has to be extremely high. In term of thermal energy, most of fusion reaction rates $n\langle\sigma v\rangle$ reach their maximum for temperatures higher than $T \approx 10keV$, or $T \approx 100$ millions of degrees 1.1. This range of temperature is even not found in the center of the Sun, but has to be reached in the reactor to access an efficient fusion reaction rate. In that temperature range, the atoms are fully ionized and form a plasma.
The energy extraction from the fusion reaction follows roughly the same principle as fission reactors : the reaction product - namely neutrons - escape the reaction medium and heat water contained in a dedicated system to produce electricity from a steam machine. But the great difference compared to a fission reactor is the absence of radioactive reaction products 1.1.

reactions					T (keV)	$\langle\sigma v\rangle / T^2$ $m^3.s^{-1}.keV^{-2}$
$D+T$	$\rightarrow$	^4He (3.5 MeV)	+	n (14.1 MeV)	13,6	$1,24 \times 10^{-24}$
$D+D$	$\rightarrow$	^3He (0.82MeV)	+	n (2.45 MeV)	15	$1,28 \times 10^{-26}$
	$\rightarrow$	T (1.01MeV)	+	p^+ (3.02 MeV)		
$D+^3He$	$\rightarrow$	^4He (3.6MeV)	+	p^+ (14.7 MeV)	58	$2,24 \times 10^{-26}$
^3He+Li	$\rightarrow$	^4He	+	p^+ (16.9 MeV)	66	$1,46 \times 10^{-27}$
$p^+ + B$	$\rightarrow$	^4He		(8.7 MeV)	123	$3,01 \times 10^{-27}$

(1.1)

Having in mind the extreme plasma temperature required and the technical possibilities to achieve these conditions, the reaction chosen for a power plant reactor should be the best compromise between high collision efficiency and low reaction temperature - see table 1.1: the $D-T$ reaction is proposed for the first generation of fusion reactors.

1.2.2 The Lawson criterion

The ability of the fusion reaction to produce energy with a reliable economic efficiency depends on the power balance of the reaction: We have to initiate extremely energetic conditions for the reaction to happens and the effective output of energy - via neutrons - has to exceed the external energy input. This criterion is usually hold on the *amplification factor* Q - defined as the ratio of electrical power produced from neutrons over the external input power needed to sustain the reliable plasma conditions. Hopefully the reaction is exothermic for the plasma, meaning that Helium nuclei produced by fusion reactions are potentially able to heat the reactant plasma via collisions. A real power balance has to consider also the energy losses from the medium - via radiations and kinetic losses - and comes to the definition of specific plasma

conditions to obtain the desired amplification factor. A crucial energy loss parameter involved in the definition of these conditions is the energy confinement time τ_E, defined with respect to the thermal energy stored by the plasma W_{th} and the power losses P_{loss} : $P_{loss} = W_{th}/\tau_E$. The final relation is known as the *Lawson criterion* :

$$nT\tau_E = f(Q) \tag{1.2}$$

Where n and T are the plasma density and ion temperature. In practice, an economically viable reactor would require $Q \geq 40$, such that the triple product has to exceed $nT\tau_E \geq 2,7.10^{21}\mathrm{m}^{-3}.\mathrm{keV.s}$.

1.2.3 Inertial versus magnetic fusion

The relation 1.2 highlights three fundamental factors determining a reactor efficiency. As discussed previously, the plasma temperature is somehow imposed to maximize the fusion reaction rate such that plasma parameters that can be manipulated are density and confinement time. Mainly two different approach of the Lawson criterion are effectively considered :

- *The inertial confinement* involves extremely dense plasmas ($n \approx 10^{31}\mathrm{m}^{-3}$) and very short confinement time $\tau_E \approx 10^{-11}$s. The principle is already applied in a thermonuclear weapon and is unfortunately the only current proof of feasibility. The civil use for energy production is based on the compression of small D-T balls with extremely powerful lasers. The confinement time is just the implosion time of the ball.

- *The magnetic confinement* is based on the property of charged particles to be confined into a magnetic field. The densities are lower $n \approx 10^{20}\mathrm{m}^{-3}$ and confinement times are on the order of $\tau_E \approx 1$s, denoting a very efficient confinement technique. Among the variety of magnetic field configurations able to confine a plasma, the *tokamak* configuration represent the most advance scenario toward a power plant application.

1.2.4 The main current tokamaks and the ITER project

Currently, a great number of tokamaks are in activity all around the world. Tore Supra is the tokamak on which have been performed the following studies, located at CEA Cadarache. We could also name ASDEX-Upgrade in Germany, DIII-D in California or JT-60U in Japan. The biggest machine currently running is the *Joint European Torus* (JET) located in England. The purpose of these experiments is to characterize "high performances" plasma conditions in view of building a reactor demonstrator. Up to now, principal limitations are related to the magnetic field sustainment, high power load on the plasma chamber and physical unknown about the plasma itself - confinement time. Although most of the tokamak are not designed to achieve fusion reactions but other specific related issues, the Lawson criterion is hardly achieved: only the JET tokamak has been able to reach $Q \approx 1$ for a few seconds.
Tore Supra is a large tokamak compared to currently existing machines, designed to address a variety of technical and physical issues related to long time discharges. Whereas standard tokamaks are limited to a few tens of seconds due to ohmic heating of their magnetic field coils,

Tore Supra is equipped with supra-conducting coils and active cooling systems for the plasma chamber. That is, a world record has been established in 2003 with a discharge duration of more than 6 minutes and 1.1 JG of energy injected into the plasma [van Houtte 04].
The next tokamak generation is represented by the *International Thermonuclear Experimental Reactor* (ITER). The purpose of this project is to proof that a tokamak can be run in high performance conditions necessary to produce commercial electricity from fusion reactions. The goal is to achieve an amplification factor of $Q \approx 10$, making use of all technologies developed over the world during these last twenty years. In particular, ITER will be the fist machine coupling supra conducting magnetic field coils, high performances heating systems and heating from fusion reactions. As illustrated by the following table, the main difference between a standard tokamak and ITER is on the size of the machine, a crucial technical parameter influencing the energy confinement capability. Indeed, the confinement time scales with the machine size since energy content is roughly proportional to the plasma volume and losses to the surface.

Tokamak	**Tore Supra**	**JET**	**ITER**
Major radius (m)	2.4	3	6.2
Minor radius (m)	0.72	1.25	2
Plasma volume (m^3)	25	155	840
Plasma current (MA)	<1.7	<7	15
Toroidal magnetic field (T)	<4.5	<3.4	5.3
Confinement time (s)	<0.2	<0.9	4
Discharge duration (s)	<minute(s)	<60	>400
Heating power (MW)	<15	<40	100
Fusion power	< kW	(<10MW)	500 MW
Amplification factor Q	$\tilde{0}$	(≈1)	>10

1.3 The tokamak configuration

1.3.1 Confinement of charged particles and magnetic geometry

The magnetic confinement is based on the principle that a charged particle - composing a plasma - follows a cyclotron orbital transversal to the magnetic field that prevents the plasma to reach the wall chamber due to thermal expansion. For a particle of mass m and charge q in a rectilinear magnetic field of strength B, the cyclotron motion is characterized by the Larmor radius ρ_L, that depends on the particle velocity transversal to the magnetic field:

$$\rho_L = \frac{mv_\perp}{qB}$$

Now considering a plasma, the average transversal velocity is roughly the thermal velocity $v_\perp \approx \sqrt{\frac{k_B T}{m}}$. Thus for a burning plasma of $T \approx 10$keV in a magnetic field of about 3T, the

averaged Larmor radius is of the order of $\rho_L \approx 5.10^{-3}$m. Compared to the typical size of the confinement volume - meter-, we effectively have a confinement of the particle motion in the transversal direction. To confine the plasma in the third direction - along the magnetic field, the idea applied in the tokamak configuration consists on closing the magnetic field to form a torus 1.4. Then, particles are in principle trapped in a closed toroidal motion.

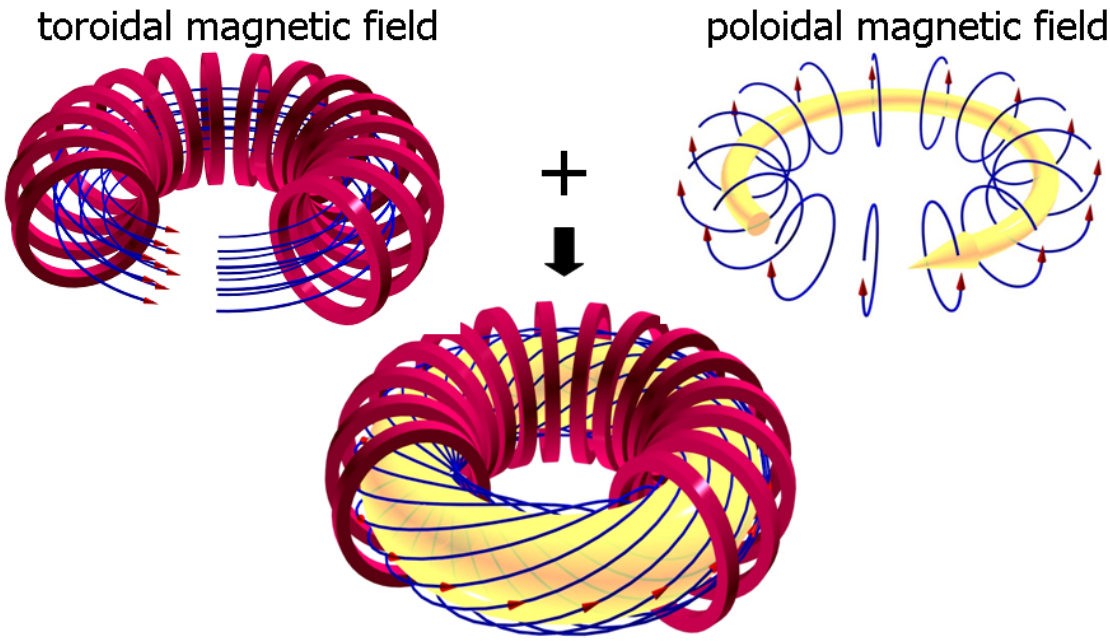

Figure 1.4: *The toroidal magnetic field is produced with a closed solenoid. The poloidal magnetic field is produced by an induced plasma current. The sum defines helix field lines lying on torus surfaces.*

However, the primary configuration consisting on bending the field lines to close them is not efficient to confine the particle. The reason is by bending the magnetic field we create spatial inhomogeneities of the field strength. For a torus configuration, the Ampere's law directly expresses that the toroidal magnetic field strength is inversely proportional to the distance from the center of the torus. For that particular reason, we describe as *high field side* (HFS) the region of the plasma close to the vertical torus center, and *low field side* the region at the outboard of the torus - see figure 1.5. That being, a particle experiences a small variation its Larmor radius during a cyclotron period due to the magnetic field variation along the path - see figure1.5. The result in a tokamak is a vertical drift, whose direction depends on the charge of the particle. Therefore ions and electrons experience a vertical charge separation, leading to the onset of a vertical electric field. The electrostatic drift effect - presented in the next chapter 2.39- leads to a radial lost of particles toward the outer wall of the chamber. For the Tore Supra configuration, the toroidal magnetic field only gives a energy confinement time of about $\tau_E \approx 1$ms.

The initial vertical drift is a secular effect : the particles experience a change of the magnetic field over a distance - Larmor radius - several order of magnitude lower than the scale length

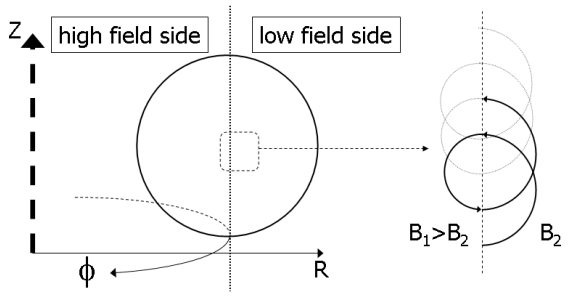

Figure 1.5: *In a non uniform magnetic field, a charge particle experience a secular drift transversal to the magnetic field gradient.*

of the magnetic field variation, meaning that a particle can experience several toroidal turns before effectively leaving its field line. Hence, the drift can be compensated by the free and fast parallel motion of the particle if the field line is enrolled as a helix around the cross section of the torus. Then a particle changes from the plasma bottom to the plasma top during its toroidal motion. The helix geometry of the field lines is obtained by adding a poloidal component to the magnetic field - see figure 1.4. In a tokamak, this component is created by a current flowing into the plasma and the resulting poloidal magnetic field is typically one order of magnitude lower than the toroidal field.
The easiest way to drive this current is by induction : a vertical solenoid is placed in the centre of the torus 1.6 that induces a toroidal electric field in the plasma, accelerating the electrons along the toroidal direction. But for that reason, the discharges are pulsed since it is not possible to induce a steady-state electric field over an infinite time. Some tokamaks like Tore Supra are quipped with electromagnetic wave launchers -Lower Hybrid frequency - able to drive a steady-state parallel electric field in the plasma for a long time.
The electric field drives a constant plasma current due to ohmic dissipations : $j_{//} = \sigma E_{//}$ where σ is the parallel plasma conductivity. A side effect is the ohmic plasma heating by the current flow : on Tore Supra, usual electron temperatures of about 1keV are obtained with no needs of external heating systems. However, since the conductivity increases with plasma temperature , the ohmic heating reaches a maximum before the plasma reaches a temperature in accordance with the Lawson criterion. additional heating systems are then required.

1.3.2 Flux surfaces and conventional coordinates

The detailed geometry of the field lines is in fact more complex than a simple overlay of toroidal and poloidal components, since the plasma is a conducting fluid that influences the onset of magnetic fields in its medium. A relevant approach of the magnetic equilibrium in a tokamak plasma is performed via the magnetohydrodynamics (MHD), and details about the magnetic field geometry can be found in the beginning of the next chapter 2.1.
As a result of the MHD, the magnetic field lines are organized on magnetic flux surfaces corresponding to strictly encased torus - see figure 1.6. A position on these surfaces is labeled by the toroidal angle ϕ , the minor radius r and the poloidal angle θ - see figure 1.8.

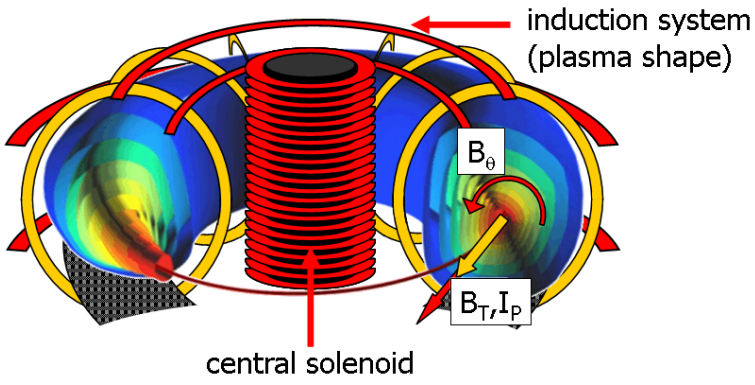

Figure 1.6: *Illustration of the magnetic configuration of Tore Supra : a set of 18 toroidal magnetic field coils creates the toroidal magnetic field component. A central solenoid and a set of vertical magnetic field coils (red) create the poloidal magnetic field component and control the shape of the plasma. The magnetic equilibrium is composed of torus surfaces strictly encased - blue to red surfaces. A bottom toroidal limiter delimits the extent of the confined plasma region*

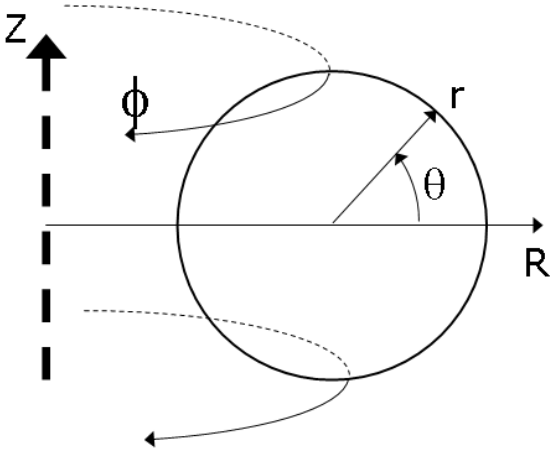

Figure 1.7: *System of coordinates used to describe the geometry of flux surfaces in a tokamak configuration : The vertical axis of toroidal revolution defines the vertical coordinate Z, around which turns the toroidal coordinate ϕ. The major radius coordinate R lyes on the horizontal plane and originates from the torus centre. The minor radius r and the poloidal angle θ defines the coordinates on flux surfaces transversally to the toroidal direction.*

The plasma equilibrium on these surfaces can be in first approach described by a force balance in the ideal MHD approximation :

$$\mathbf{j} \times \mathbf{B} = -\nabla P$$

Where $\mathbf{j}$ and P are respectively the local plasma current and the plasma pressure. Since the local magnetic $\mathbf{B}$ lyes on the flux surface - by definition, the pressure gradient is oriented transversally to the flux surfaces, ensuring that the plasma pressure is in first approximation uniform on the flux surfaces. This property is easily understood by the fact that particles have an almost free motion along the magnetic field. Secondly, the plasma current creates a pressure gradient oriented along the minor radius, leading to an equilibrium where the pressure is higher

at the centre of the flux surfaces. Two major consequences appear : The burning conditions can be fulfilled at the centre of the plasma, and thus energy is better confined with respect to particle losses to the walls. Then, the low pressure at the edge of the plasma ensures a relatively low heat transfer from the plasma to the walls.

1.3.3 Limiter and divertor configurations

The geometric expansion of the plasma is limited by the size of the reaction chamber : close to the walls, the field lines intercept a material component and energy is deposited by the plasma particles. The heat fluxes involved at the wall are extremely high, due to the high temperature of the plasma : the ordering is about tens of $MW.m^{-2}$. In order to prevent wall damages, dedicated components are placed in the chamber to receive and extract this heat load from the plasma. In Tore Supra, a bottom toroidal limiter is installed -see figure 1.6 & 1.8. This limiter is the first material component intercepting the field lines with respect to the plasma centre : it defines the *last closed flux surface* (LCFS), delimiting the core region where field lines are *closed* to the plasma boundary where the field line are *open* and intercept the limiter. We usually call this boundary region the *scrape-off layer* (SOL) where the plasma-wall interaction takes place.

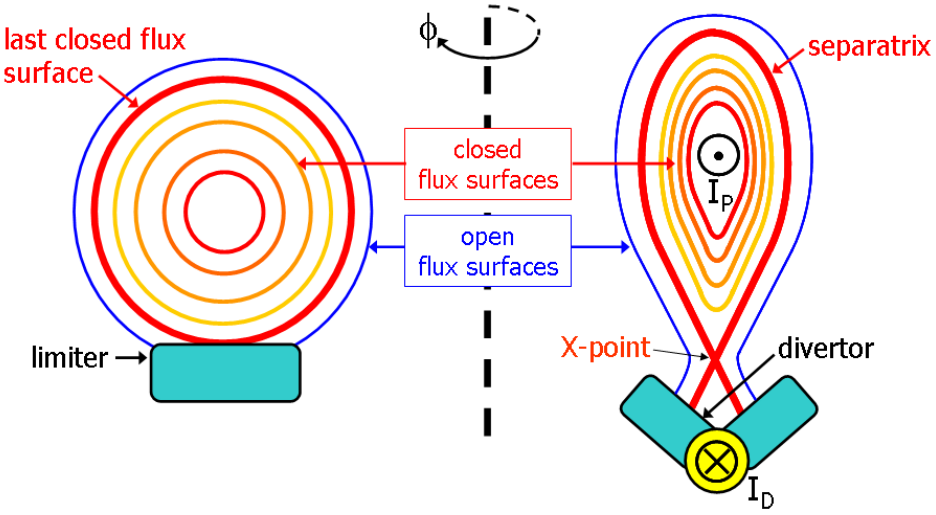

***Figure 1.8**: Poloidal cross section of two geometric configurations. Left : limiter configuration with circular plasma (Tore Supra). The last closed flux surface delimits the border between closed field lines and open field lines. Right : divertor configuration with elongated plasma (JET, ITER). The separatrix delimits the border between closed and open field lines. The poloidal magnetic field is null on the separatrix, that is due to a current flowing into the divertor opposite to the plasma current direction.*

In that limiter configuration the confined region is very close to the limiter and the latter receives a relatively important heat load from the confined plasma. In order to reduce this heat load, the confined region can be effectively put aside from the limiter by changing the magnetic topology in the chamber : this is the x-point configuration - see figure 1.8. Now the main limiter is called *divertor* and receives a lower heat load form the confined region since the

plasma have more distance to flow and can cool down before reaching the divertor surface. An interesting property of a x-point configuration is that the poloidal magnetic field component is null on the separatrix. Hence particles flowing along these field lines can not intercept the divertor - in contrary of particles flowing on the LCFS of a limiter configuration.

1.4 Transport and turbulence

The confinement efficiency of the tokamak configuration is based on the fast parallel motion of the plasma with respect to transversal transport processes 2.3, since it determines how long a particle can survive in the confined plasma. The helix field lines configuration previously introduced is a consequence of that characteristic. However, the pressure gradient caused by the MHD effects leads to an effective plasma state that is out of thermodynamical equilibrium. For instance, the plasma temperature varies over several order of magnitudes from the plasma centre to the last closed flux surface: over a distance of typically one meter. Thermodynamical forces are generated and are responsible for radial transport processes that reduce the energy confinement efficiency.

1.4.1 Neoclassical description

Historically, the first mechanism considered to describe the transport across the flux surfaces was the Colombian collisions between particles. Two particles circulating along two closed field lines can indeed interact via electrostatic forces and drift on other field lines. These collisional effects can be described as a diffusion process since it implies somehow a random walk in a gradient field : this is the *classical transport*. The particle flux transversal to flux surface is proportional to the density gradient and the local diffusion coefficient - classical :

$$\mathbf{\Gamma}_\perp = -D_\perp^c \nabla n$$

Following the idea of a random walk, the classical diffusion coefficient is simply built form the collision frequency ν_c and the typical scale length over which a collision displaces a particle transversally to the magnetic field: the Larmor radius.

$$D_\perp^c = \nu_c \rho_L^2$$

The collision frequency depends on the local density and temperature of the plasma - next chapter 2.23 : $\nu_c \propto nT^{-3/2}$, and varies typically from 1kHZ at the plasma centre to tens of kHz at the plasma edge. Typical values of the classical diffusion coefficient at the edge are in the range of 10^{-4} to $10^{-2}\mathrm{m}^2.\mathrm{s}^{-1}$ for Deuterium ions.
In fact, the torus geometry implies a larger variety of collisional transport processes consequently to the magnetic field inhomogeneity : this is the *neo-classical* description of the transport. For instance, a particle circulating along a field line experiences a variation of the magnetic field strength along the parallel direction - because the magnetic field is inhomogeneous. Since the Larmor precession of the particle can be interpreted as a magnetic momentum oriented along the field line, a magnetic force is effectively applied to the particle $F_{||} = \mu \nabla_{||} B$.

Particles with a low parallel velocity can experience a magnetic mirror effect along their parallel path leading to *banana* orbits located in the low field side of the torus. This particle trapping is responsible for an enhancement of the classical diffusion. Finally, the collision efficiency allows the distinction of different transport regimes characterized by different diffusion amplitudes 1.9.

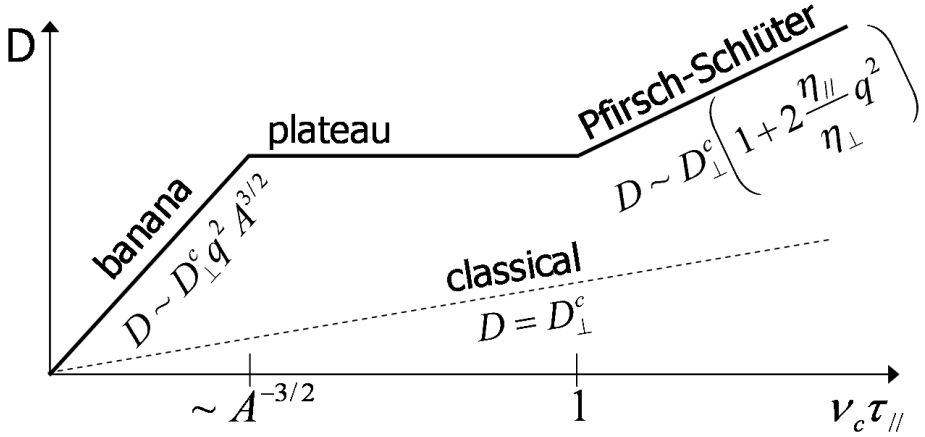

***Figure 1.9**: Classical and neoclassical diffusion coefficient function of the collision rate*

Although the neoclassical approach returns higher diffusion value than the classical description (to a factor of about 100), the model is not able to predict the diffusion coefficients measured during experiments, especially at the plasma edge - see chapter 3 3.8.
Historically, the unexpected high transport coefficient measured in the plasma received the adjective of *anomalous* since nether classical nor neoclassical theories were able to predict these values. Now, we believe and agree that turbulence is a dominant player in the onset of transport across the flux surfaces.

1.4.2 Micro-turbulence

Experimental and theoretical advances about cross-field transport have lead to the statement that thermodynamical forces trigger a strong turbulence across the flux surfaces. The plasma is indeed the place of density, temperature, potential and even magnetic fluctuations that generate transversal fluxes. The consequence of this turbulent transport influences directly the confinement capability of the plasma discharge : weaker gradients across the flux surfaces and lower pressure at the plasma centre 1.10.

One of the dominant mechanism involves a convection drift velocity across the flux surfaces, associated to the fluctuations of electrostatic potential : the *electrostatic drift velocity* - see next chapter 2.3. Electrostatic means that magnetic fluctuations are negligible. This transversal drift is efficient to transport energy or particles if a coupling in time and space exists between the fluctuations of potential - drift - and the considered plasma field fluctuations. For instance, the time averaged drift particle flux is defined as $\Gamma \propto \langle \tilde{n}\tilde{v}_{\text{drift}} \rangle_t$. Thus if the density phase is in quadrature with the velocity drift, the resulting flux is zeros. Different regimes of turbulence involve this electrostatic drift and are characterized by different phase coupling properties

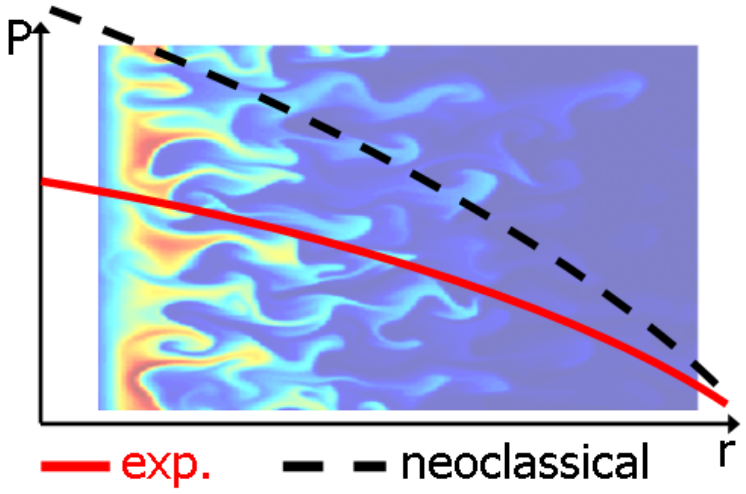

Figure 1.10: *Effect of turbulence on the pressure profiles in the confined plasma: the pressure is lower and the profile is flatter than expected by the neoclassical theory.*

between electrostatic potential and plasma fields [Scott 02].
At the edge of the plasma, the fluctuations of density and electrostatic potential are found to match relatively well the measured fluxes [Fedorczak 10]. However, experimental evidences show that the theoretical understanding of the mechanisms underlying these fluctuations is not yet fulfilled, revealing a crucial issue that current models are not able to describe locally *and* globally the transport behavior in a tokamak. Particularly, a crucial issue encountered in all tokamaks is an experimental density limit criterion, fixing the maximum density value in the confined region before the discharges collapse. A variety of evidences suggest that edge turbulence is involved in the phenomenon by influencing the amount of energy transported across the plasma boundary. But the mechanisms are not yet highlighted.

1.4.3 Transport barriers and H-mode

The turbulence is the dominant driver of energy and particle losses in a tokamak, responsible for an unexpectedly low confinement regime in usual plasma discharges. Having in mind the necessity to achieve high performance discharges, the crucial question is : can we influence this turbulence in order to increase the pressure in the confined region ? The answer is hopefully yes.
In the eighty's, a sudden transition has been observed in ASDEX (Germany) [Wagner 82] that was not predicted at all : the confinement time of the discharge was twice of the usual value together with a consequent increase of plasma pressure. Further investigations have shown that this transition from a *low confinement* (L-mode) to a *high confinement* (H-mode) regime is due to a strong reduction of the transport coefficient just inside the separatrix - the H-mode is mostly achieved in X-point geometry.

The drop of the transversal transport coefficient impacts directly the pressure gradient in that region by steeping the profiles - see figure 1.11. Consequently, the pressure increases inside the *transport barrier* for a fixed loss across the barrier : the confinement time increases.

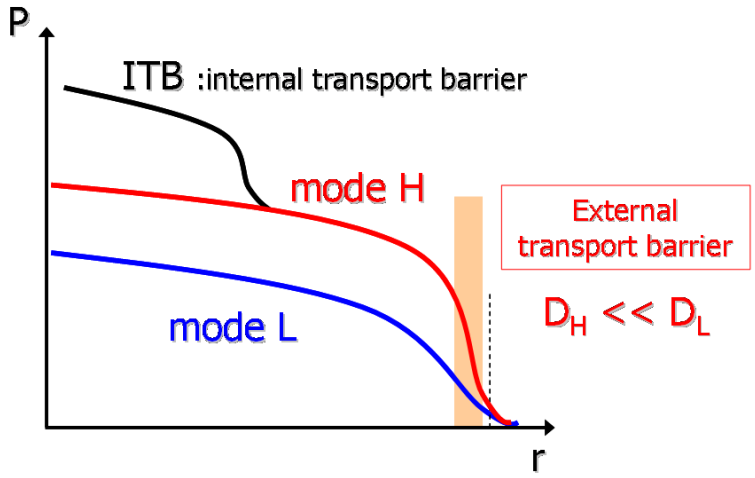

Figure 1.11: *Pressure profiles in different confinement regimes : Low confinement mode (L-mode) in blue, High confinement regime (H-mode) in red, and improved H-mode with internal transport barrier in black.*

Experimental efforts have revealed the role of velocity shear layers in the mechanisms of this transport barrier : the turbulent eddies that naturally transport energy and particles at the edge are spatially decorrelated by a thin and strong poloidal velocity shear just inside the separatrix, namely suppressing the turbulence at that location.
Historically, the H-mode was the first proof that turbulence can be partially suppressed and that a tokamak could achieve higher confinement performances. However, the H-mode is subject to a critical MHD instability that relaxes the high pressure gradient with a frequency in the range of 10 to 1000 Hz. These *edge localized modes* (ELMs) are responsible for an extremely high and transient energy deposition on the plasma facing components, critical for their maintenance. On the other hand, more recent experiments have proven that transport barriers can appear closer to the plasma center without triggering such critical instabilities 1.11. These *internal transport barriers* (ITB) are seriously considered as a further improvement of the H-mode.

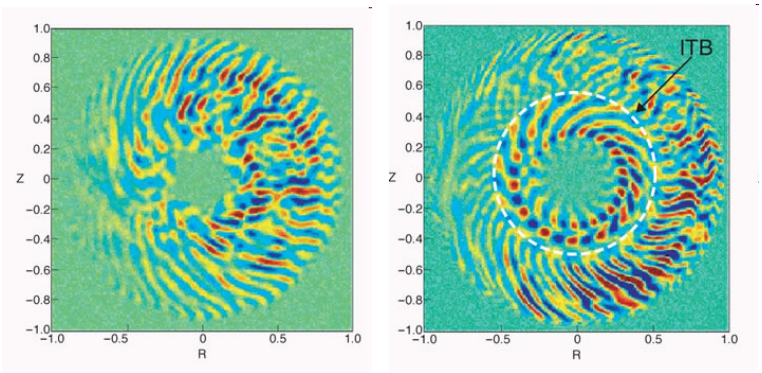

Figure 1.12: *2D map (r,θ) of electrostatic potential eddies obtained from numerical simulations .Left: in usual conditions, elongated eddies are responsible for a fully developed transversal transport from the plasma centre to the edge. Right : a poloidal velocity shear is formed at mid-radius that decorrelates the potential eddies : this is an internal transport barrier*

Numerical simulations are able to reproduce these phenomena 1.12, by forcing a velocity shear layer in the fluctuating field. However, the mechanisms underlying the onset of these barriers are not yet resolved. The critical issue in the understanding is to predict the plasma conditions necessary to trigger a H-mode on ITER, that is currently based on scaling laws built from different tokamak experiments. Some experimental evidences suggest that turbulent transport happening at the plasma boundary - outside the separatrix or last closed flux surface - can have a feedback on the confined plasma and thus participate on the onset of a transport barrier. In that framework, the studies presented in the thesis bring some crucial elements about edge transport.

1.5 Plasma edge of a Tokamak

The plasma edge is in our definition the plasma volume *outside* of the last closed flux surface or separatrix. In that region usually named *scrape-off layer* (SOL), the field lines are *open* to a material component, namely a limiter or divertor where particles deposit their kinetic energy - see figure 1.13. The SOL is therefore the boundary region between the confined plasma loosing energy and particles and the plasma facing components receiving these fluxes. Although

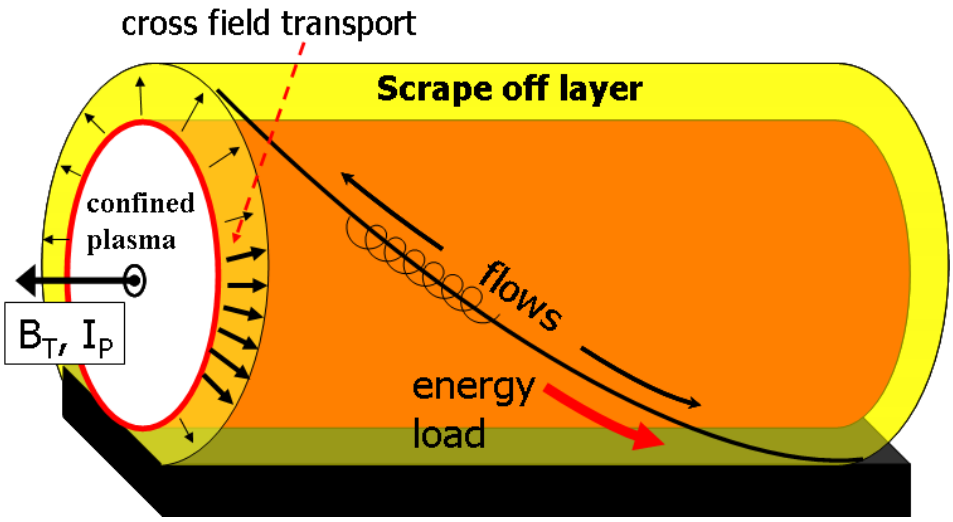

Figure 1.13: *Toroidal section of a circular plasma in contact with a bottom toroidal limiter. Outside the LCFS, the field lines end on the limiter plates, where particles deposit their kinetic energy.*

the SOL plasma does not directly participate to the balance of the confinement efficiency, its properties govern directly different key points of a discharge :

- The radial extent of the plasma in that region determines the heat load amplitude and location on the set of plasma facing component.
- It is the first environment of heating system. The propagation of electromagnetic waves from the antennae and thus their coupling efficiency of is directly influenced by this first layer.

- Strong parallel flows develop in that region, due to the symmetry breaking established by the presence of limiters. These flows have direct impacts on the migration of impurities in the chamber and *are suspected to influence the core rotation.*

The plasma edge and the related transport phenomena are in the scope of this thesis. Since the SOL is directly filled by losses across the last closed flux surface, we somehow generalize the edge plasma to the SOL plus the most external flux surfaces just inside the LCFS.

1.5.1 Losses across the last closed flux surfaces

In a tokamak, the energy lost from the confined region follows two main mechanisms : radiations and kinetic losses. The first mechanism is mainly due to the impurity content and the natural bremsstrahlung [1] emissions from hot plasmas. The second mechanism corresponds to thermal energy losses across the last closed flux surface and is a direct player in the confinement efficiency of the discharge. For instance, operational limitations (density limit) involve edge transport processes whereas the H-mode corresponds to a strong reduction of these losses.
By studying the SOL plasma, we have in fact a indirect information about its source : the losses across the last closed flux surface. Namely, we can estimate the particle flux and energy flux, and thus separate the different mechanisms transporting the energy out of the confined region : *energy convection* - carried by mass or particle transfer - and *energy conduction* - carried by momentum exchange without mass exchange. As we show along the thesis, the different mechanisms behave differently when plasma density is changed, inferring a probable mechanism in the density limit phenomenon.

1.5.2 Plasma-wall interaction

The contact of the plasma with material components - called *plasma facing components* gives raise to complex physical processes, including numerous atomic processes between the plasma particle and the material components:

1. The charged particles striking the surface are neutralized by ion-electron recombination. The neutrals produced can escape from the magnetic field trapping and migrate until they are ionized via electron collisions in the plasma. This phenomenon refuels the plasma from its losses : we call it *recycling.* We estimate that more than 95% of the particles leaving the confined plasma re-enter the confined region as neutrals.

2. Some particles like Hydrogen isotopes have a potentially high chemical affinity with the wall materials, especially with carbon. Two main processes are involved :

   - the incident ion enters the bulk matrix and is trapped their due to chemical bounds. This *retention* phenomenon is particularly annoying for a thermonuclear reactor since it means that a significant amount of Tritium could be trapped in the walls for a long term. Tritium removal techniques have to be developed especially if carbon components are present in the machine.

[1] when electrons brake duo to collisions, they emit electromagnetic waves

- The incident ion can chemically react with atoms or molecules composing the material component to form a volatile molecule that can easily detach from the surface: this is the *chemical sputtering*.

3. The incident ion has a sufficient kinetic energy to sputter particles composing the surface : this is the *physical sputtering*.

These phenomena have a direct influence on the plasma discharge by producing impurities that enter and pollute the confined plasma. The major effect is a significant contribution on the radiated losses since high Z materials sputtered from the wall can emit energetic photons even in the plasma center - this is especially the case for Tungsten machines. The discharge can even collapse due to unbalanced radiation losses from high Z impurities, defining narrow operational regimes for high performances scenarios.
On the other hand, these impurities can help to radiate the energy contained in the SOL plasma in order to decrease the heat load on plasma facing components. This is one of the main advantage of a divertor machine, since the confined plasma is in that configuration relatively far from the impurity sources.

1.5.3 The SOL width

The radial extent of the plasma in the SOL has direct consequences on the operation of a discharge. The energy flux lost from the confined region across the LCFS is directly deposited on the first limiter, over the SOL width. Thus if the SOL width double, the heat flux peak should be reduced by a factor of two, although new surface elements receive a heat flux 1.14. As we discussed it along the next chapters, the radial extent of the SOL plasma is direct conse-

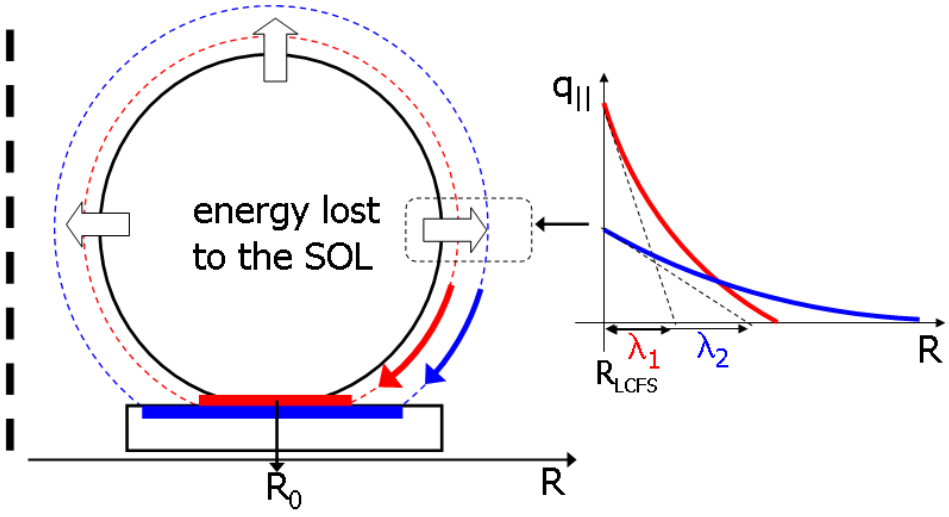

***Figure 1.14**: Poloidal cross section of a limiter tokamak. The change in the heat load pattern is illustrated when the radial width of the SOL λ is virtually changed for a given energy input into the SOL from the confined region.*

quence of the flux balance between the parallel and the radial direction : the radial profiles are mostly exponentially decaying and the radial width is proportional to the transport coefficient.

Thus, contrary to the confined region, we would prefer a large transport coefficient within the SOL to spread the heat flux on a large area. Unfortunately, the transport in the SOL is a consequence of the transport crossing the LCFS and both are not or rarely decoupled : The SOL width is large if the transport coefficient is significant in the SOL, inferring large energy losses across the LCFS. For instance, the ordering of energy loss across the LCFS of tore Supra is $P_{loss} = 1MW$. The radial SOL width is about $\lambda = 3$cm such that the deposition surface integrated toroidally is about $A = 2\pi R_0 2\lambda \approx 1\text{m}^2$, where $R_0 = 2.4$m is the major radius of the LCFS contact point and the factor 2 is to count the two striking areas in the SOL. Finally, we come up with heat flux of the order of $q = P_{loss}/A \approx 1\text{MW.m}^2$ on the main limiter, inversely proportional to the SOL width.
An other important issue related to the SOL width is the density profile facing the wave launchers. A lot of efforts are done to simulate and predict the heating waves coupling efficiency with the confined plasma, and this efforts have revealed that the density profile in the SOL and in the closed vicinity of the antenna surface is a key parameter especially for LH waves. Most of the time, the launchers are hidden behind limiters and the SOL plasma in that region is hardly measurable with conventional diagnostics. Then a density transport model has to be used to evaluate the density profiles in that regions, but the modeling faces a critical issue : do we precisely know the local value of the transport coefficient ?

These issues related to the SOL width and its relation with the transport mechanisms in the SOL are investigated along the thesis.

1.5.4 Parallel flows

The plasma equilibrium in the SOL is dominated by the physics related to plasma-wall interaction - developed in the next chapter. In particular, near sonic flows are driven along field lines to the limiter plates due to particular electrostatic boundary conditions. But the distribution of these flows around the plasma is directly influenced by the transport mechanisms. In turns, these flows have a direct consequence on impurity migrations, since heavy neutrals are subjects to drag forces driven by the plasma. It leads to preferential deposition areas where impurities accumulate and can form thick and volatile deposits dangerous for high performance discharges. The knowledge of these areas location is critical to establish the discharge scenario, but needs knowledge about the underlying mechanisms : the flows.
More recently, experiments have highlighted the possible role of these boundary flows on the rotation of the confined plasma. Indeed, the velocity shear layers related to transport barriers are a particular property of the plasma rotation field and the influence of the boundary conditions setup in the SOL are worth being evaluated carefully.
Along the thesis, we focused on the mechanisms able to drive the parallel flows in order to build a global picture of the flow distribution around the plasma.

1.5.5 Diagnostics dedicated to edge plasmas

Experiments are based in a simple principle, that phenomena can be observed. From these observations, we can draw conclusions by means of analysis and then build models to explain the different observed behaviors. That how physics evolve.
The observation in a tokamak is critical due to extreme conditions imposed by the hot plasma. Diagnostics have to suffer strong magnetic fields, high ambient temperatures due to plasma heating. Data suffer relatively high noises due to strong electrostatic fluctuations in the plasma chamber. Since decades, the expertise has increased in the field of diagnostics : new principles to measure given plasma parameters, new electronics allowing better data acquisitions.
On Tore Supra, the set of diagnostics have taken benefits of the improvements : radars to probe the plasma with waves, ultra-fast visible imaging to picture the turbulence, fast electronic acquisitions for probes to record the electrostatic fluctuations are some illustrations.
For the experimental investigation of the turbulent transport proposed along the thesis, we made use of mainly three diagnostics:

- A reciprocating Langmuir probe, operating at the plasma top. It consists on a probe head composed of electrodes that collect the charged particles. The voltages or currents measured give informations about the time averaged : plasma density, temperature, electrostatic potentials, parallel flows. The probe can move vertically from the wall to typically the LCFS by means of hydraulic systems. The full reciprocation into the plasma lasts less than 200ms to avoid an over heat load on the probe.

- A second reciprocating probe located at the top, but consisting on small arrays of collectors dedicated to fluctuations acquisition with a high frequency (1MHz). The system was new when we started the experiments with, and we had to develop the acquisition and control systems as well as treatment routines. We experienced the extreme conditions suffered by the electronics in a tokamak environment, like changing once a day some electronics components. More dramatically, we learned about the disastrous mistake of using the probe at the wrong time in the wrong plasma, resulting in the full melting of the collectors. But finally, crucial informations about the local plasma fluctuations have been obtained.

- A fast visible camera installed at the beginning of the thesis, that could be used to picture some particular transport phenomena at the plasma edge with a temporal resolution of about 30kHz. Observations have revealed crucial qualitative informations about the spatial distribution of fluctuations around the plasma.

Preparing a diagnostic on a tokamak is really time demanding, especially when the system is new and has not been validated by a routinely use. But the result of all these efforts shared with other experimentalists is that during dedicated experimental sessions, we have been able to operate these three diagnostics with success.
We used data collected by other diagnostics when possible, to confront the observations or conclusions drawn from the previous systems. For instance, the density measured with the

probe has been compared to the density measured with a sweeping reflectometer and a laser interferometer. The velocities measured on the fluctuating field of the fast imaging have been compared to the velocity profiles measured with a Doppler back-scattering reflectometer - see figure 1.15.

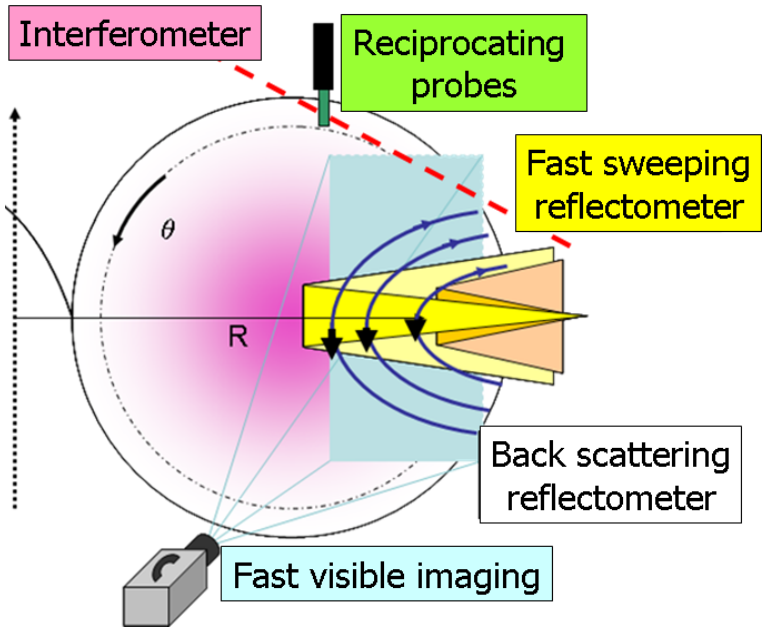

Figure 1.15: *Poloidal cross section of the Tore Supra tokamak, illustrating the set of diagnostics used during the thesis*

1.6 Thesis outline

Experimental investigations of edge transport have been performed on a variety of tokamaks since decades, and have highlighted critical issues to resolve in order to build a consistent transport model from observations : Why local fluctuations amplitude do not quantitatively match the radial extent of density profiles ? How fluctuations are distributed around the plasma ? What are the mechanisms able to drive the near sonic parallel flows encountered at the plasma edge ? How does the turbulence across the LCFS evolves at high density? Finally, do we have a global model for the transport at the edge, consistent with all experimental observations ? the obvious reason why we look for a global transport model built on experimental observations is that theoretical models are not yet able to explain or predict the encountered plasma behaviors. For instance it has been accepted for decades that edge turbulence is homogeneous along the field lines such that 2D models should give a reliable picture of edge transport. But recent experimental evidences suggest that the turbulence is strongly non uniform along the field lines, resulting in critical 3D effects like parallel flow generation, out of the scope of 2D models. Similarly, this 2D assumption has somehow formated the ideas that local turbulence properties reflect the global plasma behavior. For that reason the confrontation of different observations have often lead to contradictions.

Our approach of the problem has been only based on the idea that turbulence is potentially non uniform around the plasma. By making use of the set of diagnostics available on Tore Supra, we confronted different informations :

- The time averages probe profiles of density or parallel flow strength, that consist on a *quantitative and global* information about the turbulent transport all around the plasma.
- The fluctuations measured with the other reciprocating probe, that is a *local and quantitative* information about the local turbulence.
- The fast imaging gives a qualitative understanding of the *spatial distribution* of the fluctuations.

Namely, we have *a priori* a closed set of observations toward a consistent experimental model able to conciliate the link between local turbulent flux, spatial asymmetries, density profiles and parallel flows.
Apart from this model, we have tried when possible to characterize the effect of density on the transport parameters at the last closed flux surface.

In the second chapter of this manuscript we present the basics physics of magnetized plasma in the frame work of our investigation. We first introduce the fluid model and approximations followed in a pragmatic approach. Then we describe the fundamental concept of drift velocities that are the basement of transport processes across the field lines. Afterward we present in detail the particular physics of open field lines (the SOL physics) by focusing on the plasma-wall interaction phenomena. Finally we describe the principle of Langmuir probes and the related theoretical models, and their consistency is discussed in the scope of experimental evidences.

In the third chapter, we focus on data collected by probes and their interpretation in terms of particle fluxes. The first part is devoted to steady-state approach of density and parallel flows profiles in term of flux balance. We show that at least in Tore Supra, the parallel flows are mainly driven by the radial particle flux asymmetry and we propose a model to evaluate the radial flux integrated along field lines. We demonstrate a first evidence of the particle flux asymmetry, mainly located at the low field side of the torus. The second part is dedicated to electrostatic fluctuations. After a brief introduction to the new diagnostic, we introduce the particularities of edge plasma fluctuations : intermittency, coherency and phase coupling between fluctuating fields. Some precautions and issues related to usual treatments are highlighted, like electric fields under-sampling or evaluation of phase velocities from time lags. Finally, the radial flux from drift fluctuations is presented and coherency with density profiles is discussed.

The forth chapter is devoted to the fast visible imaging. The diagnostic setup is described and the critical plasma conditions for the visualization of plasma fluctuations are presented : fluctuations imaging needs either very high plasma density or gas puffing to increase artificially the local visible emission. *Passive* and *Active* imaging are treated in two different parts. The

spatial properties of the fluctuations are focused, namely the spatial nature of the fluctuations, if they exist inside and outside the last closed flux surface and if they are uniformly distributed around the plasma. When possible, the velocity fields are extracted and compared with other diagnostic measurements.

The fifth and last chapter is dedicated to put into consistency all the observations : steady-state flux asymmetries, local turbulent flux and nature & asymmetries of fluctuations revealed by the fast imaging. We present a dedicated experiment aiming at mapping the spatial asymmetries of the steady-state radial flux in the SOL, and then check the consistency of this mapping with a variety of experimental observations. We conclude that the spatial asymmetries of the turbulent flux are resolved, as their role on the onset of near-sonic parallel flows. Finally we discuss the possible mechanisms that could explain these crucial spatial properties of the turbulence and open the discussion about the parallel flows influence on the confined plasma rotation.

Chapter 2

Description of particle transport at the plasma edge

This chapter is devoted to the description of the physical concepts underlying the experimental study of particle transport at the plasma edge. In the first part we present the magnetic geometry of a tokamak plasma. Our intention is focused on the circular geometry of Tore Supra plasmas and the related analytical simplifications we performed to describe the field lines geometry. In the second part we introduce the general system of fluid equations related to plasma particle transport, then simplified according to the previous geometrical considerations and some experimental evidences. The fundamental concept of drift velocity in magnetized plasma is described in the third part, leading to further simplifications of the fluid model. Then in a forth part, we describe the particular physics of opened field lines - the scrape-off layer, where the plasma equilibrium is dominated by the plasma-material interaction through the physics of plasma sheath. The last part is dedicated to the issue of plasma-probe interaction, where we present the principle and models related to Langmuir probe measurements. We bring some elements of validation and limitation of the models, in the scope of experimental evidences obtained during Tore Supra experiments.
The ideas and conclusions presented herein are a personal effort of synthesizing some common descriptions of magnetized plasma physics.

2.1 Description of the magnetic geometry

When studying plasma transport in a strong magnetic field, a convenient system of coordinates can be adopted that is defined by the magnetic field lines. Generally speaking, the motion of a charged particle can be divided into a fast gyro motion around a gyro centre that follows an almost free trajectory along the magnetic field lines, except some lower order orthogonal drifts. Consequently, field lines and thus magnetic flux surfaces on which they lie are of constant pressure, which makes a label of those surfaces of great interest. Moreover, some effects of orthogonal transport - including orthogonal drifts - directly involves spatial properties of the magnetic topology like magnetic field gradients, that makes a local parametric description of the magnetic field a necessity to study the plasma transport.
In a tokamak, the magnetic field is a sum of contributions from the set of external coils and

from the current flowing into the plasma, either induced by the central solenoid or in some specific cases continuously generated by dedicated systems. In general, the equilibrium is calculated via the ideal magneto-hydrodynamics (ideal MHD) that describes the electron force balance - involving the local pressure p and current $\mathbf{j}$ - coupled with Maxwell equations:

$$\nabla p = \mathbf{j} \times \mathbf{B} \tag{2.1}$$

$$\nabla \times \mathbf{B} = \mu_0 \mathbf{j} \tag{2.2}$$

$$\nabla \cdot \mathbf{B} = 0 \tag{2.3}$$

The magnetic component due to external coils is often calculated as a vacuum component - without plasma - via the equation 2.2, from the currents distribution in the set of external coils. For instance the toroidal magnetic field component is approximately :

$$\mathbf{B}_T(R) = \frac{\mu_0 N I_{TOR}}{2\pi R} \mathbf{e}_\phi \tag{2.4}$$

Where N is the total number of spires composing the set of coils, I_{TOR} is the oriented circulating current in one spire and R is the major radius coordinate. In fact, this expression is a toroidal average over the magnetic field modulation - called *ripple* - due to the discrete number of coils 2.1.

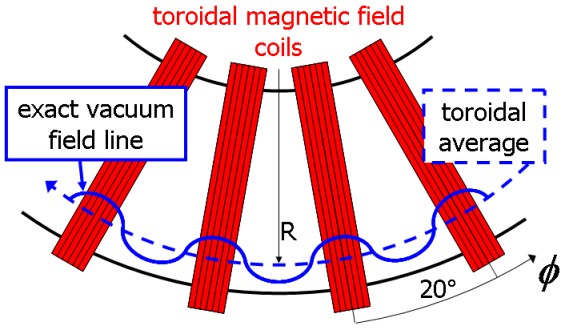

Figure 2.1: *Top view of a toroidal section of a tokamak with schematic toroidal field lines. Due to the discrete distribution of coils, the vacuum magnetic field is not toroidally uniform but is stronger under the coils. The vacuum field lines experience a radial modulation called ripple. On Tore Supra, the poloidal wave length is 20 ° and the radial modulation is in the order of 1cm.*

On Tore Supra, the modulation amplitude is relatively high (about 8%), which does lead to specific transport phenomenon in the confined region [Connor 73] concerning plasma rotation. Concerning the SOL, the dominant effect is a modulation of the plasma footprint on the toroidal limiter going aside with a complex picture of field line connection very close to the last closed flux surface, complexity that we have decided to let aside from our study due to its very localized characteristics.
The poloidal component of the magnetic field can be deduced from the previous MHD system rearranged in a convenient expression known as the Grad-Shafranov equation [Garbet 07]. This equation involves the poloidal magnetic flux variable, defined as the magnetic flux across a surface enclosed by a toroidal field line. The divergence free 2.3 of the magnetic field ensures

that for a given poloidal flux value, the corresponding set of surface outlines describes a new surface on which lies the magnetic field, namely a *flux surface* 2.2 labeled by the poloidal flux value.

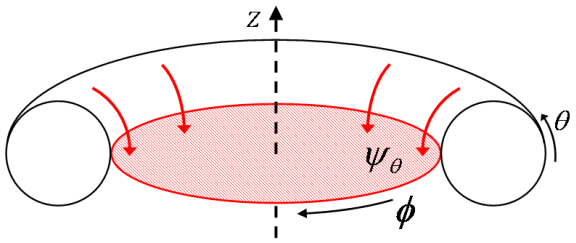

***Figure 2.2**: Illustration of a poloidal magnetic flux surface (red) centered on the vertical axis. For a constant flux, the outline curve describes a surface named magnetic flux surface (black) on which lies the field lines.*

Again, the divergence free of the magnetic field ensures that these surfaces are strictly encased and therefore can be labeled by an unique parameter that is obviously the poloidal flux value, but could be their minor radius as well. Different numerical codes are routinely used to solve the Grad-Shafranov equation from experimental parameters, like the vacuum magnetic field created by external coils, plasma current profiles, wall induced currents and boundary magnetic measurements given by sensors surrounding the vacuum vessel. The main source of errors stands in the uncertainty related to the current profile calculation when dedicated diagnostics are not available, and consequently in the inward extrapolation of boundary magnetic measurements.
In the case of SOL magnetic equilibrium the previous issues are less dramatic due to the proximity of the sensors, and the local current is known to be very weak or null due to the local high resistivity and low density. The local poloidal magnetic field is thus assumed to be created by the bulk current only which is easily measured. On the Tore Supra experiment, a dedicated edge magnetic reconstruction tool [F. Saint-Laurent 08] has been developed and validated, that extrapolates the local magnetic field vector and allows a precise field line tracing with a less than 1% error in the SOL. The local parallel connection length defined as the length of a field line between its two strike points is easily readable as well as the position of these two boundaries, which are crucial informations we need in the scope of precise SOL transport studies.

2.1.1 Circular approximation

Generally speaking, solving the Grad-Shafranov equation requires a numerical approach to deduce the local magnetic field components and thus the field line geometry, that is not convenient in order to work with relatively simple analytical descriptions of transport equations. A convenient way to reach that state of description is to follow some simplifications related to the equilibrium geometry: the ripple is neglected, we assume a toroidal symmetry of the plasma and we consider that magnetic flux surfaces are assimilated to torus with circular cross sections - that is almost true in Tore Supra. The geometry is also assumed to be in a large aspect ratio limit, meaning torus of large major radius compared to their minor radius. As

it is explained in the following, this set of simplifications lead to a relatively simple analytic description of the field lines geometry.
As a starting point, it is worth introducing a reference flux surface defined as the Last Closed Flux Surface (LCFS) with minor radius a and center major radius R_{pl}. This surface is defined within the set of enclosed magnetic flux surfaces from the plasma center as the first one intercepting the main limiter. The inverse aspect ratio $\epsilon = \frac{a}{R_{pl}}$ is the perturbative parameter for Taylor expansions of equations describing the flux surfaces - standard Tore Supra equilibrium gives $\epsilon \approx 0.3$. We also introduce the normalized minor radius of any flux surface to the LCFS radius $\rho = r/a$. The circular geometry implies that a flux surface is completely labeled by its

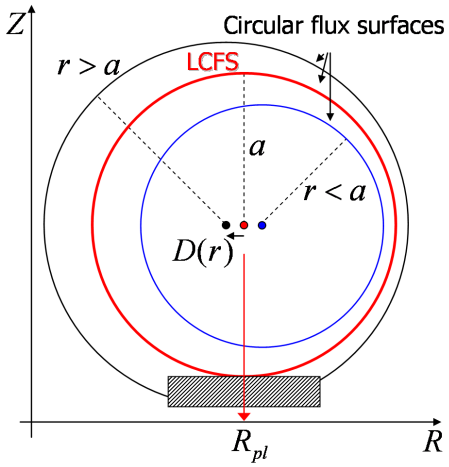

Figure 2.3: *Shifted circular equilibrium in the poloidal plan. The Shafranov shift $D(r)$ is defined from the center of the LCFS*

normalized minor radius ρ, dealing either with its shape or its center - since they are strictly enclosed. On the other hand, the position of the center is not straightforward since the pressure equilibrium described by ideal MHD 2.1 together with the non-uniformity of the magnetic field strength 2.4 - due to torus curvature - leads to a concentric radial shift of the full equilibrium towards the outboard: this is the well known Shafranov shift 2.3. In our equilibrium description, it is convenient to define that shift $D(r)$ with respect to the LCFS center: given a labeled flux surface with center position $R_c(\rho) = R_{pl} + D(\rho)$, the $D(r)$ expression will be derived from the poloidal magnetic field expression. For the SOL magnetic field description, the latter is a direct and only consequence of the bulk current and should be obtained with the Maxwell-Ampere equation. However the torus curvature leads to a poloidal inhomogeneity of the component, and the Grad-Shafranov equation is again needed to explicit it. An explicit formulation in a first order expansion has been taken from the literature [Garbet 07], that indirectly links the poloidal magnetic field component with the Shafranov shift :

$$\mathbf{B}_p(r,\theta) = b_p(r)\left[1 + \rho\epsilon\Lambda\cos\theta\right]\mathbf{e}_\theta \tag{2.5}$$

Where we introduced a dimensionless parameter $\Lambda = (\beta_p + l_i/2) - 1$ involved in the Shafranov shift: β_p is a pressure parameter and l_i is an internal inductance parameter. They are defined as integrals over the plasma enclosed by the surface of interest, but in the case of edge consideration

the contribution for $\rho \geq 1$ is negligible. Thus the parameter Λ is assumed to be constant in the SOL and corresponds in fact to an output validated parameter of a Tore Supra discharge. In the same manner, the current is neglected in the region $\rho \geq 1$ leading to the expression of the mean part of the poloidal field :

$$b_p(r) = \frac{\mu_0 I_{pl}}{2\pi r}$$

For geometrical considerations it is convenient to introduce the *edge safety factor* defined with the magnetic field strength at the reference position :

$$\boxed{q_a = \epsilon \frac{B_{T,pl}}{b_p(a)}} \tag{2.6}$$

Where $B_{T,pl}$ is the toroidal component amplitude at the LCFS center and $b_p(a)$ is the poloidal mean component on the LCFS. As shown in the following, the safety factor describes the helicity of field lines lying on the LCFS. From MHD stability criteria, this safety factor should not be less than units (typically 3), fixing a upper limit to the plasma current with respect to the given geometry and toroidal field strength. That said, the introduction of this parameter in the magnetic field expression makes almost explicit the ordering in ϵ expansion:

$$B_T(r,\theta) = \frac{B_{T,pl} R_{pl}}{R_p l + D(r) + r\cos(\theta)} \tag{2.7}$$

$$B_p(r,\theta) = \epsilon \frac{B_{T,pl}}{q_a \rho} \left[1 + \rho\epsilon\Lambda\cos\theta\right] \tag{2.8}$$

Remains only the Shafranov shift expression to obtain the fully explicit expansion of the magnetic field components.

The Shafranov shift The shift expression can be directly deduced from poloidal flux conservation criteria in the circular approximation. Let us consider two flux surfaces (r_1, r_2) infinitesimally close $|r_1 - r_2| \ll r_1$, centered on R_1 and R_2. For convenience, let us introduce the generic positions $r \approx r_1 \approx r_2$ and $R \approx R_1 \approx R_2$. About incoming geometrical flux considerations, the picture 2.4 can be helpful. Let us consider a magnetic flux surface, labeled with the radius r. By definition of the poloidal magnetic flux associated to that flux surface, the flux calculated across a surface (Z=constant) strictly inside the circular section is null. From the picture 2.4, we get $\Psi_\theta^{S_1} = \Psi_\theta^{S_2} = 0$, where S_1 and S_2 are the surface lying inside the circular sections r_1 and r_2. Thus, an equality is obtained on flux calculated across the two annulars surrounding the smaller circular section, that are the complementary parts of S_1 in S_2 : $\Psi_\theta^{S_L} = -\Psi_\theta^{S_H}$, rewritten in term of magnetic field and surface $S_L B_p(r,\pi) = S_H B_p(r,0)$. The surface area are easily expressed from geometrical parameters involved in the problem, assuming the Shafranov shift to be a second order term in ϵ:

$$S_L = \Delta_L 2\pi(R - r) = 2\pi(r_2 - r_1)\left(1 - \partial_r D(r)\right)(R - r)$$

$$S_H = \Delta_H 2\pi(R + r) = 2\pi(r_2 - r_1)\left(1 + \partial_r D(r)\right)(R + r)$$

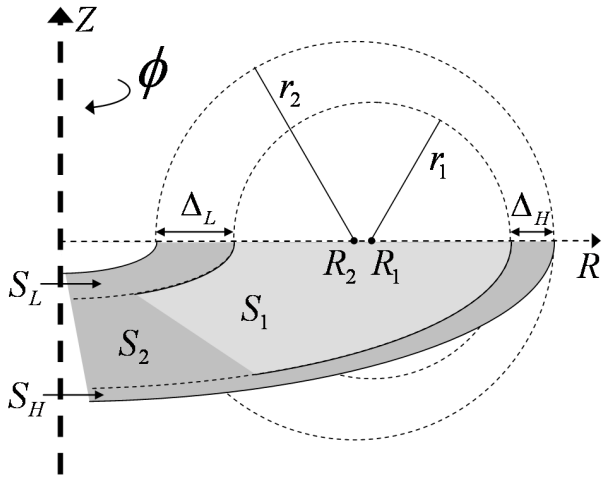

***Figure 2.4**: Picture of a circular equilibrium, with two poloidal sections r_1 and r_2 and different poloidal flux surfaces: S_1 for the flux strictly inside the section r_1, S_2 strictly inside the section r_2 as well as S_H and S_L for the complementary parts of S_1 inside S_2.*

From the previous poloidal magnetic field expression 2.8, we turn out a differential equation on the Shafranov shift function of the minor radius:

$$\partial_r D(r) = -\epsilon(1+\Lambda)r$$

By definition, the boundary condition is $D(a) = 0$ leading to the final expression of the Shafranov shift in circular approximation function of the label ρ :

$$\boxed{D(\rho) = \frac{1}{2}\epsilon^2(1+\Lambda)\left[1-\rho^2\right]R_p l} \tag{2.9}$$

We have *a posteriori* checked the second order assumption of the shift, that can be inserted in the magnetic field expression.

2.1.2 Field line parametrization

The previous analytical expressions of the magnetic field give a straight way to write the parametric equations describing the SOL field lines. As a matter of interest, we will introduce a curvilinear system of coordinates defined with the local magnetic field on a given flux surface 2.5. Transport equations involving magnetic fields - described in the next part - can be strongly simplified by projecting them along the local magnetic field, which make such a curvilinear coordinate system convenient. The parallel coordinate is oriented along the magnetic unit vector $\mathbf{b}$ and the radial coordinate is along the minor radius axis $\mathbf{e}_r$. The orthonormal referential is completed by introducing a transverse axis tangent to the flux surface and normal to the magnetic field : $\mathbf{e}_\perp = \mathbf{b} \times \mathbf{e}_r$. The curvilinear position is labeled either by the poloidal or toroidal angle from the set of equations describing a field line:

$$\rho = \text{constante} \tag{2.10}$$

$$\frac{r d\theta}{R d\phi} = \frac{B_p}{B_T} \tag{2.11}$$

$$ds_{||}^2 = R^2 d\phi^2 + r^2 d\theta^2 \tag{2.12}$$

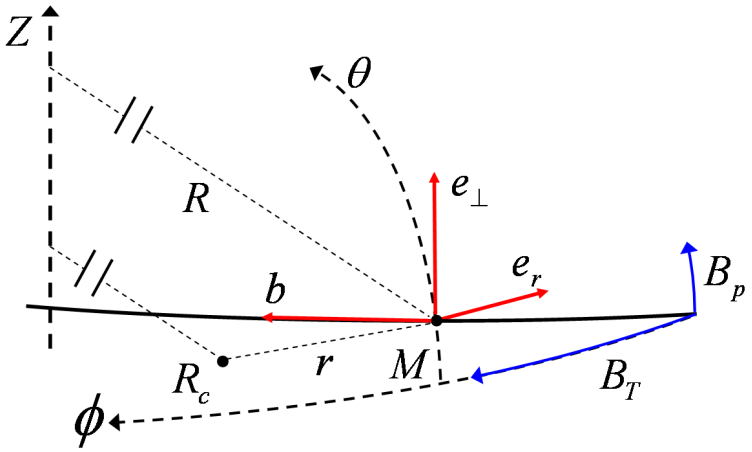

Figure 2.5: *Geometry of a field line section in the referential* (R, Z, Φ) *and* $(s_{||}, r, \hat{t})$ *where* $s_{||}$ *is the curvilinear coordinate aligned with the magnetic vector* $\mathbf{b}$, r *is the minor radius oriented with* $\mathbf{e}_r$ *and* $\hat{t}$ *is the transverse coordinate oriented with* $\mathbf{e}_\perp$, *unit vector tangent to the flux surface and normal to the magnetic field.*

From the previous magnetic field expressions 2.7, 2.8 and the Shafranov shift 2.9, the field line can be analytically described by the change of coordinate $\theta(\phi)$ and $s_{||}(\theta)$:

$$d\theta = \frac{1}{q_a \rho^2} \left[1 + \epsilon\rho(2+\Lambda)\cos\theta\right] d\phi \tag{2.13}$$

$$ds_{||} = R_{pl} q_a \rho^2 \left[1 - \epsilon\rho(1+\Lambda)\cos(\theta)\right] d\theta \tag{2.14}$$

The first equation illustrates the common picture of the safety factor set as the number of toroidal turns for one poloidal turn of a field line lying on the LCFS. On the other hand, these relations are in fact expressing a more general property of helical configurations : the gradients on flux surfaces are linked to one another, which leads to crucial simplifications about flows equilibrium description.

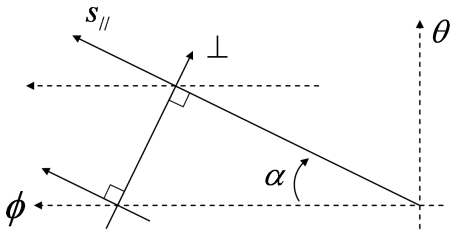

Figure 2.6: *Local field line geometry on a flux surface.*

gradients relations Let us consider a field line defining an angle α with the toroidal axis 2.6, this angle being directly related to magnetic field components. The usual assumption of *toroidal symmetry* leads to a straightforward relation between parallel and transversal gradients:

$$\nabla_\perp = \frac{1}{\tan\alpha} \nabla_{||} = \frac{B_T}{B_p} \nabla_{||}$$

Which can be expressed in the first order expansion with ϵ :

$$\boxed{\nabla_\perp = \frac{q_a \rho}{\epsilon}\left[1 - \epsilon\rho(1+\Lambda)\cos(\theta)\right]\nabla_{||}} \tag{2.15}$$

divergence in curvilinear coordinates The set of transport equations describing the plasma state involves divergences of flux vectors. In the curvilinear system of coordinates, the divergence formulation is not straightforward to to the local definition of unit vectors and implies some approximations in order to get pragmatic expressions. Let us consider a vector written in the curvilinear system of coordinates $\mathbf{A} = A_{||}\mathbf{b} + A_r\mathbf{e}_r + A_\perp \mathbf{b}\times\mathbf{e}_r$. The vector divergence is then decomposed over the different contributions and involves the divergence of unit vectors:

$$\nabla\cdot\mathbf{A} = \nabla_{||}A_{||} + \nabla_r A_r + \nabla_\perp A_\perp + A_{||}\nabla\cdot\mathbf{b} + A_r\nabla\cdot\mathbf{e}_r + A_\perp\nabla\cdot(\mathbf{b}\times\mathbf{e}_r)$$

Where the operator $\nabla_X = \mathbf{e}_X\cdot\nabla$ is the projection of the *nabla* operator on the coordinate of interest. The three first terms of the RHS compose the usual divergence in the slab geometry and the three remaining terms are corrections due to curvatures, whose amplitudes are derived at the lowest order in ϵ:

$$\nabla\cdot\mathbf{b} \approx -\frac{\epsilon}{q_a\rho R_{pl}}\sin\theta \tag{2.16}$$

$$\nabla\cdot\mathbf{e}_r \approx \frac{1}{a\rho} \tag{2.17}$$

$$\nabla\cdot(\mathbf{b}\times\mathbf{e}_r) \approx -\frac{1}{R_{pl}}\sin\theta \tag{2.18}$$

In order to check the consistency of considering a slab divergence, the ordering of the corrections terms are compared to the respective slab ones. In that way, gradients lengths are introduces such that $\nabla_X A \approx \frac{A}{\lambda_X}$. Considering parallel gradients, further discussions on parallel profiles 2.4.3 underscore that the parallel gradient length is of the order of the field line connection length, giving raise to the following ordering of the correction terms :

$$\frac{A_{||}\nabla\cdot\mathbf{b}}{\nabla_{||}A_{||}} \approx \frac{L_{||}\epsilon\sin\theta}{q_a\rho R_{pl}} \approx \epsilon\rho\sin\theta \tag{2.19}$$

$$\frac{A_r\nabla\cdot\mathbf{e}_r}{\nabla_r A_r} \approx \frac{\lambda_r}{a\rho} \tag{2.20}$$

$$\frac{A_\perp\nabla\cdot(\mathbf{b}\times\mathbf{e}_r)}{\nabla_\perp A_\perp} \approx \frac{A_\perp\epsilon\sin\theta}{R_{pl}q_a\rho\nabla_{||}A_\perp} \approx \epsilon\rho\sin\theta \tag{2.21}$$

The relation 2.15 has been used to estimate the orthogonal gradient. Considering the radial term ordering, experiments highlight radial gradient length of the order of some centimeters, meaning one order of magnitude lower that the plasma minor radius - $a \approx 70cm$ and for that reason the radial correction term is neglected. Now considering the parallel and orthogonal terms, the previous expressions suggest a correction scaling with ϵ, and thus the slab divergence would lead to an error of maximum 30%, but effectively reduced by the trigonometric dependancy. Anyhow, the slab approximation is followed for the incoming fluid transport equations and will be matter of disccussion when possible.

2.2 Fluid equations

2.2.1 The Fokker-Planck equation

To describe the dynamics of a species s filling a volume of plasma, a first approach is to solve the dynamics of each particle, leading to a 6 dimensional (3 for position, 3 for velocity) problem on N bodies composing the volume, coupled by Coulomb interactions (charged particles) and evolving in external electromagnetic fields. Considering the large number of particles composing an elementary volume of tokamak plasmas - at the plasma edge the density is about $10^{13} cm^{-3}$, this approach appears to be unrealistic with respect to current and future computers capabilities. The issue is anyhow to describe the global properties of the plasma in term of transport efficiency or response to solicitations, and it is worth following a statistical approach to study the particle behaviors. For that reason the probability distribution functions are introduced, calculated over the degrees of freedom. Dealing with dynamics of particles in term of position $\mathbf{x}$ and velocity $\mathbf{v}$ we introduce the function $f_s(\mathbf{x}, \mathbf{v}, t)$ describing the statistical distribution in the phase space $(\mathbf{x}, \mathbf{v})$ at the time t. The evolution of this function is governed by the Fokker-Planck equation [Wesson 04]:

$$\frac{\partial}{\partial t} f_s + \mathbf{v}_s \cdot \nabla_{\mathbf{x}} f_s + \frac{\mathbf{F}_s}{m_s} \cdot \nabla_{\mathbf{v}} f = \left.\frac{\partial f}{\partial t}\right|_{coll} \tag{2.22}$$

In our case of a magnetized plasma, the force field seen by charged particles is the usual Lorentz force $\mathbf{F}_s = q_s (\mathbf{E} + \mathbf{v} \times \mathbf{B})$ where electromagnetic fields are deduced from the Maxwell equations. The source term $\left.\frac{\partial f}{\partial t}\right|_{coll}$ implicitly describes the momentum transfers via collisions including sink and sources from ionisation processes.

This statistical approach has been intensively studied for fusion plasma simulations, since it leads to remarquable reduction of the number of variables: If the distribution on one degree of freedom is sampled on N' boxes, the resulting total number of variables is N'^6 which can easily be chosen negligible compared to the $6N$ variables of the direct approach, where N is the total number of particles. An further simplification can be done by averaging the motion on the gyrophase of the particles , leading to the gyrokinetic approach [Grandgirard 06].

2.2.2 the fluid approach

The fluid description is an other step in the simplification process by reducing the previous equation to a system of similar equations 2.26,2.27 involving the statistical moments of the distribution function. These moments as defined by formula 2.25 stand for statistical averages over the velocity space and correspond to macroscopic properties of the medium like density, group velocity or temperature. This approach implies necessarily that distribution functions are regular enough to be described by a limited set of moments. For instance a Maxwellian distribution 2.7 is completely defined by its 3 first statistical moments, and the evolution of a related medium can be characterized by a set of limited number of equations. Fundamentally, collisions lead to a relaxation of the distribution toward a Maxwellian [Garbet 09], and the fluid approach infer that kinetic effects are regulated by collisions.

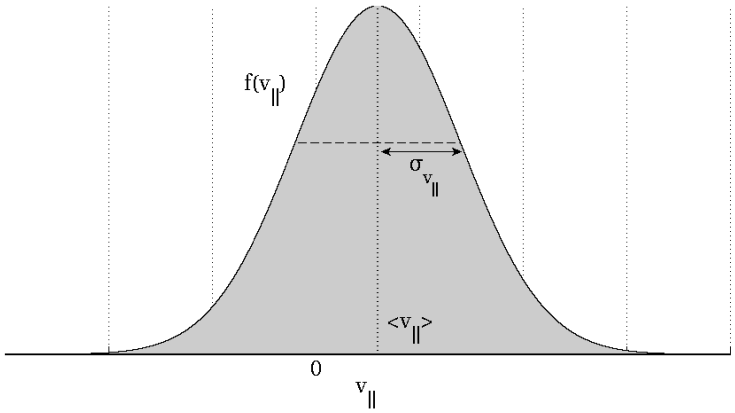

***Figure 2.7**: Illustration of a general Maxwellian distribution.*

In a case of a classical fluid, the high collision rate together with the small mean free path of particles ensures almost systematically the fluid model validity. For a Tokamak plasma this approach has to be considered carefully, since the collision rate may be very small leading to mean free paths larger than the typical confinement size of the plasma. Dramatic consequences on global plasma behavior are due to non linear resonant effects triggered by small fractions of the particle population [Heidbrink 08], and a kinetic description remains in that case a necessity.
The statement is hopefully less dramatic in the case of edge plasma. On the one hand, the relaxation time of the electron distribution is one order of magnitude inferior to the characteristic time scale of edge turbulence [Spitzer 65], meaning that distributions are in principle relaxing faster than the plasma evolution. On the other hand, the open field line topology cancels any resonant phenomena, leading however to an other crucial issue : How small are the relaxation times of distributions compared to parallel transit times, after which particles are absorbed by the wall ? This important criterion for fluid model validity at the plasma boundary can be hold by the collisionality parameter which is defined as the number of collisions experienced during a parallel transit $\nu^* = \frac{\tau^{coll}}{\tau_{||}}$. Characteristic relaxation times for electrons and ions - of charge Z- can be defined as follow [Wesson 04]:

$$\text{electron collision time} \qquad \tau_e = 3(2\pi)^{3/2}\frac{\epsilon_0^2 m_e^{1/2} T_e^{3/2}}{n_i Z^2 e^4 \ln\Lambda} \tag{2.23}$$

$$\text{ion collision time} \qquad \tau_i = 12\pi^{3/2}\frac{\epsilon_0^2 m_i^{1/2} T_i^{3/2}}{n_i Z^4 e^4 \ln\Lambda} \tag{2.24}$$

where the temperature implicitly involves the Boltzmann constant and $\ln\Lambda$ is a parameter almost independent of plasma conditions : $\ln\Lambda \approx 10-20$. Experimental conditions at the edge of Tore Supra discharges suggest a collisionality value in the range of 5 to 300, justifying the fluid approach by the rough but sufficient statistical condition $\nu^* > 5$. From that consideration let us introduce the fluid system, starting with fluid variables:

The moment of order k is a tensor of order k :

$$M_s^{(k)}(\mathbf{x},t) = \int_{-\infty}^{+\infty} \underbrace{\mathbf{v}_s \otimes \cdots \otimes \mathbf{v}_s}_{k} f_s(\mathbf{x},\mathbf{v},t) d^3\mathbf{v}_s \tag{2.25}$$

The physical meaning of these integrals are described for the first orders :

$$M_s^{(0)}(\mathbf{x},t) \equiv n_s(\mathbf{x},t)$$

Defines the local particle density for the specie s.

$$M_s^{(1)}(\mathbf{x},t) \equiv \mathbf{\Gamma}_s(\mathbf{x},t)$$

Defines the local particle flux and the local velocity field : $\mathbf{\Gamma}_s = n_s \mathbf{u}_s$.

$$M_s^{(2)}(\mathbf{x},t) \equiv \frac{1}{m_s} p_s \mathbb{1} + \frac{\mathbf{\Gamma}_s \otimes \mathbf{\Gamma}_s}{n_s} + \frac{1}{m_s}\mathbf{\Pi}_s$$

This second order tensor can be decomposed as a sum of different contributions that are respectively : the thermodynamical isotropic pressure, the Reynolds stress and a non diagonal tensor counting for possible pressure anisotropies and viscosity stresses. The pressure p_s introduces the local thermodynamical temperature $p_s = n_s T_s$, and the isotrope property implies that such temperature definition is an average over the full velocity space:

$$T_s \equiv \frac{m_s}{n_s} \int |||\mathbf{v}_s - \mathbf{u}_s|||^2 \, f_s(\mathbf{x},\mathbf{v},t) d^3\mathbf{v}_s$$

Anisotropies are hidden in the diagonal terms of the pressure tensor $\mathbf{\Pi}_s$, whose expression can be derived from the common Braginskii closure [Braginskii 65]. However, due to the relatively high collision rate in the plasma edge, isotropy stands for a relatively fair assumption. The evolution equation of the previous fluid quantities can be directly derived from the Fokker - Planck equation 2.22 by applying the moment integral 2.25. For the particle flux study, only the equations belonging the the two first moments are presented:

$$\frac{\partial}{\partial t} n_s + \nabla \cdot (\mathbf{\Gamma}_s) = S_s(\mathbf{x},t) \tag{2.26}$$

$$\frac{\partial}{\partial t}(m_s \mathbf{\Gamma}_s) + \nabla \cdot \left(n_s T_s \mathbb{1} + \frac{m_s}{n_s} \mathbf{\Gamma}_s \otimes \mathbf{\Gamma}_s \right) = q_s \left(n_s \mathbf{E} + \mathbf{\Gamma}_s \times \mathbf{B} \right) - \nabla_{\mathbf{x}} \cdot \mathbf{\Pi}_s + \mathbf{R}_s \tag{2.27}$$

The equation 2.26 describes the density or mass conservation where S_s is a particle source or sink term due to ionisation processes and the equation 2.27 illustrates the momentum conservation, where the term $\mathbf{R}_s$ counts for momentum transfers by frictions with other species.

2.2.3 system closures and approximations

The first issue revealed by the previous system of fluid equations is that a continuity equation related to a moment k implies higher order moments. That said, a rigorous solving procedure would imply an infinite system of equations that does not bring any simplifications. On the other hand if the distributions are regular enough the highest statistical moments are

directly related to lowest ones, as it is the case for a Maxwellian. In that case, conservation equations on highest moments are just an other writing of lower order ones. As mentioned above the Maxwellian approximation for edge plasma distributions is quite realistic which closes the conservation system to 3 equations - One for the temperature conservation that has not been presented. The resulting system is anyhow complex due to entanglements in between equations of a given specie and indirectly between electrons and ions by electro-magnetic effects, but can be simplified with further physical closure assumptions:

- Concerning the pressure tensor $\mathbf{\Pi}_s$, isotropy is assumed due to the relatively high collisionality and viscosity stresses are reduced to a simple expression, leading to the following simplification :$\nabla \cdot \mathbf{\Pi}_s = (\nabla \cdot \eta_s \nabla)\, \mathbf{u}_s$ where η_s is the dynamic viscosity matrix.
- Friction forces are neglected : $\mathbf{R}_s = \mathbf{0}$.
- Due to the high value of the parallel thermal conductivity, the temperatures are assumed to be constant along field lines [Stangeby 00] :$\nabla_{||} T_s \approx 0$.
- The plasma current is neglected at the edge : $Ze\mathbf{\Gamma}_i \approx e\mathbf{\Gamma}_e$.

Concerning the electromagnetic field, the distinction will be done between electrostatic field from the plasma itself and constant external magnetic field. At the edge, it is indeed assumed that current is null and magnetic field fluctuations are very small - in the order of de 10^{-4} [Zweben 07], such that steady-state magnetic field from bulk current and external coils are only considered.

2.2.4 steady-state model

As a matter of facts, edge transport phenomena involve high fluctuation levels of plasma parameters - in the order of 10 to 50%, but a remarquable property of these phenomena is about the strong reproducibility of related time averaged quantities. That said, and because diagnostics are often measuring time averaged plasma parameters, a steady-state approximation of the conservation laws are worth beeing expressed in order to describe the edge equilibrium. In particular will be introduced the notion of maxwellian electrons considered as a leading closure approximation.
The steady state conservation system can be written as an average of the time variable:

$$\nabla \cdot (\mathbf{\Gamma}_s) = S_s \tag{2.28}$$

$$\nabla \cdot \left(n_s T_s \mathbb{1} + \frac{m_s}{n_s} \mathbf{\Gamma}_s \otimes \mathbf{\Gamma}_s \right) = q_s \left(n_s \mathbf{E} + \mathbf{\Gamma}_s \times \mathbf{B} \right) + (\nabla \cdot \eta_s \nabla)\, \mathbf{v}_s \tag{2.29}$$

And the Poisson equation is set to describe the electrostatic field :

$$-\nabla^2 V = \nabla \cdot \mathbf{E} = \frac{1}{\epsilon_0} \sum_s q_s n_s \tag{2.30}$$

Although the different terms have not been modified in their expression, a special care has to be taken about nonlinear terms whose expressions implicitly involve fluctuations coupling.

For instance, it will be shown in an other chapter that local density and radial velocity are fluctuating in phase, leading to a common non-linear finding : $\langle \Gamma_r \rangle_t \neq \langle n \rangle_t \langle v_r \rangle_t$. This issue might be the most limiting argument for rejecting a simplified steady-state model in which most of the non linear coupling are set aside. On the other hand such a model can be considered as a "first principle" approach essential for an experimental study of transport phenomena. Along the thesis, the non linearity will be kept implicit when possible and just canceled if needed for further simplifications.

2.2.4.1 Boltzmann electrons approximation

An interesting property of the ion-electron bi-fluid model is the strong difference of mass between the two species $\frac{m_i}{m_e} \approx 1836$, which in turns implies a great simplification for the electron dynamics description due to a negligible inertia component. First, we can make the fair assumption of energy equipartition between ions and electrons, meaning $T_i \approx T_e$ - Measurements performed on Tore Supra suggest an ion temperature one to ten times higher than electron temperature [Kocan 08]. Then, the assumption of no flowing current at the edge leads to the fact that electron and ion fluid velocities are of the same ordering. Having these remarks in mind and considering electron momentum conservation law 2.29, the inertia term can be compared to electron pressure term:

$$\frac{m_e n_e v_e^2}{n_e T_e} \approx \frac{m_e v_i^2}{T_i} \approx \frac{m_e}{m_i} \left(\frac{v_i}{c_i} \right)^2 \ll 1$$

Where c_i is the thermal ion velocity. In the realistic conditions of sub-sonic or even near-sonic flows, the inertia term is negligible. therefore we can now consider the electrons as an inertia free species, whose pressure field is directly balancing the force field if the viscosity is in first order neglected :

$$\nabla P_e = -e \left(n_e \mathbf{E} + \mathbf{\Gamma}_e \times \mathbf{B} \right) \tag{2.31}$$

Reading this equality along the magnetic field axis leads to a parallel force balance equation relating the parallel electric field to the parallel pressure gradient. Using now the isothermal property of field lines, an equality is deduced between electron density profile and electrostatic potential :

$$\boxed{\nabla_{||} n_e = n_e \frac{e}{T_e} \nabla_{||} V}$$

That is immediately solved by introducing a reference position along the field line - labeled by 0 :

$$n_e = n_e^0 e^{\frac{e}{T_e}(V - V^0)} \tag{2.32}$$

This formulation introduces a dimensionless expression of the plasma potential $\Phi = \frac{e}{T_e} V$ that will be used in the following.

This last relation is the so-called *Boltzmann electron approximation*, traducing the absence of electron inertia. An important remark has to be done: as introduced here, the parallel electron density profile is following the electrostatic potential profile, but it does absolutely not mean any phase coupling between density and potential fluctuations, as assumed in the *adiabatic*

electron approximation : $\frac{\tilde{n_e}}{\bar{n_e}} = \tilde{\Phi}$. As an experimental results, it will be shown that the latter approximation is wrong at the edge.

2.2.4.2 quasi-neutrality approximation

The Boltzmann electron approximation read in its preliminary vectorial form - absence of inertia - does relate the local electric field to the electron pressure and velocity field. Thus the ion fluid description can be simplified by substituting the electrostatic term with electron fluid parameters. Using specific edge assumption as zero current and electro-neutrality $Zn_i = n_e$, the ion momentum conservation law can be described as a total plasma pressure balanced with the ion inertia:

$$\nabla \left(n_i c_S^2 \mathbf{I} + \frac{1}{n_i} \mathbf{\Gamma}_i \otimes \mathbf{\Gamma}_i \right) = + \nabla \left(\eta_i \nabla \cdot \mathbf{v}_i \right) \tag{2.33}$$

The plasma pressure defined as the sum of ion and electron pressure can be expressed by introducing the ion acoustic velocity:

$$c_S = \sqrt{\frac{ZT_e + T_i}{m_i}}$$

Finally, a new system is obtained for ion equilibrium in zero current and quasi-neutrality assumptions:

$$\nabla \cdot \mathbf{\Gamma}_i = S_i \tag{2.34}$$

$$\nabla \left(n_i c_S^2 \mathbf{I} + \frac{1}{n_i} \mathbf{\Gamma}_i \otimes \mathbf{\Gamma}_i \right) = \nabla \left(\eta_i \nabla \cdot \mathbf{v}_i \right) \tag{2.35}$$

$$\frac{\nabla_{||} n_i}{n_i} = \nabla_{||} \Phi \tag{2.36}$$

The last equality relating the ion density field to the electrostatic potential is just a consequence of quasi-neutrality coupled with the Maxwellian electron approximation.
The latter system and relating assumptions are giving an interesting point of view on the plasma equilibrium: Due to quasi-neutrality, the large electron mobility forces the plasma to behave as inertial ions but with a higher fluid pressure $p_e + p_i$. Indeed ion sound speed - or acoustic velocity - is now defined with an ion and an electron thermal contribution, and the ion velocity can be expressed as a dimensionless variable, namely the ion Mach number : $\mathbf{M}_i = \frac{\mathbf{v}_i}{c_S}$.

2.3 Drift velocities

To that point, the previous conservation system involves four degrees of freedom that are the local density and the 3 particle flux components. First of all, other quantities such as plasma temperatures are involved in the system, but are considered as control parameters in our experimental approach of particle flux analysis. Secondly, the strongly magnetized feature of tokamak plasma implies that flows components orthogonal to the magnetic field are not free quantities, but can be interpreted as drift effects forced by other plasma fields.
As an introduction this drift effect is described for a test particle, and then generalized to the fluid model.

2.3.1 the transverse drift phenomenon

The drift effect in a magnetic field is easily identified in the test particle approach. So let us consider a charged particle (m, q) moving in a magnetic field and an imposed force field. The particle trajectory $(\mathbf{x}_p, \mathbf{v}_p)$ is described through the particulate momentum conservation law:

$$m\frac{d\mathbf{v}}{dt} = \mathbf{F} + q\mathbf{v} \times \mathbf{B} \tag{2.37}$$

This equation can be rewritten to introduce the magnetic angular moment $\mathbf{\Omega}_c = \frac{q\mathbf{B}}{m} = \omega_c \mathbf{b}$ directing the fast cyclotron precession of the particle. As a first step, the equation can be easily solved through the assumptions of mean field approximation : the external fields $\mathbf{B}, \mathbf{F}$ are assumed uniform and constant over several cyclotron periods, that can be read as the ordering : $\frac{d\omega_c(\mathbf{x}_p,t)}{dt} \ll \omega_c^2$ and $\frac{dF}{dt} \ll \omega_c F$. In particular, the magnetic field is supposed to be rectilinear, such that the particle trajectory is solved in the plan orthogonal to $\mathbf{\Omega}_c$. The solution in the velocity space is then composed of an oscillating term at the frequency ω_c and a constant term identified as the drift velocity:

$$\langle \mathbf{v}_\perp \rangle_{\tau_c} = \frac{\mathbf{F} \times \mathbf{B}}{qB^2} \tag{2.38}$$

The latter expression 2.38 describes the drift motion of the particle guiding center over mean field approximation, as illustrated on the figure 2.8. Interestingly the case of a pure electrostatic force gives rise to an ambipolar drift, meaning a global plasma motion with no charge separation either due to charge or mass effects. On the other hand, the drift term can be expanded over smaller velocity scales by overstepping the mean field approximation. For instance, magnetic field curvature and other spatial inhomogeneities can be taken into account over a cyclotron transit to give lower order secular effects that are not charge independent. Dealing with turbulence, these lower orders are crucial to describe some driving instability mechanisms [Scott 02]. However the resulting electrostatic turbulent transport is well described by the mean field approximation.

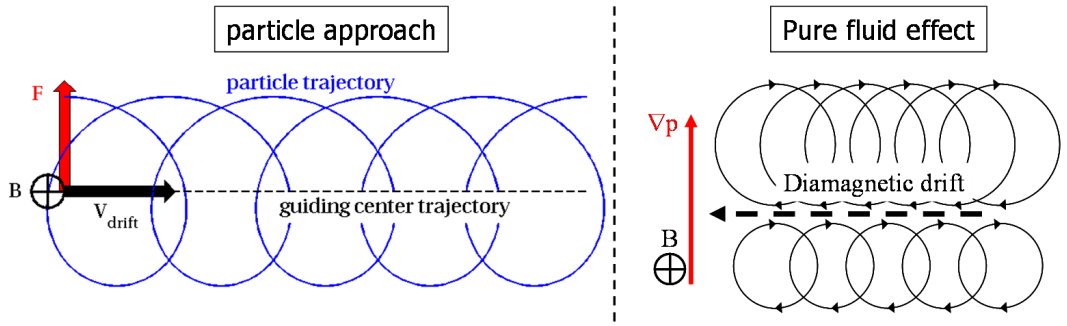

Figure 2.8: *Left : Positively charged particle trajectory in a magnetic field with an over imposed transversal force. The particle guiding center is drifting with a velocity oriented with* $\mathbf{F} \times \mathbf{B}$. *Right : in the fluid approach, the drift velocity is also composed of a pure fluid component called diamagnetic drift velocity, whose existence can be infer to a spatial inhomogeneity of cyclotron trajectory distribution.*

2.3.2 fluid drift expression

The drift described above for a test particle is easily understandable as a global effect, and thus should find its fluid analogy. However the phase averaged nature of fluid model implies first an other way to solve the drift effect and then the existence others drift terms due to assembly effects. Anyhow, the first orders drift terms in the fluid hierarchy have to be consistent with the kinetic approach and thus mean field approximation is again applied and enlarged to fluid fields invoked in the momentum conservation law 2.27: n_s,∇p_s & $\mathbf{\Gamma}_s$:

$$\nabla \cdot \left(p_s \mathbb{1} + \frac{m_s}{n_s} \mathbf{\Gamma}_s \otimes \mathbf{\Gamma}_s \right) = q_s \left(n_s \mathbf{E} + \mathbf{\Gamma}_s \times \mathbf{B} \right)$$

Again, the magnetic field defines a parallel axis oriented with the unit vector $\mathbf{b}$ and a transversal plan : $\mathbf{A} = \mathbf{A}_{||} + \mathbf{A}_{\perp}$ with $\mathbf{A}_{\perp} = (\mathbb{1} - \mathbf{b} \otimes \mathbf{b}) \cdot \mathbf{A}$ where the label $\perp$ exceptionally describes the transversal plan and not only the orthogonal direction. Now, let us consider the vectorial product of the previous equation with the magnetic field :

$$\nabla p \times \mathbf{B} + \nabla \cdot \left(\frac{m_s}{n_s} \mathbf{\Gamma}_s \otimes \mathbf{\Gamma} \right) \times \mathbf{B} = q_s n \mathbf{E} - q_s B^2 \mathbf{\Gamma}_{\perp}$$

The transversal flux is easily identified if the inertia term is negligible:

$$\frac{\left| \nabla \cdot \left(\frac{m_s}{n_s} \mathbf{\Gamma}_s \otimes \mathbf{\Gamma}_s \right) \times \mathbf{B} \right|}{|q_s B^2 \mathbf{\Gamma}_s^{\perp}|} \approx \frac{\nabla (n v^2)}{\omega_c n v} \approx \frac{vk}{w_c} \approx \frac{w_{fluc}}{w_c}$$

Under the mean field approximation, the fluctuation time scales are assumed to be larger than the cyclotron frequency - for the same reason, the time variation of the fluid momentum has be omitted - and thus the first order drift flux is easily read:

$$\mathbf{\Gamma}_s^{\perp} = \frac{n_s \mathbf{E} \times \mathbf{B}}{B^2} + \frac{-\nabla p_s \times \mathbf{B}}{q_s B^2} \tag{2.39}$$

The first component called electrostatic drift $\mathbf{v}_E$ is the direct analogy of the particulate drift. The second term is the diamagnetic drift $\mathbf{v}^*$ and is a pure fluid effect due to phase average - a geometric illustration is found on the right figure 2.8. As for the kinetic approach, the mean field approximation can be overstepped to introduce higher orders terms over the Larmor radius expansion. As mentioned above, the first order drift description is enough for our experimental approach of particle fluxes, and it is worth noticing that the drift fluxes expressions are valid with regards to common edge plasma fluctuations. Indeed, we show in this study that electrostatic drifts are key effects in the establishment of edge equilibrium by their fluctuating parts driving the radial transport.

2.3.3 Discussion on flows balance

Looking in more details at the drift components of the particle flux, their contribution appears trough a divergence term in the particle flow balance 2.34 that can be easily simplified in order to discuss their orderings:

$$\nabla \cdot \mathbf{\Gamma}_s^{\perp} = \mathbf{v}_E \cdot \nabla n_s + n_s \nabla \cdot \frac{\mathbf{B} \times \nabla V^{pl}}{B^2} + \nabla \cdot \frac{\mathbf{B} \times \nabla p_s}{q_s B^2}$$

The two last terms are easily rewritten by considering $\nabla \times \mathbf{B} = 0$, thus assuming a steady-state and no current SOL plasma :

$$\nabla \cdot \mathbf{\Gamma}_s^{\perp} = \mathbf{v}_E \cdot \nabla n_s + \left(n_s \nabla V^{pl} + \frac{\nabla p_s}{q_s} \right) \cdot \frac{2\mathbf{b} \times \nabla B}{B^2}$$

We recognize a magnetic curvature term in the right hand side that is explicit in the circular and large aspect ratio geometry : $\frac{2\mathbf{b}\times\nabla B}{B^2} = \frac{1}{B_{T,pl} R_{pl}} (\sin\theta \mathbf{e}_r + \cos\theta \mathbf{e}_\theta) + \sigma(\epsilon)$. The two contributions of the drift flux divergence can be compared via an ordering on gradient length. Considering steady-state flows, the orthogonal components of the drift fluxes are of interest - along $\mathbf{b} \times \mathbf{e}_r$ - and the term $\mathbf{v}_E \cdot \nabla n$ scales like $\frac{v_E n}{r}$ that is one order of magnitude higher than the curvature term in the ϵ ordering. Thus, the main contribution of the drift flux divergence scales like $\nabla \cdot \mathbf{\Gamma}_s^{\perp} \approx v_E \nabla_{\perp} n$ where the $\perp$ direction is along $\mathbf{b} \times \mathbf{e}_r$. Considering now the total flow balance equation, the latter expression can be approximated as a parallel gradient by roughly assuming a uniform electrostatic drift, leading to a total parallel divergence involving the parallel and orthogonal fluxes :

$$\nabla_{||}(n v_{||}) + \nabla_{\perp} \mathbf{\Gamma}_{\perp} \approx \nabla_{||} \left(n v_{||} + \frac{q_a \rho}{\epsilon} v_E n \right) \tag{2.40}$$

The latter expression finds all its interest in the experimental study of the radial particle flux from parallel flow measurements. Before coming to that point an introduction to the opened field line physics has to be done in order to describe either the particular SOL equilibrium and the Langmuir probes theory.

2.4 Physics of open field line

Outside the last closed flux surface, the field lines intercept by definition a material component generally called limiter. This connection is a crucial element involved in edge the plasma equilibrium : First, charged particles moving along the magnetic field end their motion by intercepting a limiter where they are neutralized. Thus, limiter plates act as ideal sinks of particles, and as a recycling effect act as a source of neutrals for the whole plasma. Secondly, these objects are generally not driving any macroscopic current from the plasma, and for that reason specific boundary conditions have to appear on their surface in term of electrostatic charge to respect the charge flux ambipolarity. The case of probes or polarized limiters is particular in a way that a net current can be collected, but boundary conditions are similar to those of a standard limiter.

In that section the plasma equilibrium along open field lines will be described from previous fluid equations, coupled to the boundary conditions that will be introduced in a first part : the essential notions of sheath and presheath illustrating the plasma-wall interaction phenomenon. That presented, the principle of Langmuir probes and measured quantities will be described. For the full section, *the magnetic field is considered orthogonal to the surface.*

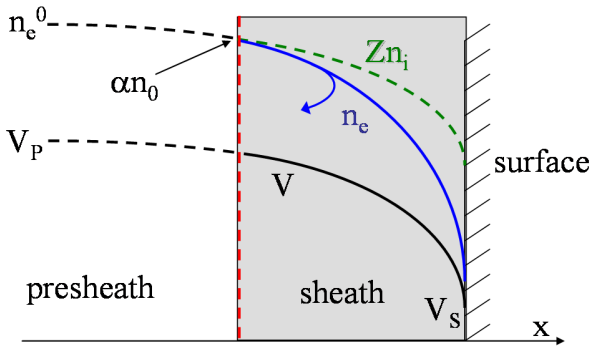

Figure 2.9: *Illustration of the plasma equilibrium in front of a limiter surface. The sheath is defined as the plasma volume where neutrality is broken*

2.4.1 Plasma-material interaction: the electrostatic sheath

As a qualitative description of the plasma-limiter interaction, let us first consider a plasma flowing to a neutral isolating surface. Because electrons are moving faster than ions - due the mass ratio, the surface should receive an electron flux higher than the ion flux, breaking the ambipolarity conditions imposed by the surface. In fact the initial electron flux is responsible for a negative charge accumulation on the surface leading respectively to the repulsion and attraction of incoming electrons and ions. The generated electric field in front of the surface is self consistently sustained to preserve the charge ambipolarity. Its strength has to counter-balance the strong unbalance between ion and electron thermal velocities, inferring a break of quasi-neutrality close to the surface: the sheath is defined as the plasma volume where the charge separation occurs. Anticipating further discussions, this volume is necessarily of a Debye length scale that is ,compared to the characteristic scale length of the field lines, illustrating the concept of boundary layer. We will first discuss the sheath physics in terms of potential drop and velocity conditions for ions. Then the plasma behavior along the quasi-neutral field line - named presheath - will be focused in term of response to the sheath presence.

2.4.2 Physics of the sheath

Sheath width The sheath width orthogonal to the surface can be asymptotically deduced from a perturbative approach on the Poisson equation 2.30. First, let us consider a reference position at the sheath entrance - labeled by $s.e$, where quasi-neutrality is assumed but starts its divergence. As a second approximation ion density is considered as a spacial constant, and electrons drive the charge separation through their Maxwellian feature. Considering the Poisson equation for the normalized potential:

$$\nabla_{||}^2 \Phi = \frac{e^2 n_e^0}{\epsilon_0 T_e} \left[e^{\Phi - \Phi_0} - \frac{Z n_i^0}{n_e^0} \right]$$

The Debye length appears naturally from the equation on dimensionless variables : $\lambda_D = \sqrt{\frac{\epsilon_0 T_e}{e^2 n_e^{s.e}}}$. The linear expansion of perturbative variations : $Z n_i^{s.e} = n_e^{s.e}$ and$\Phi \approx \Phi^{s.e}$ lead to a

linear differential equation on the potential Φ:

$$\nabla_{||}^2 \Phi = \frac{1}{\lambda_D^2} [\phi - \phi^{s.e}]$$

For which the solution are easily identified as exponential functions $e^{\pm \frac{x}{\lambda_D}}$. Physically, the flux ambipolarity implies a strong drop of potential to repeal electrons, such that physical solutions are selected to be exponentially diverging, illustrating the notion of boundary layer. Considering common edge plasma parameters, $n_e = 10^{18} m^{-3}$, $T_e = 10eV$, the characteristic scale length of the sheath width is of the order $\lambda_D \approx 25\mu m$ to be compared with the typical length of field lines $L \approx 100m$.

The Bohm criterion In the sheath plasma, the electric field resulting from the exponential decay of the potential gives rise to a strong acceleration of ions toward the surface. As it will be shown, the parallel ion flow in the sheath has to exceed the ion acoustic velocity and the so-called *Bohm Criterion* brings a definition of the transition border between the supersonic sheath and the subsonic presheath where ions are accelerated to $\left|M_{||}\right| = 1$.
The next step in the sheath description includes ion density variation through the set of equations 2.28 & 2.29, assuming a collision free sheath volume since collisions mean free paths are largely exceeding the sheath width. Thus neutrals emitted from the surface are assumed to travel freely through the sheath : the ionisation source is null $S_i = 0$. In the same way, the orthogonal flux is neglected in the sheath equilibrium, which is then characterized by the parallel conservation of the ion flow. Dealing with momentum conservation, orthogonal sources are neglected as well since the parallel electric field is strong enough to drive alone the equilibrium. Finally, the temperatures are assumed to be constant within the sheath. We propose here a derivation of the Bohm criterion for thermal ions, as an extension of the mono-energetic formalism [Chen 03] [Choruda]. The ion conservation system is written in a dimensionless form:

$$\nabla_{||} \left(n_i M_{||} \right) = 0 \tag{2.41}$$

$$\nabla_{||} \left[n_i \left(M_{||}^2 + \beta \right) \right] = -(1-\beta) n_i \nabla_{||} \Phi \tag{2.42}$$

$$\tag{2.43}$$

where a thermal ion parameter has been introduced for convenience : $\beta = \frac{T_i}{ZT_e + T_i}$, the square of the thermal Mach number. From the latter set of equations, parallel gradients of density and parallel Mach number are identified :

$$\frac{-\nabla_{||} M_{||}}{M_{||}} = \frac{\nabla_{||} n_i}{n_i} = -\frac{1-\beta}{\beta - M_{||}^2} \nabla_{||} \Phi \tag{2.44}$$

Again, the Poisson equation is linearized in a perturbative approach at the sheath entrance where quasi-neutrality is assumed : $n_i = n_i^{s.e} + \delta n_i$ et $\Phi = \Phi^{s.e} + \delta \Phi$:

$$\nabla_{||} \delta \Phi = -\left(\frac{\delta n_i}{n_i} - \delta \Phi \right)$$

From the previous equality 2.44 the perturbative density parameter can be related to the potential to give a new differential equation where the ion Mach number appears in a control parameter:

$$\nabla^2 \delta\Phi = \left(\frac{1 - M_{||}^2}{\beta - M_{||}^2} \right) \delta\Phi \tag{2.45}$$

The previously introduced exponential divergence of the potential implies a sign condition for the control parameter : $\left(\frac{1-M_{||}^2}{\beta-M_{||}^2} \right) > 0$. Two distinct conditions appear for the parallel Mach number: $M_{||}^2 < \beta$ or $M_{||}^2 > 1$. The subsonic condition corresponds via equations 2.45 and 2.44 to a solution involving a slow down of the ion flow toward the surface, that is not physically acceptable. The second and supersonic condition for the Mach number gives effectively a diverging solution for potential and velocity. The *Bohm condition* is then defined for the ion velocity along the sheath:

$$M_{||}^2 > 1 \text{ along the sheath} \tag{2.46}$$

The flow is assumed subsonic along field lines so that flow continuity leads to define the *Bohm Criterion* for the sheath entrance:

$$\boxed{M_{||}^2 = 1 \text{ at the sheath entrance}} \tag{2.47}$$

An important remark belongs to the fact that this criterion is implicitly true for any incident current on the surface, the only condition being to have effectively a drop of potential and thus an ion acceleration in the sheath . In particular, the Bohm criterion will be intensively used in the Langmuir probe theory within the validity of previous potential drop hypothesis.
As a matter of discussion, the sheath physics can be developed in more details by taking into account kinetic effects [Rienammn 91] or secondary electron emission from the surface. Concerning geometrical aspects, the angle formed between field lines and the surface can be included in the model to take care of ion cyclotron motions close to the surface [Choruda 82], as well as drift velocity effects [R.H. Cohen 95]. Nevertheless these finer models leads to correction terms, and in our pragmatic approach of the open field lines physics we restrict our boundary conditions to the Bohm criterion exposed from simplified considerations.

Sheath potential The Bohm criterion defined above allow us to evaluate the potential drop within the sheath via a current balance in the ambipolar approximation. From previous considerations 2.41 and 2.47, the ion flux is assumed constant from the sheath entrance to the surface and is $\Gamma_i^{surface} = n_i^{s.e} c_S$. For electrons, an unidirectional flux calculation is performed on the velocity distribution function. The assumption is made that the distribution remains Maxwellian within the sheath, and the mean electron velocity is neglected compared to the thermal electron velocity since it is of the order of ion acoustic velocity in the approximation of negligible plasma current. From that considerations, the electron flux through the surface can be defined as :

$$\Gamma_e^{surface} = n_e^{surface} \sqrt{\frac{m_e}{2\pi T_e}} \int_0^{+\infty} v_{||} e^{-\frac{m_e v_{||}^2}{2T_e}} dv_{||}$$

Giving after integration the electron flux at the surface:

$$\Gamma_e^{surface} = n_e^{surface}\sqrt{\frac{T_e}{2\pi m_e}} \tag{2.48}$$

The potential drop in the sheath is then derived from the Maxwellian electron approximation coupled with the flux ambipolarity condition:

$$n_i^{s.e} c_S = n_e^{s.e} e^{\Phi^{surface}-\Phi^{s.e}} \sqrt{\frac{T_e}{2\pi m_e}}$$

Giving:

$$\boxed{\Delta\Phi_s = \Phi^{surface} - \Phi^{s.e} = \frac{1}{2} ln\left(\frac{2\pi m_e}{m_i}\frac{ZT_e + T_i}{T_e}\right) \approx -2.3} \tag{2.49}$$

Anticipating the presheath description, let us consider a reference position - labeled with 0 - along the quasi-neutral field line, and define a density attenuation factor α relating the density value at the sheath entrance to the density at the reference position : $n_i^{e.g} = \alpha_0 n_i^0$ - as illustrated on the figure 2.10. The potential drop from the reference position to the sheath entrance is then directly obtained from the Maxwellian electron approximation 2.36:

$$\Phi_{s.e} - \Phi_0 = \ln(\alpha_0) \tag{2.50}$$

And thus the whole drop of potential along the field line is derived from a reference position 0 to the limiter surface:

$$\boxed{\Delta\Phi \equiv \Phi^{surface} - \Phi^0 = \frac{1}{2} ln\left(2\alpha_0 \frac{2\pi m_e}{m_i}\frac{ZT_e + T_i}{T_e}\right)} \tag{2.51}$$

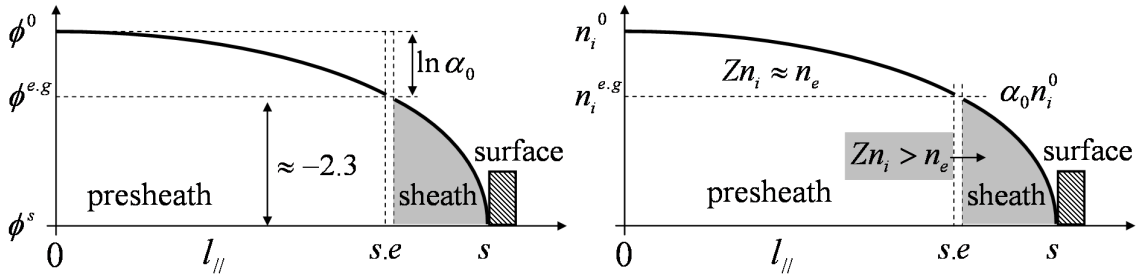

***Figure 2.10**: Illustration of plasma profiles along the presheath and the sheath. Left: for the dimensionless potential. Right : for the density.*

As a comment, the potential drop is significant either along the presheath or within the sheath, since the α parameter describing the drop of density along the presheath is generally speaking a small parameter between 0 and 1. Thus, the quasi-neutrality approximation for the presheath has to be considered carefully. In fact, the parallel scale length appears to be the control parameter for such consideration - via the Poisson equation, and if the Debye scale length of the sheath implies a strong charge separation, the scale length of the presheath is several order of magnitude higher - as discussed in the next parts, and leads to the validation of the presheath quasi-neutrality approximation.

2.4.3 Physics of the pre-sheath of a limiter

The transition layer previously introduced in term of Mach number for the sheath entrance defines the boundary conditions for the quasi-neutral presheath, where ions are accelerated to the ion acoustic velocity. As mentioned earlier, a residual electric field is generated in that region in order to drive the ion acceleration, but can be alternatively understood as an electron pressure effect. In the following the properties of density and flow profiles along the presheath will be discussed in the framework of the steady-state quasi-neutral model. The particular case of probe presheath will be treated in a particular part since specific geometrical considerations are on tasks 2.11.

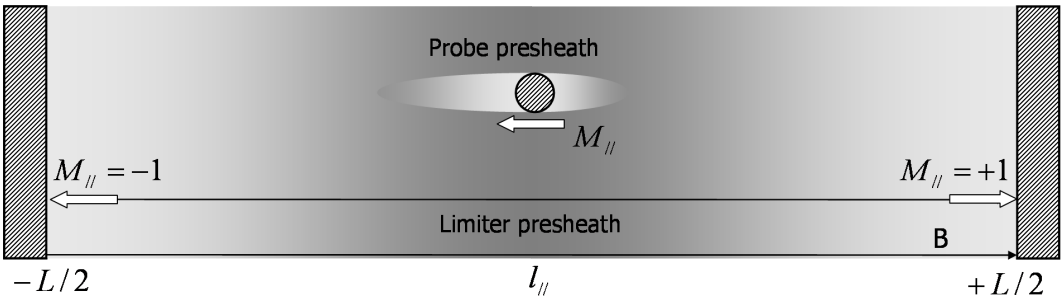

***Figure 2.11**: Picture of the plasma equilibrium along the presheath of limiters and probes. In the latter case, the presheath volume is influenced by the surrounding plasma.*

The ion fluid equilibrium in the presheath is described through the set of equations 2.34 & 2.35. The matter of final interest is to derive a simplified pragmatic model that can be used to interpret local probe measurements in term of radial transport variable. First the related set of approximations are presented, and then some properties of the model are discussed.
Since Mach probes measure a local parallel flux, the momentum conservation equation is first restricted to its component projected along the field line. Then the viscous momentum transfer is neglected since the typical limiter geometry does not imply strong velocity gradients, and mainly because of the complexity of including that term in a pragmatic model. In the same way, the transversal transfer of parallel momentum from the Reynolds tress is neglected. Concerning the mass conservation, contributions from transversal flows are restricted to the radial flux from previous considerations 2.3.3. Finally a conservation law remains on a generalized pressure defined as the thermal pressure plus the parallel kinetic energy, the sum being considered as constant along the field lines:

$$\nabla_{||}\left(n_i c_S M_{||}\right) = \left(-\nabla_r \Gamma_r + S_{\text{ionisation}}\right) \equiv S \tag{2.52}$$

$$\nabla_{||}\left[n_i c_S \left(1+M_{||}^2\right)\right] = -\frac{1}{c_S}\nabla_{\perp}\left(\Gamma_{\perp} c_S M_{||}\right) \approx 0 \tag{2.53}$$

Exceptionally for this formulation, the transversal label $\perp$ notes the plan orthogonal to the magnetic field, meaning the radial and transverse axes.
As a controversial remark, the transversal mass transfer in the mass conservation has been kept as the source of particle, whereas its analogous momentum transfer has been neglected. Over the direct reason of simplification, it is convenient to express a conserved quantity

$n_i c_S \left(1 + M_{||}^2\right)$ that is locally known - since $n_i c_S$ & $M_{||}$ are both measured by probes. Thus, the plasma equilibrium along SOL field lines is studied under strong approximations in order to derive *first order* particle transport features [Gunn 07] [LaBombard 04]. As soon as possible, the validity of such a model will be discussed under the scope of experimental results. As a first element of validation, 2D simulations of edge particle transport have performed [1], based on the same set of equations but keeping a viscous term describing the transversal momentum transfer. It is shown that this viscous term does not lead to a significant departure from the pressure conservation assumption, within 10%.

Concerning the density profile along the field line, the previous conservation equation allows us to evaluate its dependence with the local flow strength. Since the Mach number is defined at the field lines boundaries by the Bohm criterion : $M(-L/2) = -1$ & $M(L/2) = +1$, the flow continuity condition implies there is a position 0 along the field line where the flow is stagnant $M_0 = 0$. The local density along the field line is thus linked to the local flow velocity via the relation :

$$n_i = \frac{n_0}{1 + M_{||}^2}$$

In particular can be identified the boundary density conditions, previously introduces via the attenuation parameter α :

$$n_i(\pm L/2) = \frac{1}{2} n_0 \qquad \text{Thus } \alpha = \frac{1}{2} \tag{2.54}$$

That is, the whole density profile along the field lines can not be explained since the parallel flow is imposed by the parallel distribution of the particle source S via the equation 2.52. An elegant approach is however possible by defining a new parallel coordinate that is related to the source distribution along the field line [Gunn 07]:

$$s(l_{||}) = \frac{\int_{-L/2}^{l_{||}} S dl_{||}}{\int_{-L/2}^{+L/2} S dl_{||}} \in [0, 1]$$

This s coordinate describes the source fraction collected along the field line from an origine to a given position. Integrating the mass conservation equation 2.52 from a field line boundary to a given position yields a flow expression function of the source coordinate s. The pressure conservation leads to an explicit dependence of the flow velocity, and consequently of the density:

$$\frac{M_{||}}{1 + M_{||}^2} = s - \frac{1}{2} \tag{2.55}$$

As a matter of interest, the previous expression shows that the flow is stagnant at the position where the source is equally distributed on each side of that position $s = 1/2$. Profiles in real geometry are not available until a parallel distribution of the source is not estimated. For instance, an uniform source of particles would give a straightforward identity between the parallel and the source coordinate describing a stagnation point in the middle of the field line. As it will be presented in a next part, the parallel flows measured in the SOL of Tore Supra and

[1] SOLEDGE2D developed and used by G. ciraolo, E. serre, L. Isoardi, G. Bufferand et al, M2P2 Marseille

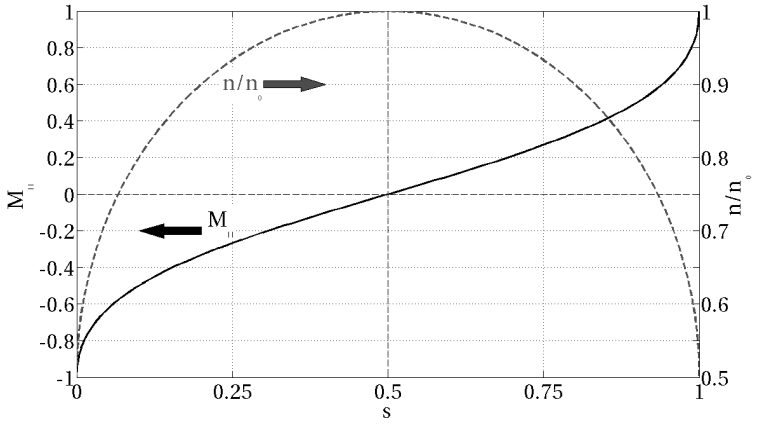

***Figure 2.12**: Parallel profil of the density and parallel flow velocity function of the source coordinate.*

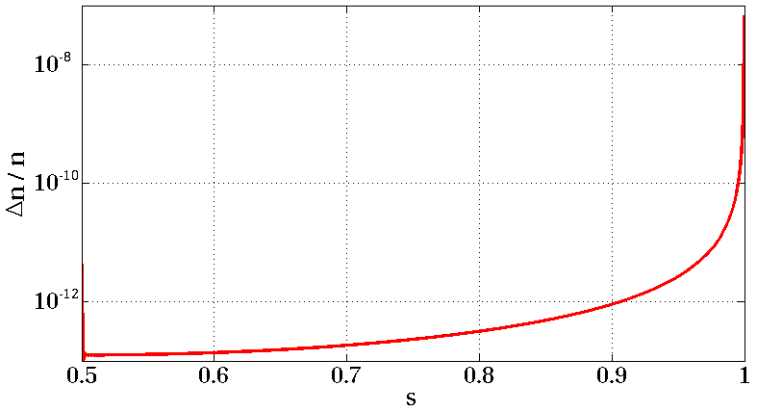

***Figure 2.13**: Parallel profil of the charge separation rate in a case of uniform particle source.*

other tokamaks are not in agreement with that description, meaning a more complex source distribution.

Coming back to the quasi-neutrality assumption and its validity, the previous density profile illustrated in the uniform source case can be a starting point for a proof of principle. The potential is linked to the density via the Maxwellian electron approximation and the charge separation is linked to its parallel gradient via the Poisson equation, leading to the expression:

$$\frac{\Delta n}{n} = \lambda_D^2 \nabla_{||}^2 \ln n$$

Where $\Delta n = Z n_i - n_e$ notes the charge separation. Considering again some standard plasma conditions : $n_e = 10^{18} m^{-3}$, $T_e = 10eV$, $L_{||} = 100m$, the quasi-neutrality indicated by the ratio $\frac{\Delta n}{n}$ is checked along the field line. As intuited, the quasi-neutrality is fairly justified for the whole profile 2.13, except close to the limiter where the separation start diverging. In fact, this remark is not surprising since the sheath is an asymptotic boundary of the field line, and we did not treat carefully the transition between quasi-neutral presheath and the sheath entrance. For considerations, a case with non uniform particle source gives the same trend since the departure of the neutrality is effectively a matter of limiter interaction.

2.5 Plasma-probe interaction

The electrostatic probes are usually small collectors inserted into the plasma to measure plasma parameters and from the previous description of plasma-material interaction, is is fair to consider probes as intrusive or disturbing diagnostics. On the other hand, if the probe is small enough compared to the whole SOL size, the related disturbance is confined to a relatively small fraction of the field lines intercepting the probe and for that reason does not disturb the whole plasma but rather the measured quantities. From previous considerations, some qualitative descriptions of the plasma-probe interaction can be made in term of measure corrections:

- In order to measure the plasma potential, the sheath potential drop as be be considered.
- For a density measurement, the density attenuation along the presheath has to be taken into account.

Thus, the presheath equilibrium in the framework of plasma -probe interaction has to be precisely described in order to relate the probe measurements to undisturbed physical quantities. This section starts with some generalities about plasma variables measured with Langmuir probes, and then the plasma-probe interaction is carefully treated in the framework of the *Hutchinson* approach.

2.5.1 Principle of Langmuir probes

A probe is usually composed of electric collectors fixed on an isolating head. These collectors are possibly polarized in order to measure three local plasma parameters that are the plasma density, the electron temperature and the floating potential. The latter one is simply the potential of the collector when no current is collected, thus given by the previous description of the plasma-limiter interaction2.49. When the probe is polarized, a current is collected and its trend function of the voltage value depends on the density and electron temperature : if the probe is polarized strongly negatively, all electrons are repealed and the collected current is an ion data related to the plasma density. While increasing the applied voltage, an increasing fraction of the electron distribution is collected and the trend depends on the electron temperature. The underlying model is well described by the previous steady-state approach 2.48 while assuming now that a net current can be collected by the surface.
Let us consider a reference position 0 along a field line ending on a probe collector and express the current received by the collector surface:

$$j_{probe} \equiv Ze\Gamma_i^{probe} - e\Gamma_e^{probe} = Ze\alpha n_i^0 c_S - en_e^0\sqrt{\frac{T_e}{2\pi m_e}}e^{\Phi_s-\Phi_0}$$

Rewritten as:

$$j_{probe} = e\alpha n_e^0 c_S\left[1 - e^{\Phi_s-\Phi_0-\Delta\Phi}\right] \tag{2.56}$$

where have been introduced the density attenuation factor α along the presheath and the sheath potential drop $\Delta\Phi$ 2.51. It has to be kept in mind that this expression remains true while the

Bohm criterion can be applied to the sheath entrance. Thus a potential drop is assumed to exist within the sheath, that fix an upper limit to the probe potential :$\Phi_s \leq \Phi_0 - \ln(\alpha)$. The latter expression of the collected current can be rewritten to explicitly involve the probe potential and the electron temperature. An other parameter is defined as the *saturation current* : $j_{SAT} = e\alpha n_e^0 c_S$:

$$j_{probe} = j_{SAT}\left[1 - e^{\frac{eV_{probe}}{T_e} - (\Phi_0 + \Delta\Phi)}\right]$$

From that formulation, any Langmuir probe quantities are well described depending on the acquisition mode :

characteristics :The probe potential is swept in time and a set of data (j_{probe}, V_{probe}) are collected to form a *characteristic* current/voltage. An exponential fit gives the three parameters j_{SAT}, T_e and $\Phi_0 + \Delta\Phi$ 2.14. Of course, the swept period is limited by the capability of electronic systems: usually, a characteristic is composed of hundred points taken over a millisecond. Thus for typical fluctuations time scale $10-100\mu s$, the evaluated parameters are time averaged [2].

saturation : The probe voltage is fixed to a strongly negative value (-200V) so that $j_{probe} \approx j_{SAT}$. In that case fluctuations are worth being measured since no sweeping are needed and the saturation current somehow reflects the density fluctuations.

floating : The collected current is fixed to zero so that the probe potential is imposed by the ambipolar interaction with the plasma to give the measure of the *floating potential* :$V_{probe} = V_0 + \Delta V$.

In the characteristics mode, the electron temperature estimation allows to evaluate the ion acoustic velocity c_S, by nevertheless assuming the ion temperature value - for instance $T_i = 2T_e$. Finally, the density or the product nc_S can be evaluated from the saturation current if the attenuation factor is known. As it will be shown hereafter, the value $\alpha = 1/2$ obtained in the limiter case is not applicable to the probe theory due to the non conservation of the generalized pressure along the probe presheath.

2.5.1.1 Hutchinson model

Interpreting the probe measurements has been the task of numerous works aiming at giving a precise model for the equilibrium between the plasma and a small collector. The mostly used model is the one introduced by Hutchinson [Hutchinson 88], in which the momentum transfers from the surrounding plasma are treated to describe probe presheath equilibrium 2.15. The reason to consider momentum transfer in the case of a probe and not for the whole SOL is because the probe intrusion implies strong velocity gradients between the probe presheath and the surrounding plasma, that are not present in the natural SOL.

[2]The issue is more complex due to the non linearity of the collector current and the coupling between plasma density, temperature and potential fluctuations during the acquisitions. For instance, the link between evaluated temperature and real time averaged temperature value is not straightforward

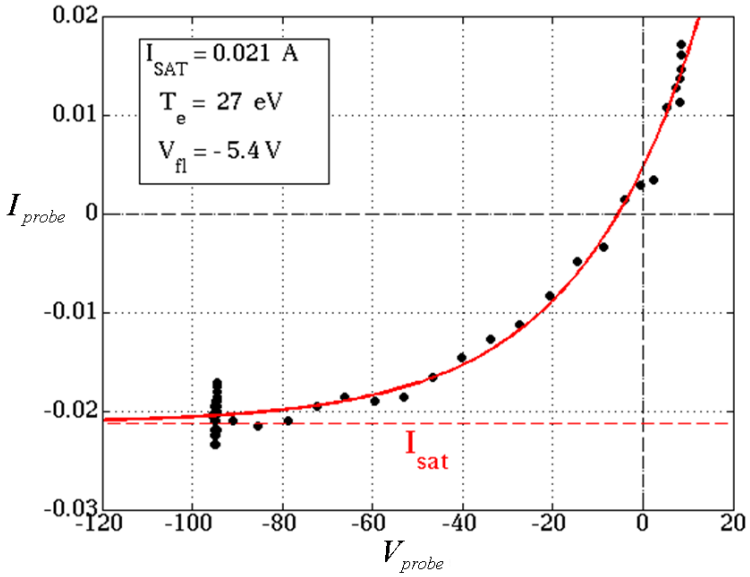

Figure 2.14: *Illustration of a characteristic current/Voltage collected in the SOL of Tore Supra (black dots) with a sampling frequency of 128 points/ms. The current sign convention corresponds to a positive current flowing out of the probe. The experimental points are extrapolated with an exponential function (red curve), returning the plasma parameters as indicated. The polarization range validity is a posteriori checked while calculating the threshold polarization value :* $V_{probe} \leq 56V$

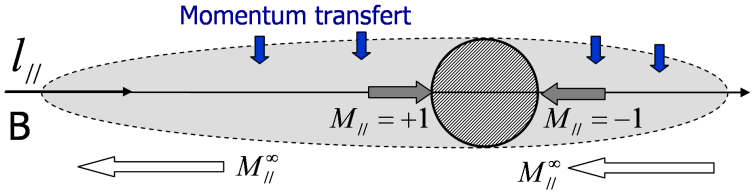

Figure 2.15: *Illustration of the probe presheath in a surrounding plasma flow. Viscous stresses have be taken into account at the edge of the presheath.*

The key point of the Hutchinson model is to describe the orthogonal transfers of mass and momentum from the surrounding plasma - labeled by ∞ - to the probe presheath using a tank model. The reason is clear if we consider first that the probe is not disturbing the orthogonally surrounding plasma and secondly that the orthogonal probe size a fixes a scale length to the transfers processes: Orthogonal gradients at the transition between the surrounding plasma and the presheath are expressed in a simple form : $\nabla_\perp A = -\frac{A^\infty - A}{a}$. the second but not least key point of the model is the assumption that the probe presheath is short enough to involve uniform boundary conditions along the presheath: the medium labeled by ∞. In our model, the mass and momentum fluxes are described within a convective approach $\Gamma_\perp = nv_\perp$. Although the original approach was diffusive $\Gamma_\perp = -D_\perp \nabla_\perp n$, the resulting simplified model is not changed. The reason for such revisited approach is the experimental conclusion that edge transport mainly involves convection of density bursts. The plasma equilibrium is described through the usual set of equation 2.52 & 2.53, where the ionisation source is omitted since it is assumed negligible when considered as the recycling on a small surface. The tank assumption

for fluxes leads to the following writings:

$$\nabla_\perp \Gamma_\perp = -v_\perp \frac{n^\infty - n}{a} \qquad \text{and} \qquad \nabla_\perp \left(\Gamma_\perp c_S M_{||}\right) = -v_\perp c_S \frac{n^\infty M_{||}^\infty - n M_{||}}{a}$$

The final system is written in a fully dimensionless form by introducing a parallel scale length : $\lambda = \frac{a}{M_\perp}$ and by normalizing the density to the undisturbed value n^∞ :

$$\begin{aligned} nM\nabla_{||}M + \nabla_{||}n &= M^\infty - M \\ n\nabla_{||}M + M\nabla_{||}n &= 1 - n \end{aligned} \tag{2.57}$$

By defining the origine of the parallel coordinate at the probe surface, the boundary conditions are $n(+\infty) = 1$, $M(+\infty) = M^\infty$ & $M(0) = -1$. Again it is reminded that the presheath length is assumed to be less than the typical parallel gradient length of the surrounding plasma. The previous differential system does not lead to analytical solutions and is for that reason solved numerically. The resulting profiles 2.16 are similar to the ones obtained for the limiter case, except that the generalized pressure $n\left[1 + M^2\right]$ is not an invariant. In particular the density attenuation along the presheath to the sheath entrance depends on the sign of the surrounding velocity : in the presheath facing the flow, the density is higher than in the probe wake where the pressure is intuitively lower. As a remarquable result, the density attenuation factor at the sheath entrance is a function of the surrounding velocity only, which introduces the principle of a Mach probe discussed in the following part.
Before coming to that point, the assumption followed of an uniform tank as to be confronted to the model results. For that, let us define the presheath length as the distance from the probe to recover 95% of the undisturbed density, and let us consider an extreme case of a strong flow $M^\infty = 0.8$. The presheath length varies from 0.1λ in the presheath facing the flow to 4λ in the probe wake. Now let us quantifiy these values by considering a probe size of $a = 2cm$ - typical radius of probe heads used on Tore Supra- and an orthogonal flow of the order of $M_\perp \approx 1\%$ - ordering of the poloidal flows measured in the SOL of Tore Supra - the typical presheath length can vary from some centimeters to about ten meters. Considering now that the typical parallel gradient lengths are of the order of the field line length $L \approx 100$m as it can be infered from the previous limiter presheath model -except close to the limiter surface- the uniform tank approximation is justified at least for not to strong plasma flows.

2.5.1.2 Mach probe principle

The variation of the attenuation factor at the probe sheath entrance can be easily compiled with the previous model, solved for a variety of surrounding flow velocities 2.18. A first and clear result is highlighted : the attenuation factor varies from 0 to 1 when the flow velocity varies from -1 to 1 meaning that if the parallel flow velocity is unknown, the probe calibration is *a priori* not possible. Of course the probe design is an important factor in that consideration. If the collector is a small pine out of the probe head wakes, and thus receiving a plasma flux from both side of its body, the resulting average current could be independent of the flow velocity. On the other hand, a particular probe geometry is taking benefit of this attenuation variation

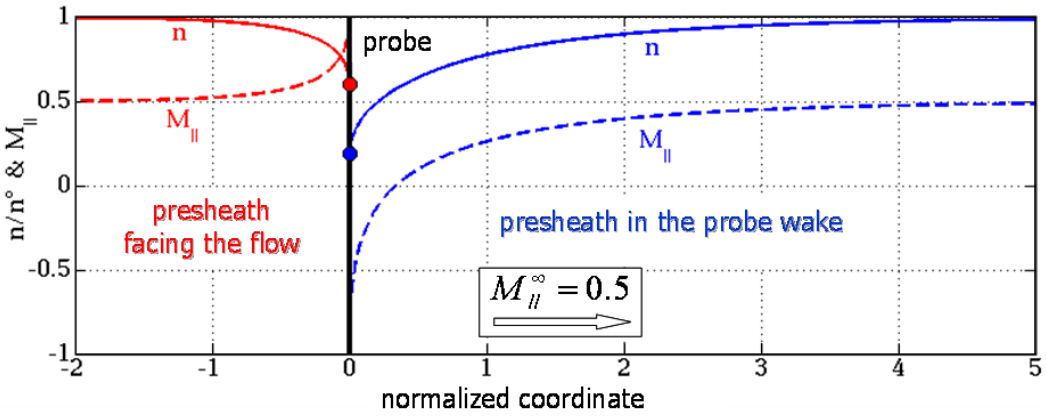

Figure 2.16: *Parallel profiles of density and flow velocity in the presheath of a probe immersed in a surrounding flow $M^{\infty} = 0.5$. Both the presheath facing the flow and the probe wake are presented. The difference in the density attenuation factor is easily noticeable.*

and makes possible an estimation of the flow velocity : this is the Mach probe configuration 2.17, the essential tool of transport study in the SOL.

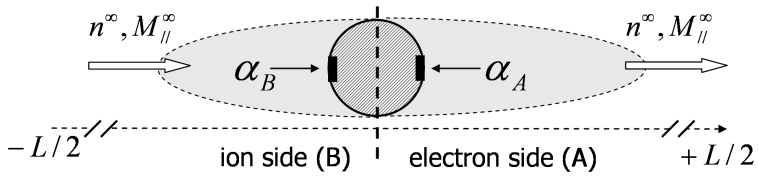

Figure 2.17: *Illustration of the plasma-probe interaction in the Mach configuration : two collectors are placed on both sides of the probe body with respect to the magnetic field. The attenuation factor is then measured in the presheath facing the flow and in the wake.*

Let us consider a probe head in a surrounding parallel flow, with two collectors in both sides of the probe with respect to the field line direction. The Hutchinson model predicts that the attenuation factor is different for the two collectors : in the wake, the pressure drop leads to a lower attenuation factor than in the presheath facing the flow. Since the boundary conditions are assumed to be the same in both sides of the probe, the difference of current collected from the two collector is only due the the attenuation difference. As a particular model result, the attenuations ratio is a bijective function of the surrounding Mach number, and thus highlights a tool for measuring the local flow velocity 2.18.

In a common picture of Mach probe configuration the collector facing the magnetic field is on the *ion* side of the probe -labeled by B, whereas the other collector is on the *electron* side - labeled by A. The simplest way to evaluate the flow velocity is to compare the saturation current collected on the two sides : J_{SAT}^{A} & J_{SAT}^{B}. Since the Hutchinson model does not lead to an analytical solution, a correct approximation can by easily used for evaluating the surrounding plasma quantities with an error less than 10%:

$$M_{||}^{\infty} \approx 0.4 \ln\left(\frac{j_{SAT}^{B}}{j_{SAT}^{A}}\right) \tag{2.58}$$

$$en_e^{\infty} c_S \approx 3\sqrt{j_{SAT}^{A} j_{SAT}^{B}} \tag{2.59}$$

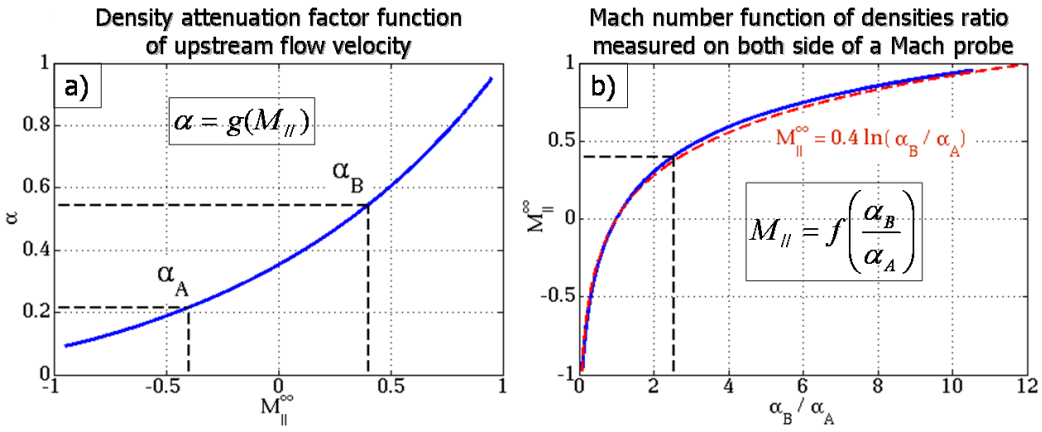

Figure 2.18: *Left : Variation of the attenuation factor function of the flow facing the probe. Right : Link between flow velocity and attenuations ratio in a Mach configuration. An exemple is shown for a surrounding flow* $M^{\infty} = 0.4$

In order to minimise the error related to probe measurements and to stay in a coherent experimental approach with respect to the steady-state model, the choice has been done to perform a data interpretation directly from the previous simulation results:

$$\text{data} : \left(j_{SAT}^{A}, j_{SAT}^{B}\right) \Longrightarrow M_{||} = f\left(\frac{j_{SAT}^{B}}{j_{SAT}^{A}}\right) \Longrightarrow (\alpha_A, \alpha_B) = g\left(M_{||}\right)$$

This interpretative model is the basement of probe measurements with respect to the steady-state transport study in the SOL, since it gives quantitative informations on the local parallel flux : velocity and strength.

2.5.1.3 The cylindrical collectors

In the sight of the Hutchinson model, particular attentions to the standard Langmuir probe configuration can be paid: a cylindrical collector plunged into the plasma 2.19. The interest holds in the fact that this configuration is used for turbulent probes as it will be illustrated in the following, to measure saturation current and floating potentials. In that simple configuration, the collector receives a plasma flux from both side of its body, and thus does collect an averaged current. Due to sophisticated plasma-cylinder interaction, let us just assume that the Hutchinson model is valid for the attenuations taking place on both side of a cylindrical collector. That is, the collector measures a saturation current that is an average over the two sides of its body, with no possible correction from the surrounding flow velocity. It appears that the averaged value of the attenuation factors is not constant and leads to a error in the ordrer of 20% as illustrated on the figure 2.19. Concerning the floating potential measurements, the dependence on the attenuation factor raised by the equation 2.51 turns to give about 10% error by considering also an averaged value from the two sides of the probe. In fact that way of considering the potential measurement might be wrong since the cylinder might be effectively polarized with an uniform potential. But the underlying result is that the error is not too important.

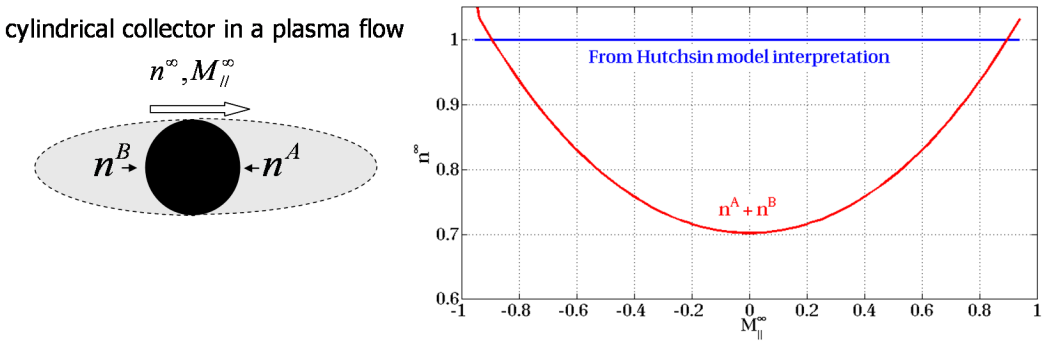

Figure 2.19: *Left : Geometry of a cylindrical collector plunged into a plasma flow. Right : Depending on the flow velocity, the measured density is plotted in the case of a Mach probe (blue) and in the case of a cylindrical probe (red), whose measurement is a simple average over the two sides of the collector body*

2.5.2 On the validation of the plasma-probe model

Hutchinson model The set of approximations underlying the plasma/probe interaction model can be partially validated. First can be tested the property that the probe size has no influence on the density attenuation factor. For that purpose, let us consider the radial rake probe used on Tore Supra : the probe head is a massive boron nitrite cylinder 4 cm in diameter - figure 2.20, on the sides of which are anchored radial beams of small collectors. The pines are separated by 3 mm in the radial direction, and thus the characteristic radial probe size belonging to each collector are different, although the poloidal sizes are equal. During a probe plunge, the saturation currents collected by each pine are compared for a given local position in the plasma profile, thus for the same undisturbed quantities. The comparisons are summarized on the figure 2.20. As a validation, the saturation current amplitude measured by such a probe is independent of the collector position on the probe head.

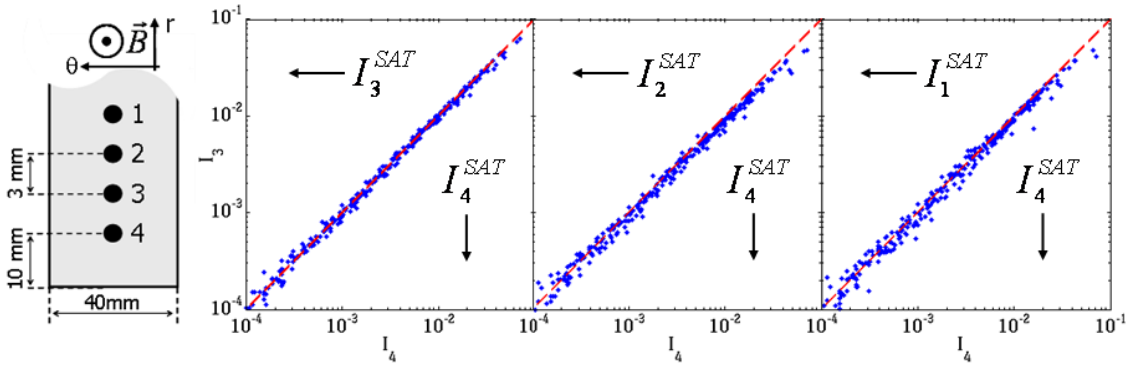

Figure 2.20: *Left : Picture of the radial rake probe used on Tore Supra. Thin collectors are placed along a massive isolating probe body. Right : Comparisons of saturation currents collected by for pines placed on the same probe face. During a radial motion of the probe, data are considered at the same distance from the LCFS, thus in a similar undisturbed plasma medium.*

electron temperature measurement The principle of electron temperature measurement as exposed earlier 2.14 involves an implicit but strong assumption : the temperature is evaluated from the wings of the electron distribution and not from the distribution bulk. Indeed, the strong sheath potential drop imposed close to the saturated regime - left part of the characteristic - implies that only the fastest electrons reach the probe collector. In other words, it is assumed that the distribution width is well described by its wings, and thus is a pure Maxwellian.
Considering a Mach probe in a characteristics acquisition mode, the temperature is estimated in both side of the probe with respect to the parallel direction and thus offers a double estimate of the electron distribution by analyzing the negative and positive velocity wings. A common finding underlined by experiments on Tore Supra and other tokamaks [LaBombard 04] is that the evaluated temperatures are not identical on both sides of a Mach probe.
In a standard Tore supra plasma configuration - meaning the plasma in contact with the main limiter, the measured temperature is almost always higher on the ion side by a factor of about 1.4. The observations are similar when the plasma is in contact with the inboard limiters 2.21. On the other hand, the tendency is less pronounced and even reverses when the plasma is pushed to the outboard limiters. As an attempt of qualitative explanation, the main difference in between these configurations is the location of sinks and sources of energy and particles (limiter plates) with respect to the measurement position. But up to now, there is no concrete theory and models able to reproduce the changing asymmetries and giving a rigorous interpretation of collected data. Anyhow, the danger in evaluating a Maxwellian temperature from the distribution wings is to face kinetic effects that are not described by the fluid approach. In particular the presence of a suprathermal electron population can seriously mislead the data interpretation [Rompuy 08].
As a conclusion, the Maxwellian distribution approximation for electron may be wrong due to experimental evidences of asymmetries. The pragmatic approach followed for the temperature estimation consists on averaging the temperatures measured on both sides of the probe, keeping in mind that the electron distribution bulk is not diagnosed by the measurements [Batishchev 97].

plasma density measurement the last but not least element of validation concerns the density evaluation in the characteristic acquisition mode with a Mach probe to take care of attenuation effects. Since the density is in fact evaluated from a multi-step process, the full probe theory can be roughly validated:

- The characteristic fit returns on both sides of the probe the saturation currents and the electron temperature.
- The attenuation factors are deduced from the saturation currents collected on both sides of the probe through the Hutchinson model, and returns an evaluation of the local undisturbed quantity $n_e c_S = n_e \sqrt{\frac{1}{m_i}(ZT_e + T_i)}$.
- The electron temperature is averaged over the two sides of the probe, the rough assump-

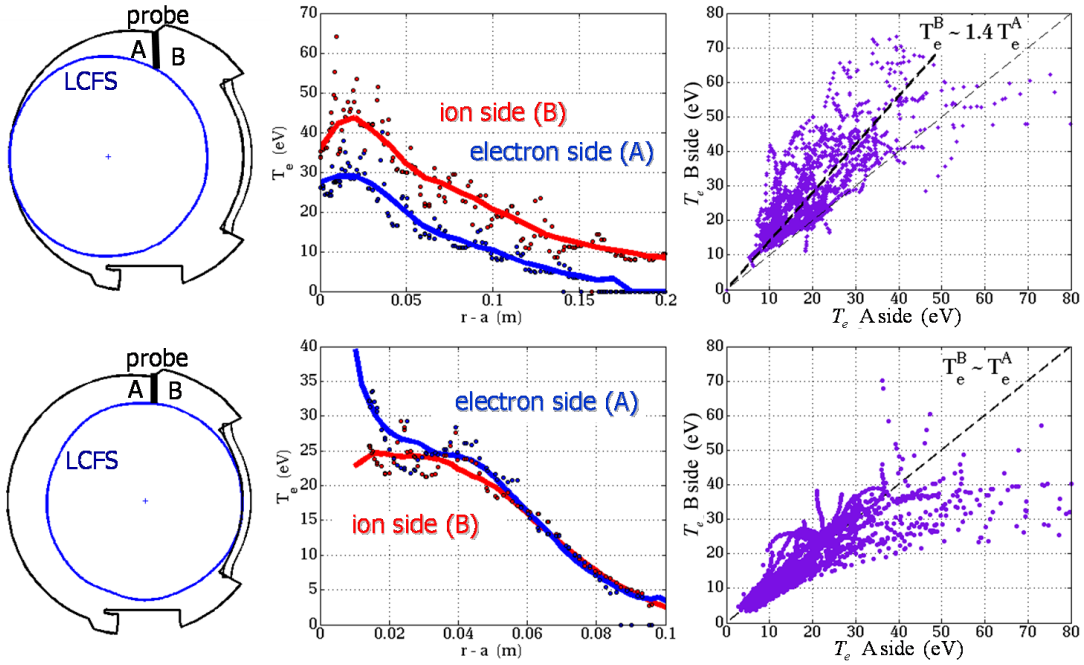

Figure 2.21: *Comparison of the electron temperature measurements with a Mach probe (segmented tunnel probe) run in characteristic mode. Upper part : the plasma is in contact with the inboard limiters as illustrated on the left by the poloidal cross section. On the middle are presented temperatures profiles measured on both sides of the probe function of the distance to the LCFS for one particular discharge. On the right are directly compared the local temperature measurements between the side A and the side B. Data are collected during about 50 probe plunges performed on 7 ohmically heated plasmas. The ion side temperature is higher in the trend than the electron side temperature. Lower part : the plasma is in contact with the outboard limiters. Now, the temperatures are more or less equals.*

tion $T_i = 2T_e$ [Kocan 08] is done for the ion temperature that gives in return an evaluation of the ion sound speed and thus the electron density.

In order to proceed to a validation of the probe density measurements, a comparison with other diagnostics is worth being performed particularly with well calibrated systems. In that way the density profiles from probe are cross validated with the interferometer system whose setup can involve a laser line of sight going through the SOL only for some specific plasma geometry. On the other hand the comparison is not straightforward since the interferometer density is a line integrated quantity, whereas the probe returns a radial profile of the local density 2.22. A way to proceed is to use an edge magnetic reconstruction and map the probe density profiles to the interferometer line of sight, assuming constant density along field lines. This last assumption may lead to a relatively small error - 10% - since the field line section along which is performed the extrapolation is small compared to the parallel gradient length 2.12. The comparison shown in figure 2.22 is performed on data acquired during ohmic shots limited on the inbord limiter, in order to place the edge interferometer line of sight inside the SOL only. In such geometry, the probe plunges are deep enough so that no extrapolations of the probe density profiles are needed to be mapped on the laser line. As a result, the density measured by the probe is in

excellent agreement with the interferometer data, since the quantitative matching is followed over at least two decades of density amplitude. It has to be mentionned that the interferometer diagnostic is subject to fringe jumps that can lead to relatively significant mismeasurements at low density [3], and for that reason the possible disagreement of the comparison for the lowest densities is not fully relevant.

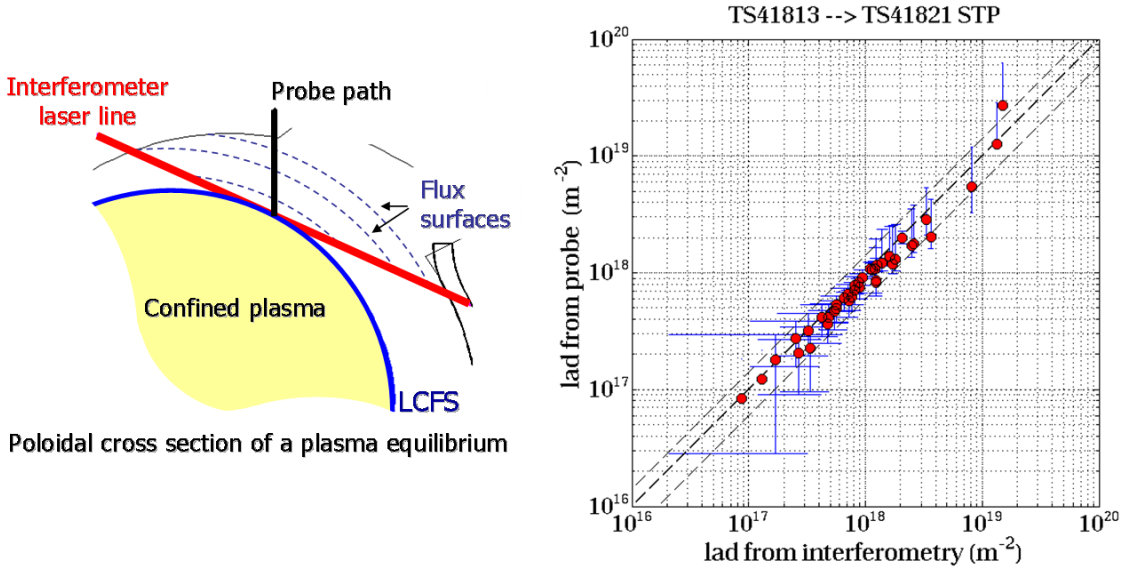

Figure 2.22: *Cross comparison of density measured by interferometry and Mach probe (STP). The first measurement being a line integrated data along the line of sight, the local probe measurements are mapped along the flux surfaces to the laser path. Left : the geometry is illustrated. Right : Comparison of the line averaged density measurements for a set of about fifty plunges performed on ohmically heated plasmas. Parallel to the bisectrix (black large dashed line) is shown a deviation of ±40% (thin dashed lines) .*

[3]Private communication with C. Gil

2.6 Summary

This chapter has been dedicated to the introduction of essential physical notions related to the experimental investigation of particle transport at the edge of tokamak plasmas :

- The circular magnetic geometry of Tore Supra plasmas is of great help to approximate the torus geometry to a slab geometry with errors less than 30%.
- The fluid description is a good compromise between the simplicity needed for an experimental approach and the description of dominant effects related to edge transport and flows equilibrium.
- The drift effects that characterize the plasma dynamic orthogonal to the field lines contains all physical ingredients necessary for the description of the turbulent transport, especially the electrostatic drift.
- The open field lines physics is strongly influenced by the presence of limiters. First of all, these limiters defines strong boundary conditions in term of parallel flow velocity through the *Bohm criterion*. Then the plasma profiles along field lines is imposed by a balance between these boundary conditions and the parallel distribution of the particle source. The latter point based on a generalized pressure conservation along field lines is of pragmatic interest for experimental investigation and will be developed along the next chapters.
- The Langmuir probes theory needed in our approach has been described, in particular the Mach probe principle. Partial validations from experiments have been performed and infer the reliability of the diagnostic. In the next chapter a novel probe is introduced, dedicated to electrostatic fluctuations and further elements on the reliability of the flow measurement will be discussed.

In the next chapter the edge radial transport is addressed in the scope of Langmuir probes measurements and models described previously. To that point and further, any specific assumptions have been made about the nature of the radial transport in order to avoid any speculations from common believes. Rather, the transport properties at the edge of Tore Supra will be stepwisely documented and interpreted. That is, the last chapters address the three dimensional properties of edge transport in the highlight of fast visible imaging and cross-coherence from multi-diagnostic investigations.

Chapter 3

Probes and particle transport

This chapter is devoted to the experimental investigations of edge particle transport with reciprocating Langmuir probes. In a first section the steady-state particle equilibrium is considered under the scope of Mach probe measurements. After a discussion on the reliability of Mach probes to evaluate the flow velocity, the different mechanisms potentially involved in the drive of parallel flows are investigated. Following the related simplifications on the particle flow balance, radial profiles of density and parallel flows are interpreted in terms of radial particle flux variables. Properties of this steady-state radial flux are discussed. The second section is dedicated to fluctuations measurements, starting with the presentation of a new probe diagnostic installed on Tore Supra : *DTURB*. After a discussion about common properties of fluctuations in SOL plasmas, we focus on the reliability of dedicated diagnostics to quantify some specific phenomena : phase velocities or radial flux. Finally we present the principal evidences about the electrostatic turbulent radial flux : nature and amplitude.
The analyzes and interpretations presented herein are personal and do not summarize the contributions from other persons - except when noticed. This work has not been done in isolation but received the support of numerous comments and advices from theorists and experimentalists.

3.1 steady-state approach : parallel flows and radial transport

In this section we introduce the tools used to investigate the steady-state particle transport : diagnostics and models. First of all we clarify what is a probe reciprocation and how the data are labeled with a spatial coordinate. Then, we discuss on a long date issue related to the measurement of the parallel flow speed in SOL plasmas: is there a reliable probe geometry ? After, we comment on some evidences about the parallel flows and highlight the dominant driving mechanism. Quantitative informations about the radial particle flux are finally derived from the parallel flows.

3.1.1 Notion of probe reciprocation

During an experiment, a probe can be manipulated in the SOL plasma where it collects particles in order to determine the local plasma parameters. The backside of this direct and

local measurement is a fast overheating of the probe body due to the strong heat flux carried by plasma particles. To avoid irremediable damages the probes are usually manipulated from the wall with a fast driving mechanism. On Tore Supra, the probe heads are mounted at the extremity of a hydraulic piston able to move the probe from the wall to the LCFS and the return in less than 200ms, short enough to avoid a probe damage. The *reciprocation* of the probe is thus a necessity when measurements close to the LCFS are on request and is in fact really convenient for studying the plasma equilibrium in the SOL since a reciprocation delivers a radial profile of the plasma. For that reason the acquisition systems are designed with a time sampling optimized for a complete and precise profile reconstruction during a reciprocation. Moreover, a probe plunge is always considered fast enough to assume that the plasma is in a steady-state equilibrium during the motion, such that the whole collected profile does describe the SOL plasma parameters belonging to the given global plasma state. On the other hand the statement is not true during transient events like super sonic molecular beam injections (SMBI) or edge radiative instabilities (MARFE).

As it is introduced later on, the study of SOL plasma equilibrium is mainly based on the radial evolution of the density from the LCFS. For that reason it is convenient to label the probe position according to the position of the last closed flux surface [1]. In the following the probe position is always labeled by the parameter $r - a$ where r and a represents respectively the minor radius of the flux surface supporting the collector and of the LCFS. The distance is calculated at the probe position - plasma Top - and is not extrapolated to the outboard midplane, as usually done. A small difference exists however due to the Shafranov shift 2.1.1 but without any consequences on the analysis and interpretations.

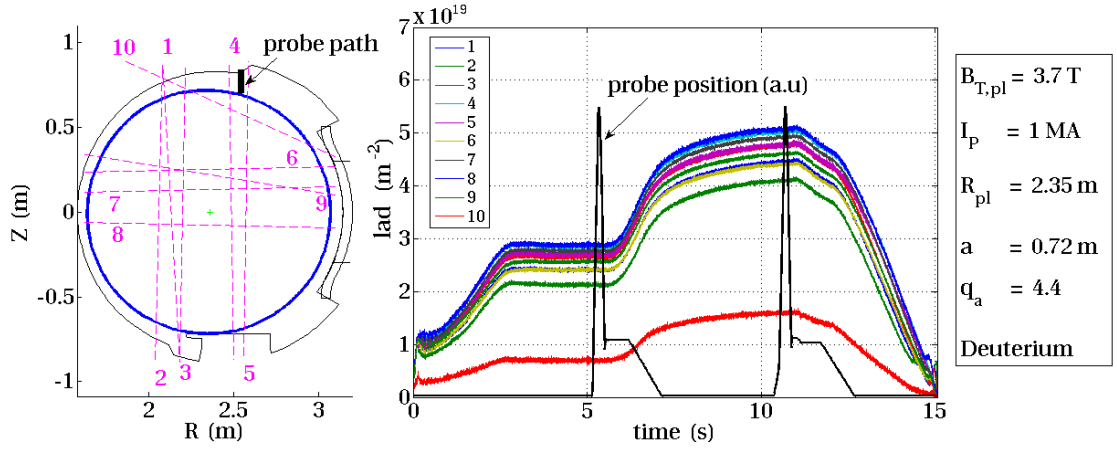

Figure 3.1: *Illustration of a discharge on Tore Supra. Left: poloidal cross section of the magnetic equilibrium in the steady-phase, plus the interferometer geometry. Right : density evolution function of time measured by the interferometer. The plasma current evolution is illustrated (black dashed line) and the probe motion is displayed with 2 plunges at two different densities. Some plasma parameters constant on the discharge plateau are shown on the right.*

[1] On Tore Supra, the probe position during a reciprocation is even controlled in real time according to the instantaneous position of the LCFS, offering a certain flexibility and simplicity for the use of the diagnostic in a variety of magnetic configurations.

3.1.2 Reliability of a Mach probe design

The probe theory has been investigated earlier, but a missing and crucial point as not been discussed yet : the collected currents are proportional to the collection area of the collectors and thus the undisturbed plasma parameters can only be deduced from these currents if the collection areas are precisely known. Different collector designs have been tested on Tore Supra since a decade and a summary of geometrical effects on the plasma collection is proposed:
The first reciprocating Langmuir probes installed on Tore Supra where designed with shielded collectors 3.2 in a Mach configuration. The plasma collection by the shield through the hole has been investigated in [Gunn 01]. It has been proven that the fraction of plasma flux transmitted to the collector is hardly evaluable, concluding that a precise calibration of the effective collection area is not possible.
In order to eliminate in theory all uncertainties about the effective collection area and thereby rendering the measurements of parallel flows more reliable [Gunn 02], the tunnel probe has been designed 3.2. Due to the concave geometry, the electrostatic sheath usually influencing the collection area is now localized inside the tunnel and do not participate to the effective increase of the collection area. As shown previously on the figure 2.22, the density measured with a tunnel probe in a Mach configuration (segmented tunnel probe, or STP) is fairly matching the density measured by the interferometry (a well calibrated diagnostic). This good matching is not obtained with standard collectors.
More recently new probe heads have been tested in Tore Supra to investigate the turbulence : the rake probes - see figures 3.16 & 3.17, composed of arrays of small cylindrical collectors. This kind of probe has been and is currently intensively used on other tokamaks either for fluctuations or steady-state investigations. But it is well established that ions are effectively collected over an area larger than the geometrical projection [Dejarnac 07] when the collector size is only slightly larger than both the ion gyroradius and the sheath thickness around it. The result is a relatively large uncertainty about the effective collection area for such collectors. We would like to address in this part the consequences on the Mach number evaluation. Further comments on the collection area are presented latter on.

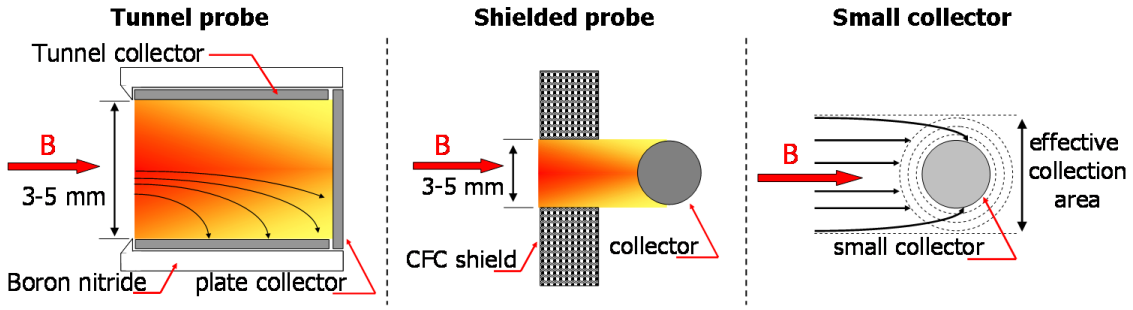

Figure 3.2: *Illustration of the different collector configurations used in Tore Supra. Left to right: the tunnel probe, the shielded probe and the small collector (for turbulence)*

The tunnel probe and the poloidal rake probe offer a similar geometry : a 4cm in diameter probe body on sides of which are installed collectors in a Mach configuration. The tunnel

probe is thus composed of two tunnel collectors mounted back to back and the poloidal rake probe is composed of two small cylindrical collectors mounted on each sides of the probe body. The only difference in the Mach configuration between the two probe heads is the size of the collectors. The two systems are installed in the plasma chamber at the same poloidal position, separated toroidally by 120 degrees. Thus assuming a toroidal symmetry of the plasma profiles and considering two plunges performed simultaneously, the comparison of data collected by the two probes is fairly possible. As a matter of facts the probe control system does not allow to perform simultaneous plunges but with a delay of a least 0.5 seconds, having however no consequences if the plasma discharge is slowly varying.
Let us consider a pair of plunges performed in a steady-state plasma. The Mach probe is run in a characteristic mode and therefore returns parallel flows variables as well as density, temperature and floating potential. The poloidal rake probe is run in a saturation mode (-200 eV), and thereby measures saturation currents on the Mach collectors and on the poloidal rake. The volume quantities are obtained by defining the effective collection area of the small collector as their geometrical projection on a plan orthogonal to the magnetic field. Data collected by both probes are averaged over sub-windows of 1 cm width centered on a fixed mesh defined along the radial profiles. A set of ohmically heated discharges - either limited on bottom or high field side with a fair toroidal symmetry- has been diagnosed by both reciprocating probes to form a set of 15 pairs of plunges covering a wide range of plasma parameters.
A comparison of local Mach number evaluated from both diagnostics is presented on figure 3.3. We notice that the Mach number measured by the tunnel probe is always positive for these particular experiments. In facts we chose plasma geometries for which we know that the parallel flow at the plasma top should be directed from low field side to high field side (positive Mach value), comforting the assumption that tunnel probes give a correct estimate of the parallel flow velocity. On the other hand we notice that for the same plasma conditions the poloidal rake probe can measure negative Mach numbers, inconsistent with the experiment. These few points on the graph already shows that small cylindrical collectors are not fully adapted to the measurements of parallel flows. Now looking at the full set of points, we notice that most of the Mach numbers evaluated by the rake probe are positive, thus in agreement with the expectation. However their amplitudes are smaller than Mach numbers given by the tunnel probe, by a factor of about two. Under the assumption that the tunnel collectors are not disturbed by sheath effects, the difference in the measurements can be attributed to the small size of collectors composing the rake probe. On that prob the Mach collectors have presumably different effective collection areas depending on the probe side and plasma parameters, making hard any attempt to calibrate the probe for Mach measurements.
Furthermore, the flow strength nc_S measured by the rake probe is unambiguously higher than the tunnel probe measurement by a factor of about 2 3.3. This shows that the effective collection areas for the small cylindrical collectors are larger than their geometrical projection. These observations raise some doubts on the consistency of parallel flow measurements performed with small collectors. Measurements with concave collectors -like the tunnel probe - are rarely found in other tokamaks where probes are more often composed of small collectors, either in

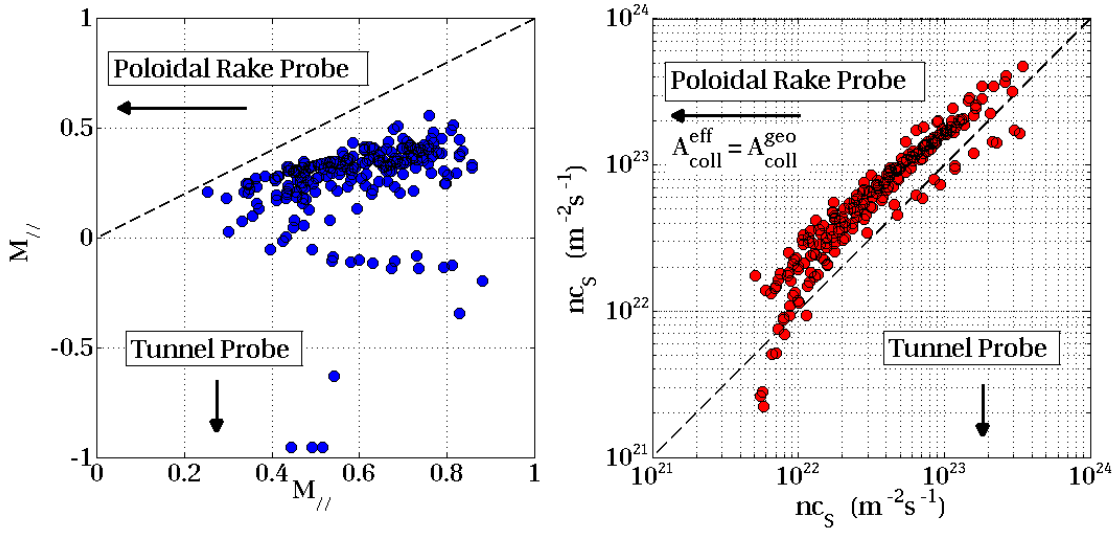

Figure 3.3: *Parallel flow variables extracted from the Mach collectors of the two probes. For the poloidal rake probe, the effective collection area is defined as the geometrical projection of the collector. Left : Comparison of the Mach number evaluated at every positions in the profiles of all discharges. Right : Comparison of the flow strength nc_S.*

JET [Silva 04] or in TCV [Garcia 07a] or in C-mod [LaBombard 02] or in DIII-D [Watkins 97]. Although the effective collection area can be effectively deduced from a calibration with other diagnostics - other probes or reflectometers or Thomson scattering, the calibration holds only for the density amplitude and can not be applied as corrections for the parallel Mach number. Our conclusion is that small collectors mounted in a Mach configuration can not be applied for measuring the parallel flow velocity due to the large uncertainty on their effective collection areas.

3.1.3 First approach on parallel flow velocity and density profile

Some informations about radial transport are easily readable by looking at the parallel flux profiles measured by a Mach probe. Let us consider a steady-state discharge, ohmically heated - figure 3.1, during which a probe plunge is performed. About geometrical considerations that might be too early but necessary, the plasma/limiter geometry is set as following : the probe is magnetically connected only to the main limiter located at the plasma bottom - TPL - and not to outboard objects. We will see in the following that the presence of a second limiter intercepting the field line at the outboard midplane is of crucial importance when considering the particle flux balance in the SOL.

As a starting point, a remarquable and direct observation can be done : at the plasma top, the parallel flow is near sonic : $M_{||} \approx 0.5$ close to the LCFS 3.4. This statement of quasi-sonic flow measured at the top and directed from the outboard midplane is almost universal for that standard plasma configurations on Tore Supra - it does not depend on particular plasma parameters like plasma current, density or safety factor. Observations are similar when performed on other tokamaks [Erents 04][Pitts 07][LaBombard 04][Müller 07] even in divertor geometry. A first step in understanding the parallel flow amplitude is to interpret the flow

velocity in term of particle source distribution, as introduced in the previous section 2.4.3. A Mach number of 0.5 would correspond to a particle source localized for 90% at the Low Field Side, in a parallel section between the bottom limiter and the probe counting for less that 40% of the field line length. Of course the particle source is generally speaking a sum of different contributions like radial transport and ionisation process. On the other hand, relevant arguments exposed in the following allow us to think about radial flux asymmetry as the major contribution for driving the source asymmetry.

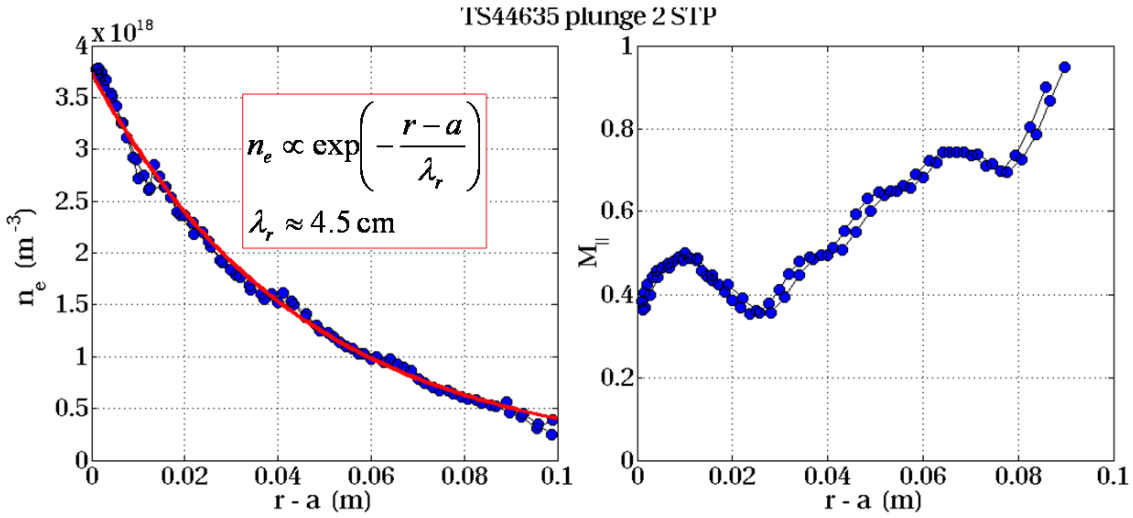

***Figure 3.4**: Left : Density profile n_e at the probe position plotted function of the distance to the last closed flux surface. An exponential fit is performed to give the radial gradient length λ_r. Right : The respective parallel Mach number, oriented from the low field side to the high field side at the probe location (top).*

Now let us consider the radial profile of the plasma density n_e at the plasma top, by noticing the exponential decay when moving radially away from the LCFS. This property is well understandable if we think about in term of particle trajectory : a test particle entering the SOL by any deconfining process from the confined region experiences a parallel motion to the limiters where it will be absorbed after a parallel transit time $\tau_{||}$. By that time, any radial transport process involved in the SOL displaces the particle trajectory outward with a radial extend limited by the parallel transit time. In a diffusive approach, the radial extent of the particle trajectory λ_r is the result of a random walk experienced during the parallel transit time : $D_r \equiv \frac{\lambda_r^2}{\tau_{||}}$. That time is simply defined as the averaged parallel transit length walked by the particles $\frac{L_{||}}{2}$ divided by the characteristic velocity scale c_S involved in the parallel motion, giving rise to the following expression of the diffusion coefficient :

$$D_r = \frac{2\lambda_r^2 c_S}{L_{||}} \tag{3.1}$$

Translating the mass conservation equation in term of effective parallel sink and diffusion leads

to:

$$\nabla_{||}(nv_{||}) = -\nabla_r \Gamma_r \quad \longrightarrow \quad \begin{aligned} \frac{nc_S}{L_{||}/2} &= D_r \nabla_r^2 n \\ \Rightarrow n &\propto e^{-\lambda_r r} \end{aligned} \tag{3.2}$$

This simple calculation reveals the exponential dependence of the radial density profile. Considering the experimental plasma parameters evaluated during the plunge : $L_{||} \approx 65m$ & $c_S \approx 5.510^4 m^2 s^{-1}$, the diffusion coefficient is found to be $D_r \approx 3.5 m^2 s^{-1}$. A more quantitative expression of the diffusion coefficient returns a similar value which is found to largely exceed the neoclassical diffusion and for that reason receives the qualification of *turbulent* transport coefficient.
This approach of steady-state flow profiles in the SOL is already rewarding : parallel flows amplitude is a cloud of some spatial asymmetries of the particle flux, and the radial scale length of density gradient is found to be very large compared to neoclassical predictions. The next step in the radial flux study consists in precisely quantifying its amplitude over the previous simple order of magnitude and needs for that purpose a realistic description of the flow balance in the SOL. The influence of the different terms driving the parallel flows is investigated in the following.

3.1.4 Discussion on driving parallel flow mechanisms

The parallel flow velocity expressed from the particle source distribution was an interpretation of the SOL equilibrium model:

$$\nabla_{||}\left(nc_S M_{||}\right) = -\nabla_r \Gamma_r - \nabla_\perp \Gamma_\perp + S_{ionisation} \equiv S \tag{3.3}$$

$$\nabla_{||}\left[n(1+M_{||}^2)\right] = 0 \tag{3.4}$$

Where the parallel flow is driven by a local source of particle S, composed of the radial flux, the ionisation source and for generality a contribution from the orthogonal drifts 2.3.3. As discussed later on, this SOL model allows an appreciable quantification of the radial flux from local probe measurements, but only under the assumption that the flows are driven by the radial flux. In that statement, it would be of great interest to quantify the effect of the ionisation source and orthogonal flows on the equilibrium.

3.1.4.1 ionisation source

The ionisation source in a general approach is composed of two main contributions : the local gaz injection aiming at controlling the plasma density and the local recycling on main limiters. The first one is performed by nozzles localized in the walls and lead to local fueling in front of the injection. Thus the related possible ionisation source happening in the SOL is spatially localized and might influence the SOL equilibrium seen by the probe only for specific magnetic configuration when the field line intercepting the probe is passing in front of the nozzle. The recycling on main limiters is subject to more precautions, since the toroidal

uniformity of the main limiter - or divertor - leads to a toroidal uniformity of the plasma recycling on it and thus may influence the flow equilibrium on any field line of the SOL.
On the other hand, the limiter geometry of Tore Supra is of great help in the reduction of the ionisation source in the SOL, since the confined plasma is very close to the recycling source. Considering also that for Tore Supra ohmic discharges the edge plasma is not very dense and hot, the mean free path of neutrals emitted from the main limiter is typically larger than the SOL width and most of the neutrals are ionized inside the LCFS and thus not in the SOL. Of course the story is more complicated since the recycling phenomenon involves a variety of neutral species, each of them passing through different excitation stages: energetic neutrals back scattered from the limiter, desorption of thermal D2 molecules that are in thermal equilibrium with the limiter surface, etc. Thus a consistent and quantitative estimate of the ionisation source from limiter recycling would require a numerical simulation of dominant atomic processes involved in the recycling phenomenon. Such tool has been already developed and intensively used to estimate the ionisation source for a variety of divertor or limiter tokamaks : the Monte-Carlo code EREINE. In our case we used the version 2D [2].
Considering an incident ion to the limiter surface, neutralisation occurs at the striking point and a neutral is re-emitted with a given set of probabilities defining the molecular or atomic state, the kinetic energy and the quantum state of electrons population. During the motion of the recycled particle in the edge plasma, excitation processes due to plasma ion and electron collisions are computed until the full ionisation is reached. Collisions and quantum excitation parameters are fully determined using the ADAS database [3] [Whiteford 09] applied to local plasma parameters : density and temperatures.
The numerical simulation is run with respect to realistic background conditions : the magnetic geometry of flux surfaces, the radial profile of ion flux to the limiter and a 2D-map of plasma density and temperatures. Finally a 2D-map of electron ionisation source is computed, that is self consistently equal to the source of incident particles. On the other hand the simulation does not consistently treat the ionisation source as a source of incoming particles since the code does not include transport equations, but rather gives an estimate of its spatial distribution for given plasma parameters. Since the Monte-Carlo simulations are time-demanding, the source calculation is not performed for every steady-state discharges of interest but has been rather estimated for a given set of parameters defining a standard case of reference 3.5. The results of the Monte-Carlo simulation are illustrated on the figure 3.6. As expected, the ionisation source contribution from atomic recycling is mainly localized in the confined region and the main contribution in the SOL is due to molecular desorption. Anyhow, the total amount of ionisation is mainly localized in the confined region, just inside the LCFS: Looking at the poloidal average of the 2D map, the incident particles flux is re-emitted as electrons and ions for 15% in the SOL and the rest in the confined region. Considering that the only sources of particles in the SOL plasma are the radial losses from the confined region and the ionisation source from recycling, we come to the conclusion that radial losses across the LCFS correspond

[2] private communication with Y. Marandet
[3] The Atomic Data and Analysis Structure

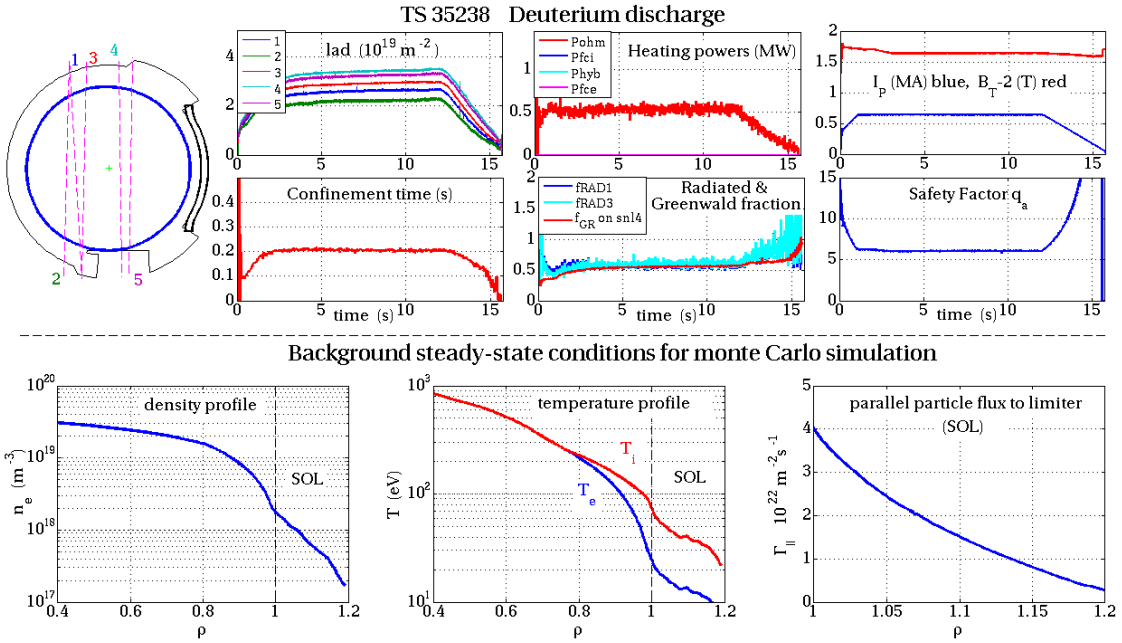

Figure 3.5: *Tore Supra Ohmic discharge used for the ionisation source estimation from recycling on the main limiter. Top : Evolution of given discharge parameters are plotted versus time. Bottom : profiles of the background conditions for the Monte-Carlo simulation : plasma density measured by reflectometer in the confined region and probe in the SOL, electron temperature measured by ECE in the confined region and probe in the SOL - $T_i = T_e$ is assumed in the confined region and $T_i = 3T_e$ in the SOL - and parallel particle flux to limiter compiled from probe measurements.*

to about 85% of the SOL fuelling, and thus dominate the global equilibrium in the SOL. We make the assumption that *the flow balance equation in the SOL is at first order not influenced by the ionisation source.*

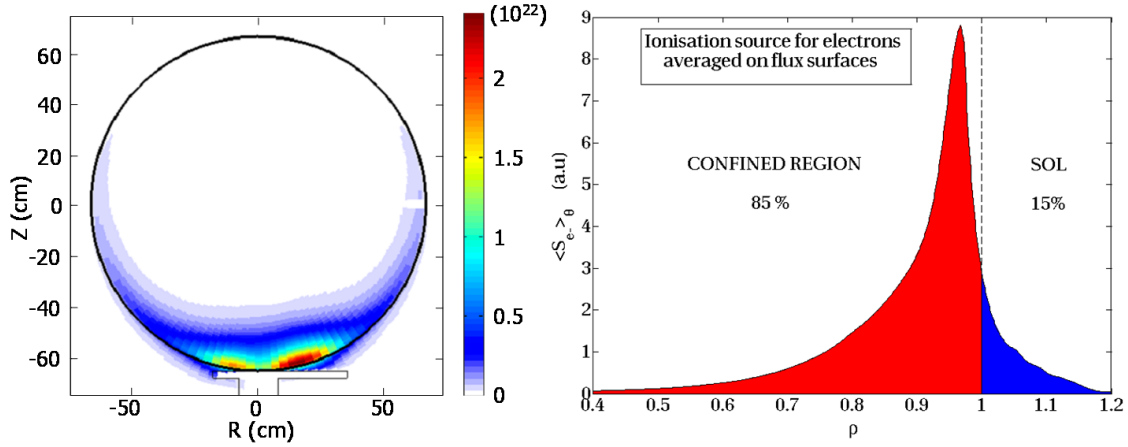

Figure 3.6: *Ionisation source calculated with EREINE from a given Ohmic plasma equilibrium. Left : 2D map of the electron ionisation source from deuterium neutrals emitted from the main limiter. Right : Poloidal average over the flux surfaces of the total electron ionisation source, including D_2 molecules. The averaged quantity is plotted function of the normalized minor radius. Only 15% of the ionisation occurs in the SOL.*

3.1.4.2 orthogonal flows

Now that the ionization source has been treated, let us pay attention to the orthogonal flow term present in the flow balance equation in order to clarify the influence of that term as a parallel flow driver with respect to the radial particle flux. In that purpose the flow balance is written again along the source coordinate 2.4.3, by considering the drift flow as a control parameter. For convenience and without reducing too much the generality of the problem, let us consider a spatially uniform drift flow in order to simplify the flow balance equation 2.40 :

$$\nabla_{||}\left(nv_{||} + n\frac{q_a\rho}{\epsilon}v_{E_r}\right) = -\nabla_r\Gamma_r \equiv S \tag{3.5}$$

$$\nabla_{||}\left(n\left[1+M_{||}^2\right]\right) = 0 \tag{3.6}$$

By rewriting the first expression in a dimensionless form, a drift flow parameter is introduced $\beta = \frac{q_a\rho}{\epsilon}\frac{v_{E_r}}{c_S}$. As done previously, the parallel flow can be expressed along the parallel source coordinate s counting for the radial flux only:

$$\frac{M_{||}+\beta}{1+M_{||}^2} = s_\beta - \frac{1}{2} + \frac{\beta}{2}$$

The subscript β placed on the source coordinate is set to keep in mind that the coordinate is indexing the parallel flow in presence of a drift flow β. Now let us define the influence of that drift flow as follow : for a given parallel Mach number, how does the corresponding particle source change in amplitude if the drift flow is considered or not ? The source coordinate s_β can be thus compared to a reference coordinate s_0 defined as the flow driver without drift flow $\beta = 0$:

$$\Delta s \equiv s_\beta - s_0 = \frac{\beta}{1+M_{||}^2}$$

So the source variation with or without drift flow is bounded by the value β. Considering standard Mach probe measurements in characteristics mode, the steady-state radial electric field can be estimated from the floating potential and the electron temperature 2.10, to give an estimate of the β parameter. It turns out that for a variety of ohmic discharges, the drift flow parameter β is centered around 7% and does not exceed 15% (see figure 3.7), and for that reason *the drift flow term is neglected in the flow balance equation.*

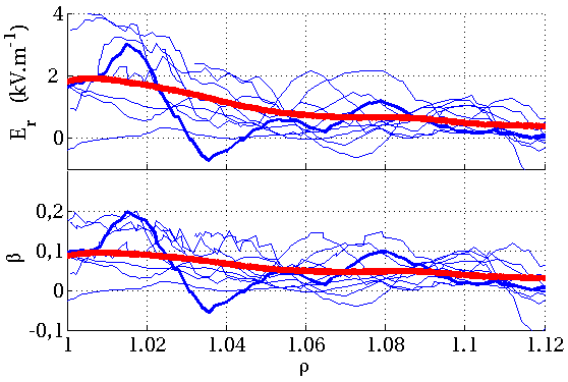

Figure 3.7: *Top : radial profile (normalized minor radius) of radial electric field measured with the reciprocating Langmuir probe during a variety of plasma conditions. Bottom : radial profile of the β parameter. Red curves show the average over the different reciprocations.*

3.1.5 Quantification of the radial flux

3.1.5.1 Diffusion coefficient

The previous discussions allow to consider the radial flux as the dominant driver of parallel flows, leading to a desired simplification of the flow balance equation. Paying attention to the previous ordering of the diffusion coefficient, a more quantitative approach for interpreting the radial decay length of the density profile is done by manipulating the SOL equilibrium system, in which the radial flux is described as diffusive. For simplicity and without affecting the generality of the approach, let us consider a diffusion coefficient radially constant, but depending on the parallel coordinate to take care of the possible radial flux asymmetry:

$$\nabla_{||}\left(nc_S M_{||}\right) = D_r \nabla_r^2 n \tag{3.7}$$

$$\nabla_{||}\left(n\left[1+M_{||}^2\right]\right) = 0 \tag{3.8}$$

The first equation can be integrated along the full field line to get rid of the parallel gradient, then replaced by parallel flow boundary values. The right hand side term is rewritten by defining a sort of line averaged transport coefficient defined as follow:

$$\langle D_r \rangle = \frac{1}{n_0 L_{||}} \int_{-L_{||}/2}^{-L_{||}/2} D_r n dl_{||}$$

Where the density n_0 is defined at the stagnation flow position : $M_{||}^0 = 0$. The flow boundary values is expressed function of the density at the stagnation position through the pressure conservation, leading to the following differential equation for the density profile:

$$n_0 c_S = \langle D_r \rangle L_{||} \nabla_r^2 n_0 \tag{3.9}$$

The simplest solution is exponentially decaying with a scale length given by : $\lambda_r = \sqrt{\frac{L_{||}\langle D_r \rangle}{c_S}}$. Experimentally, the density at the stagnation point is easily treated as $n_0 = n_{\text{probe}}\left[1+M_{\text{probe}}^2\right]$ and shows a similar decay length than the density profile at the probe position : $\lambda_r^0 = 5cm$ for the treated case 3.4. The line averaged transport coefficient is thus evaluated $\langle D_r \rangle = 2.1 m^2 s^{-1}$

, close to the previous ordering.
An important remark underlined by this manipulation of the flow equilibrium equation is that *the radial density profile in the SOL is a consequence of the line average of the radial transport efficiency and does not give any information about the related asymmetries.*

The *turbulent* feature of the radial transport in the SOL is highlighted by comparing the

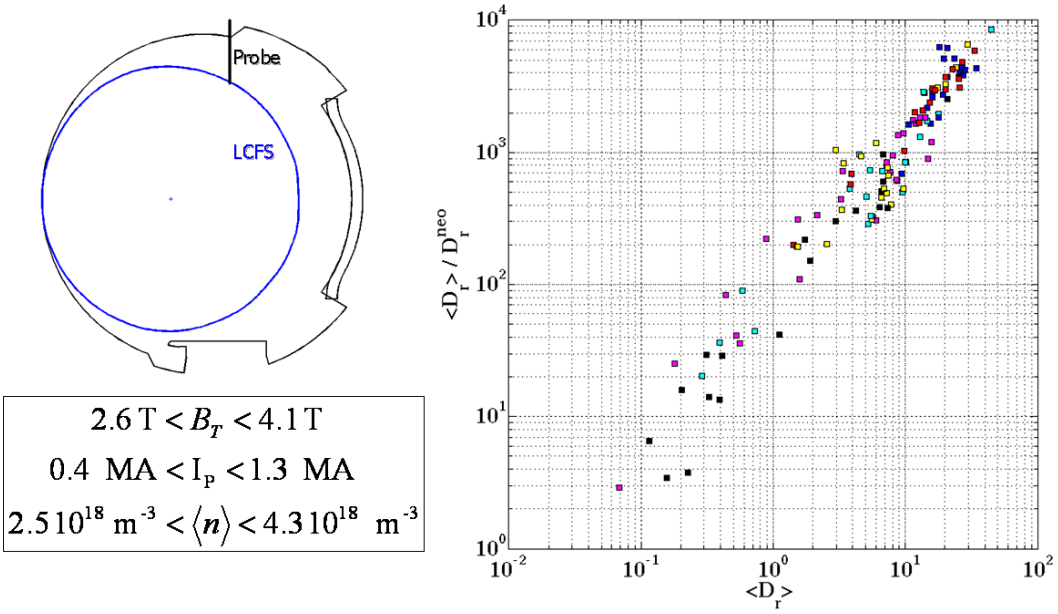

***Figure 3.8**: Left : Plasma equilibrium cross section for the set of selected discharges. The plasma parameters are illustrated on the bottom part, and form an almost independent set of variables. Right : The ratio of experimental diffusion over the neoclassical value is plotted function of the experimental diffusion. The effective experimental transport largely exceeds the neoclassical component.*

experimental diffusion coefficient to the neoclassical prediction for a broad set of experimental conditions. Let us consider a set of Ohmically heated plasmas in contact with the inboard midplane 3.8. In such plasma geometry, the SOL plasma is found to be similar to a standard configuration 3.1 but we are sure in that case to be free of limiter connections on the outboard midplane that could lead to misunderstanding for SOL profiles analysis. The transport coefficients are evaluated at the LCFS position from Langmuir probes measurements : T_e^{LCFS} & n_e^{LCFS} are used to estimate the neoclassical diffusion [Fundamenski 07] - almost always Pfirsch-Schlüter in the SOL, and density profiles are fitted to read the experimental transport coefficients. It turns out that for most of the plasma conditions, the transport is highly exceeding the neoclassical prediction, as shown on the figure 3.8. Beyond any current predictions, this strong transport is at least beneficial since a neoclassic SOL width would have been of a few millimeters and for a given heat loss from the confined plasma, the conducted heat load on limiter plates would have been enormous compared to the already high values measured in Tokamaks - in a ratio $\sqrt{\frac{D_r^{exp}}{D_r^{neo}}}$. On the other hand the high values of the transport coefficient infer high particle losses across the LCFS that is not beneficial for confinement efficiency. That point is discussed latter, after presenting the quantification of the radial particle flux along the

SOL radius and especially at the LCFS.

3.1.5.2 Line integrated radial flux

We have previously evaluated an experimental diffusion coefficient describing as an line averaged value the transport efficiency in the SOL. But in order to perform more quantitative analysis of transport at the edge, we would like to evaluate the radial flux as a very plasma parameter without any assumptions on its diffusive or convective nature and taking into account the probable geometrical asymmetries. In fact the SOL equilibrium model together with the probe profiles offer such an interesting tool: According to considerations and related simplifications we did, *the parallel flows are a direct consequence of the radial flux crossing the field lines*. On other words, the radial flux is totally transfered to parallel sink at the limiter plates, and thus evaluating the total parallel sink at the limiter plates is a way to read the total radial flux feeling this region 3.9

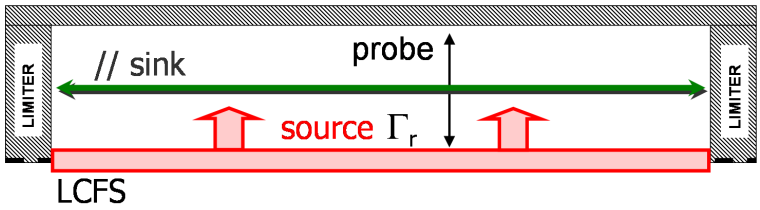

Figure 3.9: *Picture of the flow balance $(||, r)$ in the SOL. The radial flux is read as parallel sink at the limiters surface.*

In fact, the line integrated radial flux can be derived between two positions where the parallel flow is known, namely the probe position and indirectly the limiter plates. For more generality, let us write the SOL equilibrium system for a Mach probe set of variables $(nc_S, M_{||})$ such that the model and its application do not suffer the uncertainty about temperatures measurements:

$$\nabla_{||}\left(nc_S M_{||}\right) = -\nabla_r \Gamma_r \tag{3.10}$$

$$\nabla_{||}\left(nc_S\left[1+M_{||}^2\right]\right) = 0 \tag{3.11}$$

Now let us consider two positions (a, b) along a field line where the parallel flow is known and let us integrate the equation 3.10 between the two boundaries:

$$\left[nc_S M_{||}\right]_a^b = -\int_a^b \nabla_r \Gamma_r dl_{||}$$

The local radial flux is turned to a line integrated variable $S_r^{a,b}$ defined as : $S_r^{a,b} \equiv \int_a^b \Gamma_r dl_{||}$ and the matter is to derive an equation on that new variable, considering that the field line length depends on the radius - thus the line integration and the ∇_r operator does not commute. A convenient way to solve this problem is by a pragmatic approach : In usual magnetic configurations, the poloidal angle of boundary positions does not vary too much along the radius - $\approx 5\%$ - compared to the connection length $\approx 30\%$. Thus the equation on S_r is easily written by introducing an intrinsic poloidal angle θ^* and a safety factor $q(r)$ depending on the radial

position whose definitions are set through the relation $dl_{||} = R_{pl}q(r)d\theta^*$ - In the framework of a circular equilibrium approximation 2.14, the safety factor is simply $q(r) = q_a\rho^2$ and the intrinsic poloidal angle $d\theta^* = (1 - \epsilon\rho(1+\Lambda)\cos\theta)\,d\theta$. Assuming that the intrinsic poloidal coordinate of boundary positions does not vary with radius, the following equation is obtained for the *radial source* variable :

$$\nabla_r \frac{S_r^{a,b}}{q(r)} = -\frac{1}{q(r)}\left[nc_S M_{||}\right]_a^b$$

Considering now that the radial particle flux is negligible far from the LCFS - $S_r(\infty) = 0$, the latter equation is easily integrated along the radius from the vessel wall to a given radial position in the SOL :

$$S_r^{a,b}(r) = q(r)\int_r^\infty \frac{1}{q(r)}\left[nc_S M_{||}\right]_a^b dr \tag{3.12}$$

Over the geometrical corrections involving $q(r)$, the latter expression is straightforward : given a box in the $(||, r)$ coordinates, the radial flux entering the box is equal to the parallel flux flowing out of the box, which is a direct interpretation of the flow balance equation. The boundary parallel flow values are then deduced from values measured at the probe position, directly if the probe is considered as a boundary or via the pressure conservation 3.11 if a limiter is considered. Finally, the radial source estimation is possible in 2 distinct regions : In the Low Field Side, namely from the limiter to the probe via the outboard midplane, and in the High Field Side from the probe to the limiter via the inboard midplane:

$$S_r^{LFS}(r) = q(r)\int_r^\infty \frac{1}{q(r)}\frac{1}{2}nc_S^{probe}\left(1 + M_{||}^{probe}\right)^2 dr \tag{3.13}$$

$$S_r^{HFS}(r) = q(r)\int_r^\infty \frac{1}{q(r)}\frac{1}{2}nc_S^{probe}\left(1 - M_{||}^{probe}\right)^2 dr \tag{3.14}$$

$$S_r^{TOT}(r) = S_r^{LFS} + S_r^{HFS} \tag{3.15}$$

An application of that model is illustrated on the figure 3.10 corresponding to the plunge already discussed 3.4. To that point, two important remarks have to be done. First, the radial source evaluation can be performed from the wall to the LCFS if the probe plunge is deep enough, and thus gives an evaluation of the total radial flux of particles crossing the LCFS from the confined region. Dealing with confinement property of a discharge, important information can be obtained from that estimation. Secondly the model allow to discriminate the radial flux fraction traveling on the LFS from the fraction on the HFS side and thus returns a more quantitative information about the radial flux asymmetry.

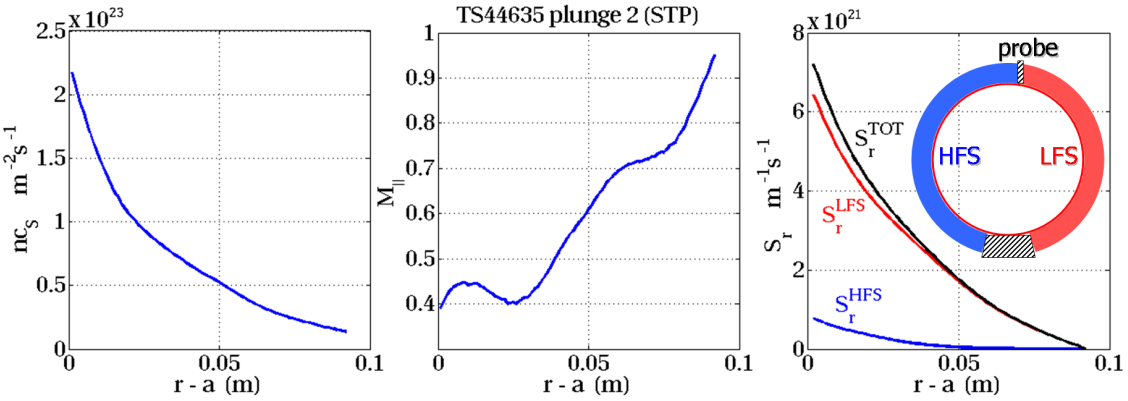

Figure 3.10: *Left : saturation current nc_S function of the distance to the LCFS. Middle : Parallel Mach number. These data are collected with a tunnel probe set in a Mach configuration. Right: Radial source calculated on the two parts of the SOL : LFS and HFS. The total radial source is plotted in black.*

As illustrated on the figure 3.10, the radial source on the HFS is almost negligible compared to the source on the LFS, even if the field lines fractions are in the same proportion. Similar to what was found directly from the Mach number amplitude read as a source coordinate 3.1.3, the source of particles close to the LCFS is for 90% in the LFS section (between the probe and the limiter). But as an improvement, the radial flux distribution was previously done by looking at its radial derivative - as a parallel source of particle - whereas the new calculation directly involves the radial flux amplitude. The result does not vary with plasma parameters, and it is always found that a very high fraction ($\approx 85\%$) of the radial flux is localized on the low field side of the torus, whereas a poloidally uniform radial flux along the poloidal section would have given a flux fraction of 35% (the probe is not exactly at the plasma top and the field line helicity is stronger in the low field side such that the field line length in the low field side is shorter than in the high field side).

3.1.5.3 geometrical considerations about limiters

Further analysis on the steady-state radial flux and its spatial properties are performed in the last chapter. Taking care of the experimental approach, an important remark has to be done about the radial source calculation as presented above. By looking at the principle followed to extract the radial source value - line integrated radial flux, the basement is a radial integration of the parallel losses estimated at the parallel boundaries of the region of interest. Thus it has been assumed that the whole set of radially traveling particles in that region are lost along the field line crossed by the probe, that is not the case if a second limiter is present in the SOL 3.11. Let us consider a discrete limiter - with a small toroidal extent - inserted from the wall to a given radial position in the SOL - labeled by $r_0 - a$ from the LCFS - and let us assume that this limiter is magnetically connected to the reciprocation path of the probe. Thus the limiter defines a private region behind its extremity that is not diagnosed by the probe. When the probe is behind the limiter extremity - $r_{probe} - a > r_0 - a$ - the measured radial source corresponds to the radial transport in that region between one plate of the main limiter

and the second limiter. So when the probe reaches the second limiter extremity the radial source value corresponds to what is feeling that region, and the integral cannot be performed closer to the LCFS since the flux filling the private region is unknown and corresponds to a missing part of the integral. Thus a special care about the magnetic connections has to be taken when calculating the radial source from a given plunge. On Tore Supra these second limiters corresponds to antenna protections located on the outboard midplane. For experiments dedicated to SOL transport, a special care was taken to step back these limiters as far as possible from the LCFS to reduce the influence of unknown flux fractions. On the other hand, the principle of tailoring the flux distribution with a second limiter will serve as the leading experimental tools for mapping the radial flux asymmetry, as presented in the next chapter.

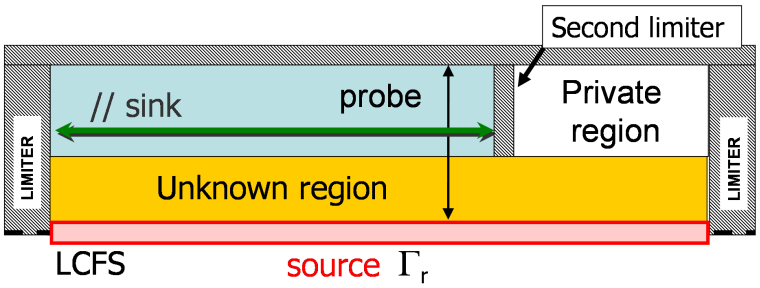

Figure 3.11: *Picture of the SOL in between the two main limiter plates, in presence of a second discrete limiter inserted from the wall. A private region appears in the shadow of the second limiter with respect to the probe, filled by a radial flux that is not measured. Thus, the radial flux between the LCFS and that second limiter is unknown due to that missing fraction.*

3.1.6 Particle losses across the LCFS

Taking care of the limiter configuration, the radial particle flux crossing the last closed flux surface can be estimated as the total parallel losses integrated along the SOL radial profile. This time averaged quantity is of great interest when dealing with confinement phenomena, such like the operational density limit faced in every tokamak, since it is strongly believed that edge transport is one of the major player on that universal phenomenon [Greenwald 01]: When increasing the plasma density of ohmically heated plasmas, the radiated fraction from the confined plasma is observed to increase non-linearly and the discharge reaches rapidly a radiative collapse. Since a major contribution of the radiation losses is due to recycling of deconfined particles and impurity contamination from the limiter surfaces, a special interest is found in understanding the edge particle and energy transport evolution across the LCFS when density is increased. An other point of interest concerns the fast visible imaging presented in the next chapter and its crucial limitation that turbulence can only be pictured at high density.

3.1.6.1 Evolution with core density

First of all, the density dependence of the radial flux amplitude at the LCFS can be investigated. A set of ohmically heated plasma discharges are selected, corresponding to small

plasmas limited on the high field side 3.12 to avoid any second limiter shadowing on the outboard midplane. A set of standard ohmically heated discharges has been selected as well, for which secondary limiters are fully retracted. That is, Mach probe reciprocations are performed on a wide range of independent plasma parameters : plasma current $0.4 < I_p < 1.4$ MA, toroidal magnetic field $B_T \in [2.6, 4.1]$ T, line averaged density $5.510^{18} < lad < 6.510^{19}$ m^{-2}. The radial flux variable at the LCFS is defined as the line averaged radial flux, that is simply:

$$\langle \Gamma_r(0) \rangle_{||} = \frac{1}{L_{||}(0)} \int_{-L/2}^{L/2} \Gamma_r(0) dl_{||}$$

Where the field line integral corresponds to the radial source variable previously described.

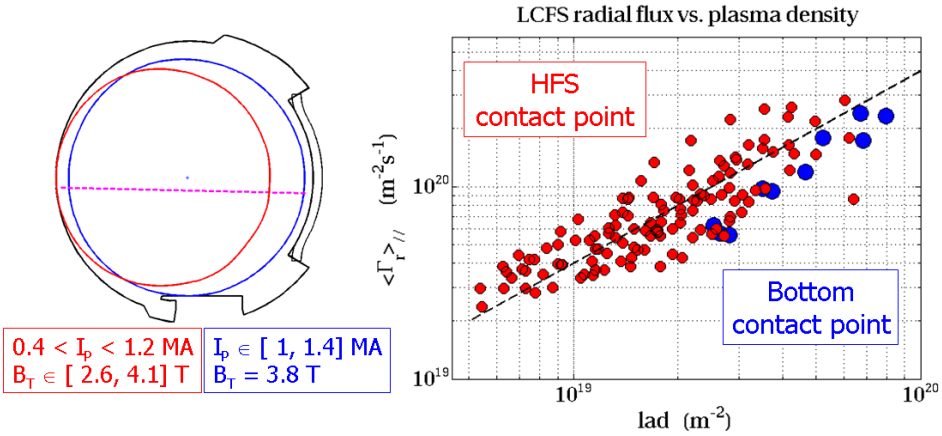

Figure 3.12: *Left : magnetic configuration of the discharges of interest, limited either on the low field side (red) or bottom (blue). Secondary limiters are fully retracted. The interferometer laser line used to estimate the line averaged density is shown in magenta. The range of plasma current and toroidal magnetic field are indicated in red and blue for each configuration. Right : Dependence of the line averaged radial flux crossing the LCFS function of the central line averaged density, in red for the high field side contact point, in blue for the standard configuration. The black dashed line illustrates the linearity*

As a matter of facts, the radial flux is observed to vary almost linearly with the core density, as illustrated on the figure 3.12. Although a relatively large scatter is found the tendency is relatively clear on one density decade. Similarly, the density profile is not observed to flatten when core density is increased **??**. These results are in apparent contradiction with findings in other machines like Alcator C-mod [LaBombard 01] [LaBombard 08] where the radial flux is observed to increase strongly non linearly with line integrated density. That is, the radial flux evaluation in the SOL of Alcator C-mod is performed differently since SOL plasmas are mostly in a high recycling regime -called "main-chamber recycling", such that the radial particle flux is estimated from the ionization source profile [LaBombard 00].

3.1.6.2 Energy losses and density limit

.

As presented above the radial particle flux crossing the LCFS of Tore Supra does not present any particular tendency that could be related to density limit as observed in C-mod. But more

details on the energy deconfining mechanisms can be addressed in the scope of radial particle transport .

In steady-state scenarios, the input power (equal the ohmic power in ohmically heated discharge) is lost across the LCFS by two mechanisms : radiations from the confined region that are measurable with arrays of bolometers, and kinetic losses that are not directly known. The radiations are known to be relatively low in the SOL of Tore Supra, such that kinetic losses across the LCFS are entirely deposited on the limiters. It has be proven that, by considering the radiation losses and the energy absorbed by the limiters - transfered to the active cooling system - we were able to close the global power balance (within 10 % of error) during a Tore Supra discharge [Carpentier 09]. Thus, the global power balance can be safely used to estimate the kinetic losses across the LCFS if the input power and radiations are known :

$$P_{SOL} = P_{IN} - P_{RAD}$$

The power lost kinetically in the SOL (P_{SOL}) is again the sum of different contributions. We only retain the two dominant terms that are the convected energy by the particle flux and the conducted energy transported by the temperature gradient. Other contributions like fast ion losses or ripple losses are simply neglected in ohmically heated plasmas, such that the power lost across the last closed flux surface is defined by the energy flux summed over each plasma species :

$$P_{SOL} \approx S_{LCFS} \sum_s \left[\langle \Gamma_r^s \rangle_{||} E_s - n_s \chi_s \nabla_r T_s \right]$$

Where S_{LCFS} is the LCFS area, $\langle \Gamma_r^s \rangle_{||}$, $E_s = \frac{3}{2} T_s$, n_s, χ_s and T_s are respectively the line averaged radial particle flux, the energy carried by one particle, the density, the temperature diffusivity and the temperature of the specie s at the LCFS. The convection term is calculable quantity since the radial particle flux is known, and we can use the rough estimate $T_i = 2T_e$ for the ion temperature. The conduction term is a fair unknown due to the crucial lack of informations about the conduction phenomena. Indeed, the classical description corresponds to collisions transfers, that exchange momentums without mass, but the dominant effect corresponds to adiabatic electrons turbulence, that transports energy without mass via electrostatic drift effects. Therefore the conduction term appears as a result of the power balance and not as an element of validation.
In order to quantify the influence of the particle transport on the energy losses, we focus on the fraction of the convected energy with respect to the total power lost in the SOL : $f_{CONV} = \frac{P_{CONV}}{P_{SOL}}$. Results are summarized on figure 3.13 for Deuterium and Helium discharges. As a first observation, the fraction of convected energy across the LCFS is of the order of 50% showing that the particle flux participates actively to the energy power losses with respect to conduction phenomena.
Coming back to the density limit subject, the convected power fraction seems to depend on the density via the Greenwald density fraction :

$$f_{GW} = \frac{< n_e >_{20} \pi a^2}{I_p}$$

This parameter turns out to be a pragmatic parameter defining the operating density domain for all tokamaks $f_{GW} < 1$. As a matter of facts, the convected fraction is observed to increase with the Greenwald fraction 3.13. The result was first highlighted for the Helium discharges, for which the tendency is clear. The Deuterium case shows more scatter, but the statistic is higher and the tendency shows an increase of the convected fraction with the Greenwald parameter. On the other hand, the range of Greenwald fractions accessible in Deuterium discharges is narrower than in the Helium case, since radiative collapse appears for lower Deuterium densities.

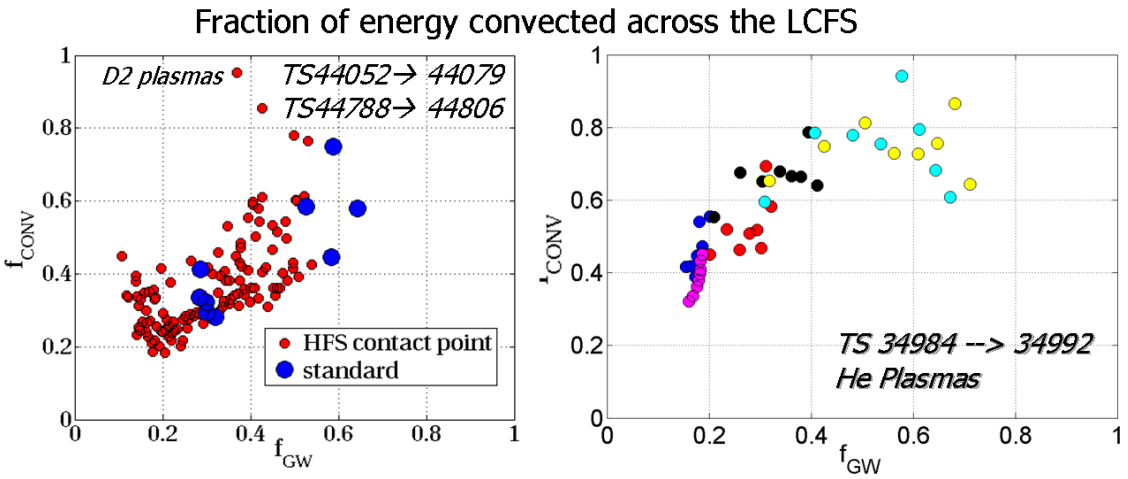

Figure 3.13: *Evolution of the fraction of convected energy with respect to SOL losses versus the Greenwald density fraction. Left : for the deuterium discharges presented above 3.12. Right : for Helium discharges.*

To conclude, we showed that the particle flux is directly involved in the energy losses across the LCFS and could count for a dominant mechanism when high density is reached. To that point, the results are too ambiguous to draw any conclusion on the task of particle transport in the density limit encountered in Tore Supra. But fluctuations induced transport presented in the following are rather consistent with an increase of the turbulent transport across the LCFS. Similarly, the use of the fast visible imaging diagnostic shows clearly that at high density the edge transport (across the LCFS) involves plasma filaments, when they are believed to exist only in the SOL.

3.1.7 summary

As a summary, the parallel flow measurements with a reciprocating Mach probe are of major interest for studying the radial transport in the SOL. Due to the low recycling regime of the Tore supra Scrape-off Layer and the negligible effects of transversal flows, the main parallel flow driver is found to be the radial particle flux. First by looking at the radial width of the density profiles, clear information about the *non classical* feature of the transport at the edge is highlighted, either in the far SOL or at the LCFS. This points out the turbulent nature of the transport deconfining the particle and energy from the confined region and spreading the

heat load on plasma facing components. On the other hand, a clear poloidal asymmetry of the radial flux is highlighted by the parallel flow strength at the top. The issue raised by that first proof of asymmetry is really challenging: First of all, it offers a simple explanation for the near-sonic parallel flows measured in the SOL understood as return flow to balance the parallel pressure, and then no current simulations are able to predict such transport phenomenon. Dedicated SOL flow experiments performed on Alcator C-mod [LaBombard 04] have yield the same conclusion that the transport is enhanced on the outboard midplane. Furthermore, multiple machine experiments have yield the conclusion that, at the outboard midplane the turbulent transport in SOL plasma is related to interchange instability [Garcia 07a] [Smick 10]. The growth rate is known to be instable at the outboard midplane and even stabilizing at the inboard midplane, inferring a possible asymmetry. That is, a consistent picture of the edge equilibrium has not yet been drawn in the scope of both edge plasma flow equilibrium and local turbulent measurements, that we attempt to present in the last chapter. The next part is devoted to electrostatic fluctuations at the top of Tore Supra SOL, with a focus on the turbulent radial flux properties.

3.2 Electrostatic fluctuations

The inability of neoclassical approaches to predict the radial transport level at the edge is a clear proof of a missing ingredient: the electrostatic drift effects. Indeed, it is now well admitted that fluctuations of electric field in the SOL is able to transport an important amount of particles [Zweben 07] [Boedo 03] [Garcia 07a]. As introduced in the previous chapter 2.39, a fluctuating poloidal electric field gives rise to a fluctuating radial velocity leading to a time fluctuating radial particle flux:

$$\tilde{\Gamma}_r = \tilde{n}\tilde{v}_r \approx \frac{1}{B}\tilde{n}\tilde{E}_\theta$$

The effectiveness of such phenomenon on the global particle transport is highlighted by its time averaged value, in other words by the non linear coupling of density and electric field fluctuations. In the framework of spectral descriptions, the radial flux at a given mode number k directly depends on the phasing between density and electric field : $\Gamma_r^k \propto \cos\delta\phi(n^k, E_\theta^k)$. For instance, the assumption of adiabatic electrons $\frac{\tilde{n_e}}{\tilde{n_e}} = \tilde{\Phi}$ leads to the direct result that density and electric field are in quadrature : $n^k \propto iE^k$ such that density is not effectively transported radially. On the other hand experiments performed on almost every tokamaks indicate an opposite behavior in the SOL : density and transversal electric field are more or less in phase, leading to a net outward transport of density.

Langmuir probes are probably the only diagnostics able to measure both density and electrostatic potential fluctuations in tokamak plasmas, with a sufficient time and spatial precision to resolve the local turbulence. Nevertheless, the probe design is of crucial importance with respect to either turbulent scales or the intrusive nature of the diagnostic, and is sometimes responsible for misinterpretation of collected fluctuations [LaBombard 02]. For instance the poloidal electric field is deduced from a spatial difference of electrostatic potential and the separation length between collectors has to be small enough to resolve the typical scale length

of the electrostatic eddies. Measurements collected in almost all magnetically confined plasmas suggest that the turbulence at the edge has some universal behaviors : the frequencies are in the range of 1kHz to 100kHz, the phase velocities of fluctuations are in the range of 1% to 10% of the ion sound speed, and the transversal scale length involved in the turbulence is of the order of some millimeters to centimeters [Zweben 07] [Carreras 05] [Naulin 07]. The first important remark is that in such frequency range, the probes are hardly driven in a characteristic acquisition mode. The main reason is that in a tokamak environnement, a probe diagnostic is composed of tens of meters of conducting cables, and driving a voltage sweep at a high frequency involves capacitive and inductive effects within the wires that are hardly treated. For that reason most of the probe diagnostics dedicated to fluctuations are driven in saturation or floating modes and measure neither directly the density nor the plasma potential fluctuations, but rather the saturation current and the floating potential 2.5.1.
First of all are presented the diagnostic and probes design dedicated to electrostatic fluctuations in the SOL of Tore Supra. Then some specific statistical properties of the fluctuating fields are discussed in the framework of turbulent transport. Finally we consider in detail the evaluation of the radial flux,its nature and its amplitude.

3.2.1 DTURB and the rake probes

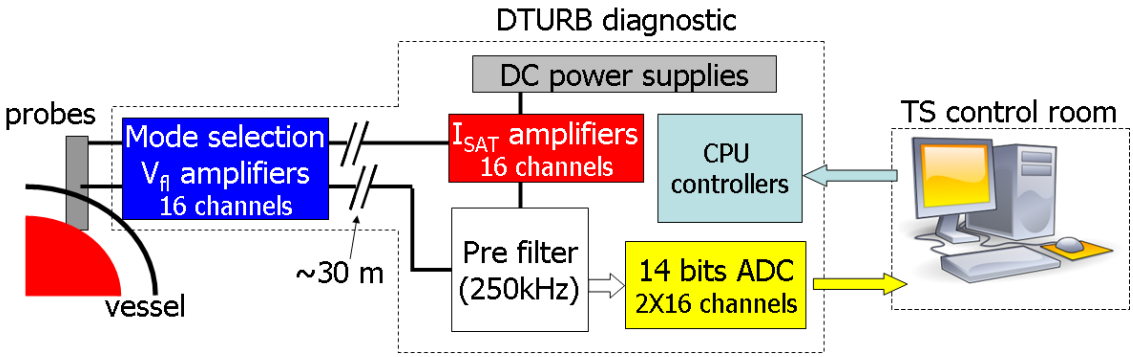

***Figure 3.14**: Schema of the DTURB diagnostic. The system setup is fully operable remotely.*

Let us briefly describe the acquisition system that we developed in the scope of the turbulence study. During the thesis, we were in charge of the final design and maintenance of the diagnostics, implying numerous days of coding and plugging the control system, optimizing the amplification stages and changing the electronic components suffering the Tokamak conditions. As an overview, the diagnostic is able to run a 1MHz temporal acquisition on 32 channels. The main advance is the presence of an anti-aliasing pre-filter and a 16 bits digitizer (ADC), compared to the previous system only composed of a 12 bits ADC. However due to strong specifications on electric groundings, the electronics contains some components and isolation stages that effectively reduce the digitizing over 14 bits. Coupled with ajustable gain amplifiers, the diagnostic is able to fully resolve the plasma fluctuations from the LCFS to the wall, where the plasma is rare and collected current very small. The current collection is in the range of $\pm 2A$ and the floating potential in the range of $\pm 250V$, making the diagnostic able to

collect measurements in a wide range of plasma conditions. The system has been designed to operate on 16 collectors simultaneously with control on the acquisition mode for each channel : saturation current or floating potential. DC power supplies of 800W are delivering the biasing voltage for saturation collection, each supply being connected to 4 collectors. In that version, the saturation biasing can be up to -200V, large enough to reach the effective saturation of the probe in Tore Supra SOL plasmas. Concerning the operational specificities, the internal memory is large enough to allow a continuous acquisition at 1MHz during a full reciprocation of the probe 3.15.

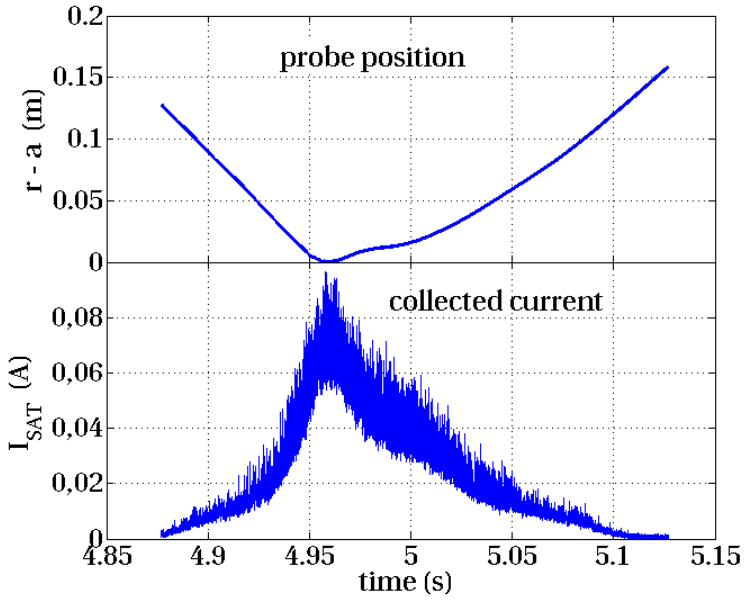

Figure 3.15: *Illustration of a saturation current collected during one probe reciprocation by the diagnostic DTURB*

The anti aliasing filter is an important update in the fast acquisition diagnostic. As an important remark, fluctuations collected with the previous acquisition system were polluted with a high frequency component - up to 30% of the fluctuation spectra - originated either from electronics or aliasing effect. By cutting the high frequency part at 250 kHz the new data do not suffering from such pollution.
Now that the acquisition system has been rapidly presented, let us focus on the crucial part of the diagnostic : the probe heads dedicated to turbulence.

3.2.1.1 The poloidal rake probe

A dedicated probe head for turbulence measurements has been designed in Tore Supra and build in Canada : the poloidal rake probe. For two years we have intensively used it in order to collect a large amount of data concerning electrostatic fluctuations in the SOL of Tore Supra. The important part of the design is a poloidal array of 6 small collectors, aligned with the standard flux surfaces and separated by 3 mm. Each collector is a 1.27 mm in diameter stainless steel pine, providing a good electric conduction and low erosion rate. On the other

hand the probe has to be manipulated with care in the plasma due to the possible melting of the steel, as we experienced. Two other collectors of the same size are mounted on the probe sides in a Mach configuration, 3 mm behind the poloidal rake 3.16.

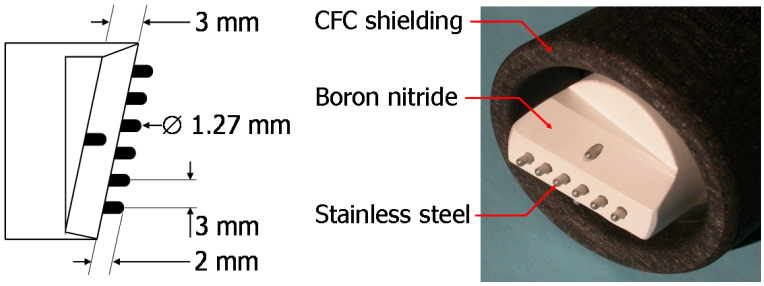

Figure 3.16: *Poloidal rake probe used in Tore Supra. On the the right picture the probe is mounted with its CFC shield, designed to protect the probe body except the extremity part where the collectors are lying.*

The probe configuration allows multiple points analysis of the turbulence, including:

- The evaluation of the poloidal electric field from potential measurements, and thus the local fluctuating radial flux.
- The evaluation of the poloidal sizes of eddies or structures present in the fluctuations of density and potential fields.
- The evaluation of the phase velocity of fluctuations flowing across the rake.

The probe design offers a crucial advantage that the pins composing the rake are directly inserted into the undisturbed plasma and are not or at least less influenced by the probe body. A coherent understanding of how the fluctuations or even the transport are disturbed by the probe has been hardly achieved [LaBombard 02] and the poloidal rake probe offers the ideal geometry in that context.

3.2.1.2 The radial rake probe

An other probe has been design to assess the radial properties of the turbulence in the SOL : the radial rake probe. Two radial arrays of small collectors are placed on both side of the probe, in a Mach configuration. Each collector is a 1.2mm in diameter stainless steel pine, separated from each other by 3 mm. In that configuration, the measurements are potentially suffering the plasma probe interaction, but the Mach setup is worth evaluating such effects by paying intention on the differences observed between both sides of the probe.

The probe was built by the Belgian university of Gent after some delay due to uncertainties about the final design and was used only at the very end of the 2010 spring experimental campaign on Tore Supra. For that reason the amount of collected data is quite low and the main fluctuation studies were performed on the data collected by the poloidal rake probe.

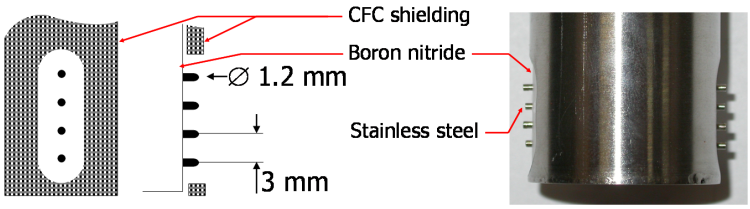

Figure 3.17: *Radial rake probe used in Tore Supra. The CFC shield in not shown on the right picture. As illustrated on the left schema, the shield is drilled with two elongated holes to let the plasma interact with the collectors arrays.*

3.2.2 Discussion on collected data with the poloidal rake probe

Referring to the issue of small collectors and effective collection area previously discussed 3.1.2, the calibration of the saturation currents in term of volume quantities as well as the floating potential interpretation is not straightforward for the poloidal rake probe. In that context and before starting any discussions on fluctuations, the consistency of collected data is worth to be verified with respect to reliable measurements performed with the tunnel probe.
In the first part of this chapter, we already showed that the collectors composing the rake probe suffer from a large uncertainty of their effective collection area 3.1.2. Now, we pay attention to the saturation current and floating potential in the scope of fluctuations interpretation.

3.2.2.1 Saturation current and density fluctuations

The fluctuations of the density field are often mixed up with saturation current fluctuations, as a consequence of the linearity linking both quantities, and this is the natural interpretation we would give to data collected by the poloidal rake collectors. However, two points have to be discussed: First of all, the expression of saturation current obtain from the Hutchinson model 2.5.1.3 applied to a cylindrical collector as been deduced from a steady-state model. Secondly, the saturation current involves other possibly fluctuating parameters like the plasma temperature or the effective collection area of the collector :

$$I_{SAT} = A_{coll}^{eff} e n_e \sqrt{\frac{T_i + Z T_e}{m_i}}$$

The steady-state approximation of the Hutchinson model has been followed to describe the equilibrium of the collector presheath with the surrounding plasma and the simplest criterion to validate the steady-state approximation is to consider a measurement time scale larger than the time needed by the plasma to flow along the probe presheath. Considering the previous estimation of the probe presheath length 2.5.1.1 applied to the small rake collectors and the typical plasma flow velocity c_S, the presheath equilibrium time scale is found to be less than $1\mu s$ for the small collectors composing the poloidal rake probe. Thus the latter expression of the saturation current collected by a small collector remains true for fluctuations in the range of $f_{fluc} < 1$MHz.
Coming to the second point, the temperature fluctuations are hardly measurable with a standard diagnostic and the fluctuations of the collection area is *a priori* unknown. The first step

proposed to clarify this ambiguity is the following: to find a time averaged parametric expression of the effective collection area of the rake collectors, and then assume the parametric dependence true for fluctuations. The previous data set collected by the tunnel and the rake probes can be manipulated to find the steady-state dependence of the effective collection area with plasma parameters. It turns out that the effective collection area is a decaying function of the local plasma temperature 3.18 extrapolated with a power law dependence: $\frac{A^{eff}}{A^{geo}} \propto T_e^{-0.53}$. Surprisingly, the latter dependence cancels the temperature parameter in the expression of the saturation current and thus infer that the saturation current amplitude is linearly driven by the plasma density 3.18. Extrapolating the steady-state behavior to the fluctuations suggests that saturation current fluctuations are directly reflecting the density fluctuations.

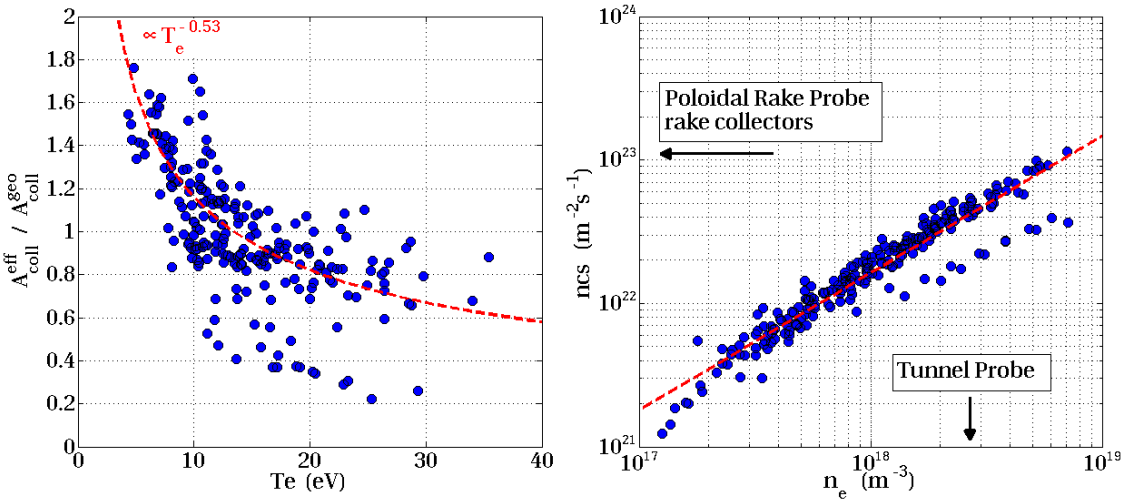

Figure 3.18: *Left : Effective collection area of rake collectors normalized by the geometrical value function of the local electron temperature. The dashed line illustrates a power law trend with T_e. Right : Saturation current collected on the rake - and defined with the geometrical collection area - compared to the local density measured with the tunnel probe. The dashed line illustrates a linear trend.*

3.2.2.2 The floating potential

The floating potential is the only measurable quantity giving information on the plasma potential. However a fair understanding of the measured quantity has been hardly achieved: When considering a probe run in a characteristic mode, the floating potential is defined as a time averaged parameter resulting from an extrapolation of the collected current function of the applied voltage:

$$I(V) = I_{SAT}\left(1 - \exp\frac{V_{float} - V}{T_e}\right)$$

Due to the strong non-linearity of the latter expression and the natural coupling in between fluctuating plasma parameters $\left(\tilde{n}_e, \tilde{T}_e, \tilde{V}_{plasma}\right)$, the resulting effective value of the floating potential deduced from the extrapolation is subject to some ambiguities. On the other hand, when the probe is run in the floating mode, the collected current is forced to zero and the collector potential is in theory equal to the floating potential. However, due to the varying

effective collection area of the small collectors composing the rake probe, ions and electrons might not be collected within the same area leading to a probable overestimation of the floating potential. When comparing the time averaged value of the floating potentials measured by the tunnel and the rake probes, coherency is hardly found. The floating potentials measured on both sides of the tunnel probe are completely different, and only the potential measured on the ion (B) side shows some coherent trend with the rake probe measurements 3.19. The inconsis-

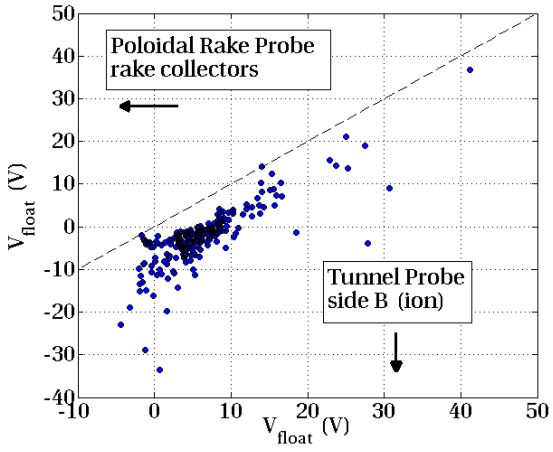

Figure 3.19: *Comparison of the floating potentials measured either by the poloidal rake collectors or on the ion (B) side of the tunnel probe.*

tency between measurements performed with the different probes reveals a crucial aspect for the interpretation of the floating potential : the measurements depend strongly on the probe geometry, and current models are not yet able to explain or predict the observed discrepancies. In that framework, no validation can be effectively done and the only assumption followed is that the poloidal rake collectors geometry insures the minimum of disturbance with respect to the floating potential measurements.

An other essential aspect of the measurement is the inclusion of a temperature dependent term in the floating potential expression : $V_{float} \approx V_{plasma} - 3T_e$, leading to a clear uncertainty in the interpretation of floating potential fluctuations in term of plasma potential fluctuations - the right plasma parameter governing the electrostatic turbulence. Again, nothing robust can be done expect following some assumptions based on experimental observations. The temperature fluctuations are rarely measured, but the few observations done lead to the conclusion that the temperature field is fluctuating more or less in phase with the density field [Boedo 03] [Kumar 03], or with the electric field [Rudakov 02], depending on the plasma conditions. Following a pragmatic approach, either the temperature fluctuations are simply neglected as a floating potential contribution, or the assumption is done that the plasma temperature fluctuates in phase with the saturation current. But the exercise done, we conclude that the effect is not significant and does not change the further interpretations and conclusions about the drift turbulence. Anyhow, when the temperature fluctuations are measured it has been observed negligible effects on the radial turbulent flux calculation [Silva 04].

3.2.3 Nature of fluctuations and intermittence

Now that the DTURB diagnostic and the related measured quantities have been presented, the crucial subject of fluctuations can be addressed. The easiest way to start with is by paying attention to a time trace of density - saturation current - fluctuations collected in the SOL - see figure 3.20. Let us consider a poloidal rake probe reciprocation performed in a steady-state ohmically heated plasma. Due to the continuous probe motion in a density profile, any time trace extracted from the reciprocation is trended, making difficult any statistical treatment on the signal. For convenience, extracted time traces are detrended by subtracting a first or second order polynomial in a way that the mean value is conserved.
As a first evidence, the level of fluctuations is important, as illustrated by the scatter on the radial profile. In the region of interest (about 1 cm from the LCFS), the mean value of the saturation current is $\langle I_{SAT} \rangle = 40.10^{-3} A$ and its root mean square is $\sigma_{I_{SAT}} = 5.510^{-3} A$, defining the relative amplitude of fluctuations to be about $\frac{\sigma_I}{<I>} \approx 14\%$. Secondly, the fluctuations involve coherent events lasting a few tens of microseconds and responsible for the large and positive peaks observed on the time trace.

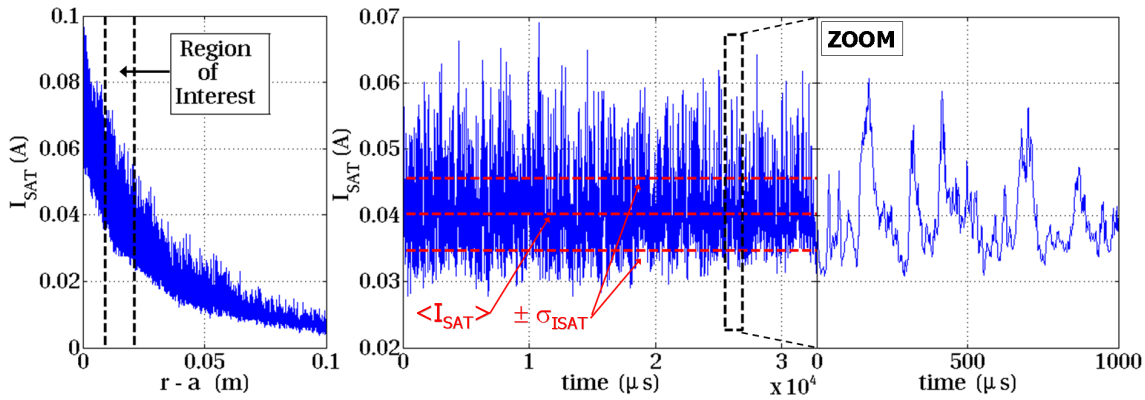

Figure 3.20: *TS44635 5s. Left : Radial profile of the saturation current collected by one collector of the poloidal rake. The region of interest where the time trace is extracted is shown. Middle : Detrended time trace within the region of interest. Are plotted in red dashed lines the mean value and the root-mean-square around the mean value. Positive and large events are noticeable. Right : Zoom on the time trace, illustrating the coherent nature of the fluctuations.*

Similarly, the floating potential exhibits large amplitude fluctuations 3.21. The main difference with the density time trace is the absence of large and positive peaks, although fluctuations are composed of coherent events.

Theses observations on fluctuations behavior are universally done in magnetically confined plasmas : SOL plasmas are characterized by fluctuations of large amplitude, composed of coherent events. In the case of density fluctuations, the notion of intermittency is often used to characterize these positive and large peaks. As it will be shown latter, these structures are found to propagate in the plasma and are participating to the transport of particle and heat. First of all, statistical properties of the fluctuations are presented and discussed. Then the fundamental notion of coherency and correlation are introduced to clarify the properties of

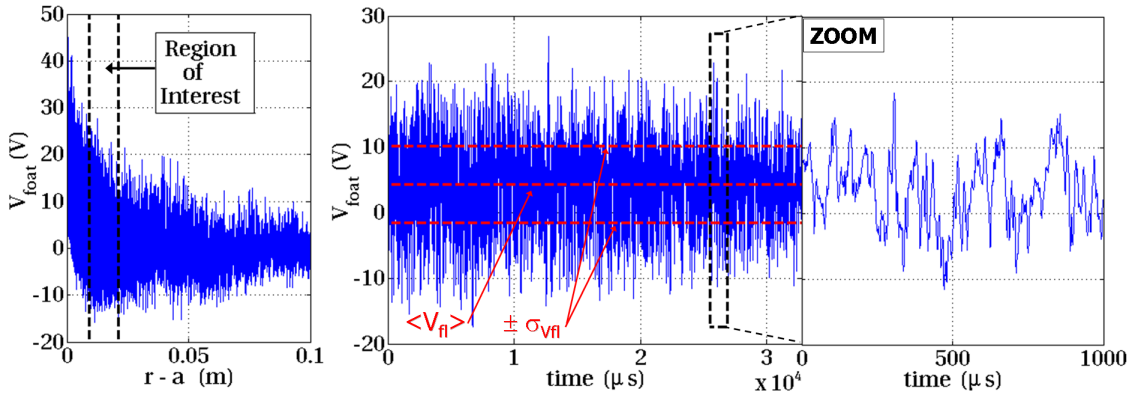

Figure 3.21: *TS44635 5s. Left : Radial profile of the floating potential measured by one collector of the poloidal rake. The region of interest where the time trace is extracted is shown. Middle : Detrended time trace. Are plotted in red dashed lines the mean value and the root-mean-square around the mean value. Right : Zoom on the time trace, illustrating the coherent nature of the fluctuations.*

theses structures of density and electrostatic potential.

3.2.3.1 Statistics of intermittency

The density fluctuation time trace illustrates an important property related to edge plasma : strong, positive and aperiodic peaks are involved, what is generally called *intermittence*. These intermittent events are largely exceeding the standard deviation around the time-averaged value and for that reason the simple statistical description of the fluctuations in term of mean value and standard deviation is not enough. Indeed, if we simply assume that these fluctuations somehow reflect the behavior of the transport of particle or heat, we expect the heat load on plasma facing components to be subject to a similar intermittency. And since these intermittent events may carry a lot of energy to the wall, instantaneously exceeding the time averaged value in a large amount, an important information is missing concerning the wall erosion if we simply describe the heat load in term of mean value and standard deviation.

The intermittency of a fluctuating signal is well qualified by paying attention on its probability distribution function (PDF), that reflects the probability of obtaining a given value in the signal. In order to compare PDFs evaluated on different signals, the common way is to first normalise the time trace by subtracting its mean value and divided by the standard deviation :

$$s \rightarrow \frac{s - < s >}{\sigma_s}$$

The PDF is then calculated on a mesh (x_i) such that $x_{i+1} - x_i = 2\delta_x$:

$$P(x_i) = \#\left\{s_i \ / \ x_i - \delta_x \leq s_i \leq x_i + \delta_x\right\}$$

A PDF is calculated for the two previous time traces of density and potential, on 2^{15} points - see figure 3.22. The density PDF shows a particular property : whereas the negative fluctuations (below the mean value) are Gaussian, the positive fluctuations form a long tail,

composed of strong events not compatible with a Gaussian type of fluctuations. Comparing the PDF with a Gaussian is meaningful, since a white noise or a regular fluctuation phenomenon such as driven by collisions exhibit a Gaussian PDF. Any departure from Gaussianity could be a proof that the system is driven by a more complex phenomenon than a simple diffusion or random walk, except that analyzing density fluctuations addresses an important issue: the density field is by nature positive and in a system of strong fluctuations like in the plasma edge a Gaussian type of fluctuation would immediately lead to rare but unphysical negative values. Thus the edge density is by nature subject to non Gaussian fluctuations.

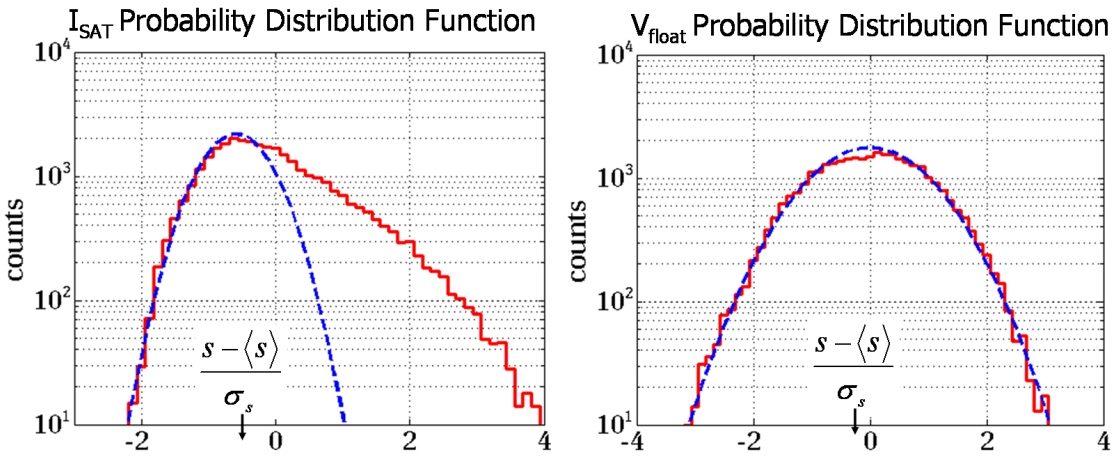

Figure 3.22: *TS44635 5s. Left : PDF of the density fluctuations shown in the previous part. A Gaussian extrapolation is performed on the negative part of the distribution (dashed blue line) . Right : PDF of the floating potential shown in the previous part. The distribution is close to a Gaussian (dashed blue line)*

The departure from a Gaussian is usually described with a statistical parameter called *skewness*, that quantifies the asymmetry of the PDF around it mean value. For instance, the density PDF shown in figure 3.22 is positively skewed due to the long tail toward positive values. The statistical definition of the skewness S of a signal $s = (s_i)$ of length N is :

$$S(s) = \frac{N}{(N-1)(N-2)} \sum_i \left(\frac{s_i - < s >}{\sigma_s} \right)^3$$

Where $< s >$ and σ_s are respectively the mean value and the root mean square (or standard deviation). The skewness of a Gaussian is 0 by definition, and more generally is 0 for any symmetric PDF around its mean value. The density PDF shown before has a skewness of about $S_n = 1$, that is relatively important. Due to the power of 3 contained in the sum, the skewness is sensitive to large and non Gaussian excursions of the signal amplitude, and is for that particular reason sensitive to the number of points composing the signal.
Referred to any statistical approach, the number of points is crucial to reach a good statistical description. In the case of a noise or incoherent fluctuations, the number of points in the time trace is the right parameter, but that is not necessarily true when fluctuations are composed of coherent events dominating the statistics by their large excursion toward positive (or negative) value. In fact the statistical approach aims at describing such events and not the time trace

taken as a general signal. Let us pay attention to the figure 3.23, illustrating the density fluctuations in the far SOL extracted from the previous profile 8 cm from the LCFS. The time trace is composed of 2^{13} points and we could think this number is large enough for a reliable statistical analysis, but when the data are visualized the statement is clear that the number of events is so low that one large event on the time trace can have a noticible pound in the statistic. Indeed, when that event is virtually removed from time trace, the skewness decreases from 1.8 to 1, showing that this latter parameter evaluated on the discussed time trace is not consistently quantifying the intermittency of the local plasma density.

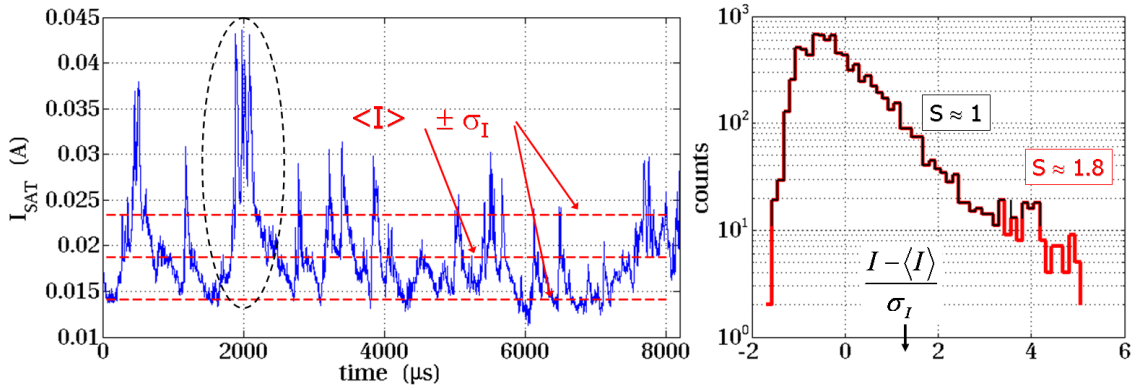

Figure 3.23: *TS44635 5s. Left : Time trace of the saturation current collected 8 cm from the LCFS. The fluctuations are composed of really large intermittent events. Right: PDF of the saturation current time trace. The skewness is about 1.8. When the largest event (encircled with a dashed curve on the left) is removed from the statistics (black PDF), the skewness decreases to about 1*

The latter observation is meaningful : density fluctuations behave differently close to the LCFS 3.20 or in the far SOL 3.23, where fluctuations are composed of rare but very strong and long positive events. The fact that the probe moves too fast in the far SOL compared to the typical event duration is the main reason why the statistical approach reaches its limits in that part of the profile. Anyhow, the statistical approach directly applied to the time traces does not reveal any aspect of the crucial property of the fluctuations, that they are composed of coherent events.

3.2.3.2 Coherency, intermittency and correlations

From the previous sections the notion of coherent events have been introduced without any definition, except what we could trivially deduce from the observation of the time traces: the coherent events are not noise, and might stand for the most general description of coherence. The coherency and intermittency find their first statement in the spectral description of the signal: it corresponds to modes coupling at a given time and are thereby related to the phase and relative amplitude between the modes in a Fourier description.
For instance, let us consider a signal s with an uniform power spectrum over the full frequency range $F(s,w) = S_0 e^{\phi(w)}$. If the complex phase of any frequency mode is defined as a linear function of the frequency $\phi(w) = t_0 w$, the resulting time signal is a Dirac $S(t) = \delta(t - t_0)$ that

defines an elementary intermittent event at the time t_0 - see figure 3.24. On the other hand, if the phases are chosen randomly, the resulting signal is a white noise, related to the notion of no intermittency.

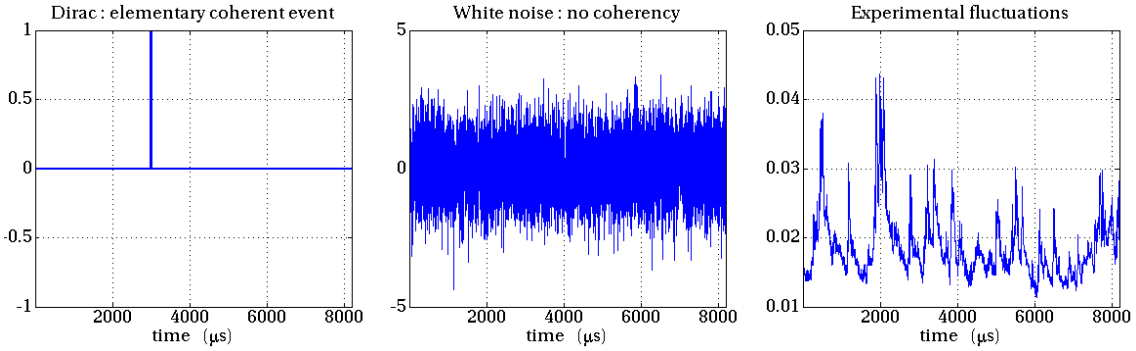

***Figure 3.24**:*

Therefore, the phase coupling between different spectral modes is one of the major parameter responsible for intermittency. This statement can be easily tested from an experimental time trace 3.25: Its Fourier spectrum is calculated and the complex phase of every spectral component is changed randomly. The new time trace built from the new Fourier spectrum shows a Gaussian PDF, in contrary to the original signal, inferring that for a same power spectrum the intermittency is due to the phase between spectral modes. On the other hand, the new signal is also composed of coherent events, suggesting that this particularity is hold by the power spectrum only.

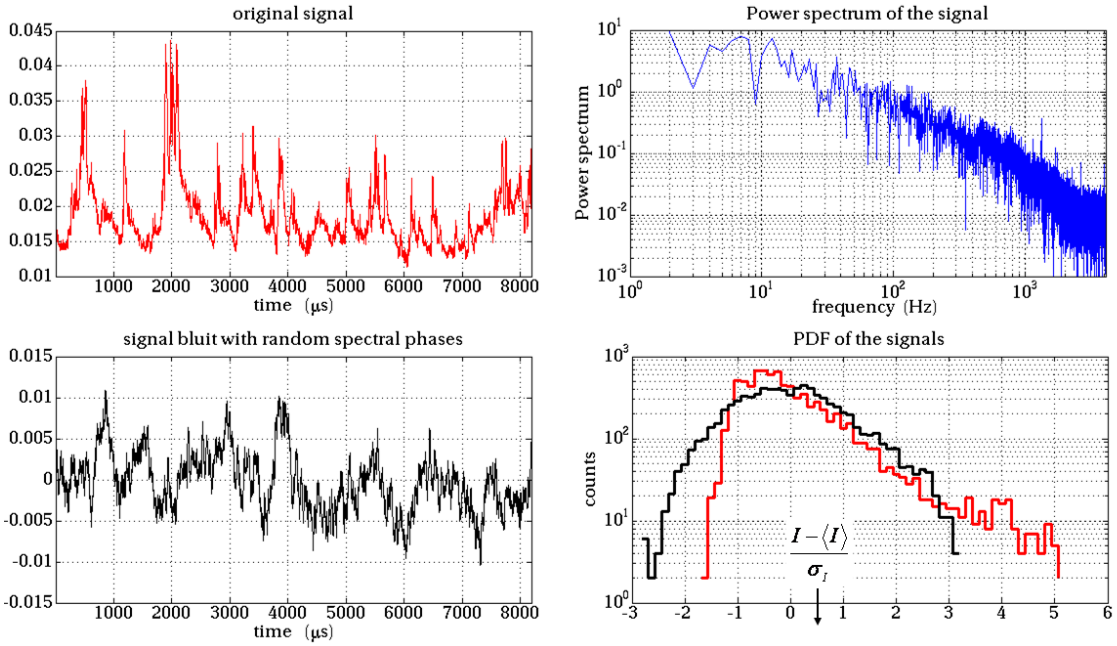

***Figure 3.25**: effect of phase coupling between spectral modes. Top left : original time trace. Top right : Power spectrum. Bottom left: real part of the signal built from the power spectrum to which has been applied random complexe phases. Bottom right : PDF of the original signal (red curve) and the built signal (black curve).*

The latter statement means that the signal coherency is carried by the power spectrum, that is in fact the spectrum of the signal auto-convolution :

$$|F(s,w)|^2 = F(s,w)F^*(s,w) = F\left(\int_{-\infty}^{\infty} s(t-t')s^*(t')dt'\right)$$

Where the sign $*$ notes the complex conjugate of the variable. Therefore, the auto-convolution of the signal holds all information about its coherency, and since the time trace is a real variable its auto-convolution corresponds to the auto-correlation function of the signal defined as:

$$C(s,s,t) = \int_{-\infty}^{\infty} s_n(t-t')s_n(t')dt' \qquad \text{where} \qquad s_n = \frac{s - < s >}{\sigma_s}$$

We may directly note that the auto-correlation function is related to the inverse Fourier transform of the power spectrum, and is therefore an even function since the power spectrum has no imaginary part. This function is a convenient tool to extract informations about the coherency of the signal. For instance, let us consider a white noise 3.24 which is characterized by an uniform power spectrum. The inverse Fourier transform or its auto-correlation is a centered Dirac, showing a width that is null. On the other hand, when the auto-correlation function is calculated on experimental time traces, its half width is non zero and shows a quantitative agreement with the width of events present on the signal 3.26. Its width is subject to some uncertainty depending on the fitting procedure used to extract the parameter, but the ordering does not depend on. In the following we decided to perform a Lorentzian extrapolation of the auto-correlation function :

$$f(t) = \left[1 + \left(\frac{t}{\tau_{corr}}\right)^2\right]^{-1}$$

The Lorentzian half width of the auto-correlation defines the auto-correlation time of the signal τ_{corr}. For the particular plunge discussed in that part, the correlation time is about $10\mu s$ close to the LCFS and increases up to $100\mu s$ in the far SOL.

3.2.4 Dynamical approach with cross-correlations

The auto-correlation function introduces a more general aspect of the fluctuation analysis, by enlarging the correlation calculation between two time traces collected on the rake probe : what can we learn about the fluctuations dynamics from spatially separated collections?
Again, the easiest way to understand the physical processes aimed by the correlation analysis is by comparing density time traces collected simultaneously on the rake probe - see figure 3.27. As a first observation, the fluctuations are similar on the consecutive collectors, since the biggest coherent events are present on all time traces. If we look more carefully, we would notice that the fluctuations are even shifted from one collector to another, inferring a phenomenon of propagation of the fluctuations. The correlation amplitude and the shift are computable with the cross-correlation function of two signals s^1 and s^2:

$$C(s^1,s^2,t) = \int_{-\infty}^{\infty} s_n^1(t-t')s_n^2(t')dt' \qquad \text{where} \qquad s_n^i = \frac{s^i - < s^i >}{\sigma_{s^i}}$$

The latter expression is just a generalization of the auto-correlation function, or a time space definition of the Fourier convolution.

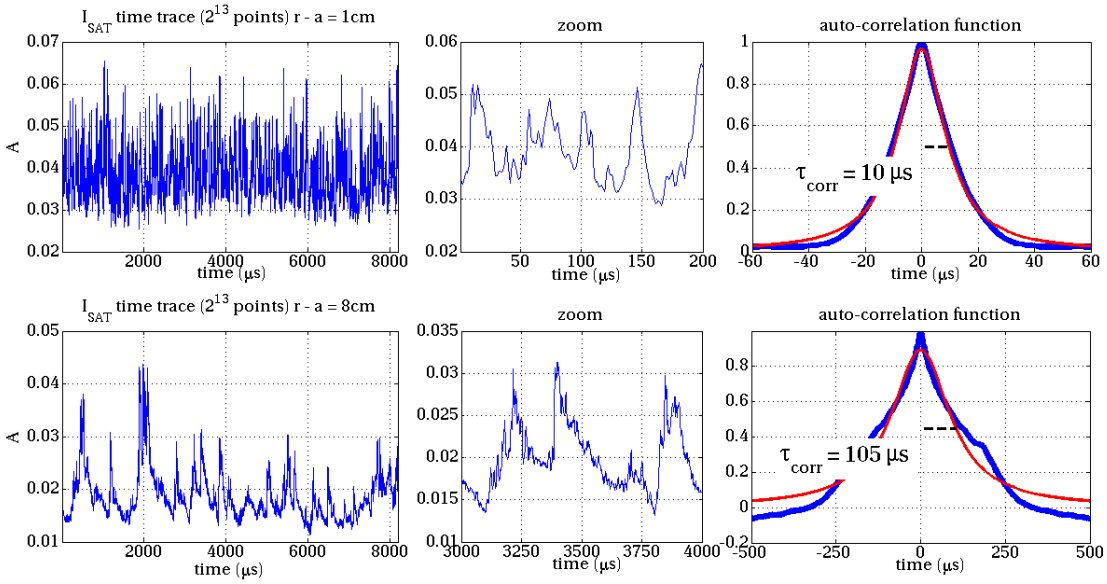

Figure 3.26: *TS44635 5s. Autocorrelation function of saturation current signals extracted at 1cm and 8 cm from the LCFS. Left : the time traces are plotted over 2^{13} points. Middle : Zoom on coherent events. Right : Autocorrelation function (blue) fitted with a Lorentzian function (red). Its half width is shown.*

3.2.4.1 Velocities

First of all, if we consider two identical signals but one is temporally shifted by t_0 : $s_2(t) = s_1(t - t_0)$, the cross-correlation function between s_1 and s_2 is equal to the auto-correlation function of s_1 but shifted around t_0 and the shift reported on the distance separating the two measurements location returns the virtual phase velocity of the fluctuations projected on the measurement axis. Now considering two similar signals as illustrated on the figure 3.27, the time position where the maximum amplitude of the cross-correlation is reached defines the time shift δ_t between the two signals. We find for the considered time traces that the time shift is $4\mu s$ for two pins separated by $3mm$ and is $8\mu s$ for two pins separated by $6mm$, the sign corresponding to a negative poloidal propagation. The linearity and the reproducibility of the shift with respect to the pin separation is a clue that the measured shift is a reliable parameter for measuring the velocity of fluctuations.

The velocity extraction method presented hereby refers to an implicit assumption about the fluctuations, namely the Taylor approximation, that fluctuations propagate in the medium in a way that the propagating spatial structures do not evolve with time. Thus two points separated spatially would measure the same signal at a different time. The validity of such assumption can be partially addressed by paying attention to the correlation amplitude of signals collected at different spatial locations: we considered the cross-correlations calculated over the full set of pins composing the poloidal rake - see figure 3.28. For the selected data, the maximum of cross-correlation M_{cc} decreases with the pins separation length Δ_θ, from about 0.8 for $\Delta_\theta = 3mm$ to about 0.2 for $\Delta_\theta = 9mm$ and infer that for large Δ_θ the cross correlation is no longer meaningful. The phase shift is increasing in absolute amplitude with Δ_θ, following

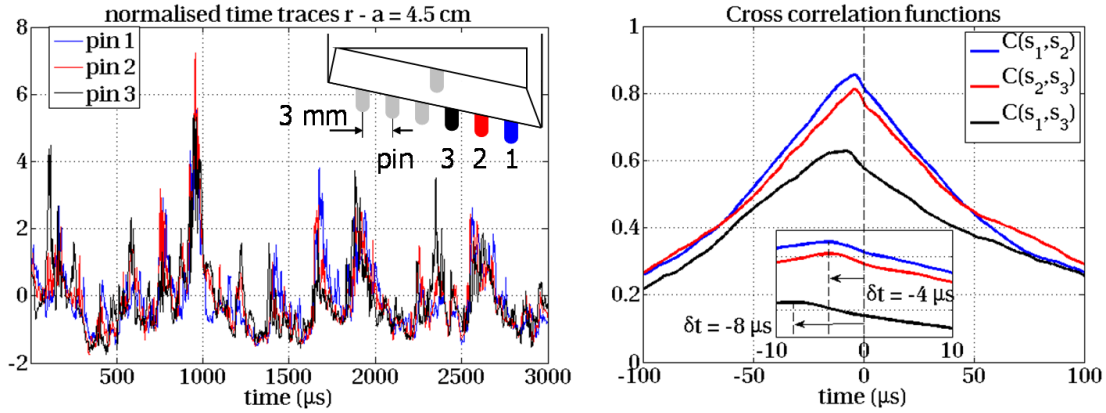

Figure 3.27: *TS42973 4s. Saturation current collected 4.5 cm from the LCFS. Left : time traces of currents collected by 3 consecutive pins. A good correlation is noticeable. Right : Cross correlations between consecutive pin signals. The maximum of cross correlation are shifted from the origine. The shift is different depending on the pin separation length.*

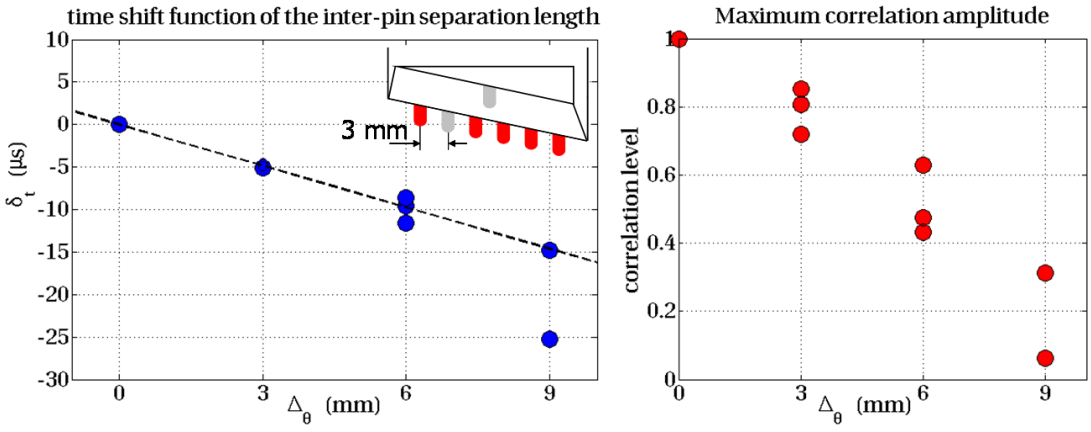

Figure 3.28: *TS42973 4s. Saturation current collected 4.5 cm from the LCFS. Left : time shift of the maximum of the cross correlation function of the pin separation length. the trend is fitted with a linear curve with respect to the cross correlation amplitude. Right : amplitude of the maximum of cross correlation, function of the pin separation length.*

a linear trend, and is more or less reproducible for different pair of pins (points plotted for the same Δ_θ). In order to take care of the correlation decay with pins separation, the velocity - defining the linear trend - is estimated from the time shifts pounded with the correlation amplitudes M_{cc}:

$$V_\theta = \frac{1}{\sum M_{cc}^i} \sum \frac{M_{cc}^i \Delta_\theta^i}{\delta_t^i}$$

For the particular experiment 3.28, the projected velocity on the poloidal axis is about $V_\theta = -0.61$ mm.μ s^{-1} $= -610$ m.s^{-1}.

Due to the rather good linearity of the time shift evolution with the pine separation length, we may conclude that the fluctuations velocity is rather uniform along the poloidal rake. On the other hand the decay of the correlation amplitude indicates either that :

- Fluctuations do not survive on a long path (of the order of the rake size), yielding the Taylor approximation questionable.

- Structures are too small to pass across all pins according to the orientation of their velocity 3.29.

- Each structure has its own velocity and the scatter leads to a correlation spreading with the separation distance.

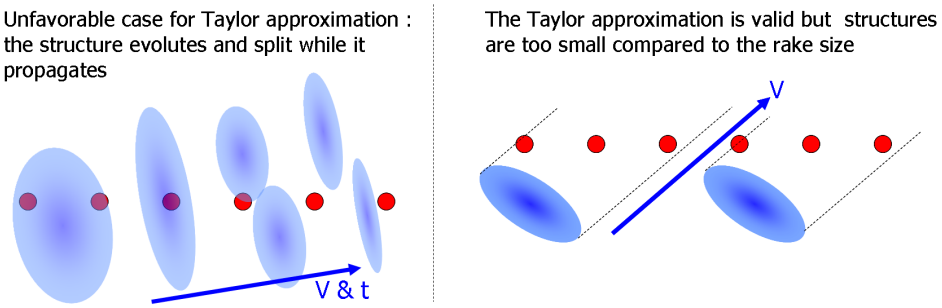

Figure 3.29: *Illustration of different effects making the correlation process questionnable*

The time lag between spatially separated time traces seems a reliable parameter to extract the phase velocity of the fluctuations. Thus we are potentially able to measure a velocity field transversal to the magnetic field related to the dynamics of fluctuations in the SOL. On the other hand the time lag analysis faces a crucial issue that has not been discussed yet, and the best illustration is by looking at the radial phase velocity evaluated with the radial rake probe - see figure 3.30. The time lags suggest that fluctuations propagates radially inward, and we could try to build a variety of interpretations in order to conciliate an outward radial transport with inward phase velocities. Especially as the electrostatic drift velocity is observed to drive an outward density convection - see next parts.

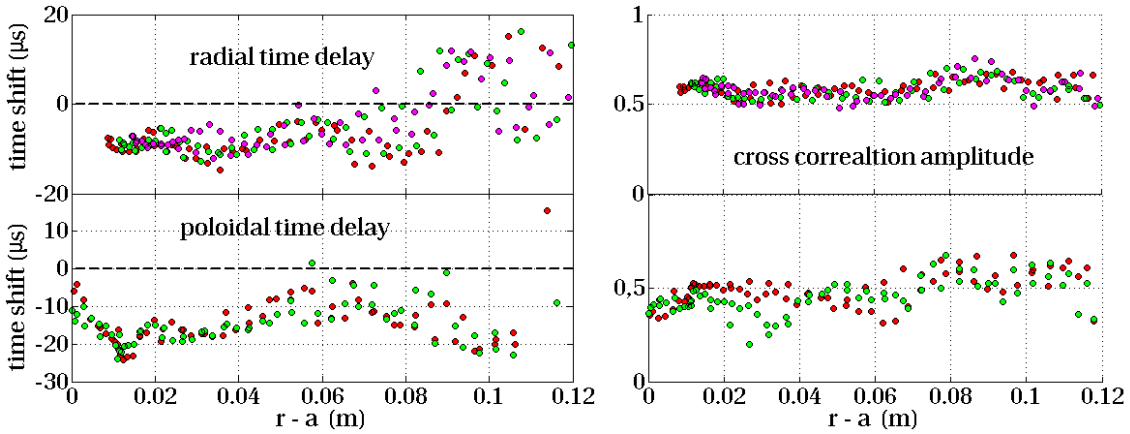

Figure 3.30: *TS44635 plunge 2 (poloidal rake probe) and TS45393 plunge 2 (radial rake probe) - identical discharges, saturation current collections. Top : Radial profile of the time shift between consecutive collectors (Δ_r =3 mm) of the radial rake probe (ion side). Different colors show different pairs of collectors. A negative time shift means an inward phase velocity. Right : Associated cross correlation amplitude. Bottom : Poloidal time shift from the poloidal rake probe ($\Delta_\theta = 6$mm). A negative shift means a negative poloidal velocity.*

To resolve this apparent contradiction, the shape and orientation of the structures have to be considered in the interpretation of the time lags in term of velocities - see figure 3.31. A coherent model for the velocity extraction needs some complements on the shape and orientation of the density or potential structures in the SOL that are not yet readable from the probe fluctuations data. That point is revisited in the last chapter devoted to the 3D property of the flux in the SOL.

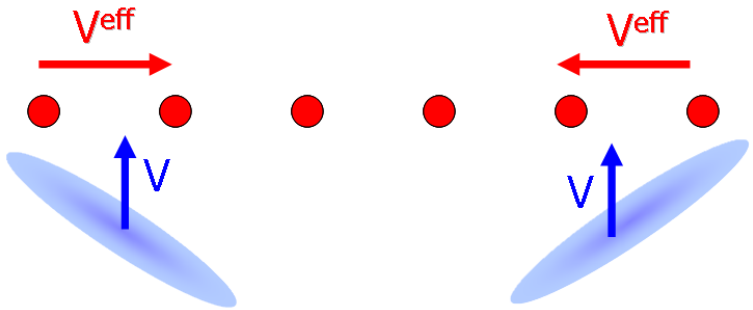

Figure 3.31: *Effects of an elongated and tilted structure on the misinterpretation of the fluctuations velocity.*

3.2.4.2 Nature of the phase velocity

Up to now, we are able to measure a phase velocity projected along a rake (poloidal or radial) but the meaning is missing due to the lack of information about the local structures shape. Anyhow, the deduced velocity corresponds to a projection of the real structures velocity and some informations are already accessible from that statement. For instance, the poloidal phase velocity (read on the poloidal rake) is almost identical for floating potential and saturation currents - see figure 3.32, inferring that plasma density and potential structures follow the same dynamic in the SOL. Secondly, it appears that the velocity (for saturation current) is a function of the magnetic field strength. As illustrated on the figure 3.32, it is even a linear function of the inverse of the magnetic field. This observation is done on a set of discharges during which the magnetic field and the plasma current are varied from $2.1 < B_T < 3.9$ T , $0.6 < I_P < 0.9$ MA, the density varies as well : $3.2 < lad < 5.910^{19}\mathrm{m}^{-2}$, to form a set of independent parameters. The velocity appears to vary only with the magnetic field, and the dependency $V \propto \frac{1}{B}$ infer the drift nature of the phenomenon.

3.2.4.3 Correlation sizes

The cross-correlation technique addresses - in the framework of our study - a last but not least information about fluctuations, that is the projection size of the fluctuating structures along the rake. Beyond the characterization of the turbulence, the information is crucial in the evaluation of the electrostatic drift from a sampled electrostatic field. Indeed if the potential structures size along the rake are smaller than the distance between the floating pins, the electric field would be for sure under-sampled. This particular issue is addressed latter, and therefore let us first discuss the size evaluation.

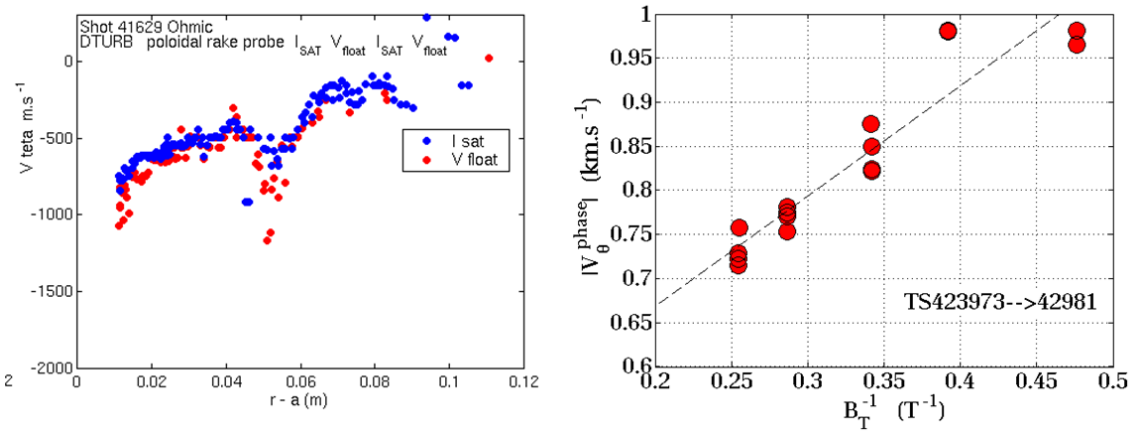

Figure 3.32: *Left : TS412628 Ohmically heated plasma limited on the LFS. Radial profiles of the poloidal phase velocity measured on the poloidal rake probe, for saturation current and floating potentials. Velocities measured with correlations above 0.5 are displayed. Right : Poloidal phase velocity measured 5 mm from the LCFS function of the inverse magnetic field strength. Data are collected during a scan of plasma current and magnetic field (independent parameters). the absolute amplitude of the velocity is shown. A black dashed line indicates the linearity.*

If we could have a long rake composed of a large amount of small collectors, the instantaneous density footprint - or potential - would have reflected the structures pattern along the rake 3.33. Therefore the same process as for the correlation time would have been applied to the spatial trace to extract the correlation length, namely the size of the structures projected along the rake. Unfortunately, the rake is composed of only 6 pins that does not allow the proposed spatial correlation technique, but that is sufficient for a diverted used of the temporal correlation functions as presented in the following. In an ideal case, the correlation length - or fluctuation size - is fitted on the spatial correlation function of the spatiotemporal field of interest $s(x,t)$, at a given time t_j :

$$\frac{1}{N_x}\sum_i s(x_i,t_j)s(x_i+\Delta,t_j) = f_x(\Delta)$$

The function f_x is for instance fitted with a Lorentzian, that might depends on time, or at least that might fluctuates with time. Let us proceed to a time average of the latter expression and permute the average over space and time :

$$\begin{aligned} f_x(\Delta) &= \frac{1}{N_t}\sum_j \frac{1}{N_x}\sum_i s(x_i,t_j)s(x_i+\Delta,t_j) \\ f_x(\Delta) &= \frac{1}{N_x}\sum_i \frac{1}{N_t}\sum_j s(x_i,t_j),s(x_i+\Delta,t_j) \\ f_x(\Delta) &= \langle C_t(s_i,s_{i+\Delta},0)\rangle_i \end{aligned} \tag{3.16}$$

The spatial cross-correlation function has been expressed with the temporal cross-correlation amplitude with zeros time delay $C_t(s_i,s_{i+\Delta},0)$. Now the number of pins in the rake does not appear be be a strong limitation for the evaluation of the Lorentzian size of the structures as soon as the temporal cross-correlation is reliable for a set of pairs of separated pins. The

process 3.16 is applied to the density time traces, as illustrated on figure 3.33. The time correlation amplitude is a decaying fonction of the inter-pin separation and is correctly fitted with a Lorentzian. As a first result, the poloidal half width of the density structures are about 4mm in that particular experiment.

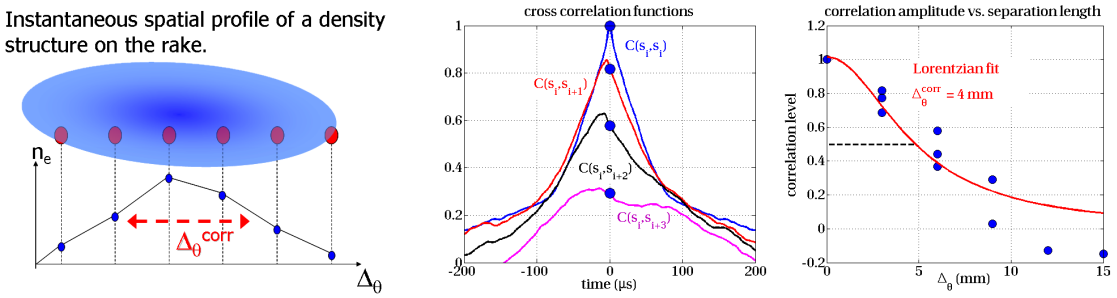

Figure 3.33: *Evaluation the Lorentzian poloidal size of the structures. Left : Schema of a structure passing across the rake and the instantaneous spatial density profile collected by the probe. Middle: Temporal cross-correlation functions for different pair of pins along the rake. $C(s_i, s_{i+1})$ defines the cross correlation of two adjacent signals. The retained information is the zeros delay correlation amplitude $C(t = 0)$. Right : The latter parameter is plotted function of the inter-pin distance Δ_θ. The related correlation decay is fitted with a Lorentzian and defines the Lorentzian poloidal size of the structures.*

Up to know, we have discussed the tool used for extracting geometrical and dynamical informations about the fluctuations : velocities and sizes. The process has been applied to a particular set of data, in order to reflect the general ordering of edge plasma phenomena : fluctuations collected by the rake probes are the signature of coherent structures of size of the order of 5 mm and moving with velocities of the order of 500 ms^{-1}. The signature of the structure motion corresponds to coherent bursts that last typically 10 μs, in quantitative agreement with the size and speed ordering.

3.2.5 $E \times B$ transport

The velocity field introduced previously has shown a drift-like dependency : density structures propagate due to an electrostatic field, and the probe design allows to evaluate this electrostatic field under some assumptions. The matter is to derive the property of the fluctuating electric field and quantify the coupling with the density fluctuations in order to deduce the property of the related radial flux.
First of all, the simple assumption is done that the electric field can be directly defined from the floating potential by neglecting the temperature fluctuations. The first issue concerns the electric field sampling and the related uncertainty linked to the size of potential eddies. However the diagnostic and the measurements does not offer any chance to quantify the error. The proposed solution is the following :

- Directly assume that the electrostatic field is sufficiently well sampled if the potential eddies are bigger than the pin separation length.

- Characterize the type of turbulence involved at the edge from the phase coupling between density and electric field fluctuations.
- Consider a numerical simulation of the related kind of turbulence and evaluate an error function due to under-sampling of the electric field component.
- Check the consistency of the experimental electric field evaluation with respect to the previous error function.

The latter method seems quite important to follow since there is *a priori* no experimental process able to cross-validate the measurements on electrostatic turbulence, and is unfortunately never mentioned elsewhere - except in [**?**] where the issue is briefly discussed.

3.2.5.1 Phase shift between density and electrostatic field

Following the previous considerations, let us pay a look to the coupling between density and electric field fluctuations in the SOL. A dedicated acquisition setup of the rake probe is required, namely with pins on the poloidal rake alternatively driven in saturation and floating modes. The electric field is estimated by the difference of floating potential surrounding a saturated collector - see figure 3.34.

Let us start by assuming that the electric field is well sampled. The time traces of density

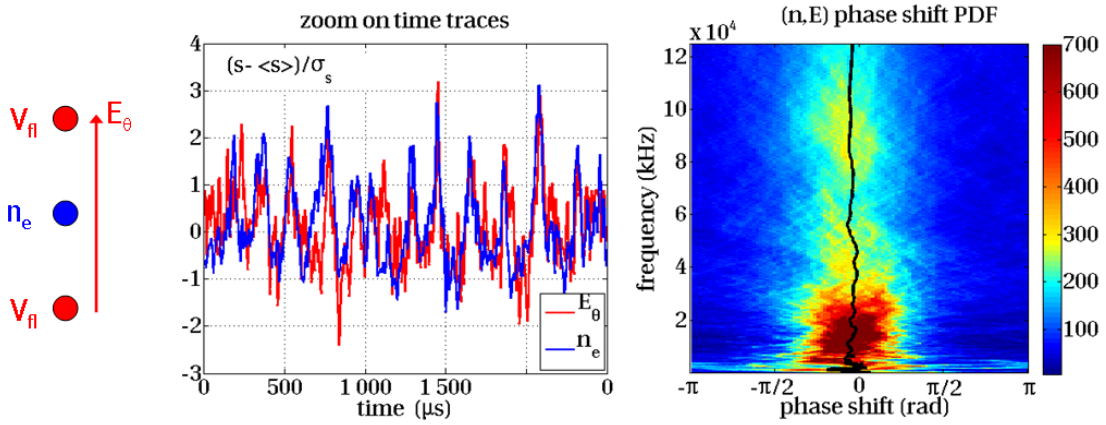

Figure 3.34: *TS44586, plunge 1, 7mm < r - a < 14 mm. Left : mode setup of the poloidal rake. Middle : Zoom on the density and electric field time traces, that show a good correlation. Right : PDF (in color scale) of the phase shift between density and electric field at each frequency. The time averaged phase shift is shown (black curve).*

and electric field fluctuations show that coherent events are more or less in phase between the two signals. The latter property is of great interest for discriminating the kind of mechanisms underlying the measured fluctuations, and needs a more reliable tool for extracting the phase shift between density and electric field. Indeed the matter is to know if a density structure is effectively convected radially, that is a local information in time. A Fourier transform might give an information about the phase shift between the two signals but unfortunately gives a non local information in time. For that reason a complex and continuous wavelet transform

is applied, that yields the local phase shift between two signals [4]: The two sets of wavelet coefficients are evaluated from the same transform and the local phase shift is evaluated for each time and each scale as the complex phase difference between the coefficients. Then its PDF is calculated over the time trace for each scale as illustrated on the figure 3.34. For this particular experiment, the phase shift shows some scatter but is well peaked on its mean value, that appears to be close to zeros for all time scales - or frequencies. In other words, the positive density peaks are in average correlated with positive poloidal electric field, interpreted as a radial outward propagation of these density structures.
The latter property is already a important information that can be used to discriminate the kind of mechanism responsible for the fluctuations. Namely, the SOL plasma can be subject to two kinds of turbulence : the drift-wave and the interchange instabilities. Roughly speaking, the first one leads to density and electric field fluctuations that are in quadrature (phase shift in average $\pi/2$) whereas the interchange leads to a phase shift that is in average 0. Experimental evidences presented here are coherent with an interchange-like type of fluctuations, even if more elements of validation are needed to draw this conclusion [Garcia 07a].

3.2.5.2 Electric field sampling : error function from simulations

Now that the type of turbulence has been highlighted, the exercice can be done to evaluate the error made on the electric field sampling from a simulation of interchange turbulence. The choice has been done to use simulation data obtained from the TOKAM-2D code. The simulated domain is a 2D grid over the radial and poloidal directions 3.35 and data correspond to density and electrostatic potential fluctuations in a steady-state regime, with time traces long enough to get a sufficient statistic on the number of intermittent events.

A virtual probe diagnostic is implemented to evaluate the poloidal electric field as a spatial difference of electrostatic potentials 3.35. The poloidal distance between floating collectors $2\Delta_\theta$ is varied and the resulting time averaged radial flux is computed and compared to the local value deduced from the real electric field:

$$\begin{aligned} E_\theta^{\Delta_\theta}(r,\theta) &= \frac{V(r,\theta-\Delta_\theta)-V(r,\theta+\Delta_\theta)}{2\Delta_\theta} \qquad \forall \Delta_\theta > 0 \\ \Gamma_r^{\Delta_\theta} &= \langle \tilde{n}_e \tilde{v}_r \rangle_t \propto \left\langle \tilde{n}_e \tilde{E}_\theta^{\Delta_\theta} \right\rangle_t \end{aligned}$$

The real local electric field is calculated with a 4^{th} order poloidal scheme on the electrostatic potential and defines the reference case $\Delta_\theta = 0$.
The reason why the estimated radial flux should depend on Δ_θ is directly related to the under-sampling of the poloidal electric field with respect to the potential eddy size, and for that reason it is worth to normalize the Δ_θ separation length with respect to the poloidal size δ_θ of the electrostatic eddies. Besides, the simulation offers the opportunity to test the approximation 3.16 set to define the poloidal size of the structures from temporal cross-correlation amplitudes. As a first result, the poloidal size of the electrostatic eddies calculated from the temporal cross correlation method is in good agreement with the spatial correlation width - see figure

[4] analysis started after a collaboration with G. Bonhomme, F. Brochard, M. Farge and R. N'Guyen van Yen. We made use of Morlet Wavelets

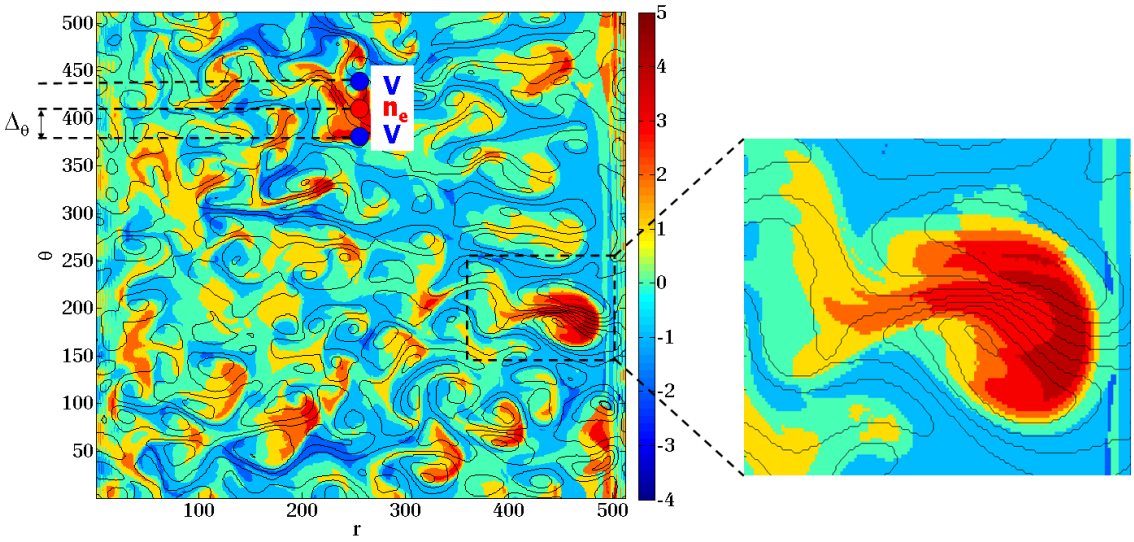

Figure 3.35: *2D (r,θ) map of density (color map) and potential (black curve contours) at a given time. For the figure, the density map is locally normalized by subtracting the time averaged value and divided by the root-mean-square to get rid of the radially decaying profile, but analysis presented hereby are done on raw data. A virtual probe is implemented to extract the local potential and density fluctuations, with a geometrical parameter Δ_θ. On the right is shown a zoom on a density structure, that is radially convected by an electrostatic potential structure.*

3.36, although the latter is strongly fluctuating in time. A possible explanation for the large fluctuation is that the poloidal extend of the simulation is too small to obtain a complete statistic along the poloidal axis (ergodic hypothesis).

The radial flux estimated with the probe configuration underestimates the local value as the poloidal separation Δ_θ increases with respect to the poloidal size of the electrostatic eddies 3.37. The error function $\Gamma_r^{\Delta_\theta}/\Gamma_r^0$ is computed for different radial position along the simulated domain and shows similar behavior function of the parameter $\Delta_\theta/\delta_\theta$. Although the error function has been calculated for only one simulation run, thus for one set of plasma parameters, we infer that the error function does not strongly depends on the plasma parameters since it is only related to the sampling of the electric field with respect to the size of the electrostatic eddies. As illustrated on the figure, the error function is well fitted with a Lorentzian, giving an analytical correction parameter depending on the normalized poloidal separation length :

$$\Gamma_r = \Gamma_r^{\Delta_\theta}\left[1+\left(\frac{\Delta_\theta}{1.4\delta_\theta}\right)^2\right] \tag{3.17}$$

Since the poloidal rake probe can measure both the radial flux and the poloidal size of the electrostatic eddies, the flux amplitude can be corrected from the latter error function. On the other hand it has to be emphasize that although the simulations are similar to what is effectively observed on experiments, we did not try to quantitatively match experimental observations with simulations. We rather point out an error that is rarely discussed but find all its interest in the quantification of the turbulent flux.

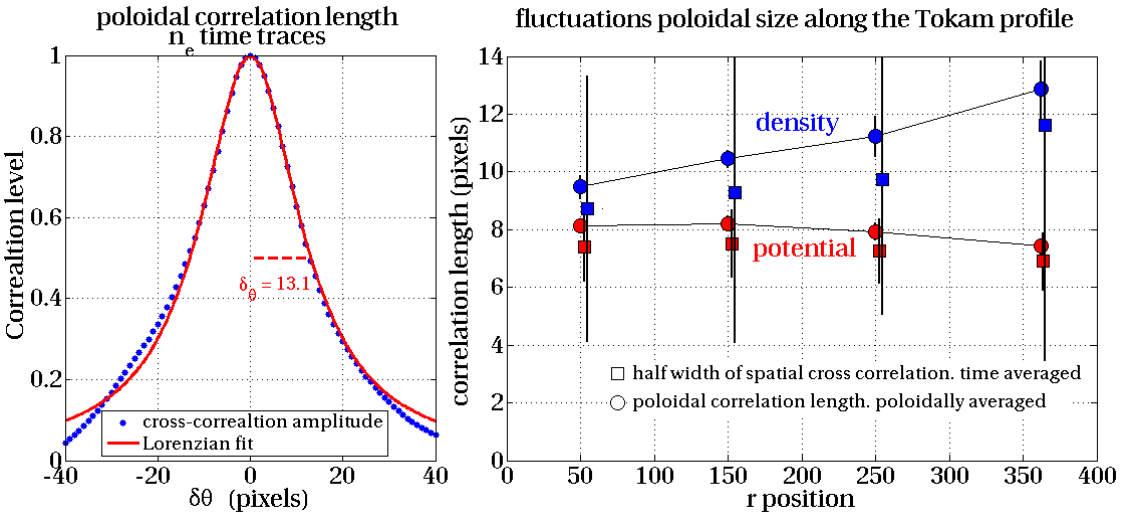

Figure 3.36: *Left : at a given radial and poloidal location on the 2D map, the density time trace is temporally cross-correlated with signal taken at various poloidal distance δ_θ. The cross-correlation amplitude is fitted with a Lorentzian as proposed in 3.16. Right : radial profile of the Lorentzian poloidal size of the fluctuating fields (density in blue and potential in red). Squares are obtained from the spatial (poloidal) auto-correlation function fitted with Lorentzian, the half width being afterward time averaged (notice the large error bars counting for the large time scattering). The circle are obtained from the time correlation technique at different poloidal location and afterward averaged over the poloidal coordinate. The two methods gives similar results, with a difference of about 10%.*

3.2.5.3 Turbulent radial flux and effective transport coefficient

The previous exercise performed on the simulation aimed at showing that the electric field can be under-sampled, leading to a possible underestimate of the $E \times B$ radial flux that is never mentioned in the literature. Therefore before evaluating the turbulent $E \times B$ radial flux from the experimental data and discussing its amplitude, the first test to make is to be sure that the poloidal size of the electrostatic eddies is larger than the length separating the floating collectors. Let us consider the full probe configuration used to collect the data presented on figure 3.34, as illustrated on the figure 3.38. The poloidal half width of potential eddies is found to be $\delta_\theta \approx 12mm$ for that particular position in the SOL, close to the LCFS. In comparison of the collector separation length $\delta_\theta = 3mm$ and assuming the previous error function is applicable to the experimental data, the conclusion is done that the electric field is well sampled and does not lead to misinterpretation.

Besides allowing the evaluation the poloidal size of electrostatic (or density) structures, the probe configuration showed on the figure 3.38 allows to calculate the turbulent radial flux on two sets of collectors, namely (V_2,I_3,V_4) and (V_4,I_5,V_6), and therefore gives an opportunity to check the consistency of the measured flux. The flux evaluated on the saturated collector i is

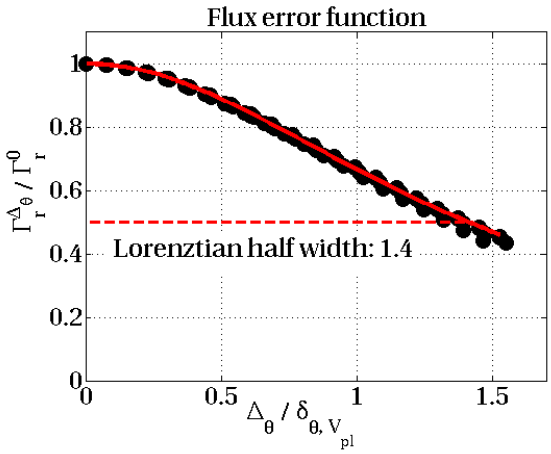

Figure 3.37: *Variation of the estimated radial flux (normalized to its real value) function of the collectors separation width (normalized to the local potential eddy size) . The points (black dots) are evaluated at 4 radial positions along the simulation profile.*

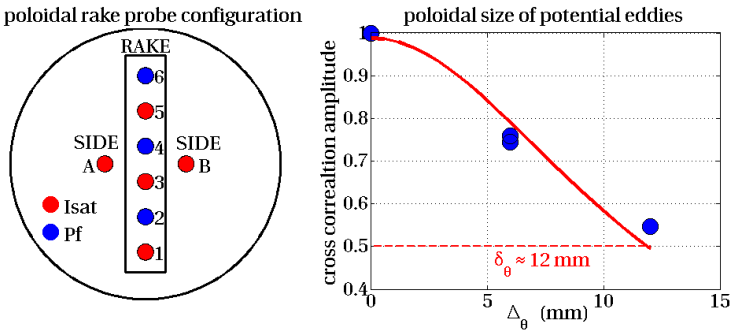

Figure 3.38: *TS44586, plunge 1, 7mm < r - a < 14mm. Left : Configuration of the poloidal rake probe, where 3 collectors are set on floating acquisition mode. Right : The poloidal size of electrostatic eddies is evaluated form the temporal cross-correlation amplitudes and is found to be about 12mm.*

defined as:

$$\Gamma_r^i = \frac{I_{SAT}^i \tilde{E}_\theta^{i-1,i+1}}{\bar{B}} \tag{3.18}$$

$$\text{with } \tilde{E}_\theta^{i-1,i+1} \equiv \frac{1}{2\Delta_\theta}\left(V_{fl}^{i-1} - V_{fl}^{i+1} - \left\langle V_{fl}^{i-1} - V_{fl}^{i+1} \right\rangle\right) \tag{3.19}$$

As it can be noticed, the density has been replaced by the saturation current (discussed just after) and the electric field is only defined as its fluctuating part, since its time averaged value has been subtracted. The reasons are that no flux from a velocity pinch is expected in the SOL (product of a constant density with a constant poloidal electric field) and mostly because the time averaged component of the poloidal electric field is not reproducible (even in its orientation) function of the considered set of floating collectors. The latter remark is attributed to an effect of electronic drift, related to the diagnostic only.
As it has been explicated previously, the saturation current collected by the rake pins is roughly proportional to the plasma density. In order to get rid of the proportionality factor linking

the two quantities [5], we decided to normalise the fluctuating flux to the local time averaged density value, in order to read the flux as a fluctuating velocity variable:

$$\tilde{v}_r \equiv \frac{\Gamma_r}{\langle I_{sat} \rangle_t}$$

The figure 3.39 shows a time trace and the PDF of the flux (velocity) calculated with the two set of collectors. the PDF's are in remarquable good agreement, the mean value and the root-mean-square differ only by about 10%. As it can be noticed, the distribution is positively skewed ($S_\Gamma = 0.7$), or in other words the most probable flux value is negative (inward) and the mean value is positive due the presence of large and rare positive bursts.

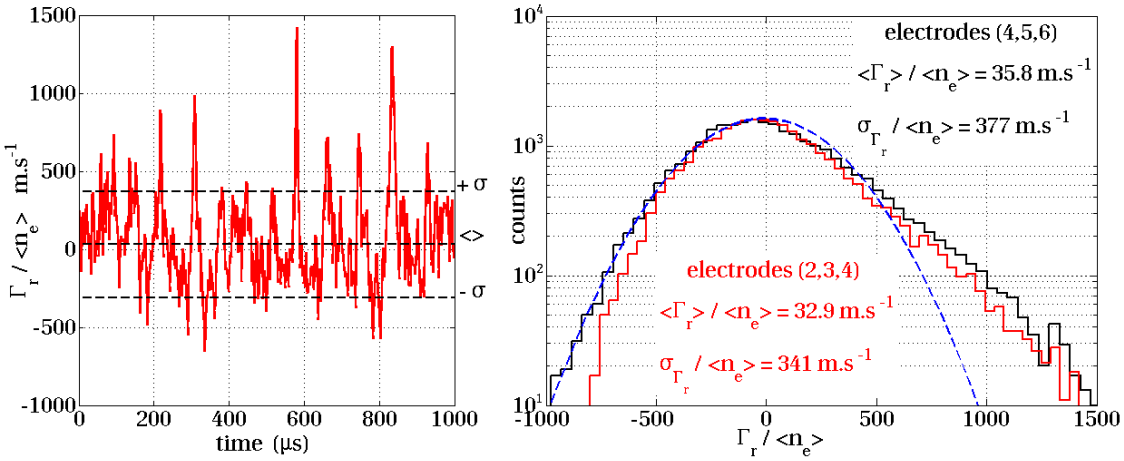

***Figure 3.39**: TS44586, plunge 1, 7mm < r - a < 14mm. Left : Time trace of radial flux normalized by the time averaged density. The mean value and the standard deviation around the mean value are shown. Right : Probability distribution functions of the turbulent radial flux normalized by the time averaged density, calculated for 2 set of collectors on the poloidal rake: in red for the collectors (2,3,4) and black for the collectors (4,5,6). The dashed blue line shows the Gaussian fit on the negative part of the flux, indicating the positively skewed behavior of the fluctuating flux.*

Interestingly, the time averaged value of the radial flux is positive and reproducible, although the fluctuation level is really large ($\frac{\sigma_\Gamma}{<\Gamma>} \approx 10$): the flux is composed of strong inward and outward convections, resulting in average in a residual outward component.

3.2.5.4 Radial transport and velocity shear

The phase between density and electric field fluctuations is of crucial importance for the propagation of density eddies. The case presented above corresponds to an optimal phase coupling and the result is a relatively important transport coefficient. On the other hand, other experiments have shown a different behavior, as illustrated on the figure 3.40. For plasma conditions that have not yet been identified, the phase shift between density and electric field can become close to $\pi/2$ and the related transport coefficient drops significantly. As the position

[5] We observed at the end of the experimental campaign that thin collectors on the poloidal rake have melt and reduce in size. We infer a slow modification of the effective collection area during the campaign

is chosen further from the LCFS, the effective velocity increases and the phase shift changes as well, toward 0. First of all, the poloidal size of electrostatic eddies (25 mm) largely exceeds the diagnostic sensitivity and the electric field under sampling is therefore not on task in the change of the electrostatic behavior.
Unfortunately, the density profiles are not available for that experiments and we can not check if the density gradient steepens in that region. On the other hand, we observed that the velocity field obtained from the poloidal rake probe shows a strong poloidal shear layer within the region where the transport coefficient is reduced - see figure 3.40. Despite the ambiguity of velocity field measured by the rake probe **??**, the qualitative picture is that strong transversal velocity gradients are present close to the LCFS, and they could be linked to the decorrelation of the transport eddies, as the theory is proposed in [Ghendrih 09] and [Ware 98].
We did not focus longer on that interesting observations due to the lake of local plasma parameters that could have been measured with the tunnel probe. Despite the different plasma conditions when this transition layer has been observed, it was found to be hardly reproducible within similar plasma conditions. Nevertheless, we mention this phenomenon has never benn observed during high density discharges, and further analysis are performed on data that does not show this particular behavior.

3.2.5.5 Comparison with global particle balance

As a summary of the previous sections, the fluctuations of density measured at the plasma top are composed of strong and intermittent coherent events, propagating in the plasma transversally to the magnetic field. The electric field is found to fluctuate in phase with the density field (for the discussed experiment), fixing the best conditions for convecting radially these density structures. The calculated radial flux is effectively directed outward the plasma center and its amplitude (in term of transport coefficient) is in the order of 30m.s^{-1} close to the LCFS. Now, let us consider this particular particle transport process in the framework of particle transport in the SOL. The local $E \times B$ transport coefficient is compiled over the whole SOL radial profile (at the plasma top), in order to be compared to the steady-state density profile measured with a tunnel probe, both probes plunging almost simultaneously in the plasma. As introduced previously 3.9, the radial decay length of density mapped at the parallel flow stagnation point n_0 can be used to estimate a field line averaged transport coefficient. Transport was preliminarily described as a diffusive process in order to be compared with neoclassical prediction 3.8 but is now expressed in term of convection since the $E \times B$ transport corresponds more to a convective phenomenon. That is, the radial decay length of the density profile is related to a line averaged convection coefficient :

$$\lambda_r = L_{//} \frac{< v_r >_{//}}{c_S} \quad \text{with} \quad < v_r >_{//} \equiv \frac{1}{n_0 L_{//}} \int_{-L/2}^{L/2} n v_r dl_{//} \tag{3.20}$$

Similarly, the line integrated radial flux can be complied from the Mach probe measurement to return an other estimate of the transport coefficient:

$$< v_r >_{//} = \frac{1}{n_0 L_{//}} \int_{-L/2}^{L/2} \Gamma_r dl$$

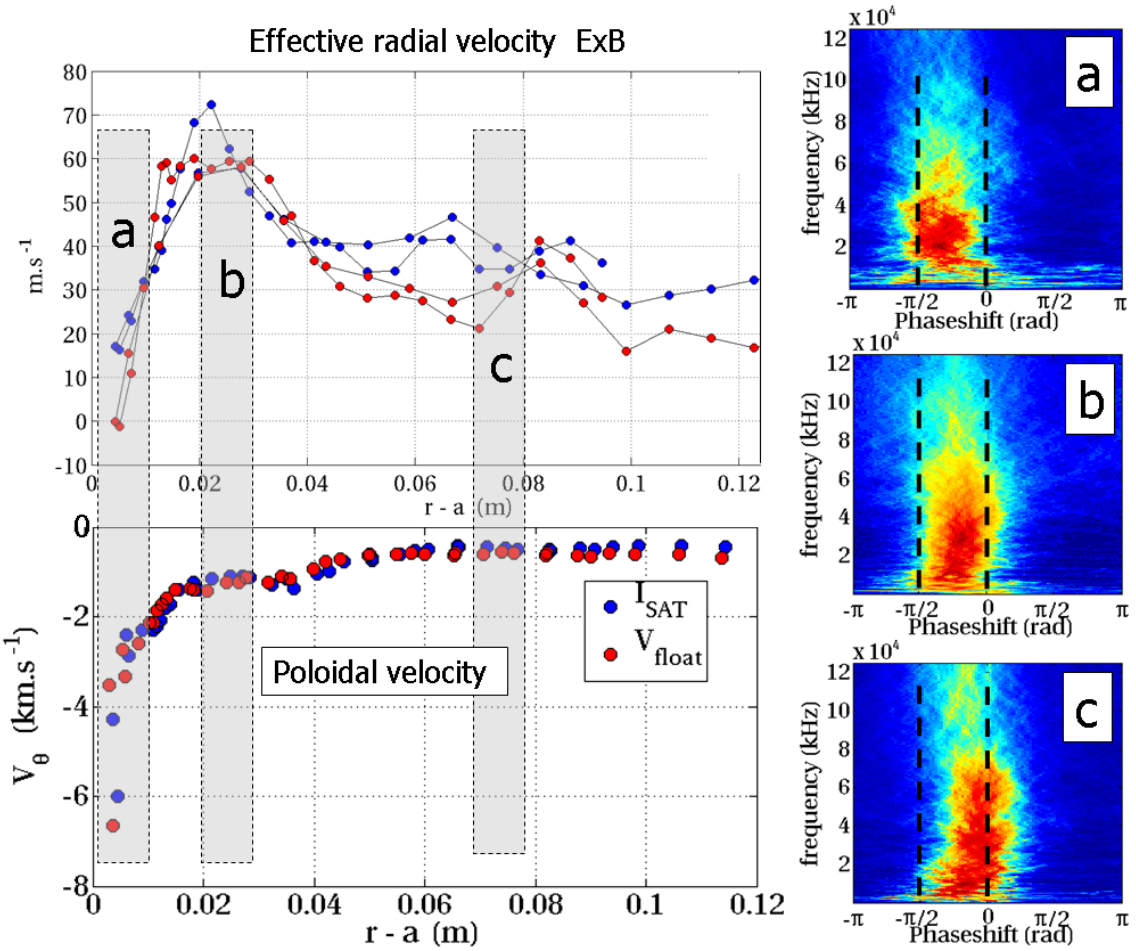

Figure 3.40: *TS44583, plunge 1. Top left: Radial profile of the turbulent radial transport obtained with the two set of collectors (blue and red). We note the data reproducibility, and the sharp velocity decay close to the LCFS. Bottom : Poloidal velocity extracted from the saturation current (blue) and floating potential (red) fluctuations. We note the sharo increase close to the LCFS. Right : Distributions of the phase shift between density and electric field fluctuations, for different positions along the profile : a) $r-a<1cm$, b) $2<r-a<3$ cm and c) $7<r-a<8cm$.*

Where the integral term is the line integrated radial flux. The radial profile of the effective transport coefficient can be compared to the local $E\times B$ value 3.41. Interestingly, all are of the same ordering (several tens of $\mathrm{m.s^{-1}}$), but do not quantitatively match over the whole radial profile. The transport coefficient built from the radial decay of the density should be considered carefully, since by definition it is assumed radially constant over the radial profile.

A first conclusion can be drawn that the local transport estimated by the poloidal rake probe is coherent with transport coefficients obtained from steady-state flow profiles. This is already surprising compared to what is often measured on other tokamaks, where the $E\times B$ turbulent flux is found to be too high to be consistent with the density profiles [Garcia 07a]. That said, the measurements done on other machines are often performed at the outboard midplane and not at the plasma top like in Tore Supra. That point is intimately related to

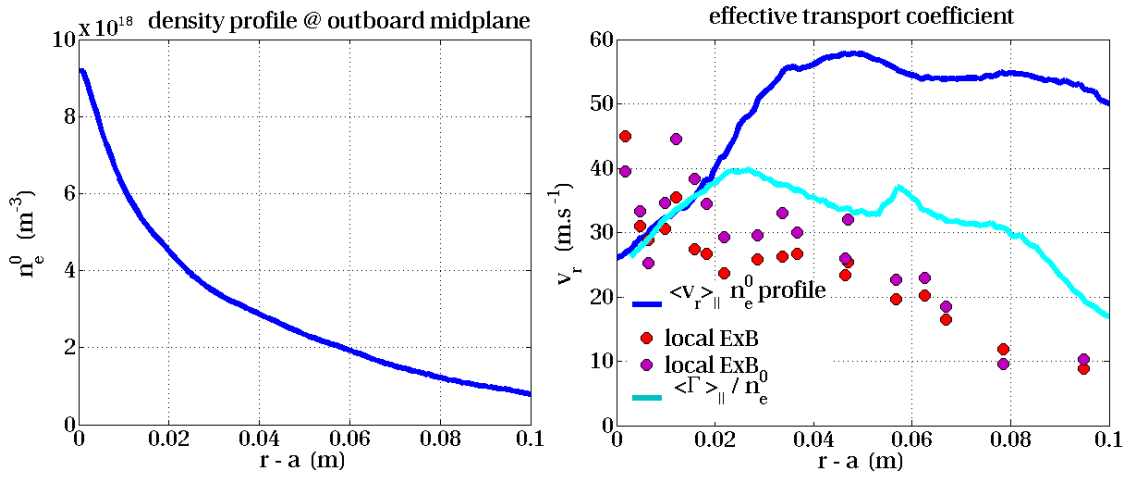

Figure 3.41: *TS44586, plunge 1 poloidal rake probe, plunge 2 STP. Left : density profile at the parallel flow stagnation point. Right: Comparison of transport coefficients evaluated by different methods along the radial profile. The blue curve shows the velocity extracted from the density decay length. The cyan curve shows the velocity from the line integrated radial flux. The full circles show the local transport coefficient from $E \times B$ turbulence.*

the issue of poloidal asymmetries of the radial flux in the SOL, as highlighted by the previous considerations on the line integrated radial flux 3.10. Therefore, there is no reason why the local flux value should match the density profile, that is consequence of the field-line averaged radial transport balanced with the parallel sinks to the limiter/divertor plates. Since we emphasize that the flux is mainly concentrated at the LFS, outboard midplane measurements of the $E \times B$ transport coefficient may overestimate its line averaged value [Garcia 07a] [LaBombard 02], as well as top measurement may underestimate it. This issue has been seriously considered to explain why simulations do no match experiments until a ballooning parameter for the turbulent radial flux is not included in the simulation [Fundamenski 07].

3.2.6 Effect of density

Again, we would like to pay attention to the effect of density on the local turbulent flux crossing the LCFS. During a set of ohmically heated discharges dedicated to density scan, the poloidal rake probe was plunged to the LCFS to measure the $E \times B$ radial flux. Unfortunately, the tunnel probe was not available so that local density at the LCFS is missing. In order to build a flux parameter reflecting the real flux value from to the local effective transport coefficient, the only reliable possibility was to consider the edge line interferometer signal - see figure 3.42. The reason is we already mentioned that the density probe measurement and edge interferometer are in quantitative good agreement, and we checked for an other set of experiments with similar plasma geometry as discussed herein that the line integrated density at the edge is proportional to the density measured with the tunnel probe at the LCFS.
The local flux variable is simply defined as the product of the edge line integrated density and the local transport coefficient extracted from the poloidal rake probe data. For the selected set of experiments, the magnetic field was constant ($B_T = 3.8T$), the plasma current was changed on two values $I_p \in [1, 1.4]$MA, and the core line integrated density varies from 3.5 to

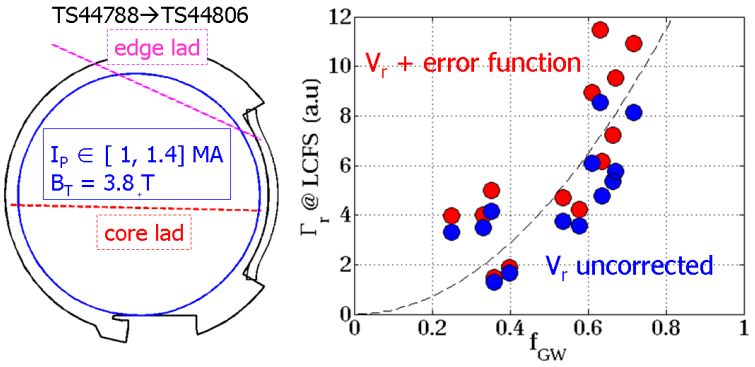

Figure 3.42: *Left : Plasma geometry, where are shown the edge line interferometry used for the LCFS density estimation and a core line used for the Greenwald fraction, Some plasma parameters are shown. Right : Evolution of the local radial flux (in arbitrary units) function of the Greenwald fraction (in blue). The radial transport coefficient can be corrected with respect to the poloidal size of electrostatic eddies (red) but does not show strong variations. The black dashed line shows a parabolic dependency.*

9.210^{19} m^{-2}. Experiments with less than 70% of radiated fractions are selected, since radiative instatilities are known to take place at the edge, interfering in the natural transport processes at the edge. As observed on the figure 3.42, the turbulent radial flux increases non linearly with the Greenwald fraction. Related to the possible error made on the sampling of the electric field, the flux is corrected with respect to the error function discussed earlier, but do not show strong deviation from the uncorrected data. The near parabolic dependency of the flux at the LCFS does not reproduce the linear behavior of the line integrated radial flux shown previously 3.12. On the other hand, this observation is in good agreement with findings from TCV, where the local radial flux was found to increase linearly with the inverse of the plasma current [Garcia 07b].

3.3 Summary

This chapter is devoted to the experiment investigation of the radial particle transport in the scrape-off layer, using probes. First of all, we focused on the instrumental reliability of diagnostics to measure dedicated plasma parameters :

- Mach probe configuration should be considered with care. As we have shown, data collected with the thin collectors of the poloidal rake probe return different parallel Mach numbers compared to the tunnel probe data, that is considered as a reliable diagnostic for plasma flow collection. The reason is a lack of information about the effective collection area of thin collectors.
- The electrostatic field sampled with poloidal arrays has been focused in the scope of radial flux evaluation. We propose an error function based on a virtual diagnostic implemented on simulation output, to estimate the effect of collector separation length on the electrostatic eddy sampling.
- We showed that the simple interpretation of time lags in between fluctuations time traces in term of phase velocity might be wrong. The shape of propagating events has to be imperatively considered in the interpretation of the time shifts.

Then, we paid attention to the steady-state properties of the transport in the SOL. In order to interpret the radial profile of parallel flow in term of radial flux quantities, we checked that the dominant player in the parallel flows is the radial particle flux:

- The ionization source in the SOL has been computed with a Monte Carlo simulation (EREINE) for one typical Tore Supra ohmic discharge: 15% of the parallel flows recyled on the limiter is effectively ionized in the SOL.
- The transversal electrostatic drift flows are estimated from the floating potential and temperature measurements: they contribute for about 10% to the parallel flow.

As a consequence radial profiles of parallel flow can be interpreted in term of line integrated radial flux along field lines. The model is able to resolve a partial poloidal asymmetry of the radial flux : the latter is mainly localized ($\approx 85\%$) on the LFS. Parallel flows measured at the top are understood as return flows balancing the parallel pressure.
Then, we observed that local fluctuations measured at the top are coherent with interchange mechanisms : density and electric field fluctuations are in phase and the related radial transport is strong. In some experimental conditions not yet identified, a sharp reduction of the $E \times B$ transport coefficient is observed within 1 cm outside the LCFS, presumably due to a velocity shear effect.
For standard conditions, line integrated and local transport evaluations match qualitatively, and we infer that a quantitative match needs further informations about the poloidal distribution of the radial flux.
Apart from these considerations, the line averaged radial flux across the LCFS is observed to increase linearly with core density, whereas the local $E \times B$ flux increases non linearly as observed on other machines. We observed that the energy convection mechanism (compared to conduction) becomes the dominant player of kinetic energy losses across the LCFS (radiation apart) when high density is reached.
As a coincidence, the fast visible imaging diagnostic presented in the next chapter is very sensitive to discharges density conditions, and is it well done that high density corresponds to high turbulence regime.

Chapter 4

Fast visible imaging of plasma fluctuations

4.1 Motivations

Visible imaging from neutral emission can be used to measure the spatial / time structure of edge turbulence. Indeed, a neutral atom propagating in a plasma experiences electron collisions and emits visible photons before being ionized. The photon emission rate is a sensitive function of the electron plasma density, temperature, and thus measuring the visible emission from neutrals present in the plasma gives information about the plasma itself. Roughly speaking, the local photon emissivity is proportional to neutral and plasma density: $\epsilon_{ph} \propto n_0 n_e$. For decades passive lines imaging have been used in tokamaks to study either steady-state plasma conditions or turbulence using arrays of optical fibers looking through the plasma with sufficient time resolution.

More recently, thanks to progress made in electronics, 2D imaging is possible with a high spatial and temporal resolution, using novel CCD or CMOS sensors. It is now possible to obtain 2D projection of the plasma visible emission, from which can be deduced the spatial and temporal properties of turbulent structures. Such diagnostics have been intensively used on magnetic confinement devices like Alcator C-mod, NSTX or MAST, where they have provided crucial informations on the dynamics and sizes of density structures at the plasma edge 4.1. The main advantage of 2D imaging stands in the spatial properties of fluctuations carried by the pictures, in comparison of one to two points measurements available with electrostatic probes. For instance, the pictures performed on MAST during L-mode discharges show with clear evidence filaments elongated along the magnetic field lines and moving transversally over large sections of flux surfaces. Similarly, acquisitions done on C-mod [ad S.J Zweben 04] or NSTX [Zweben 02] with a line of sight parallel to the local magnetic field lines show transversally small structures propagating radially and poloidally, but through a narrower opening angle restricted to the outboard midplane. Furthermore, the simultaneous use of Langmuir probes and visible imaging as performed in spherical tokamaks like QUEST [Liu 10], MAST [Dudson 08] or in linear magnetic confinement device [Oldenbürger 09] have led to the conclusion that these luminous filaments correspond to density structures. Therefore a great interest is found in the study of such luminous structures as soon as they do represent plasma events.

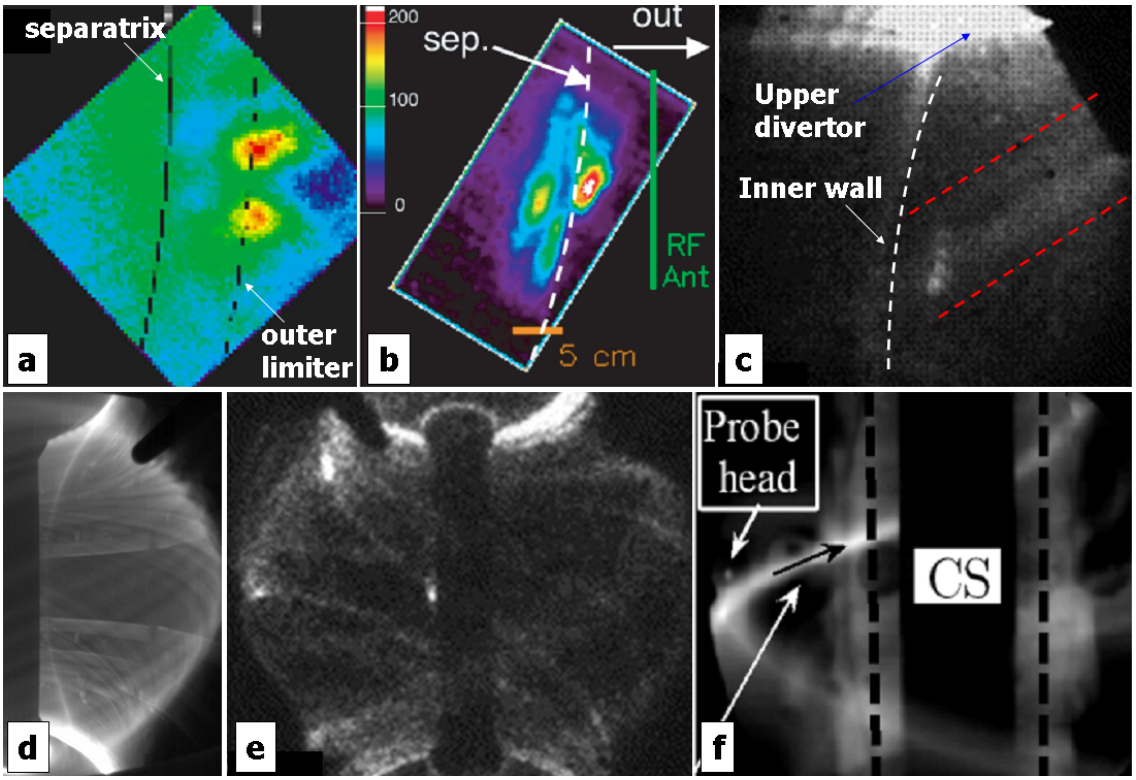

Figure 4.1: *Fast visible imaging of edge plasma fluctuations in various tokamaks. a) Alcator C-mod, L-mode plasma, tangential line of view $\tau_{exp} = 2\mu s$ using D_2 gas puffing. b) NSTX, L-mode plasma, tangential line of view $\tau_{exp} = 10\mu s$ with He gas puffing. c) ASDEX Upgrade. H-mode plasma, tokamak view $\tau_{exp} = 40\mu s$, Probable ELM surrounded by two dashed ref lines. d) MAST, L-mode, tokamak view $\tau_{exp} = 20\mu s$, SOL filaments. e) MAST, H-mode, tokamak view $\tau_{exp} = 10\mu s$, ELM's. f) QUEST , ECRH discharge, chamber view $\tau_{exp} = 20\mu s$, plasma filament aligned with the magnetic field (black arrow).*

The main challenge in the fast imaging stands in the photon emission rate in the selected region of interest. Some devices present the advantage of a high neutral pressure surrounding the whole plasma (MAST, QUEST), leading to a natural high visible radiation rate everywhere in the SOL 4.1. For standard tokamaks, the neutral pressure is mainly localized around the main limiter/ divertor since neutrals do not propagate elsewhere before being ionized. For that reason the fast visible imaging needs an artificial increase of the photon emission in the region of interest by means of neutrals injections, as it is actually done on NSTX or C-mod. The case of ELM imaging is slightly different because an ELM may lead to a strong erosion/recycling on the whole chamber section and thus increase the photon emission everywhere in the chamber, as observed on ASDEX during ELMs [Koch 07].

Besides, the fast imaging is not restricted to turbulence study, but is also intensively used for other plasma topics implying transient phases and visible photon emission. For instance the diagnostic is reliable for disruption study under massive gas injections [Reux 10], dust trajectory tracing in the chamber [Yu 09] or visualizing pellet injections.

Considering all fields of physics accessible with such diagnostic, the decision has been taken to implement one on the Tore Supra tokamak. In the following are presented the diagnostic

characteristics and the experimental conditions necessary to assess turbulence imaging during TS experiments. Finally are presented some specific evidences about the transport phenomena observed with the fast camera.

4.2 Fast visible imaging diagnostic on Tore Supra

4.2.1 Diagnostic design

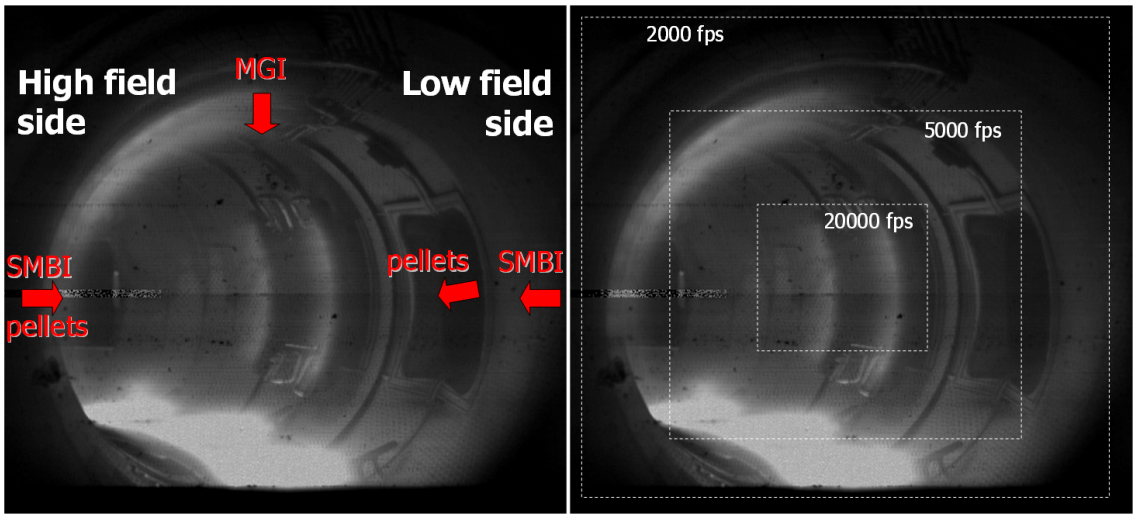

Figure 4.2: *Tangential view of the fast visible camera installed in Tore Supra, through its maximal opening angle. Left : The gas injection systems within the diagnostic view are illustrated : super sonic molecular gas injection (SMBI) in the Low field side and High field side of the torus, massive gas injection (MGI) at the top and pellet injection at the high field side and low field side. Right : While increasing the acquisition frame rate, the number of stored pixels is decreasing, and is centered on the sensor middle for the* Phantom *camera.*

The fast visible imaging diagnostic installed on Tore Supra has been designed in order to assess different topics : pellet fueling, disruption and massive gas injection (SMBI), supersonic molecular gas injection (SMBI) and edge turbulence. Most of these injection systems are installed in a relatively closed toroidal section, that has fixed the location of the visible diagnostic on the machine to be able to picture all phenomena 4.3. The optical system has been designed to look tangentially into the toroidal vessel from the outboard midplane4.2 4.3, with a wide opening angle (44^o) in order to picture both high and low field sides. A retractable periscope consisting of a prism and optical lenses collects the visible light from the vessel and transmits it to a bundle of optical fibers. The bundle extremity is directly pictured by the camera through an objective. The first necessity for a flexible optical bundle stands in the fact that the camera position is fixed and the periscope must be retracted during high power discharges in order to avoid damaging heat loads on its extremity. Secondly, the bundle extremity is mounted on a movable rack in front of the camera objective, in order to displace the vessel view transversally with respect to the camera sensor 4.3. The bundle offers the suitable flexibility, but on the other hand is responsible for a relatively low optical transmission factor and imposes probable optical aberrations.

The price to pay for the wide opening angle is a modest geometrical resolution projected onto the camera sensor, from 1 to 5 mm per pixel, depending on the location along the line of sight, but still good enough to picture turbulence related phenomena. In addition, the focus is done approximately in the middle of the line path into the chamber, thus relatively in front of all gas injection system. The diagnostic was preliminary designed with a *Phantom V7.1* camera, that allows acquisition rates up to 300 kHz with exposure time down to 2 μs, external triggering and a large internal memory. The C-MOS sensor is limited in the data reading rate, that fixes the maximum number of pixels readable per unit of time. For instance, a relatively low frame rate (1 kHz) allows an acquisition over the full sensor (800x600), but a frame rate of 100 kHz limits the acquisition over an effective sensor area of about 80*60 pixels. Moreover the hardware design of the camera implies the effective sensor area to be centered on the sensor centre, although its aspect ratio (vertical/horizontal) can be varied. This is the main reason why the bundle is mounted on a translating rack, in order to translate any vessel location onto the sensor centre when high frame rate is needed.

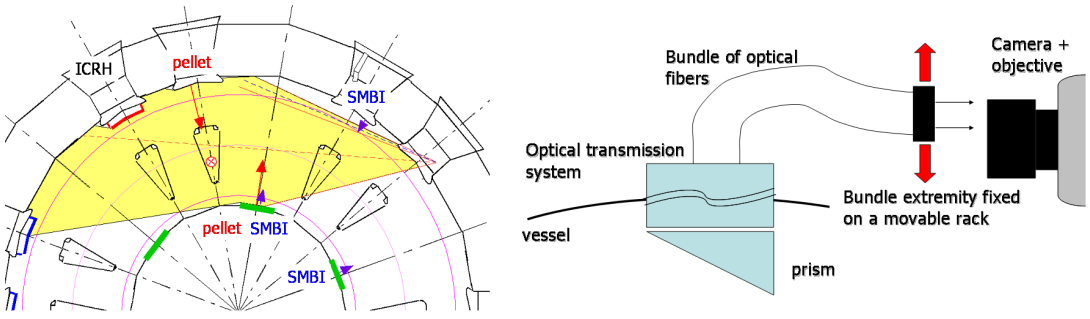

Figure 4.3: *Left : Top view of the torus, showing the maximum opening angle of the visible imaging diagnostic, and the gas injection systems. Right : Illustration of the optical path from the vessel to the camera. In order to increase the frame rate by reducing the effective poloidal opening on the camera sensor, the visible rays can be shifted with respect to the sensor in order to maintain the region of interest on the centre of the sensor*

The main visible emission in a tokamak is due to Deuterium excitation (Balmer line) or from Carbon, namely in a range of 600nm. Hopefully, the quantum efficiency of the camera sensor is maximum in that wavelength range. Besides, all the optical system is composed of glass lenses, meaning that UV emissions are not transmitted to the camera sensor. Thus the full system is sensitive to the visible emission only. For dedicated purposes, a filter can be installed in front of the camera to observe only the emission from a given plasma species (Helium, Argon). But in our research of high speed imaging conditions, filtering the image is not required to optimize the captured photon rate. In the following, the movies and pictures are obtained without specific filters, and the collected data are expressed as a number of counts per pixels.

4.2.2 Visible emission and turbulence

4.2.2.1 Diagnostic sensitivity

Previous observations performed with probes in the SOL of Tore supra suggest that the turbulent transport is dominated by fluctuations of the order of 10% to 50% corresponding to the convection of density structures, having a size transversal to the field lines in the order of one centimeter. These structures propagate locally with transversal velocities of the order of 500m.s^{-1}. We except the visible diagnostic to resolve these temporal and spatial scales with a sufficient sensitivity, and therefore we have to make a compromise: the camera sensor converts the photon fluency into digits from 0 to 255 with a typical thermal noise of 1 to 2 digits, such that the absolute signal amplitude should be greater than 10 digits to resolve fluctuations of the order of 10 to 50 %. First it implies a minimum exposure time to capture a sufficient number of photons, that depends anyhow on the experimental scenario. On the other hand a long exposure time implies a smearing of the propagating structures, that can easily exceed the turbulence scale length and thus reduce the effective diagnostic sensitivity. For instance, typical turbulence characteristics exposed above imply that 20μs of exposure time would smear the structures over about 1cm.
This compromise between number of photons and frame rate is critical for the diagnostic reliability of observing turbulence. And in fact the experimental scenario is of crucial importance : the local photon emission is proportional to the local plasma density and local neutral density. Since natural neutrals are mainly originated from recycling (Deuterium) or sputtering (Carbon), the local emission is roughly a quadratic function of the local plasma density - see figure 4.4. If we want for instance visualize the turbulence within the visible emission cloud above the main bottom limiter, we would require the highest plasma density with an exposure time greater than 10μs.
For a given experiment, the optimal compromise is not straightforward since the visible radi-

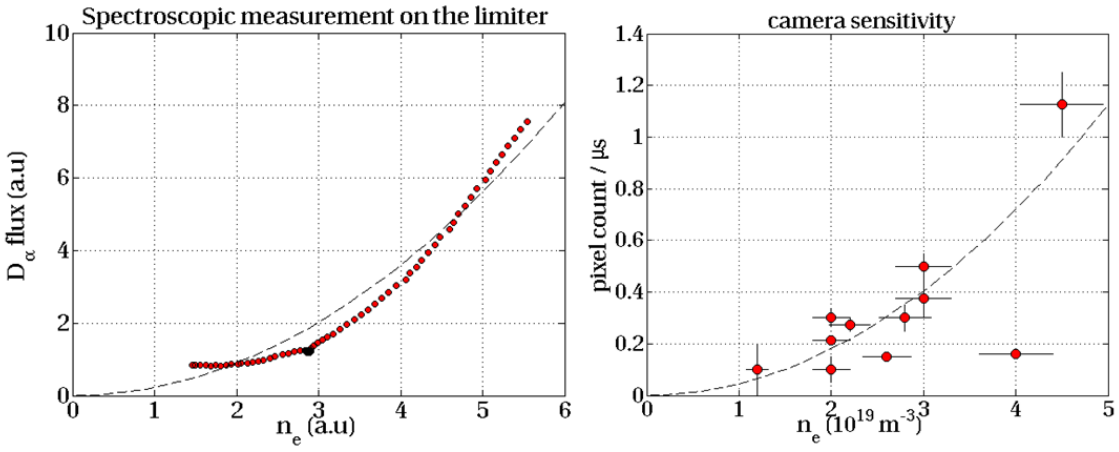

Figure 4.4: *Visible emission measured on the surface of the bottom limiter function of the plasma density (line averaged value). Left : Spectroscopic measurement of D_α emission during a density scan. The dashed line shows a quadratic dependence. Right : Visible amplitude measured from the visible camera on the bottom limiter, for a variety of plasma conditions. The amplitude unit is defined as a number of digits per unit time.*

ation rate is not completely a predictable function of the scenario. Therefore our experimental procedure was to start with a relatively high exposure time, and decrease it until the diagnostic reaches its sensitivity according to the observed turbulent pattern.

4.2.2.2 Neutrals and plasma turbulence

When visualizing a fast visible imaging picture, the easy interpretation is always done that light structures correspond to plasma structures. Hence we assume that neutrals form a more or less uniform background across which plasma structures propagate and increase locally the photon emission rate of neutrals.
A first issue concerns the origin and location of these neutrals. As presented in the next section, neutrals are not naturally present in a sufficient amount to visualize the plasma fluctuations everywhere. But the flexibility of Tore Supra scenarios is a great advantage and we were able by playing with the limiter configurations and the gas injections to obtain a global picture of the turbulence pattern all around the plasma section.

Secondly, a specific property of the interaction between neutrals and plasma turbulence has to be considered : we assume that the turbulent patterns are highlighted by a background neutral cloud. In other worlds we consider that plasma structures and neutrals propagate in the medium such that neutrals emit photons within a plasma structure that reveal its whole shape. Therefore we implicitly neglect the possibility that neutrals can be ionized before they travel trough the over-dense object, that would cause the light emission pattern to differ from the whole object shape.
A first argument is that neutral mean free path is of the order of a few centimeters in the SOL of Tore Supra such that it exceeds the typical turbulence scale length. More advances considerations have been done by the use of a Monte Carlo simulation of neutrals emission within a turbulent plasma background [Stotler 03] in plasma conditions referred to Alcator C-mod scenarios. In particular, it was shown that even in a turbulent plasma (with density and temperature fluctuating) the light emission was reflecting the plasma fluctuations only, although the light pattern was not perfectly equal to the density pattern, due to the smooth non uniformity of the neutral cloud (radial profile).
In the following, we thus assume that the turbulent pattern observed on the visible pictures correspond to the plasma pattern only, keeping in mind that neutrals are anyhow localized in a relatively confined plasma volume where they can survive : we can only picture the plasma turbulence where neutrals can penetrate, thus at the plasma edge.

4.2.3 Line of sight reconstruction and geometrical issues

Fast imaging is a remarkable tool that offers directly to eyes rich pictures of visible phenomena. But beyond the scope of qualitative understandings, the dimensionality of the data offers a large panel of analysis possibilities on the pictures in order to quantify locations, speeds or sizes of observed phenomena. To achieve that goal, a precise calibration of the diagnostic

is needed in term of spatial location of objects in the field of view of the diagnostic. A first and straightforward method would aim at considering the optical properties of every optical components of the diagnostic and compile a ray tracing algorithm from the vessel to the camera sensor, taking into account optical aberrations. Unfortunately the optical path is relatively complex (involving more than 30 components) and it has been decided within the diagnostic user team to rather simplify the reconstruction using a simple equivalent optical system describing the light transmission from the vessel to the sensor.
The first purpose aims at placing on a picture flux surfaces or field lines as seen by the camera, but without taking into account aberrations and blurring. The equivalent optical system is simply a diaphragm of zeros opening, projecting the light on a 2D sensor plate. The parameters to adjust are the diaphragm location and orientation at the low field side and the focal length between the latter and the sensor. In order to determine the optimum parameters a set of objects have been selected on the diagnostic picture of the vessel (limiter corners, pipes, tiles), their exact positions having been obtained from a *computer-aided-geometrical-design* (CAGD) of the torus. Then these *checkpoints* have been projected onto the equivalent optical system and the parameters have been adjusted to match as close as possible their exact location on the camera sensor 4.5. Due to aberrations and the simplicity of the equivalent optical system,

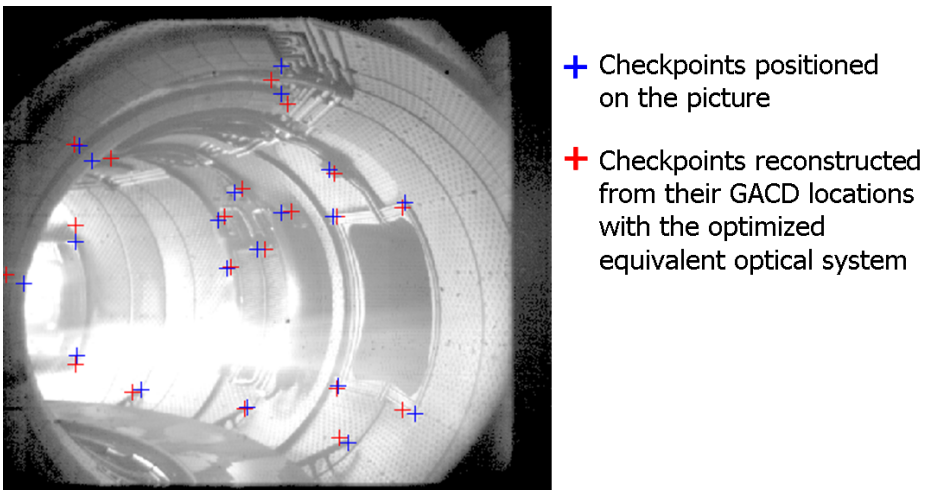

Figure 4.5: *About 20 recognizable objects have been selected on the diagnostic view of the vessel. The exact position of these objects has been obtained from CAGD. The equivalent optical system is optimized to coincide the reconstructed objects with their real position on the picture.*

it was not possible to perfectly match all checkpoints and the optimal parameters are obtained with an error between the real and reconstructed checkpoints of about 7 pixels (rms over the full set) [1]. Converted into real distance in the vessel, the error is in the order of 1 cm, and is considered acceptable with respect to the plasma size and the uncertainties about the magnetic field reconstruction.
The equivalent optical system being optimized, it is now possible to reconstruct the view of the diagnostic 4.6. For instance, the first wall can be drawn, as well as the main bottom limiter,

[1] Optimisation and checkpoints performed by C. Reux

and field lines can be placed as well. This simple exercise highlights a particularly crucial issue for turbulence imaging : following the insight of observing elongated filaments along magnetic field lines, their capture by the diagnostic implies complex shapes on the picture resulting from the 2D projection 4.6. The issue does not stand in the understanding of the pictures, but rather in the analysis we could perform on it, like velocity field extraction. Mainly, artifacts due to the overlap of projected structures infer some limits of velocity analysis that we could perform on raw data. On the other hand the tangential view has been adopted for a simple

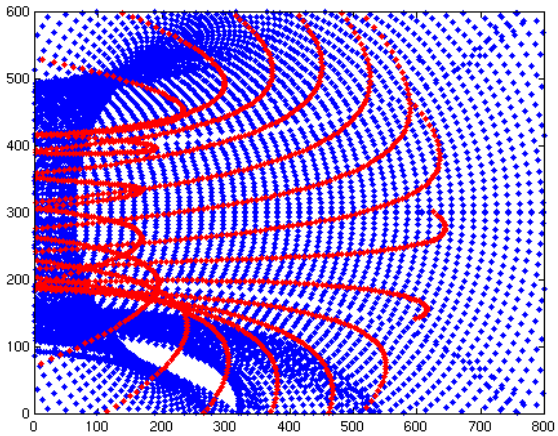

***Figure 4.6**: Reconstruction of the Tore Supra first wall (blue) with the equivalent optical system. A set of field lines lying on a flux surface (r/a <1) is shown in red*

reason : if we consider a line of sight along which the photons are collected by one pixel of the camera, the main contribution comes from the light emitted within the flux surface that is tangential to the line of sight 4.7. Although the parallel integration along the line of sight over different flux surfaces is not negligible, the following approach is considered : on the raw movies, quantitative analysis are not possible everywhere. Instead, the spatial locations where the field lines are mostly parallel to the line of sights are selected, considering that the collected light is mainly coming from that field lines.

We rapidly came to the conclusion that a rigorous movie analysis would need of a tomographic

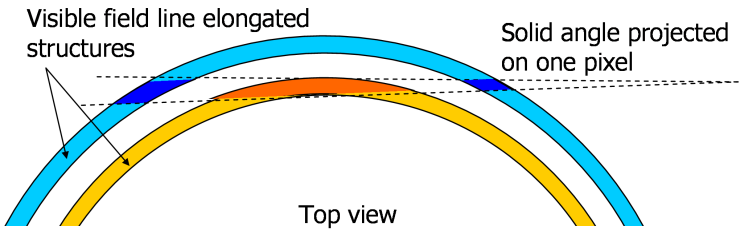

***Figure 4.7**: Illustration of the smearing effect due to the parallel integration along the line of sight. On the other hand the photons emitted within the flux surface tangential to the line of sight provide the main contribution of the collected light.*

reconstruction of the emission pattern. This reconstruction is based on the assumption that plasma fluctuations and thus visible patterns are roughly uniform along field-lines, such that it is possible to deconvolve the real 2D emission pattern from its 2D projection on the diagnos-

tic sensor. The project has been initiated in terms of a collaboration with two laboratories (LMD Paris and LPMIA Nancy) [2]. Although promising results have been obtained on artificial movies built with an exact magnetic geometry projection on the equivalent optical system, an application to real data faces critical issues: the precision of the magnetic reconstruction on the diagnostic sensor is equivalent to the scale length of turbulent patterns.
Since a tomographic reconstruction is highly sensitive to the geometry of the lines of sight and would therefore need a strong investment to obtain an appreciable result, we personally decided not to focus on the tomography. Instead, we tried to complete our global appreciation about the different turbulent patterns observed all around the plasma section. For that reason we decided to present the observations as a linear panel : The different scenarios are successively reviewed, each of them giving particular informations about edge turbulence. A global confrontation is proposed at the end of the chapter.

4.2.4 Overview of different scenarios

Observing the plasma turbulence signature on the visible light necessarily requires a sufficient neutral concentration in the region of interest. As mentioned in a previous section, the main source of D neutrals in standard plasma conditions in the recycling on the main limiter, located at the plasma bottom 4.8. *Monte Carlo* simulations of the recycling process confirm the observations : D neutrals recycled from the limiter surface are mainly ionized close to the surface and do not participate to visible photon emission elsewhere. Carbon emission is also significant above the carbon limiter : C neutrals are sputtered from the surface and emit visible photons before being ionized. This process takes place relatively close to the limiter surface.
Thus as a first and passive approach, the fluctuations within the recycling cloud can be investigated. Results are presented in the next part 4.3. Considering recycling as a local source of neutrals, limiters at the outboard midplane can be of interest. Especially during high density experiments when ICRH heating is used, the antenna in the field of view of the camera 4.8 is placed close to the LCFS. Its lateral protections suffers a relatively high plasma load resulting in a non negligible recycling and thereby photon emission within the surrounding plasma. But as it will be shown later on 4.3, the turbulence related conclusions are relatively modest. Therefore, the plasma can also be limited on inboard 4.3.3 or outboard 4.3.2 limiters in order to localize the main recycling on these locations .
Keeping in mind the passive approach for turbulence imaging, a last but not least experimental condition has been investigated, namely the “fully detached plasma”. As seen by the camera, the detached conditions consist on a relocation of the visible emission from the main limiter to the confined region, resulting in a poloidally homogeneous emissive ring at a radius $r/a < 0.7$ 4.9. Experimentally, the detachment is obtained by increasing the gas puffing at the edge until the radiated power is close to the heating power (100% of radiated power) [Lipschultz 98]. A first transition occurs as a MARFE instability and develops toward a steady-state radiating phenomenon, with a feed-back control of gas puffing on the radiated fraction. Due to the high radiated fraction (100%), the visible light emission is worth to be pictured by the fast visible

[2] R. Nguyen, M. Farge, G. Bonhomme, F. Brochard

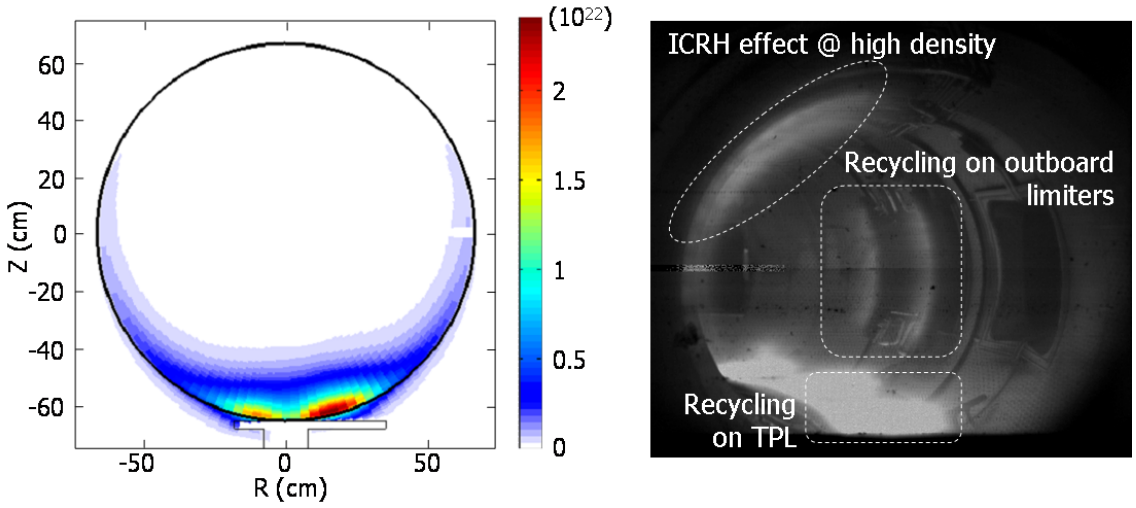

Figure 4.8: *Left : EIRENE simulation of the ionisation source of Deuterium atoms recycled on the main bottom limiter (TPL). The visible emission is localized within the ionisation cloud and thus is confined close to the limiter surface. Right : Picture of a steady-state discharge phase at high density and ICRH heating. The mains source of visible light is above the main limiter (TPL), but recycling is also observed on the bumpers of an ICRH antenna on the low field side. Some light is coming from the upper part of the high field side plasma section, that is attributed to an ICRH heating effect on the SOL plasma.*

imaging to resolve turbulence phenomena on the visible ring 4.4. In order to picture the plasma

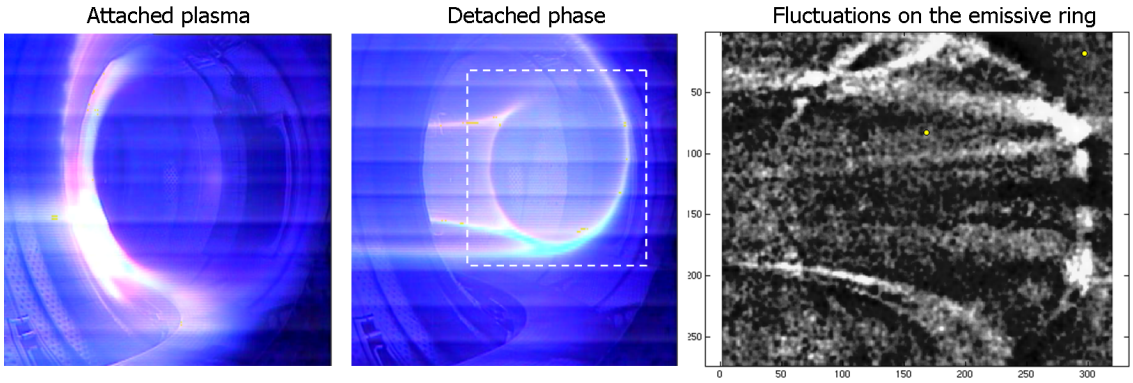

Figure 4.9: *Left : Picture (20 ms exposure time) of a ohmically heated plasma, high field side contact point. Middle : Picture taken during the same discharge, fully detached plasma (20 ms exposure time) during steady-state conditions. The visible emission has left the main limiter to form an homogeneous emissive ring in the closed field line region. Right : picture of the visible ring with the fast visible imaging diagnostic (20 μs exposure time). The time average frame has been subtracted to highlight the fluctuating pattern.*

fluctuations where natural recycling does not occur, active imaging has to be performed, that is by use of external gas puffing in the field of view of the camera. On Tore Supra, a number of gas nozzles are installed on the wall, but on the field of view of the camera. Instead, two supersonic molecular beam injectors are running on the high field side and low field side midplanes of the camera field of view, offering the unique conditions to picture the plasma turbulence at both locations. On the other hand, SMBIs consist of strong gas injections normally used

to fuel rapidly the confined plasma, and for that reason are beyond the concept of tracers for turbulence imaging. Anyhow, the neutral concentration is high and gives reliable conditions for visualizing the turbulence pattern with a high frame rate 4.10. The next part is devoted to

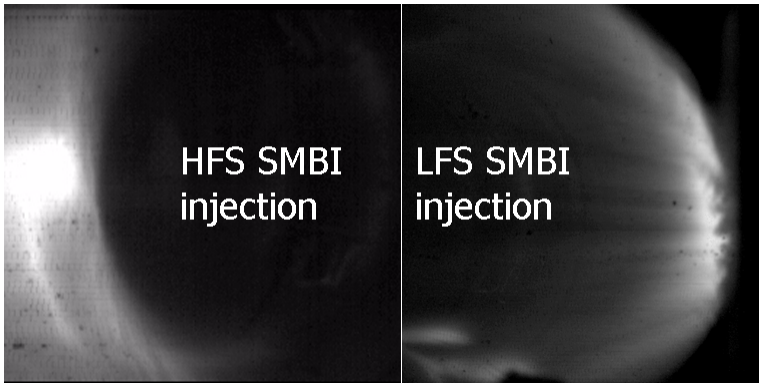

***Figure 4.10**: Steady-state ohmically heated plasma on which is performed SMBIs. Left : Picture (20 μs exposure time) of a high field side injection. Right : picture (20 μs exposure time) of a low field side injection. Filament-like structures are highlighted within the neutral cloud*

the analysis performed on the movies, simply assuming that light emission reflects the plasma fluctuation. That is, an essential aspect has not been yet considered : What is the typical scale of neutrals mean free path compared to the turbulent structure sizes ?

4.3 Natural recycling on plasma facing components

4.3.1 Recycling on the bottom limiter

Let us start the fluctuations visible observation by the most natural way : by looking at the natural recycling emission on the main bottom limiter. The usual process to highlight possible fluctuations on a movie obtained during steady-state conditions is to subtract to the movie the time averaged frame to keep only time fluctuating patterns. We put a lot of effort in defining the optimal exposure time to assess the fluctuations within the visible cloud formed at the main limiter surface, and the conclusion is that high density scenarios are needed to visualize fluctuation pattern on the limiter 4.11. For low density, the visible emission is too low, so that probable fluctuations are effectively shadowed by the thermal noise of the diagnostic. By increasing the plasma density to values close to the ohmic density limit (at which radiative instability occurs), the diagnostic is finally able to resolve fluctuations patterns on the bottom limiter 4.11. The optimal exposure time is about 20 μs, as a compromise between signal amplitude and fluctuation smearing. Unfortunately, the diagnostic was always run in a large opening angle for that particular experiments dedicated to density limit, so that the frame rate is too low (1 kHz) to access the temporal dynamics of the fluctuations. As a first result, we observe field aligned structures at the bottom of the plasma, as suggested by a field line reconstruction. A good correlation is found in between the ripple pattern suggesting a relatively low parallel number. The transversal size of the visible structures is of the order of a few centimeters, and the smearing due to structure propagation (velocity v) can be taken into

account to deconvolve the true size: $d_{eff} = d_0 + v\tau_{exp}$. Unfortunately, the velocity is unknown, but at least it can be taken as the ordering given by the probe measurement : $v \approx 500$ m.s^{-1}, leading to $d_0 = d_{eff} - 1$cm, that stays in the order of a few centimeters.
The pictures offer an other important spatial information about these plasma structures, thanks to the limiter geometry of Tore Supra: Despite the fact that the view does not allow a true reconstruction of the structures location, the visible cloud due to the recycling is localized where the plasma touches the limiter (toroidally periodic pattern due to the ripple), and for that simple reason the cloud must be localized above the point where the LCFS is defined on the limiter. Since these structures are observed above the whole surface of the limiter within the visible cloud, they are - at least partially - localized in the confined region. The velocity extraction would have help to confirm that conclusion, since it is well documented that a transversal velocity shear layer exist just inside the last closed flux surface, separating the confined region where the transversal velocity is in the electron diamagnetic direction to the plasma boundary that is rotating in the ion diamagnetic direction.
Although the amount of quantitative informations is quite reduced from this experiments, it is clear that at least at high density, filament like structures exist at the plasma bottom, near the LCFS. More informations are missing to conclude on the location of the filaments but we can think that at least at high density, a fraction of these structures live just inside the LCFS.

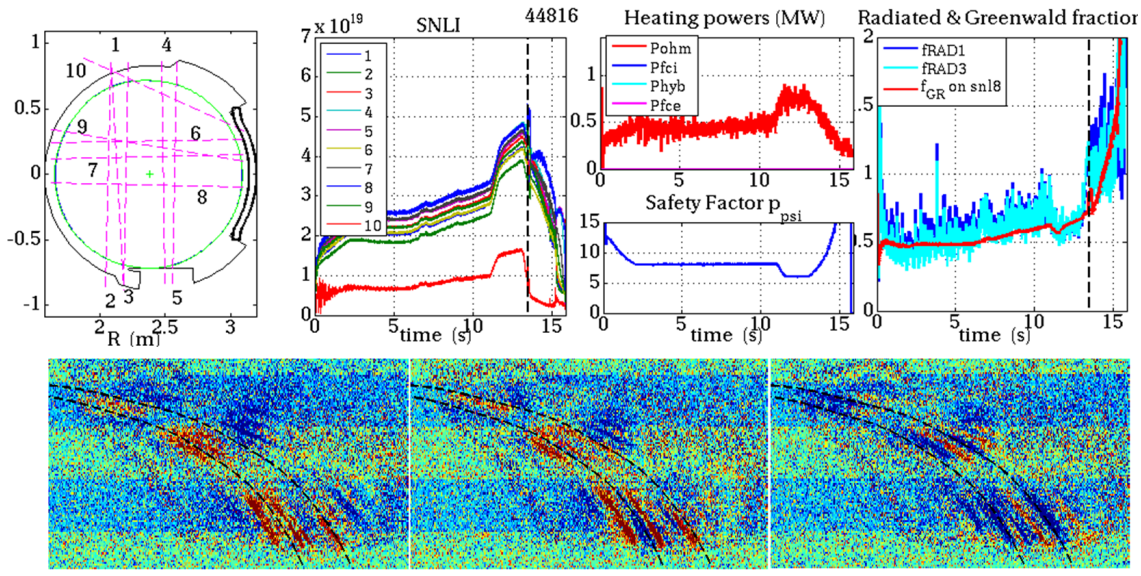

Figure 4.11: *TS44816 high density ohmically heated plasma. Top : Panel of discharge parameters. On the graph showing the line integrated density time traces is also shown the time when the fast visible imaging is triggered (at high density). As seen on the right, the movie is taken just before 100% of radiated fraction (detachement) is achieved. Bottom Left : Fast visible imaging, 20 µs exposure time and 1000 fps (wide angle on raw frames). The time average frame is subtracted and a zoom is done on the main bottom limiter. Field aligned structures are seen with the recycling cloud (dashed lines show some reconstructed field lines). Three pictures are selected along the movie. The horizontal stripes corresponds to enhanced noise area on the sensor.*

4.3.2 Recycling on outboard limiters

The diagnostic offers the possibility to picture the light emission from the outboard antenna limiter located in the line of sight. Again, some specific experimental conditions are needed to visualize the fluctuations in that region: the limiters have to be close to the LCFS to suffer high recycling, and high plasma density is needed. That is, two distinct experiments have been selected : A high density ICRH discharge in a bottom limited configuration, during which the outboard antenna is close to the plasma (1-2 cm) in order to obtain reliable power coupling conditions. The second experiment consists on a ohmic discharge limited only with outboard limiters, then subject to high recycling. The ICRH heating offers reliable conditions to assess very high density experiment (more than 150% of the density limit in ohmic conditions), and thus to make use of the passive imaging on limiters. The obtained turbulence pattern is unambigous, as seen on the figure 4.12. Besides the clear filament pattern on the bottom limiter, the outboard antenna shows the footprint of poloidal modes, with a good toroidal correlation between the two limiters. A magnetic reconstruction show that the correlation is aligned with the magnetic field and infers parallel filaments are involved. Again, the wide opening angle is fruitful for observing both bottom and outboard limiters but the temporal information is missing to extract a velocity. One could however argue that patterns observed on the ICRH bumpers are not due to plasma turbulence but rather to ICRH heating and non linear coupling with SOL plasma. But on the other hand the observed pattern is fluctuating in time whereas the ICRH power is constant.

To avoid any ambiguity, let us pay attention to ohmic plasma limited on the outboard midplane 4.13. For that experiment, the opening angle was reduced to picture only the antenna, so that the frame rate is up to 20 kHz. A compromise was found between the signal amplitude and the exposure time in order to resolve the fluctuations velocity. However, the plasma density remains a key parameter in that observation, as illustrated on figure 4.13. As for the ICRH discharge, poloidal modulations are observed on the two outboard limiters of the antenna, showing a good correlation along field lines. For low density experiments, these patterns are not observed above the diagnostic noise level.

For experiments run at moderate density (TS45331) the fluctuations are clearly observed to propagate in the poloidal direction, and it is possible to extract the velocity from a simple cross-correlation process 4.14 along the poloidal direction of the limiter. The higher density case (TS45313) could have been a more relevant dataset since fluctuations are largely exceeding the noise level, unfortunately the frame rate (20kHz) is at the sampling limit compared to fluctuations velocity. Therefore, data processing from the moderate density case are explained (TS45331), and he high density case is briefly discussed latter. A spatial mesh is defined along the poloidal direction of the limiter surface with a spatial step of about 1cm (1 sensor pixel along the poloidal direction) and time traces are extracted over 1024 consecutive frames. Cross correlations are performed between consecutive points on the mesh, and velocity is deduced as the geometrical distance between the two points divided by the cross correlation time shift. As a first result, a poloidal mapping of the velocity is obtained, as shown on figure 4.14. When the maximum of cross-correlation amplitude is below 0.4, the evaluated velocity is considered

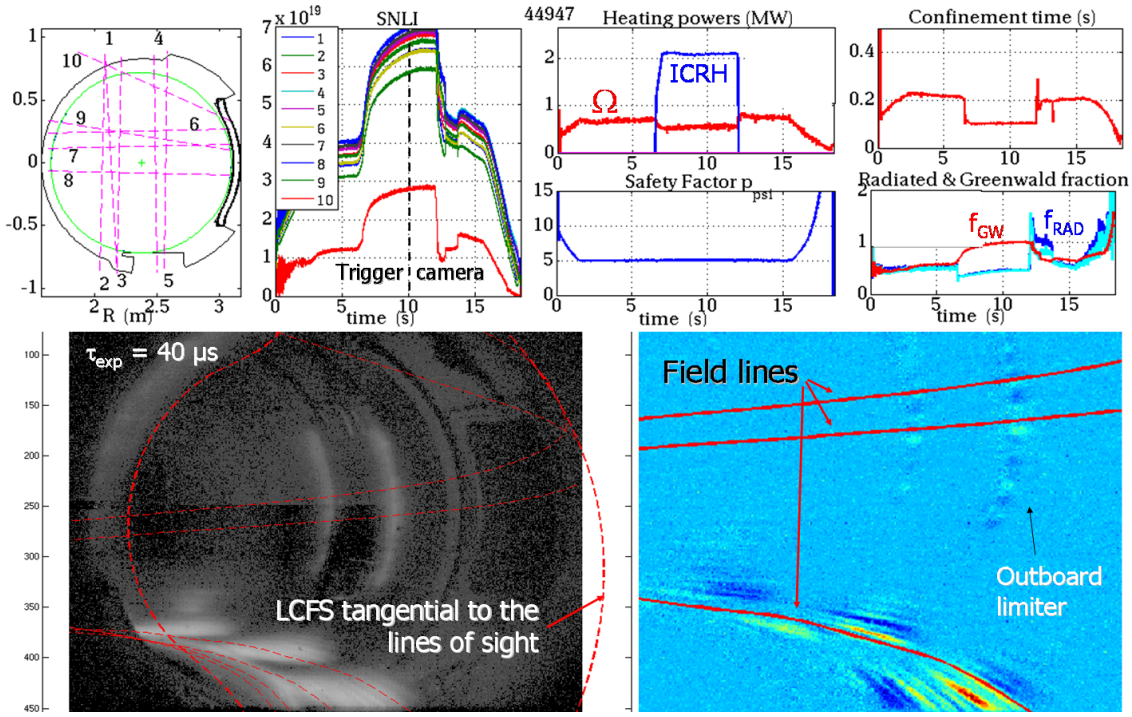

Figure 4.12: *TS44947 with FCI heating. Top : Panel of discharge parameters. On the graph showing the line integrated density time traces is also shown the time when the fast visible imaging is triggered (at steady-state high density). Bottom Left : snapshot obtained with the fast imaging (40 µs exposure time). Due to the large opening angle, the frame rate is relatively low (4700 fps). The Last closed flux surface is represented at locations where the surface is tangential to the line of sights. Some field lines lying on the LCFS are shown. On the main bottom limiter and the outboard antenna, we can notice some spatial pattern, that can be revealed by subtracting the time averaged frame. Bottom Right : fluctuation revealed frame. On the main limiter, field line elongated structures are noticeable, as well as on the outboard limiter where good spatial correlation is found between the two antenna limiter (the field lines guide the eye).*

as non relevant (in that region, the velocity does not follow any spatial trend). We find that the velocity is negative, and vary from about -1000m.s^{-1} at the top of the limiter to about -500m.s^{-1} 10 cm above the midplane.

Beyond the uncertainties related to the correlation process on noisy signals, the consistency of the velocity extraction process is defined by the reproducibility and the spatial trend along the poloidal limiter. If we think about propagating plasma filaments elongated along magnetic field lines, there is no reason why their velocity should change by a factor of two from the midplane to 30^o above, otherwise they would not stay magnetically aligned.

The apparent contradiction might be solved by considering the radial location of the visible emission, that might vary along the poloidal limiter. First of all, we can not estimate this position directly from the movie. But, the extracted velocity can be compared to Doppler backscattering measurements performed at the midplane, at an other toroidal location. This diagnostic is able to evaluate (by Doppler shift) the transversal phase velocity of fluctuations at a given transversal mode number, in the SOL and in the confined region 4.15. The velocity evaluated on the movie is a poloidal projection of the fluctuations propagation, but the differ-

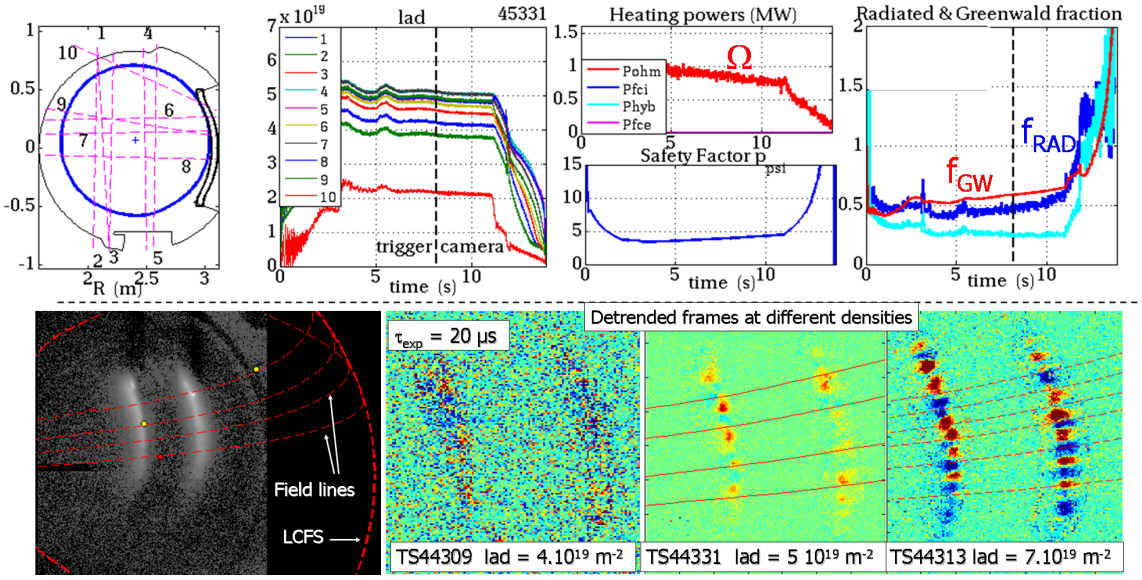

Figure 4.13: *TS45331 low field side contact point. Top : Panel of discharge parameters. On the graph showing the line integrated density time traces is also shown the time when the fast visible imaging is triggered (at steady-state density). Bottom Left : snapshot of the antenna outboard limiters obtained with the fast imaging (20 µs exposure time). The frame rate is 20000 fps. The Last closed flux surface is represented at locations where the surface is tangential to the line of sights. Some field lines lying on the LCFS are shown as well. Bottom middle to right : Spatial pattern of the fluctuations obtained by subtracting the time averaged frame, for three density conditions. for low density (lad = $4.10^{19} m.s^{-2}$ the fluctuations amplitude is below or equal to the noise level. for moderate and high density, the fluctuations pattern appears, showing a relatively good correlation parallel to the field lines.*

ence is about a few percents for the magnetic geometry of Tore Supra.
As usually observed in SOL plasmas, the fluctuations rotate in the ion diamagnetic direction (negative poloidal velocity), whereas they rotate in the electron diamagnetic direction in the confined plasma. The transition is abrupt and defines a transversal velocity shear layer just inside the LCFS. Therefore, fluctuations observed by the camera have to lie in the SOL in order to be consistent with the Doppler backscattering. Noticing the radial decrease (in absolute amplitude) of the velocity in the SOL, the poloidal variation of the velocity measured by the camera could be linked to a variation of the radial position of the emission cloud along the poloidal direction of the limiter. Indeed, the plasma is in contact with the upper part of the limiter 4.15 and if we consider - as a proof of principle - that the visible emission comes directly from the limiter surface, a radial profile of the velocity can be build from the poloidal mapping on the limiter. As observed on the figure 4.15, the velocity measured on the camera movie is in quantitative good agreement with the Doppler measurements, but a radial shift of about 13 mm is noticeable. Despite the good matching, some precautions have to be considered :

- The ad-hoc assumption is made that visible emission comes from the limiter surface.
- The limiter position is mechanically measured with an uncertainty of about $\pm 5mm$.
- The LCFS position is magnetically measured with an uncertainty particularly related to

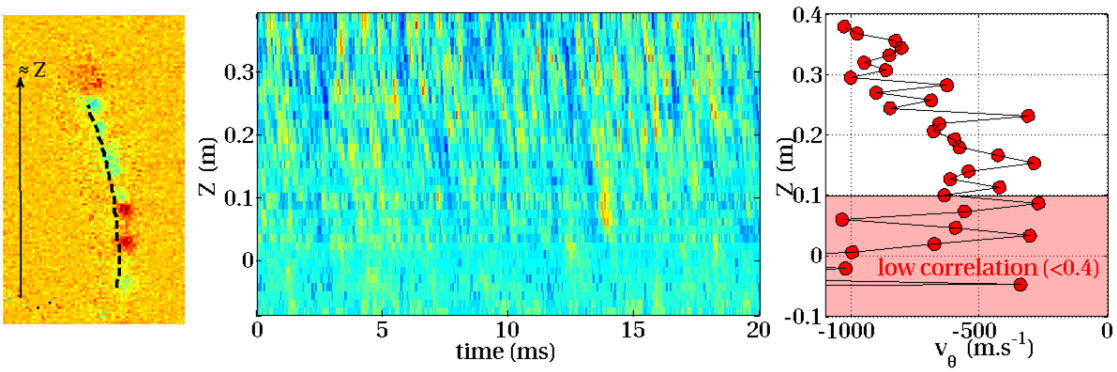

Figure 4.14: *TS45331 8s. Left : poloidal mesh defined on the outboard limiter. Middle : time traces are extracted from the movies and plotted versus time for all spatial positions (signal amplitude in color scale). Propagating events corresponds to titled structures. Right : vertical profile of the poloidal velocity evaluated from a cross correlation method. Low correlation amplitude means below 0.4.*

the limiter position, thus at least in the range of $\pm 5mm$.

- The magnetic reconstruction on the camera view is uncertain, with errors of the order of 1cm.
- The Doppler back scattering measurements are calibrated in absolute position from a density profile, generally measured either by interferometry or by a sweeping reflectometry for the SOL. The SOL density profiles from reflectometry are often inconsistent with probe measurements, that might define some relatively high error bars for the position of Doppler measurements in the SOL.
- Doppler velocities are measured for one particular transversal mode number, that is $k = 6\text{cm}^{-1}$ for that particular experiment, whereas the poloidal wave number evaluated on the visible imaging movie is about $k = 0.73\text{cm}^{-1}$. On the other hand Doppler measurements done at different wave numbers give roughly the same transversal velocity, although such low wave number is not accessible.

. Thus a variety of issues limit the quantitative comparison of both diagnostics. But the relative good matching between the two velocity field suggest that effectively, the observed structures propagate in the SOL with an ion diamagnetic velocity just in front of the limiter surface.

4.3.3 Recycling on inboard limiters

Finally, the recycling on inboard limiters can be observed with the fast imaging, when the plasma is limited on the high field side 4.16. As for the outboard midplane experiments, the plasma density is a crucial parameter for the visualisation of fluctuations. Unfortunately, a few experiments with that magnetic configuration have been run when the fast visible imaging was ready with optimized acquisition parameters, and only some discharges have the right emission property to picture the fluctuations. As seen on the figure 4.16, the plasma of interest is only limited by the high field side inboard limiter and the recycling cloud is elongated poloidally

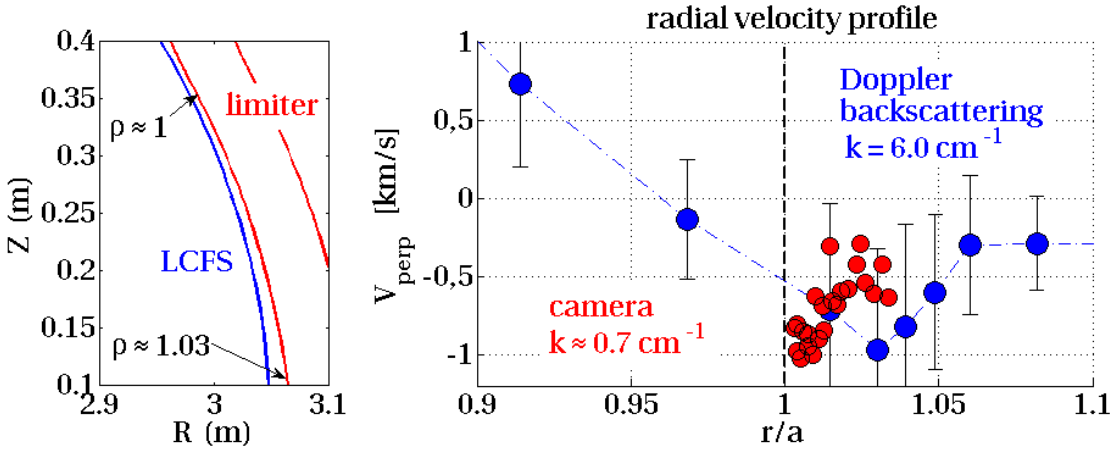

Figure 4.15: *TS45331 8.5s. Left : poloidal cross section of the magnetic equilibrium in contact with the outboard limiter. The position labeled as a minor radius along the limiter depends on the poloidal location since the curvature radius of the LCFS and the limiter are different. Right : Radial profile of the transversal velocity of fluctuations measured by the Doppler backscattering. The radial profile of the camera measurement is shown as well, by assuming that fluctuations come from the limiter surface.*

due to the relative proximity of the LCFS with the wall. When fluctuations are extracted from the fast movie (21000 fps and 40mus exposure time) , elongated structures can be observed on the bottom part of the recycling cloud, but not on the top. The magnetic reconstruction on the fluctuating movie in not possible due to the lack of information about the line of sight of the camera with respect to the torus geometry. Therefore we can not conclude on the location of these filaments, and their velocity is neither evaluable due to under sampling with respect to their dynamics. But interestingly, these filaments are not seen at the inboard midplane and seems to stop somewhere between the bottom and the midplane, that could be an argument to define their location in the SOL.

Compared to other machine experiments, the statement that filaments can exist in the high field side SOL is ambiguous. Probe measurements performed on the inboard midplane of Alcator C-mod suggest that fluctuation amplitude is strongly reduced compared to outboard midplane measurements and that no coherent events are found in the time traces [Smick 10]. As it will be shown in the next parts, other imaging experiments done on Tore Supra indirectly confirm these observations.

4.4 Fast imaging on detached plasmas

When the density is slightly increased from the conditions discussed above a radiative instability is triggered, corresponding to a partial detachment of the visible radiation from the main limiter to the high field side. The MARFE [3] is a toroidally uniform cloud of high neutral density, localized poloidally and radially 4.17. The relatively high associated visible emission gives reliable conditions for fast imaging, and more particularly because the cloud is slowly evolving compared to the turbulence time scale. Observations are the following :

[3] Multifaceted Asymmetric Radiation From the Edge

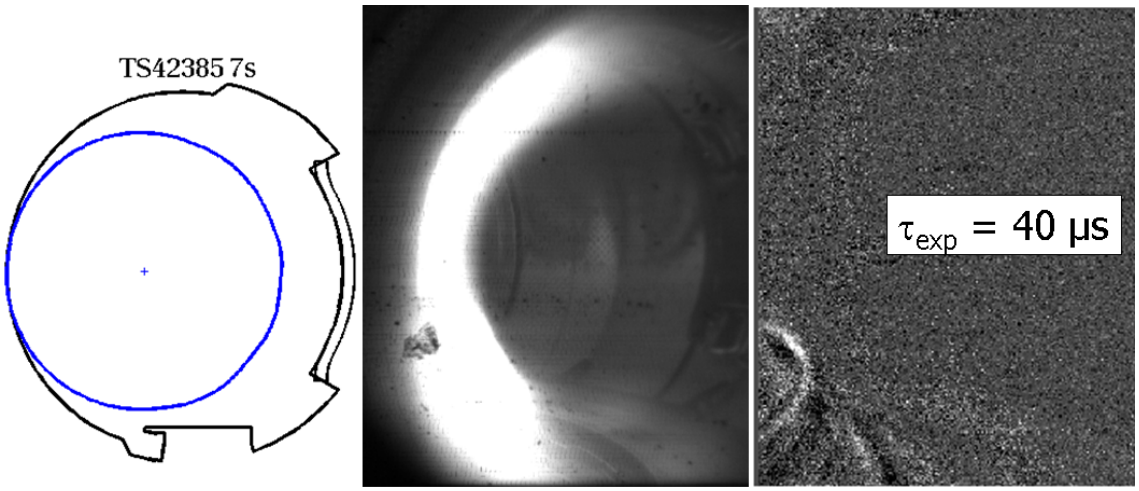

Figure 4.16: *TS42385 7s Left : poloidal cross section of the magnetic equilibrium in contact with the inboard limiter. Middle : steady-state image of the recycling cloud on the inboard limiter. Right : Fast imaging picture (exposure time 40 mus), for which the time averaged frame has been subtracted. Filament structures are observed at the plasma bottom, near the high field side*

while the MARFE leaves the bottom limiter and moves slowly toward the high field side, filament structures are observed at the plasma bottom 4.17. The visible cloud appears to be mainly localized in the confined region and no filament like structures are extractable from the cloud while reaching the inboard midplane, either in the SOL or in the confined region. When sustaining the high density conditions by gas puffing the MARFE develops into a fully

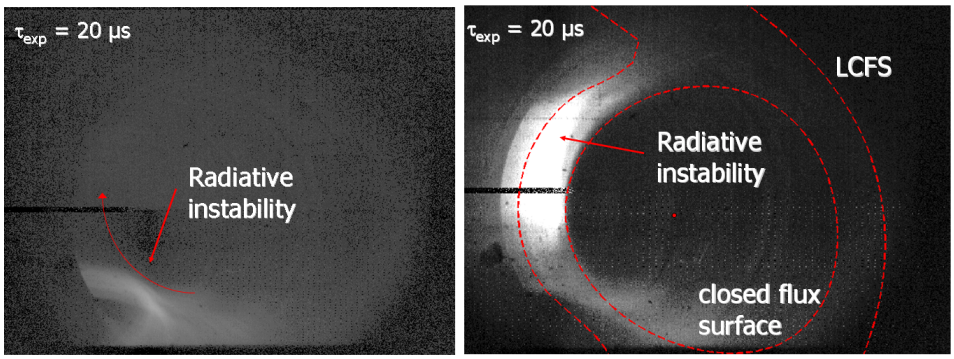

Figure 4.17: *TS44817, similar to TS44816 discharge 4.11. Pictures are taken during a radiative instability (MARFE) happening at high density. Left : Beginning of the MARFE: the visible radiation leaves the main bottom limiter and starts propagating toward the high field side. Some striations can be observed within the visible cloud above the limiter. Right : the visible cloud reaches the high field side and stays at that position for some milliseconds. A magnetic reconstruction of the LCFS and an internal flux surface shows that the visible cloud is mainly localized in the confined region and is locally elongated along flux surface. Image processing shows no fluctuation structures within the visible cloud.*

detached plasma : the localized visible cloud develops into a poloidally uniform ring lying in the confined region. By observing the visible ring with the fast visible imaging diagnostic the statement is clearly done that filaments exist within the low field side part of the ring, but not

in the high field side 4.18. A magnetic reconstruction on the picture evidences that they are aligned with the magnetic field.

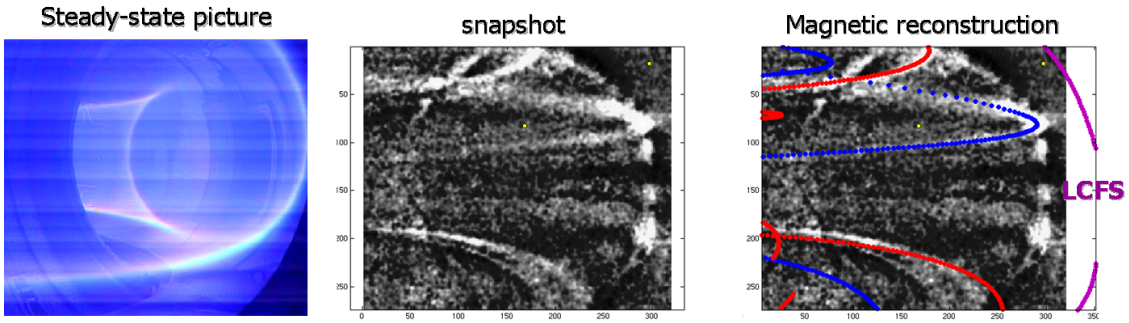

Figure 4.18: *TS42463. Left : Visible picture of the steady-state detached plasma (20ms exposure time). Middle : detrended frame (40 µs exposure time) revealing filaments on the visible ring. Right : Same picture with a magnetic reconstruction, including field lines and the LCFS.*

First of all, this simple experiment is a clear proof that plasma filaments can exist in the confined region and are not a consequence of the magnetic topology. Indeed the idea of plasma filaments is often associated with open field lines, but the phenomenon could be rather associated to local plasma parameters, like pressure gradient and/or plasma collisionality. Due to the relatively central position of the visible ring, the region is not accessible with reciprocating probes, but local plasma parameters can be obtained from interferometry, reflectometry and ECE radiometers. It is found that the local plasma temperature is about 20 eV, (matching conditions for visible emission from D ionization) and that the plasma pressure gradient length is about 6 cm 4.19, thus comparable to SOL conditions. Secondly, filaments are not present

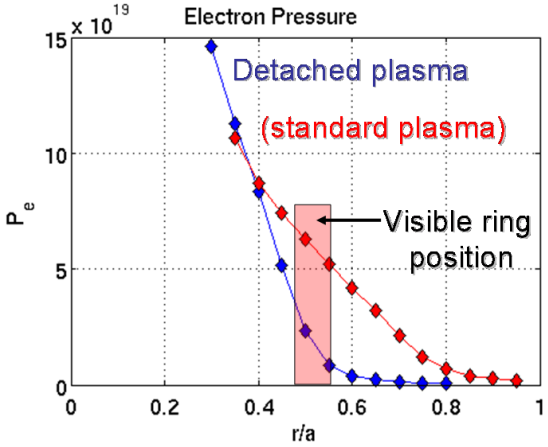

Figure 4.19: *TS42967 electron pressure profile in the confined region before and after detachment. The position of the visible ring during the detached phase is shown.*

in the high field side section of the ring, in agreement with the observations done into the MARFE, and probably justifying why nothing is observed in the recycling cloud when the plasma is limited on the high field side. Therefore the conclusion is done that plasma filaments

are linked to a phenomenon related to the low field side where magnetic curvature is favorable to instability developments, like the interchange instability. But even if filaments are created on the low field side, the fast parallel motion should in first sight lead to uniform structures along the field lines. Obviously, filaments are not uniform from the outboard midplane to inboard midplane, inferring the finite parallel extent of these transport modes.

Last but not least, the velocity of these filaments can be extracted from the movies. Dedicated experiments have been run on Tore Supra 4.20 with a more efficient fast visible camera [4] than what is usually used on Tore Supra. Due to the thin radial width of the visible ring (about 5 cm), the blurring due to overlapping flux surface is reduced, and the poloidal velocity can be calculated at the outboard midplane from temporal cross correlations. Again, the velocity can be compared to what is measured from Doppler reflectometry, and a quantitative good agreement is found between both diagnostic : fluctuations are rotating in the electron diamagnetic directions with a velocity close to 800 m.s^{-1}. Efforts have been pushed to extract detailed

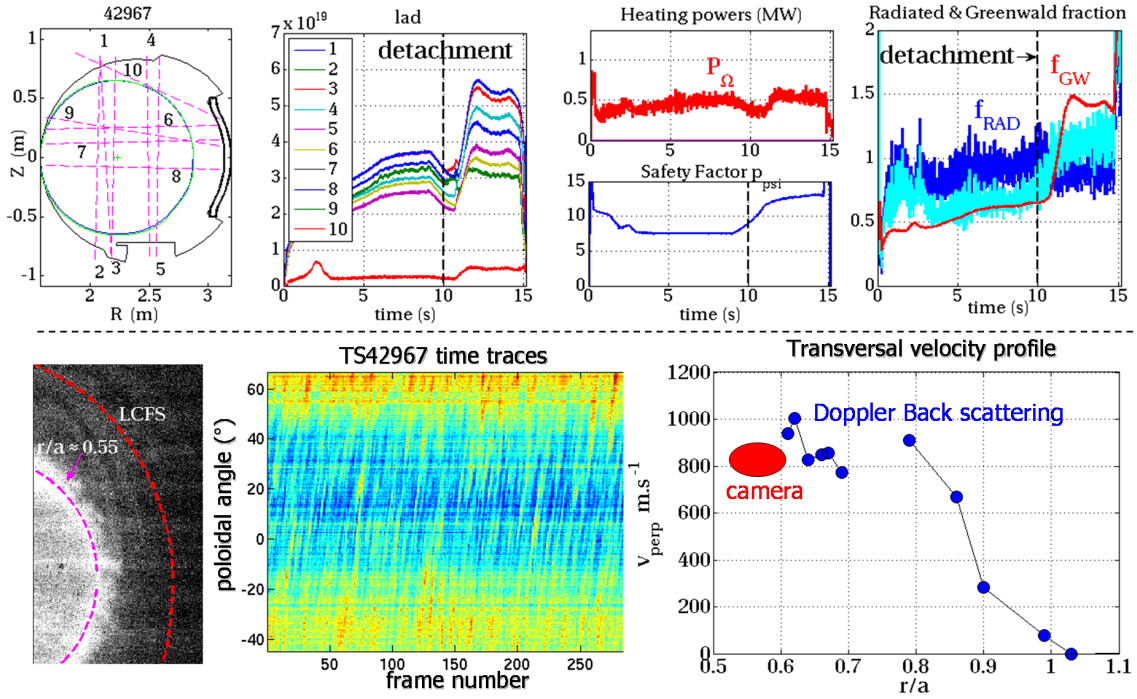

Figure 4.20: *TS42967 ohmic discharge. Top : panel of plasma parameters showing the time evolution of the discharge. The detachment occurs at 10s, when the plasma current is reduced and the fast movie starts at 12s. Bottom left: Picture obtained with the fast imaging (exposure time of 25mus). The emissive ring is found to lye on the flux surface $r/a \approx 0.55$. Bottom middle : time traces of the fluctuations (color scale) extracted for a poloidal mesh on the emissive ring. Poloidally propagating structures are recognized as tilted patterns. Bottom right : Radial profile of the transversal velocity measured with the Doppler back scattering and the camera (at the outboard midplane).*

velocity distributions using more complex analyzing processes [Brochard 09]. In terms of a collaboration with fluid turbulence experts [5], these movies have been treated with a wavelet filtering processing able to deconvolve a noise from a coherent pattern. The result is encourag-

[4] Photron FASTCAM SA1.1, collaboration with G. Bonhomme and F. Brochard, Nancy university
[5] M. Farge, K. Schneider and R. N'guyen Van Yen

ing regarding the lower signal over noise ratio 4.21 : in the coherent part of the movies remain only the largest plasma filaments. Then a special processing has been applied to the movies to extract a more detailed velocity field from the coherent fluctuations : a turbulence imaging velocimetry (TIV), developed by the LPMIA [6] for imaging in a linear magnetic device. The result is again encouraging since the velocity field extracted at least at the outboard equator is in relatively good agreement with the simple processing we applied. But the main issue faced by the TIV is the tangential projection of the field lines : spurious vectors appear in the velocity field as artifacts of the view. For that particular reason we initiated the tomographic reconstruction in terms of theses collaborations with turbulence and imaging experts.

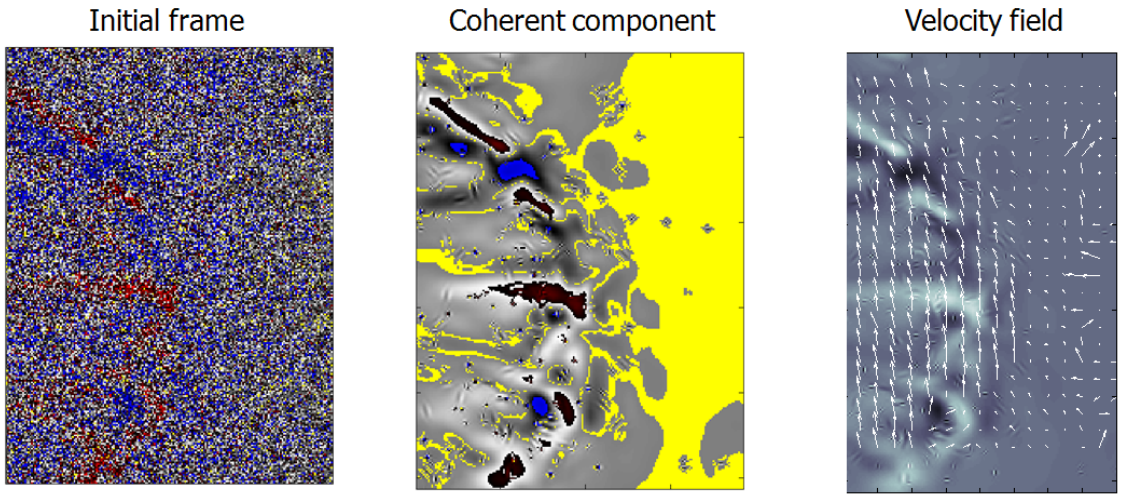

Figure 4.21: *TS42967 ohmic discharge and advanced processing performed on the frames. Left : raw picture of the detached plasma (time averaged frame subtracted). Middle : Coherent component of the frame obtained after a wavelet denoising processing : the filaments are highlighted. Right : Velocity field extracted from a TIV technique.*

4.5 Active imaging with supersonic molecular beam injection

When the discharge parameters do not correspond to fast visible imaging requirements, active imaging can be used. As introduced previously, two gas nozzle are installed in the view angle of the diagnostic that can picture the visible emission cloud formed during the gas injection. First of all are presented the outboard injection effect on the plasma density. Then observations at the outboard midplane are presented, and comparison with inboard injections is discussed.

4.5.1 SMBI injections and fast imaging

The supersonic molecular beam injection (SMBI) is a strong and pulsed puff of neutrals, normally used to fuel the plasma. As seen on density time traces 4.23, the injection is followed by a violent increase of SOL density (by a factor of 10) and a modest increase of core density(

[6] F. Brochard S. Oldenbürger and G. Bonhomme

about 20%). While the gas is ionised, the local visible emission strongly increases both by neutral density and plasma density increase, defining ideal conditions for fast imaging with a short exposure time (down to 1μs). On the other hand, the strong density disturbance created by the gas puff infers that we cannot really observe the natural fluctuations behavior, passively illuminated by the gas puff, but rather the fluctuations associated with the local density increase.
For most of the experiments dedicated to fast visible imaging on low field side gas injections the plasma was limited on the high field side, so that the outboard midplane section tangent to the camera line of sight is close to the center of the optical system to reduce edge optical aberrations. Unfortunately, that configuration implies that the injection is not localized at the tangence point, but slightly shifted toroidally 4.22.

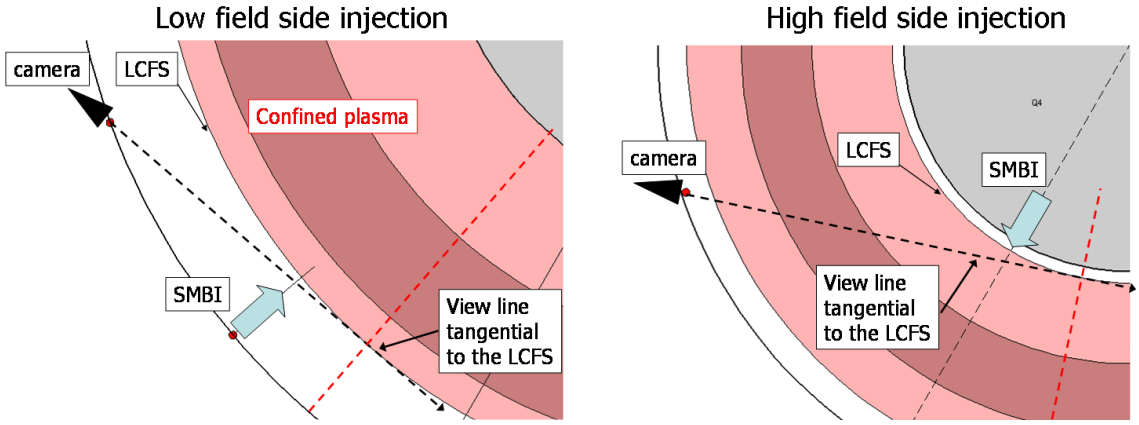

Figure 4.22: *Left : Tore Supra top view of the outboard midplane gas injection for a plasma limited on the high field side. The camera line of view tangential to the LCFS is shown, as well as the gas injection location that is slightly shifted toroidally. Right : Toroidal view of the inboard midplane gas injection for a plasma limited at the bottom (usual configuration). Again, the gas nozzle is not at the tangence location.*

The misalignment effect is quite clear on the early phase of the gas injection 4.23 and has to be seriously considered to avoid misinterpretation on the location of the visible light. Indeed, as it is discussed hereafter the early visible emission seems localized in the confined region according to the position of the LCFS at the tangential point. But it has been shown in a dedicated work that SMBI neutrals are first ionized in the SOL only [Tamain 07]. Then, when the local plasma cools down, the neutrals can penetrate further inside the confined region.

Having that fact in mind, let us observe the different phases of a gas injection on a steady-state ohmically heated plasma discharge 4.23:

t_0 The valve injection is opened and the gas flows into the chamber. A first visible emission is seen before affecting the plasma density (image 1). As discussed previously, the emission cloud seems coming from the confined region. But we infer that it lies in the SOL and the effect is due to the misalignment of the gas nozzle with the position where the line of sight is tangent to the LCFS. Striation pattern is seen within the emissive cloud, suggesting the presence of plasma filaments.

t_0 + 0.8ms The neutral cloud starts being ionized by the plasma and edge density increases. The visible emission is strong and clearly highlights plasma filaments even at the tangence point.

t_0+ 2.5 ms The edge density has increased by a factor of 5, and the movie shows a strong expulsion of plasma filaments toward the far SOL. At the LCFS position is observed a thin emissive ring, suggesting that the plasma temperature has dropped and neutrals propagate further into the plasma.

t_0+ 5.3 ms The edge density has reached is maximum and is slowly decaying. The emissive pattern corresponds to propagating filaments whose properties are more or less stationary even if the density is decreasing. Data analysis on the movie are performed on that part of the injection, since it shows the less disturbance from the gas injection.

t_0+17.2 ms The camera sensitivity is too low to access reliable informations on the movie.

As presented above, the supersonic gas injection is responsible for large disturbances of the plasma edge, either on the local density and more importantly on its gradient. Probe reciprocations are unfortunately too slow to resolve the dynamic of a gas injection, but reflectometry can be configured with the required sweeping rate [Clairet 03] of 20μs per density profile, thus almost in a frozen density background.

The reflectometer is installed at the outboard midplane, toroidally 80^o away from the SMBI nozzle, and due to the rapid parallel extend of density modulation along the field lines (at the ion sound speed $\approx 10^4 \mathrm{m.s}^{-1}$), we would infer a delay of about 10 to 100 μs that is negligible. Considering the profiles extracted for a similar experiment 4.24 as the one presented previously (for which the ultra fast reflectometry was not available), some comment are worth to be done about the dynamic of the edge density profile during the gas injection. At the beginning of the gas injection, density starts increasing inside the LCFS (reflectometry profile) as well as its radial gradient in the SOL, until the visible imaging shows a strong expulsion of plasma filaments in the SOL. At that time, the line averaged density increasing rate is lower (a slop decrease in the time variation), correlated with a strong increase of SOL density as observed by the reflectometry (magenta and orange profiles in the figure 4.24). During the relaxation of the line averaged density, the reflectometry profiles relax to the initial profile with a more or less constant gradient length. But more importantly for the fast imaging, the neutral cloud has spread toroidally and allows imaging of fluctuations at the tangential location with reduced effects of enhanced light emission just in front of the gas nozzle. That is, emission even inside the LCFS can be resolved without any evident ambiguity due to the tangential projection. Apart from the next discussion, the strong expulsion of plasma filaments from the LCFS to the far SOL observed by the fast imaging 4.25 just after the gas starts fueling the plasma is coherent with both line averaged density evolution and reflectometry profiles : the steep edge gradient due to the local fueling triggers a relaxation process. Considered as a transient phase, these plasma behavior has not been intensively analyzed since we were more focused on the after-relaxation phase. However the case deserves more interest since it brings important informations about the link between edge plasma gradients and turbulence triggering.

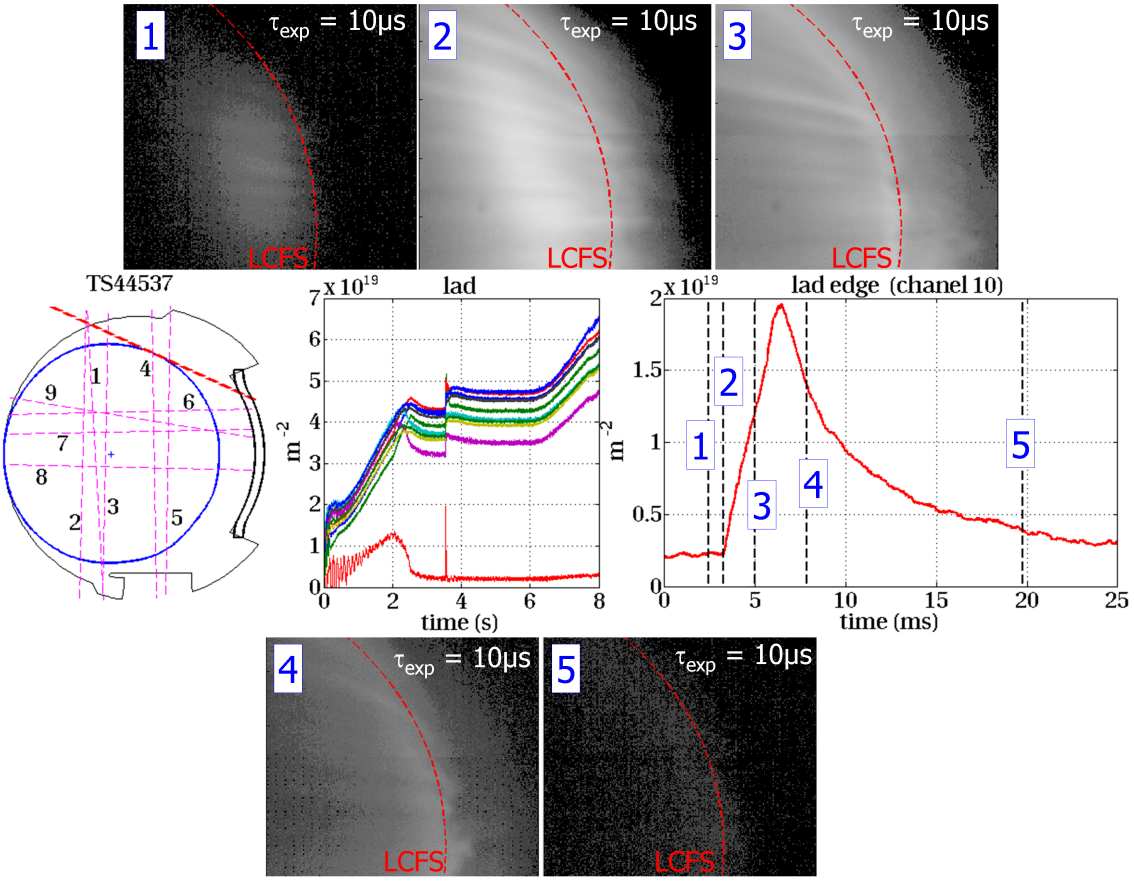

Figure 4.23: *TS44537 ohmic discharge with low field side SMBI. Middle : Poloidal cross section of the magnetic equilibrium, limited on the high field side in order to picture the LCFS outboard midplane close to the center of the chamber. The SMBI is triggered at about 3.5 s from the low field side. Effect on line averaged density is shown in the middle. On the right is shown a zoom on the line averaged density at the boundary, illustrating the LCFS density variation. Snapshots from the fast imaging illustrate the visible emission behavior during the SMBI (exposure time 10mus, 15037 fps).*

4.5.2 Fluctuations at the outboard midplane

Now let us focus on the relaxation period of the gas injection performed on the low field side. Plasma activity rapidly reduces compared to the initial ejection phase and stays in a constant dynamic although the local density and the visible emissivity decrease with time, that is highlighted by subtracting the time trend to the movie. First of all, the visible emission shows intermittent and elongated structures propagating radially in the SOL that can be followed on consecutive frames 4.26. The transversal size of these structures is of the order of one centimeter and propagate radially outward over several centimeters with velocities of the order of 500m.s^{-1}. Interestingly, elongated structures are also observed just inside the LCFS , where they propagate mainly in the poloidal direction with a positive velocity 4.27 of about 800m.s^{-1} (electron diamagnetic direction). Some structures cross the LCFS with an outward velocity of about 500m.s^{-1}, and their poloidal velocity reverses to about -400m.s^{-1} (ion diamagnetic direction) when they enter the SOL. Again, these observations are qualitatively consistent with of Doppler back scattering measurement across the LCFS. Although these profiles are

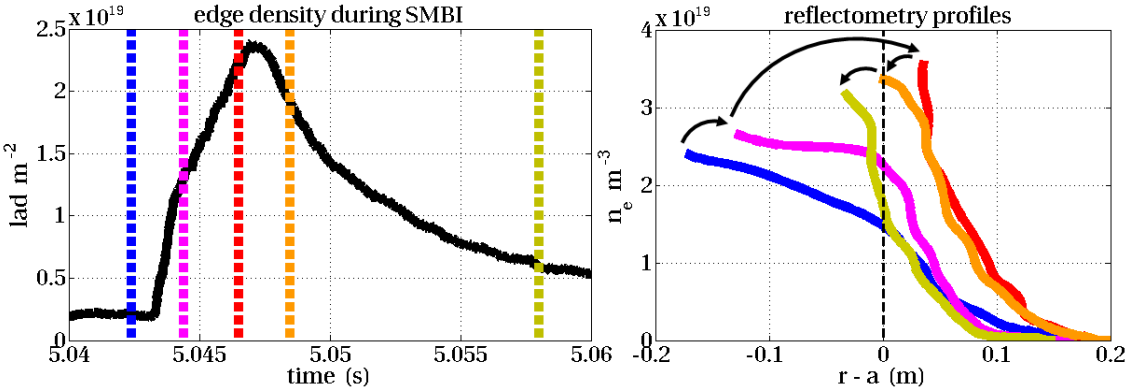

Figure 4.24: *TS45372 ohmic discharge with low field side SMBI. Left : time trace of the line averaged density at the edge (channel 10) during the gas injection. Right : Instantaneous density profiles from the reflectometry. The diagnostic is installed at the outboard midplane, toroidally 80º away from the SMBI nozzle. Profiles at different times are considered during the edge density dynamic (the timing is reported on the left graph following the color scale*

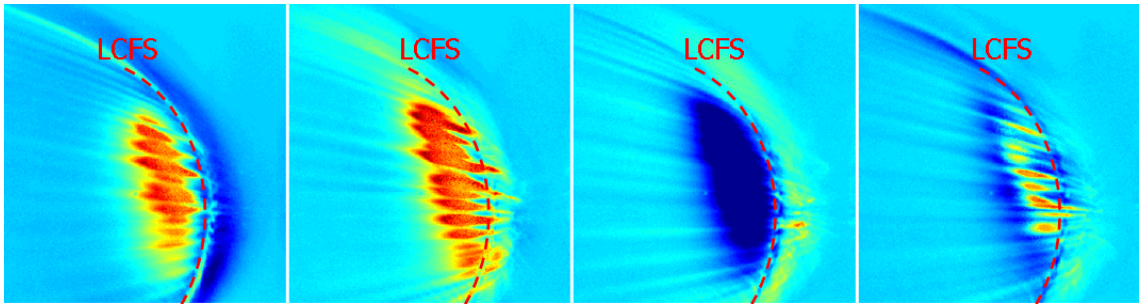

Figure 4.25: *TS45372. Snapshot of the expulsion phase during SMBI (exposure time 20μs). The LCFS at the tangence point is shown. Plasma filaments are observe to propagate from the the LCFS to the far SOL, with stronger expulsion rate than during the relaxation phase.*

not available for that particular experiment with SMBI, the shear layer is always observed just inside the LCFS 4.27, suggesting that fast visible imaging returns a consistent picture of plasma fluctuations at the edge.

On the other hand, the crucial issue raised by the tangential view and the non aligned gas injection has to be considered. When focusing in a region inside the LCFS, we are in fact looking through the SOL. But the observed electron diamagnetic modes can not be the consequence of geometrical artifacts due the projected view. Moreover, these modes show an almost poloidally periodic pattern that is obviously not the case for the intermittent structures observed in the SOL.

That is, the fast visible picture of plasma transport phenomena obtained at the outboard midplane of Tore Supra is similar to what is observed at the edge of X-point plasmas : plasma filaments propagate with a ballistic-like motion in the SOL over distances larger than their typical transversal size. When the emissive cloud crosses the separatrix, it is observed that fluctuations propagate mainly in the poloidal direction, although it has been observed in Alcator C-mod that fluctuations from visible imaging can propagate in the ion diamagnetic direction

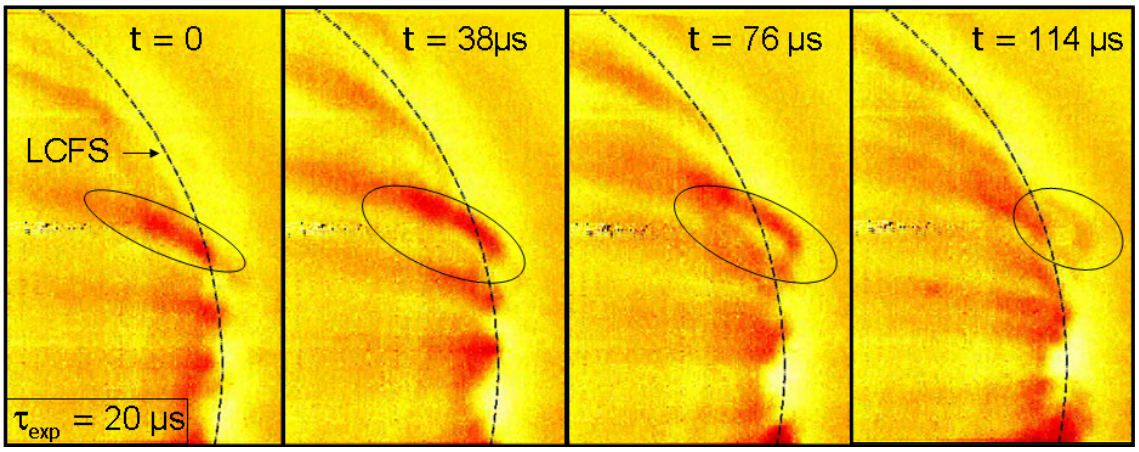

Figure 4.26: *TS44537 ohmic discharge with low field side SMBI. Fast visible imaging at 26143 fps and 20 µs exposure time. 4 consecutive frames are shown, illustrating the radial propagation of an isolated filament.*

inside the LCFS whereas probes gives an opposite behavior [Terry 05].

4.5.3 Inboard / outboard asymmetry

Last but not least, let us pay attention to the imaging obtained during high field side injections. Similar to the low field side geometry, the gas nozzle is at the midplane, slightly shifted toroidally with respect to the position where the diagnostic line of sight is tangential to the inboard LCFS 4.22. Effect of SMBI on edge density can be followed by the edge interferometer4.28. The temporal evolution of the density during the SMBI is similar to the experiment discussed previously, Although the interferometer beam enter more inside of the LCFS and not strictly restricted to the SOL. On the other hand, the visible imaging shows a completely different dynamic of the emissive cloud created by the SMBI. First of all, The emissive cloud appears at the high field side *bottom* part of the plasma when the injection is performed at the midplane 4.29. A possible explanation could be that the gas nozzle is effectively not oriented along the midplane due to the presence of an object (carbon tile) on the neutral path. Otherwise, quasi sonic SOL parallel flow directed toward the bottom in that region could be responsible for a drag force on molecules and atoms that effectively displace the emissive cloud close to the bottom limiter. The cloud then slowly propagates toward the plasma top by the high field side, and then spread poloidally toward the bottom. The emissive cloud evolution is on a time scale of order 10ms, that allows fluctuations extraction by subtracting a local time average. The result is illustrated on figure 4.29 : the emissive cloud do not involve any fluctuating pattern recognized as field aligned structures. We could however argue that an exposure time of 40μs is too long to resolve the fluctuations. On the other hand, for a similar experiment with the same diagnostic settings, the high field side SMBI is followed by a full detachment of the plasma during which field aligned structures are observed on the bottom and LFS part of the plasma.
Besides the absence of filaments during the relaxation phase after the density peak, the movies do not show any strong ejection phase as for the low field side SMBI, inferring that this

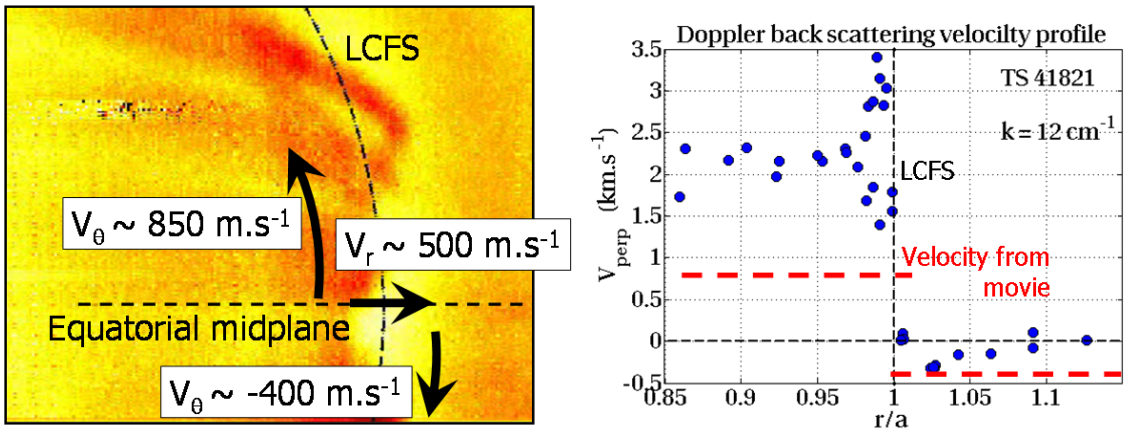

Figure 4.27: *Left : TS44537 ohmic discharge limited on high field side with low field side SMBI. Velocity field extracted at the outboard midplane from cross correlation technique. The poloidal velocity was extracted inside and outside of the LCFS, whereas the radial velocity was extracted at the LCFS. The poloidal velocity reverses across the LCFS, whereas filaments are propagating outward. Right : TS41628 ohmic discharge limited on high field side. Doppler back scattering measurements of the transversal velocity. For illustration are reported the velocity extracted on the fast imaging movie for the TS44537 experiment.*

enhanced transport triggering is related to the magnetic field curvature and could be possibly related to interchange mechanisms.

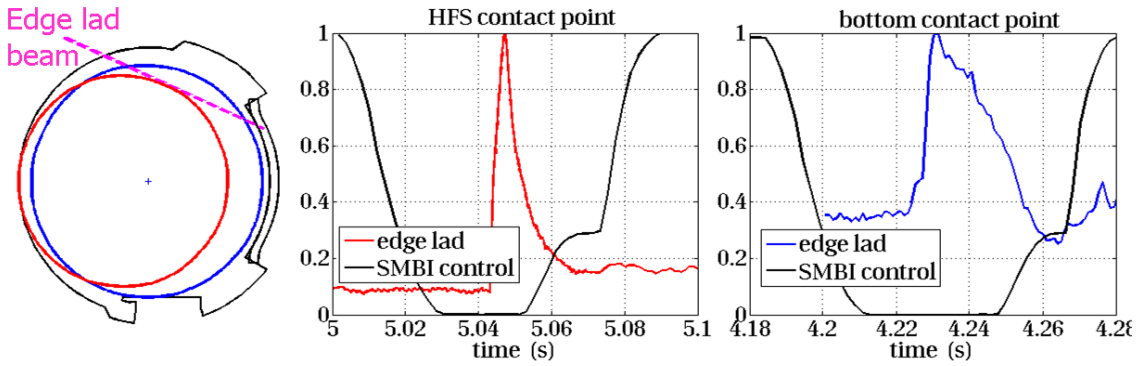

Figure 4.28: *Effect of SMBI and injection side on the edge line averaged density. Left : TS poloidal cross section showing the two magnetic configuration of interest : a high field side limited geometry as discussed previously (red LCFS) , and a standard bottom limited geometry(blue LCFS). Middle : Time traces of the edge lad (arbitrary units) and the SMBI valve control signal for the high field side geometry. Right : same figure for the bottom limited geometry.*

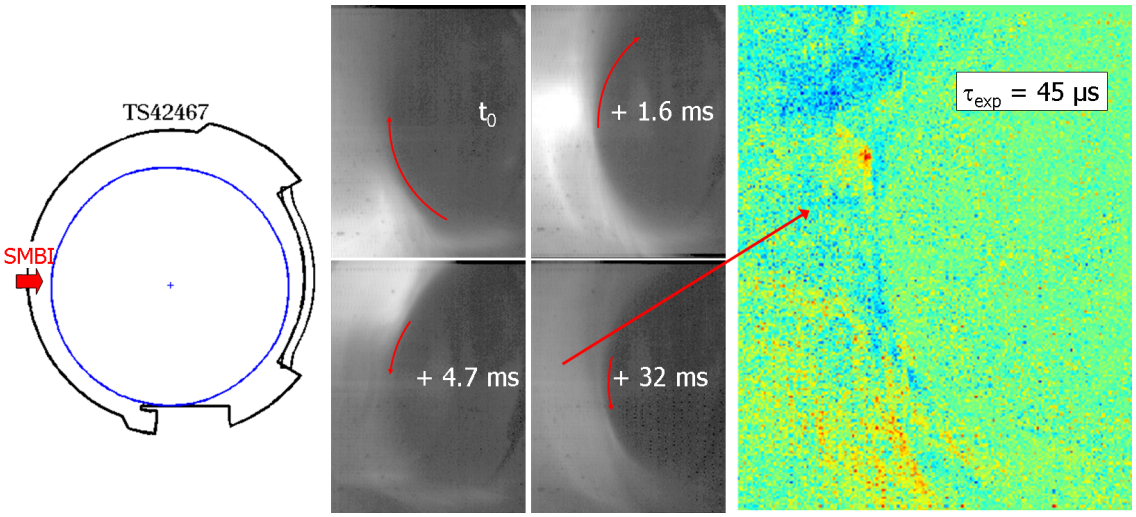

Figure 4.29: *TS42470 ohmically heated plasma, with high field side SMBI. Middle : 4 snapshots taken at 40 µs exposure time illustrating the gas injection chronology. The emissive cloud starts below the outboard midplane and propagate slowly toward the top. Then it spreads poloidally and returns to the bottom. Right : When the cloud is more or less uniform at the high field side, the detrended images do not show any filament-like structures.*

4.6 Summary

This chapter was devoted to the fast imaging diagnostic implemented on Tore Supra and the analysis of turbulence imaging obtained for a variety of experimental conditions. First of all, we presented the diagnostic setup and its limitations mainly due to a relatively low photon sensitivity, implying high density plasma conditions to perform low exposure time acquisitions. A second limitation concerning the data analysis is due to the wide tangential view and projection of the toroidal curvature of elongated fluctuations. For that reason we where not able to operate a consistent and wide data analysis but we rather qualified the nature of the observed phenomena and tried to quantify some fluctuations properties when projection was not too restrictive. We conclude that:

- Plasma filaments are observed at the plasma bottom, above the main limiter (at high density). These filaments are aligned with the magnetic field in a region surrounding to the LCFS.
- Plasma fluctuations again aligned with the magnetic field are observed within the recycling cloud of outboard limiters when they stay close enough to the main plasma - and again at high density.
- Similar fluctuations pattern are observed when the plasma is limited on these outboard limiters. The diagnostic sensitivity is able to resolve their spatial dynamic and the extracted velocity is found to be in relatively good agreement with the Doppler back scattering measurement in the SOL. Thus we suggest that these fluctuations happen in the SOL.
- When the plasma is then limited on inboard limiters, the recycling cloud does not show the same fluctuating pattern. Namely, plasma filaments are hardly observed at the plasma bottom, near the high field side.
- When the density is further increased and radiative instability occurs (MARFE), the visible could moving in the high field side of the plasma does not reveal any filament-like turbulent structures except at the plasma bottom.
- when the plasma is stationary fully detached, the existence of visible filaments at the low field side inside the confined region is unambiguously demonstrated. Their poloidal velocity is in quantitative agreement with the Doppler back-scattering measurements justifying they effectively correspond to plasma filaments. They are again not observed at the high field side of the confined region, inferring their finite extent and preferential existence at the low field side.
- When gas puffing is used, we clearly observe field-line elongated visible fluctuations either inside the LCFS or in the SOL. A poloidal velocity shear layer is resolved just inside the LCFS, as confirmed by the Doppler measurements. these filaments cross the LCFS with a velocity of about 500m.^{-1} at the outboard midplane.
- When the gas puffing is performed at the inboard midplane, no fluctuations are observed with the dynamic obtained at the outboard midplane. We thus conclude again that plasma filaments are preferentially located at the low field side and that they have a finite parallel extent that decouple the low field side fluctuations form the high field side.

Evidences of spatial asymmetries are further discussed in the next chapter, in the scope of probes measurements.

Chapter 5

3D properties of scrape-off layer radial transport

5.1 Motivations

The spatial asymmetries of the radial flux at the edge is of crucial importance for having a coherent understanding of transport mechanisms involved at the edge. The main motivation is that radial flux asymmetries drive near sonic parallel flows, that in return can influence the core rotation by fixing strong boundary conditions [Groebner 08]. Experiments performed on Alcator C-mod [LaBombard 04] have shown a coincidence between SOL flow reversal and modification core rotation in L-mode, having an impact on the L-H transition power threshold. Similarly, Tore Supra experiments performed in the scope of our work have shown a coincidence between SOL flow reversal and modification of edge radial electric field [Hennequin 10].
The key and simple question is : *How* do SOL flows influence core plasma rotation and electric field shear in L-mode plasmas ? To answer, we need a crucial unknown that is the distribution of the parallel flows across the plasma circumference, directly linked to the spatial distribution of parallel flows driver : the radial particle flux. Secondly we need to know how the Reynolds stress is able to transfer momentum from the SOL to the plasma core by means of SOL turbulence, and again the spatial distribution of the turbulent flux is required.
Along the previous chapters we have shown that transport at the edge involves poloidal asymmetry around the plasma cross-section : First of all it is known that edge plasma transport involves the propagation of elongated plasma filaments and fast imaging performed on Tore Supra suggest that these filaments are not uniformly distributed around the poloidal cross section of the plasma, but exist preferentially in the low field side. Secondly, the near-sonic parallel flows measured at the plasma top corresponds to return flows balancing the particle source distribution with respect to the pressure balance. The line integrated radial flux is localized for about 85% in the low field side . Earlier experimental evidences [Gunn 07] obtained on Tore Supra have highlighted that the flux is centered at the outboard midplane and we present in the next section a novel experiment performed on Tore Supra in order to refine this mapping. Then, local turbulence measurements have shown a quantitative agreement with the global particle flux at the edge although no consistent matching have been obtained, and we intimate that the flux asymmetry is on task in the mismatch. We show that local turbulence is

in quantitative good agreement with the steady-state poloidal mapping of the radial flux driving the parallel flows. From that mapping, we discuss the apparent inconsistency observed on other experiments, and finally we speculate on the 3D properties of plasma filaments involved in the SOL radial transport.

5.2 Poloidal mapping of the steady-state radial flux

In that section we present unique experiments (compared to other machines) performed on Tore Supra that give evidences of the radial flux asymmetry in the SOL. We start with experiments done by J.P. Gunn where strong modifications of SOL profiles are observed on identical discharges limited either on the high field side or on the low field side. The strong change in the density profiles as well as parallel flow directions are strong indication of the radial flux asymmetry. Then we present the principle of *field line tailoring experiment* that we developed in order to map the radial flux distribution along the low field side poloidal cross section. Consistency with early experiment on flow reversal are discussed.

5.2.1 Second evidences of a radial flux centered at the outboard midplane

When the subject of symmetry is discussed, as we do for the spatial distribution of the radial flux, it is always of crucial interest to perform experiments that follow some symmetry breaking properties and then pay attention to the symmetry of the measured quantities. For instance, some divertor tokamaks offer the possibility to test up/down symmetries by changing the position of the X-point from the bottom to the top. Such experiments performed on Alcator C-mod [LaBombard 04] have shown a reversal of SOL flows that could be understood only if the radial particle flux was not poloidaly symmetric. Tore Supra is not a divertor machine, and does not allow to change the limiter position from the bottom to the top as we could do with an X-point if a upper divertor was installed, but the variety of possible limiters configurations is a perfect property of the machine to test other symmetry breaking conditions.

5.2.1.1 Inboard / outboard asymmetry

The first meaningful experiment that we can perform on Tore Supra is by changing the plasma/limiter contact point from the inboard to the outboard 5.1. We emphasize that the inboard and outboard limiters are not toroidally uniform but are composed of toroidally discrete limiters distributed along the toroidal circumference of the torus. Due to the relatively high safety factor ($q_{edge} \approx 6$) the field line helicity is low enough so that any field line entering the poloidal section where the limiters lye does intercept a limiter in that region, so that toroidal uniformity is effectively assumed for the field line connection topology. Similar discharges can be operated in the two limiter configurations within mismatch of global plasma parameters less than 20%. The main discrepency concerns the core density (20%), the reason being that conditioning state of inboard and outboard limiters is not equal and no gas injection was performed during the two experiments to avoid disturbance on SOL plasmas. That is, the SOL

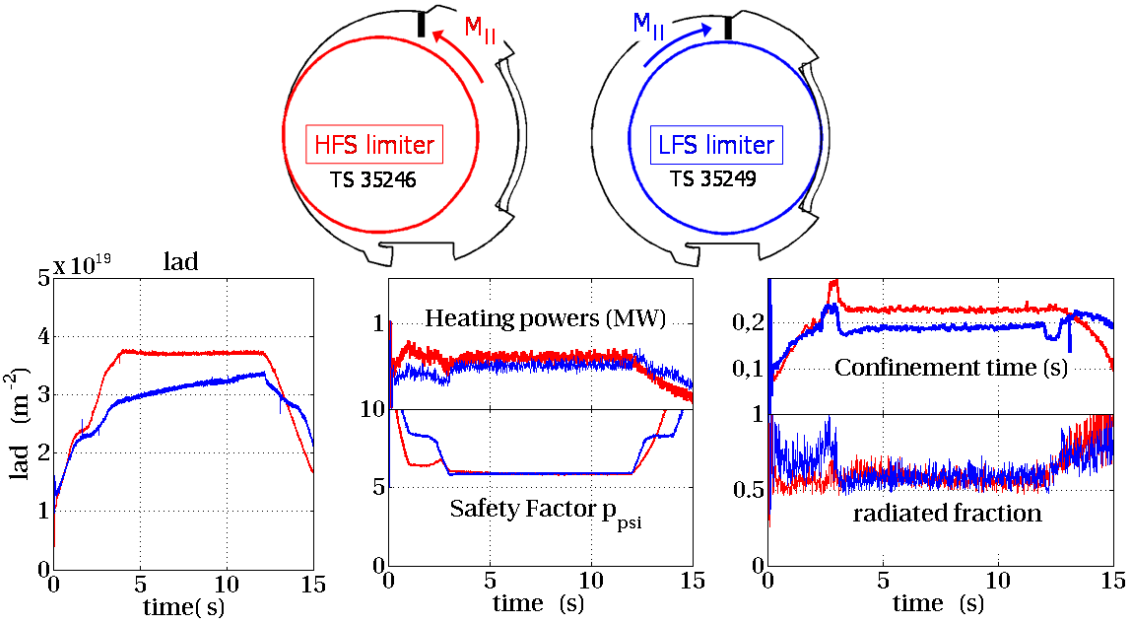

Figure 5.1: *Global plasma parameters during the HFS limited discharge TS35246 (red) and LFS limited discharge TS35249 (blue). From left to right: line integrated density through the plasma center, ohmic power, egde safety factor, energy confinement time and radiated fractions. Adjustable parameters almost match.*

plasma is in first approach a consequence of both global plasma conditions 3.12 and scrape-off layer topology : the radial decay length depends on the parallel connection length. Looking at both plasma configurations, the global parameters are relatively well matched so that we expect no influence of the core plasma on the SOL plasma. That is, probe reciprocations performed at the top during the steady-state phases show strong differences 5.2. When the plasma is limited on the HFS the parallel flow measured at the top is co-current, as observed in usual plasma configurations 3.4 3.10. Whereas for the LFS limiter configuration, the parallel flow reverses at the top, being counter-current.

At first sight, we could interpret this Mach number as a return flow from the longest field line fraction, located on the low field side for the HFS limiter experiment and located on the high field side for the LFS limiter experiment - as indicated by the arrows on the figure 5.1. That interpretation does not lead to any further information about the particle source location, except the confirmation that the parallel flows are driven by the radial flux distribution and not Pfirsch-Schlüter flows that are not sensitive to the limiter position on the field line. In fact, the main meaningful observation is done on the density profiles : Although the density (and temperature) is almost unchanged at the LCFS of the two configurations, the radial decay length is strongly different : When the plasma is limited on the HFS the density radial decay length is about $\lambda_r \approx 6.5$cm for a parallel connection length of about $L_{//} \approx 65$m, whereas is drops significantly when the plasma is limited on the LFS to $\lambda_r \approx 2.5$cm for a parallel connection length of about $L_{//} \approx 85$m. Interpreted in term of line averaged transport coefficient 3.20, we found that the radial transport efficiency *in the probed region* drops from $v_r^{eff} \approx 55\text{m.s}^{-1}$ to $v_r^{eff} \approx 16\text{m.s}^{-1}$ when the plasma is moved from the HFS limiter to the LFS

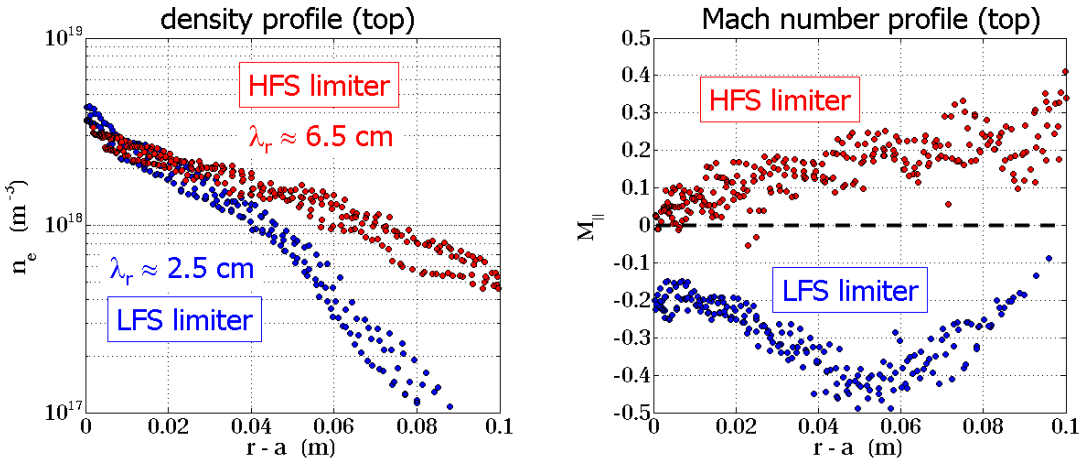

Figure 5.2: *Density and parallel Mach number profiles (3 reciprocations) for the two similar discharges limited on the HFS (red) and LFS (blue). When the plasma is in contact with the HFS, the density radial decay length is about 6.5 cm and the parallel flow are positive (co-current), whereas the density decay length is about 2.5 cm and the parallel flow is negative (counter-current) when the plasma is limited on the LFS.*

limiter. Similarly, the line integrated radial flux calculated for the two configurations from the wall to the LCFS drops by a factor of almost two - see figure 5.3. The reason is obviously not a change in the confinement property of the discharge, since the energy confinement time is even slightly lower for the HFS limiter configuration - see figure 5.1. Our interpretation is that a variable fraction of the particle flux distribution filling the SOL is intercepted in between the toroidally discrete limiters, that does not participate to the radial flux *seen* by the probe 5.4. Thus the noticeable difference of line integrated radial flux evaluated for the two limiter configuration is due to the difference in the fraction of the radial flux distribution that is hidden by the discrete limiters. That said, the field line connection topology at the LFS follows a complicated pattern due to the toroidal and non uniform discretization of the limiters in that region, and for that reason a quantitative description of the private region is hardly achievable. On the other hand, the private region defined at the HFS or at the LFS should be of the same spatial extend (in the order of 10 to 30^o poloidally) , and in that range of speculation the radial flux at the outboard midplane should be enhanced by a factor *at least 10* compared to the inboard midplane to explain the measured flux difference [Fedorczak 09].

5.2.1.2 Up / down outboard asymmetry

The previous set of experiments shows that the radial flux is enhanced at the LFS midplane, as we have inferred from the top flow measurements 3.10. An other experiment leads to the same conclusion, but now looking at the parallel flow direction. The matter is to perform an up/down symmetry breaking as is done on Alcator C-mod by changing from lower-null to upper-null configuration, but using outboard limiters of Tore Supra. Indeed, the poloidal extend of outboard limiters is $\pm 37^o$ and their curvature radius ($R_c^{lim} = 0.77$m) is larger than the minor radius of plasmas we can limit on them ($a_{min} = 0.65$m), such that the plasma can be effectively limited either above or below the outboard midplane 5.5. When the plasma is

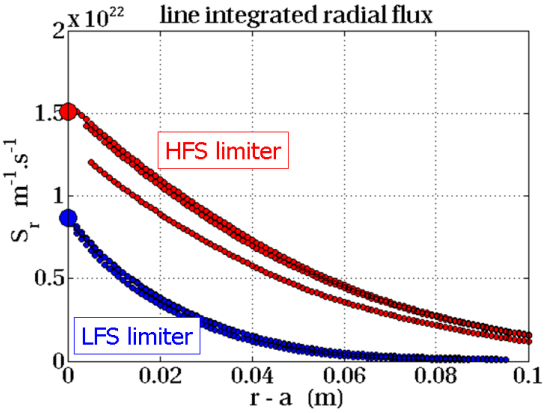

Figure 5.3: *Radial profiles of the line integrated radial flux evaluated for the two configurations : high field side limiter (red) and low field side limiter (blue). The value at the LCFS is significantly lower for the low field side contact point* $S_r(0) \approx 8.10^{21} m^{-1}.s^{-1}$ *than for the high field side contact point* $S_r(0) \approx 15.10^{21} m^{-1}.s^{-1}$*, although the parallel connection length is longer.*

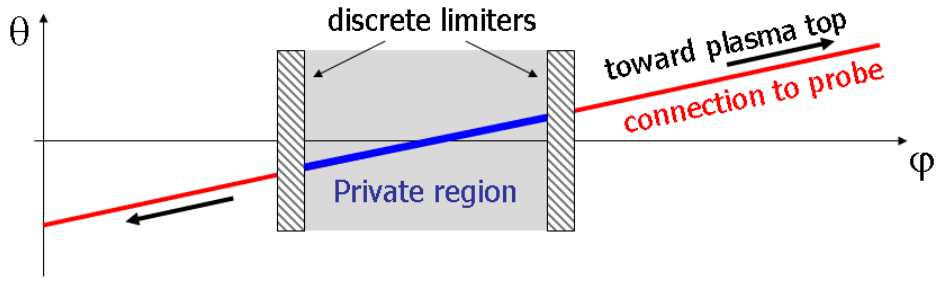

Figure 5.4: *Picture of a SOL field line in poloidal and toroidal plan intersected by a set of toroidally discrete limiters. Two limiters define a private region with respect to the probe.*

moved up / down during one single discharge, the global plasma parameters are kept constant such that we have on first sight an ideal case for testing up / down symmetry breaking. We point out that the bottom limiter may influence the SOL plasma in the *down* configuration, and will be reminded when needed. Probe reciprocations show that parallel flows reverse in the SOL when the limiter is placed above the outboard midplane 5.6. This observation does not depend on plasma parameters except that the edge safety factor has be to relatively large to assume effective toroidal uniformity of the outboard limiter. In the *down* configuration, the flow comes from the outboard midplane to the top, i.e in co-current direction. Whereas in the *up* configuration, the flow comes from the inboard midplane to the top, i.e in counter current direction. So as a matter of observation, the flow direction is always orientated *from* the region magnetically connected to the outboard midplane : our interpretation is that the plasma follows a parallel expansion from the main particle source localized at the outboard midplane.

As an attempt of quantitative approach, the experimental conditions can be refined by slowly rolling the plasma on the outboard limiters, so that the limiter position according the the outboard midplane is slowly varied poloidally. The Mach number is extracted from probe reciprocations 1cm from the LCFS and we observe a continuous variation of the flow speed

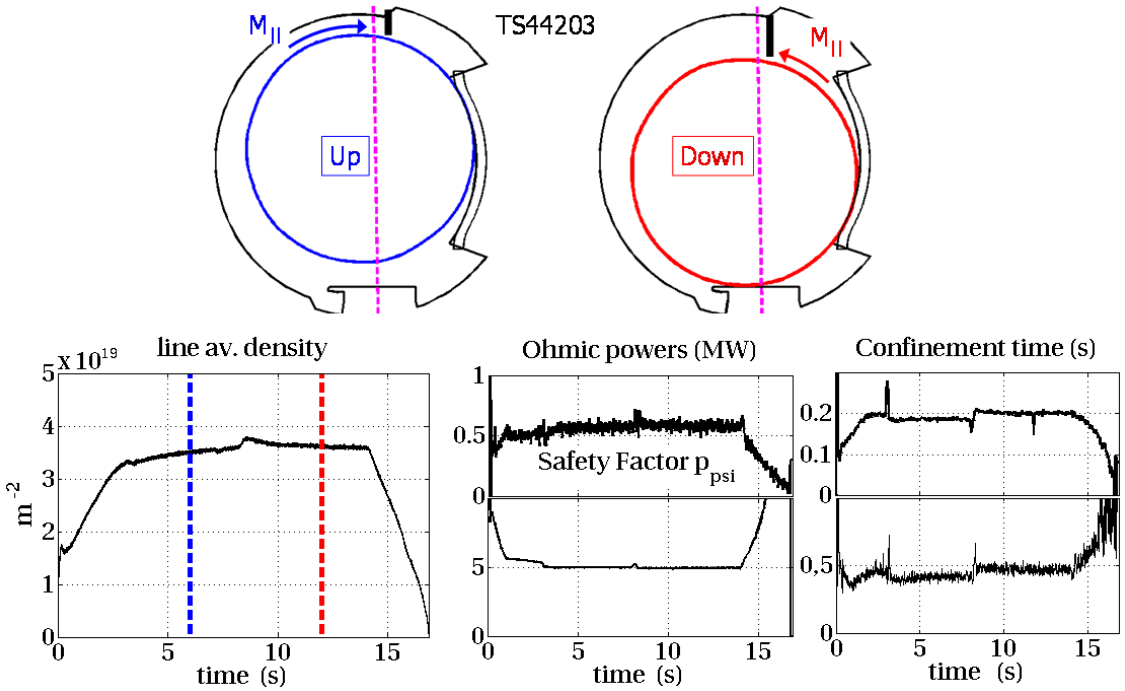

Figure 5.5: *TS44203 . The plasma is limited on outboard limiters and rolled from top to bottom at 8s. Top : Poloidal cross sections of the two limiter configurations. Bottom, from left to right : Time trace of line integrated density (along the vertical line shown on the cross sections), and the times where probe plunges are performed (7s and 12s). Then Ohmic power, edge safety factor, confinement time and radiated fraction. All global plasma parameters are equal for both configurations.*

from positive values when the limiter is below the midplane to negative values when the limiter is above 5.7. Again, our interpretation is that the particle source distribution is poloidally split by the outboard limiter and the local Mach number depends on the proportion of particle flux entering the SOL above or below the limiter with respect to the probe position. That is, we cannot yet conclude any quantitative properties for the radial particle outflux, except that it is effectively localized around the outboard midplane in order to explain these observations in the frame of a simple model.

5.2.2 Field line tailoring and flux mapping

As it has been emphasized along the previous observations, a significant fraction of the radial outflux can fill a private portion of the field lines, that is not participating to the particle flux balance in the probed region. This remark was previously done as a geometrical issue when we introduced our method for calculating the line integrated radial flux 3.1.5.3. Now we consider that effect as a possible powerful tool for estimating the spatial distribution of the radial flux in the SOL. After the introduction of the principle of field line tailoring experiments using movable outboard limiters, we present a full set of experiments and related results dedicated to the radial flux mapping around the outboard midplane.

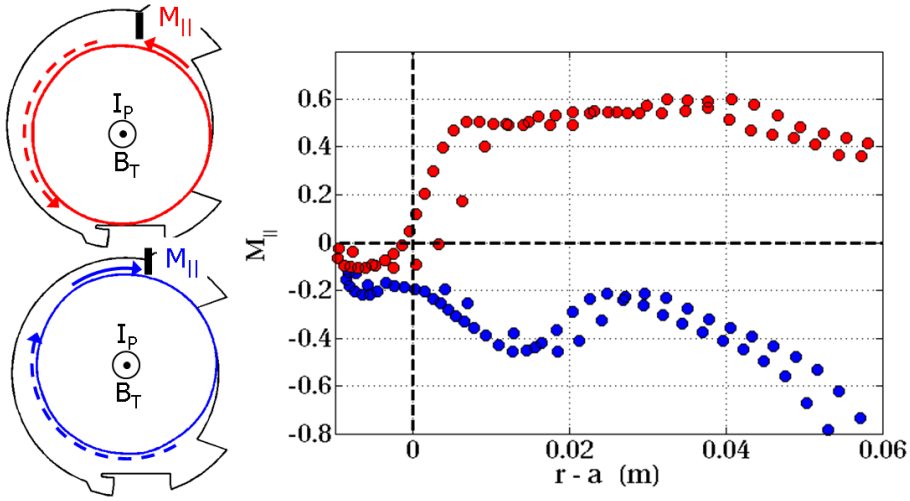

Figure 5.6: *TS44203 . Radial profiles of the parallel Mach number measured with a tunnel probe for both limiter configurations. In the SOL ($r-a>0$), parallel flows reverse when the limiter position is changed from up to down.*

5.2.2.1 Principle of tailoring experiments

Let us consider a standard plasma configuration, limited on the bottom by the main toroidally symmetric limiter. All second limiters are retracted as far as possible from the plasma to allow the SOL plasma to expand freely in the radial direction. A Mach probe reciprocation performed at the top returns local parallel flow quantities, that are interpreted in term of line integrated radial flux along the full SOL radial profile. Now, let us repeat this discharge with a discrete outboard limiter inserted radially to a given distance in the SOL $r_{lim} - a = d_{lim}$ - see figure 5.8. We take care that the toroidal position of the limiter with respect to the edge safety factor and the probe position is such that the probe is magnetically connected to the limiter, close the the outboard midplane. From the SOL flux balance point of view, we now assume that the presence of the limiter does not disturb the plasma radially upstream $r-a<d_{lim}$, such that *the radial flux along field lines remains the same as in the first experiment, between the LCFS and the limiter extremity.* At the limiter extremity $r-a=d_{lim}$, the radial flux distribution is split in two fractions : one filling the probed region and a fraction filling the private region. Of course, we assume that the parallel extent of the limiter is negligible so that the radial flux directly absorbed on the limiter side facing the LCFS is negligible. A new flux balance is then created in both regions, directly influenced by the limiter insertion since field lines are shorter and radial sources are lower (due to the split). That is, a probe reciprocation performed in the region of interest can be again interpreted as a line integrated radial flux in that region, from the wall to the limiter extremity. At that particular position, the line integrated radial flux calculated from probe data does correspond to what is filling the region of interest *only*, without any information about what is filling the private region. Now, we can compare such value to the measurements performed without second limiter, that is the sum of the radial flux virtually filling the probed region *and* the private one. Therefore, the difference corresponds to the contribution filling the private region, namely between the

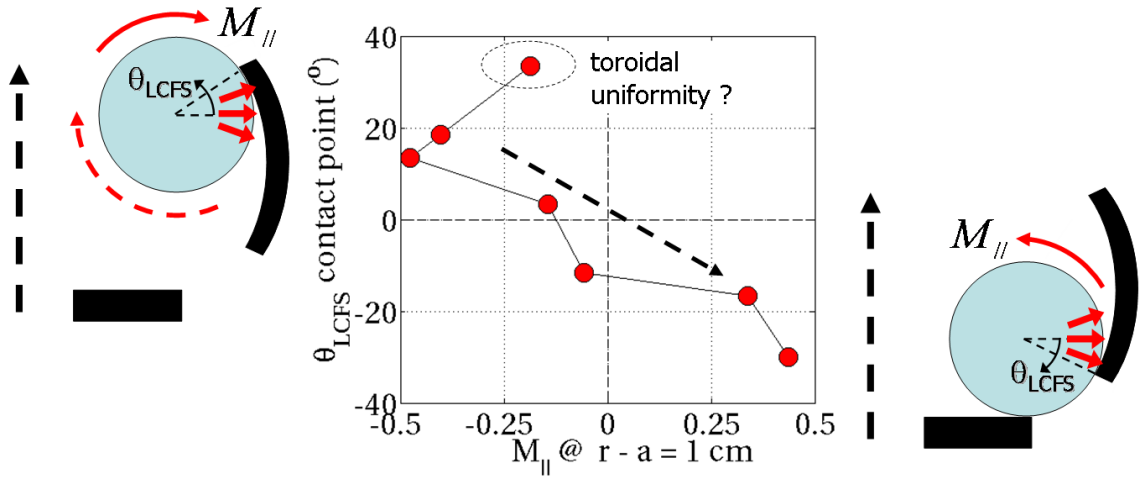

Figure 5.7: *TS42403 . The plasma is slowly rolled on the outboard limiter. The parallel Mach number measured 1 cm out of the LCFS is reported as a function of the poloidal location of the LCFS contact point with the outboard limiter. A continuous trend is observed until the plasma reaches the upper extremity of the limiter. For that location, we intimate that the effective toroidal uniformity of outboard limiters is broken.*

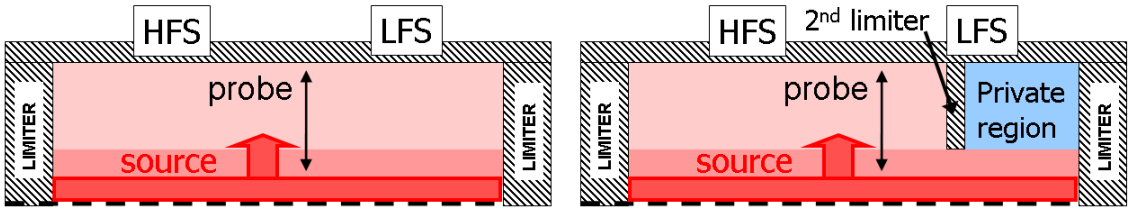

Figure 5.8: *Scrape-off layer scheme (r,//) with and without second limiter inserted on the LFS.*

bottom limiter and the outboard midplane.

As a proof of principle, let us consider the experiment performed on Tore Supra, following the previous technique 5.9. An outboard limiter is introduced in the SOL, until 2.8cm from the LCFS, and we check that the confined plasma is identical for the two discharges. After

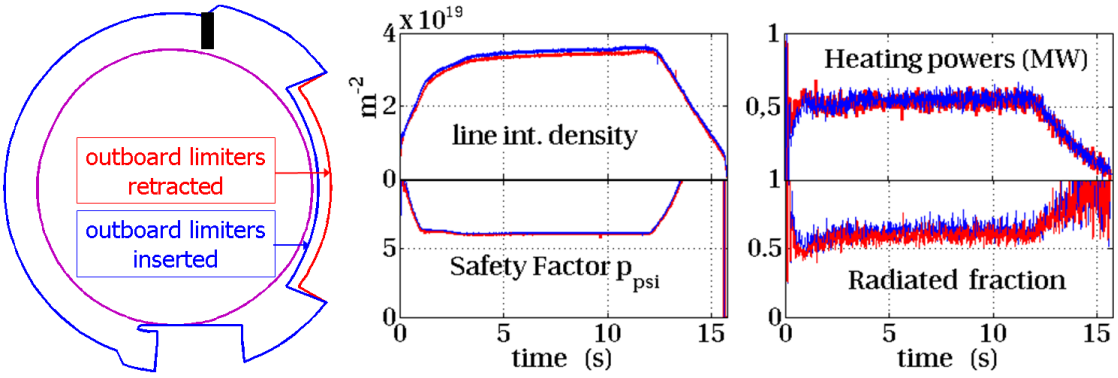

Figure 5.9: *TS35236 (with 2^{nd} limiter) and TS35238 (without). Left : poloidal cross section of the equilibrium, where is shown the radial position of outboard limiters during the two discharges. Right : the global plasma parameters are kept identical during the two discharges.*

a magnetic reconstruction, we notice that the probe is magnetically connected to the limiter, such that the field line interception is done at $\theta = -5^o$ at the limiter extremity, thus very close to the outboard midplane. The density profiles collected in the SOL can be compared and show a quantitative good matching upstream the limiter extremity $r - a < 2.8$cm, proving that in first approximation the limiter does not disturb the upstream plasma 5.10. Downstream the virtual limiter extremity, the profiles are strongly deviating since the radial decay length is $\lambda_r \approx 6$cm in the free SOL and $\lambda_r \approx 2$cm when the second limiter is inserted, whereas the parallel connection length varies respectively from 85m to 73m in the probed region. Again, the important modification of flux balance is not only related to the change of field line length, but rather to a change of the radial flux strength filling the probe region : the line averaged transport coefficient decays by a factor of about 2.5 in the probed region when the limiter is inserted. And again, our interpretation is that a significant fraction of the radial flux enters the private region, reducing the radial transport efficiency in the probed region. That is, the line integrated flux variable is able to quantify this effect . As mentioned on the figure 5.10, the total radial source at the virtual limiter position is about $S_r \approx 2.5 10^{21} \mathrm{m}^{-1}.\mathrm{s}^{-1}$, whereas it drops to $S_r \approx 1.3 10^{21} \mathrm{m}^{-1}.\mathrm{s}^{-1}$ when the second limiter is inserted. Thus, the radial source filling the private region is about $S_r \approx 1.2 10^{21} \mathrm{m}^{-1}.\mathrm{s}^{-1}$. As a matter of facts, the region in

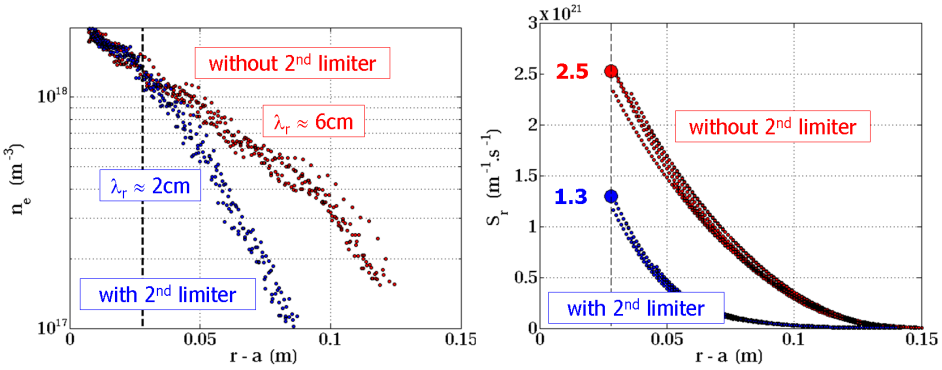

Figure 5.10: *Left : density profiles collected during 4 Mach probe reciprocations without second limiter (red) and with second limiter (blue). The radial position of the limiter extremity is shown in dashed black line. Right : Line integrated radial source for both experiment. The value at the limiter extremity is highlighted.*

between the bottom limiter $\theta = -90^o$ and the outboard midplane $\theta = -5^o$ receives almost half of the total particle flux crossing the flux surface $r - a = 2.8$cm, whereas its length is only 12m in the parallel direction thus 15% of the field line. That is, we already previously concluded 3.10 that the radial flux is located for about 85% in the low field side region $-90^o < \theta < 78^o$, that counts for 35% of the field line length, inferring that the radial particle flux is mainly localised around the outboard midplane.

We exposed the principle of field line tailoring applied to one particular condition for the poloidal position of the limiter with respect to the probe. The next part present a extension of this mapping method applied to a variety of dedicated conditions, particularly for the poloidal position of the probe connection on the limiter.

5.2.2.2 Poloidal mapping at the LCFS

In order to refine the radial source distribution around the outboard midplane, we decided to perform a scan of the poloidal location where the probe is connected to the limiter extremity. The radial position of the limiter extremity has been selected as close as possible from the LCFS to build a poloidal mapping of the radial particle flux crossing the LCFS. A first approach consists on fixing the plasma parameters and then successively inserting outboard limiters located at different toroidal angle 5.11. Unfortunately, only three movable limiters were available for that experiment, that has strongly limited the number of accessible poloidal positions of the probe-to-limiter connection for a given plasma scenario. On the other hand,

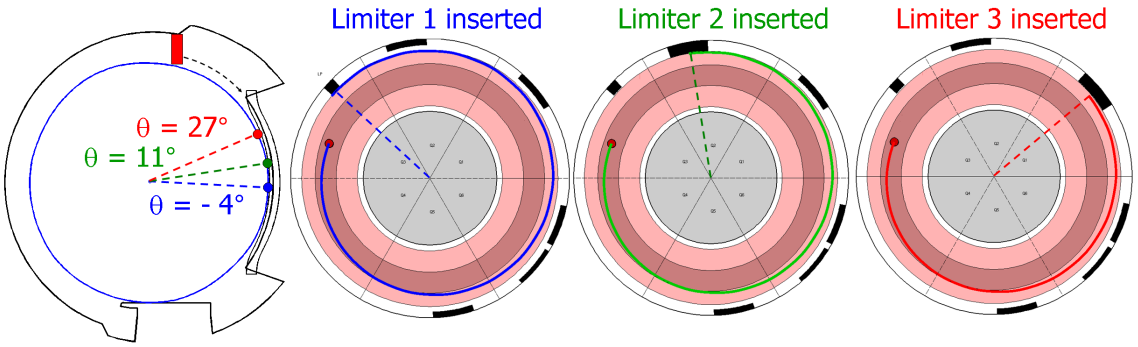

Figure 5.11: *For given discharge parameters, the poloidal location of the probe to limiter connection is varied by varying the toroidal location of the limiter.*

the source fraction measured at the probe position ($\approx 85\%$ on the LCFS) has not been observed to vary significantly, particularly with the edge safety factor. We decided to follow a first order assumption that the poloidal mapping of the radial flux does not depend on the confined plasma parameters - in a relatively closed intervall - such that the poloidal mapping can be completed by varying the edge safety factor for a given toroidal position of the limiter. The experimental session was performed over twelve discharges with an optimal range of poloidal positions along the outboard limiters :$-32^o \leq \theta_{lim} \leq 33^o$, for a range of plasma current 0.47MA$\leq I_P \leq$ 1.02MA. In order to avoid any SOL particle source artifacts from strong gas injections, the discharges were performed at natural density or low density. The price to pay is a low signal amplitude collected by the Mach probe such that radial profiles have sometimes a relatively poor radial extend 5.12. Secondly, due to recycling on second limiters, the density was not always perfectly matched between the reference and the limited experiment so that density profiles do not necessarily match at the limiter extremity 5.12. A last but not least issue concerns the fact that outboard limiters have a poloidal curvature radius larger than the plasma minor radius, such that if the poloidal position of a probe-to-limiter connection is chosen out of the midplane, the effective radial coordinate of that point is increased compared to the LCFS-to-limiter distance 5.12. Therefore, the radial position where is performed the poloidal mapping is subject to an uncertainty of a few centimeters ($\approx$ 2cm).

The poloidal mapping is effectively defined as the fraction of the radial source filling the

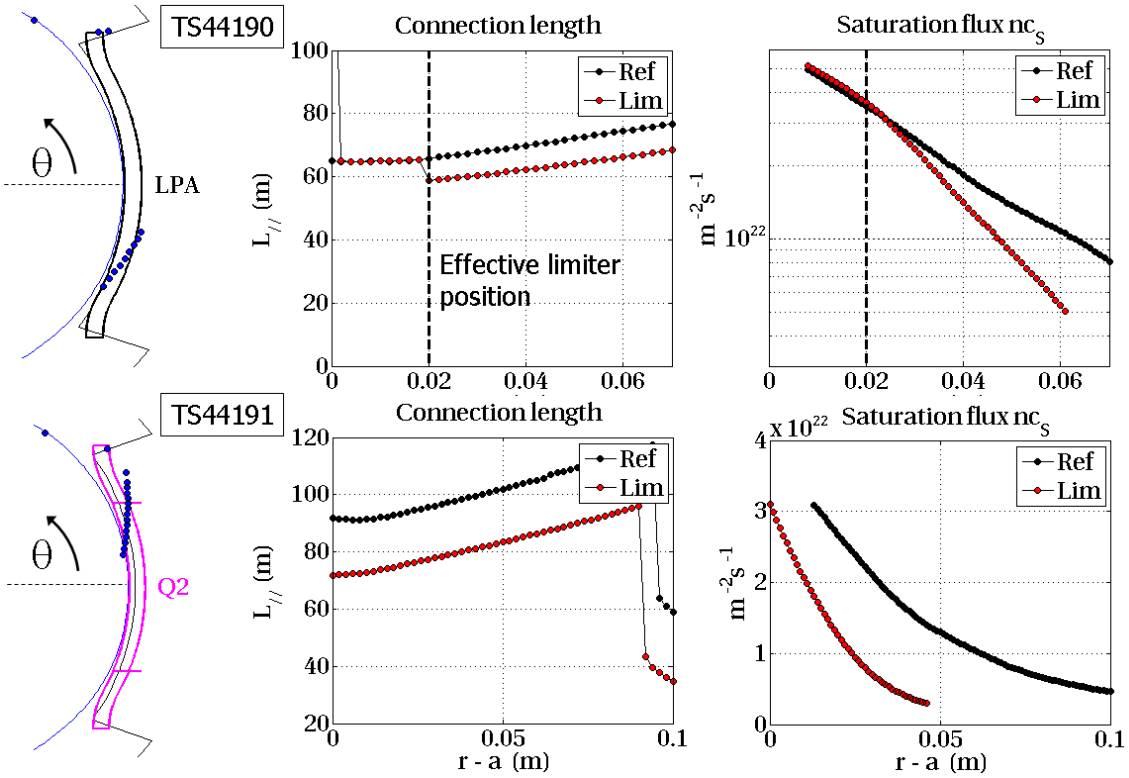

Figure 5.12: *Data collected on two different scenarios. Left : poloidal cross section of the outboard limiter where is shown the location of the probe-to-limiter connection along the probe reciprocation. Middle : radial profile of the parallel connection length experienced by the probe, with or without second limiter. Right : radial profile of the saturation flux $n_e c_S$ collected with or without a second limiter. the top case illustrates the uncertainty on the radial location of the limiter extremity, the bottom case illustrates the uncertainty on the density at the limiter extremity.*

private region, namely between the bottom limiter and the probe-to-limiter connection on the outboard midplane. Considering the line integrated radial fluxes S_r^{ref} and S_r^{lim} respectively evaluated on the reference discharge and on the discharge repeated with second limiter inserted, the source fraction is simply defined as:

$$f_S = 1 - \frac{S_r^{lim}}{S_r^{ref}} \cdot C_n$$

Where C_n is a density correction parameter counting for the discharge density mismatching, defined as the ratio of edge line integrated densities measured during both discharges.
Results are summarized on figure 5.13. As presented previously, the source fraction at the outboard midplane is close to 50% and increases with the poloidal location. Although the scatter defined by the set of experiments is relatively important, the tendency is clear and shows a continuity toward the source fraction measured at the probe location (top) during reference discharges. The mapping as it is performed does not directly yield the poloidal distribution of the radial flux, but rather an integrated distribution, obtained close to the LCFS. Before discussing the consistency with different spatial distributions of the radial flux, we present results obtained at different radial positions in the SOL.

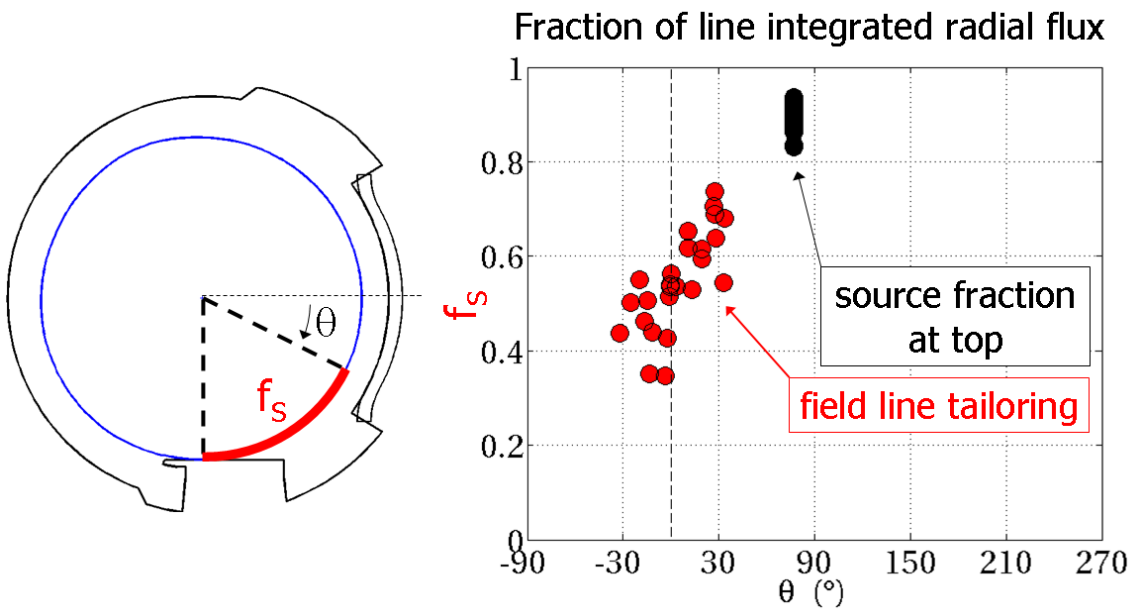

Figure 5.13: *Poloidal mapping of the fraction of line integrated radial source counted from the bottom limiter to a given poloidal location. Red points are obtained with the tailoring method applied to the previous set of experiments. The black points are calculated at the probe position during reference discharges.*

5.2.2.3 Mapping along the SOL radial profile

A similar tailoring experiment has been performed by varying stepwisely the radial location of the outboard limiter. That is, only one magnetic configuration has been used such that only one poloidal location on the outboard limiter is scanned : $\theta_{lim} \approx 10^o \pm 5^o$. The line integrated radial flux evaluated with a second limiter is compared to the value calculated without second limiter 5.14, and we found that roughly half of the radial source is located *above* the midplane for all radial locations of the tailoring process.

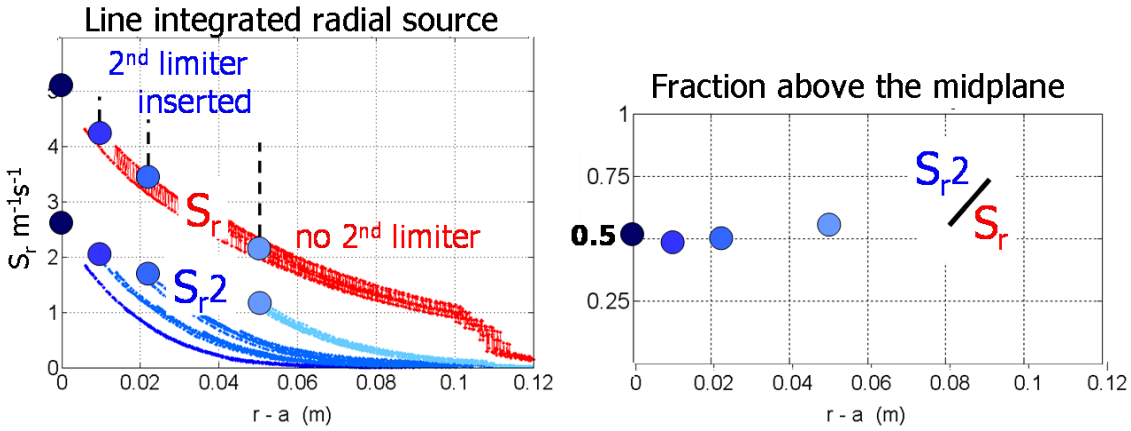

Figure 5.14: *Left : Comparison of the line integrated radial flux calculated in the reference discharge and for different radial position of the outboard limiter. Right : Radial profile of the source fraction located above the outboard midplane*

5.2.2.4 Synthetic poloidal distributions

From the set of experiments presented above, we find that the line integrated radial flux in the SOL is roughly centered at the outboard midplane. The more detailed poloidal mapping performed close to the LCFS can serve as an indirect estimator of the poloidal distribution of the radial flux. Our approach is to consider a synthetic poloidal distribution, for instance a Gaussian centered at the outboard midplane and adjust the width so that the radial source fraction estimated from parallel integral of that distribution describes the experimental mapping 5.15. As a first observation, the experimental mapping is absolutely not consistent with an uniform poloidal distribution of the radial flux as we emphasize along the chapter. Instead, a good coherency is found with Gaussian distributions centered at the outboard midplane with a half poloidal extend of about 50^o. There is obviously no physical reason why the radial

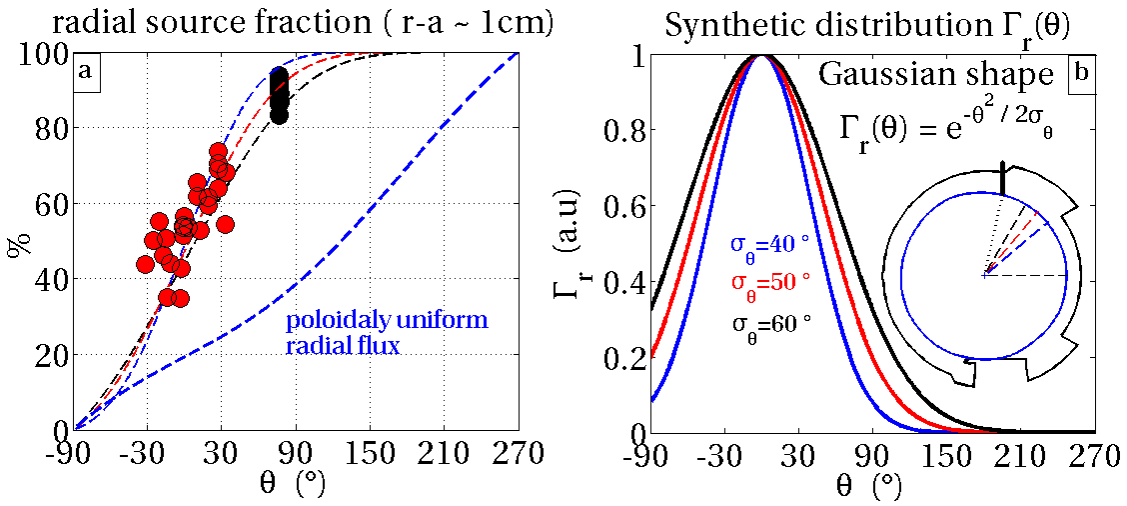

***Figure 5.15**: Left : poloidal mapping of the source fraction, compared to synthetic ditributions*

flux distribution should be a Gaussian, but we decided to use a regular analytical function to describe the radial flux as close as possible to what can be done from the experimental poloidal mapping. On the other hand we can try to build a step function that describes the radial flux enhancement at the outboard midplane, with adjustable parameters like the poloidal width and the enhancement factor. That done, we find that we need to insert a negative poloidal shift to the poloidal distribution in order to match the experimental mapping 5.16. The poloidal shift is not unlikely since we neglected in our model any transversal drifts, and we know that SOL drifts are in the negative poloidal directions.

To conclude, the experimental scatter on the poloidal distribution of the source fraction is too high to allow a precise deconvolution of the flux distribution. Rather, we decide - as a pragmatic approach - to use a Gaussian shaped distribution to describe the poloidal asymmetry of the radial flux in the SOL, since a centered Gaussian has only two adjustable parameters. In fact, we implicitly defined the Gaussian poloidal width by the extremal poloidal positions on the mapping, that are obtained directly from the probe reciprocation in a SOL free of second limiters (LFS source fraction). By assuming *a priori* that the flux is a Gaussian centered at

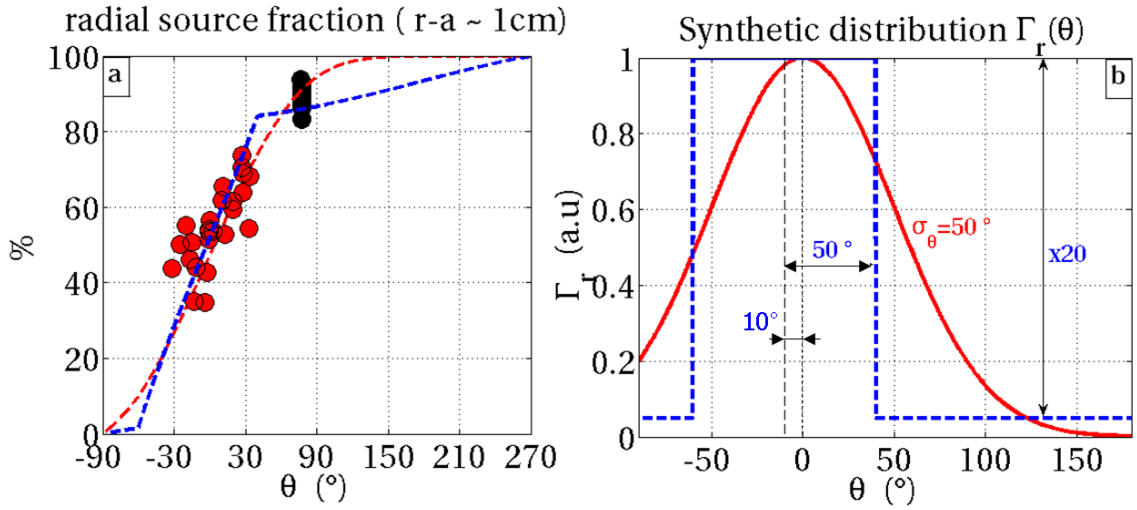

Figure 5.16: *The poloidal mapping of the radial flux can be compared to a synthetic gate function describing the flux enhancement at the outboard midplane. The function plotted has a half poloidal opening of* 50^o*, an enhancement factor of 20 compared to the background flux and a poloidal shift of* -10^o*.*

the outboard midplane, a single probe reciprocation is enough to determine the Gaussian parameters defined by its total and partial field-line integral, and thus build a particular poloidal mapping belonging to one particular experiment in order to compare that mapping to local turbulent measurements. Indeed, the line integrated radial flux evaluated from the probe reciprocation is composed of two contributions 3.10 : S_r^{LFS} and S_r^{HFS} that correspond respectively to the line integral on the LCFS from the bottom to the probe position and the integral from the probe to the HFS bottom. That is, the source fraction evaluated at the probe position $f_S = \frac{S_r^{LFS}}{S_r^{LFS}+S_r^{HFS}}$ can be directly interpreted in term of Gaussian poloidal opening 5.17.

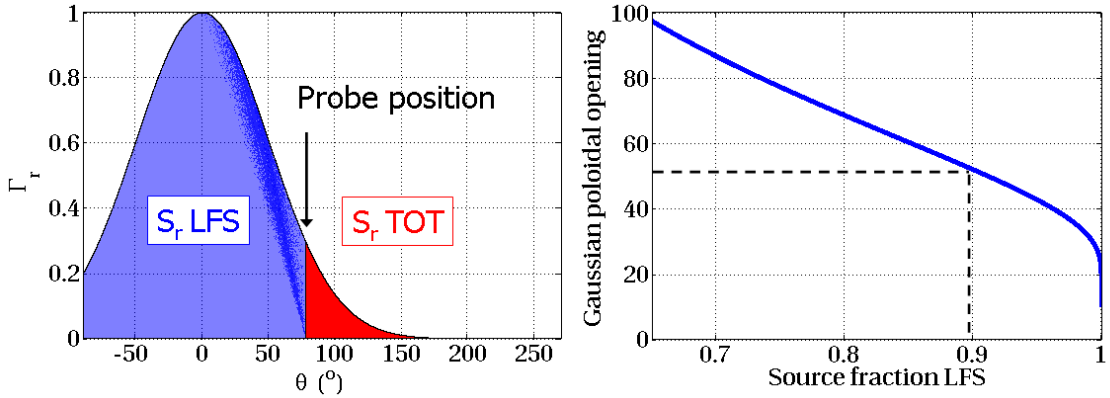

Figure 5.17: *Left : Gaussian poloidal distribution of the radial flux. The line integrated radial flux variable from a probe reciprocation is composed of both a LFS integral (blue) and a total integral (blue + red). Right : For a fixed probe position, the ratio is a bijective function of the Gaussian poloidal opening.*

We keep in mind that the local flux value extracted from the synthetic flux distribution is *a priori* not consistent since it depends strongly on the nature of the poloidal distribution, but

again, this approach is a first order tentative to conciliate global and local flux evaluation.

5.3 Discussion on the SOL model in the scope of previous results

5.3.1 Post analysis about the Reynolds stress

Now that the flux distribution along field lines is quantified, we would like to pay attention to the assumptions we made to deduce this mapping and verify their consistency. As we explained in the chapter related to physics of field lines 2.53, the SOL equilibrium is described under the assumption of constant pressure along field lines, by neglecting any transversal momentum flux. We are now able to evaluate - as a first order- the term corresponding to radial transfer of parallel momentum, since the flux distribution is approximately sufficient to evaluate the parallel velocity profile along the field line. The momentum conservation is rewritten including the transversal source :

$$\nabla_{//}\left[nc_S^2\left(1+M_{//}^2\right)\right]+\nabla_r\left(\Gamma_r c_S M_{//}\right)=0$$

Roughly speaking, the parallel flux is oriented along the field lines from the maximum of the particle flux location, namely the outboard midplane 5.18. Thus, the radial momentum source term reaches its maximum where the product of the particle flux with the parallel velocity is extremal, namely around the poloidal positions $\theta \approx \pm 45^o$. But since the momentum transfer is influencing the parallel gradient of the pressure, the effect of the momentum source on the pressure conservation is interpreted via the parallel integral of the momentum source from the probe to the limiters. In order to evaluate the relative error done by assuming a constant pressure from the probe to the limiters or to any location along the field lines, an error function $f_{Sm}(l_{//})$ is defined as the ratio of the parallel integral of the momentum source over the pressure measured at the probe position :

$$f_{Sm}(l_{//})=\frac{\int_0^{l_{//}}\nabla_r\Gamma_r c_S M_{//}}{nc_{S,0}^2\left(1+M_{//,0}^2\right)}$$

Where the position 0 notes the probe location. We simplify the latter expression by assuming a locally radially constant ion sound speed and replacing the radial gradient by the radial decay length of the particle flux:

$$f_{Sm}(l_{//})=\frac{1}{\lambda_r nc_S\left(1+M_{//}^2\right)}\int_0^{l_{//}}\Gamma_r M_{//}$$

The parallel profile of the Mach number is compiled from the parallel source coordinate defined with the parallel distribution of the radial particle flux 5.1. The error parameter is compiled for a variety of plasma conditions, and is found to be less than 20% - see figure 5.18. In standard SOL topology, namely with the main limiter either at the bottom or at the low field side, the pressure conservation criterion from the probe to the limiter is acceptable with an error not exceeding 5%, inferring that the density extrapolation from the probe to the limiter

sheath entrance 3.11 is not suffering the radial source of momentum. If the extrapolation is done toward the high field side limiter, the radial flux is very low in that region as well as the momentum source. For the low field side extrapolation the flux is strong but the field line is subject to a flow reversal such that the related momentum transfer is roughly antisymetrical with respect to the midplane, that moderates the integral from the probe to the bottom limiter. The effect is more delicate to estimate when a second limiter is inserted at the outboard midplane since the midplane symmerty is broken. the pressure extrapolation suffers an error of about 15% from the probe to the outboard midplane limiter that is considered acceptable within all asumption allready done along the study.

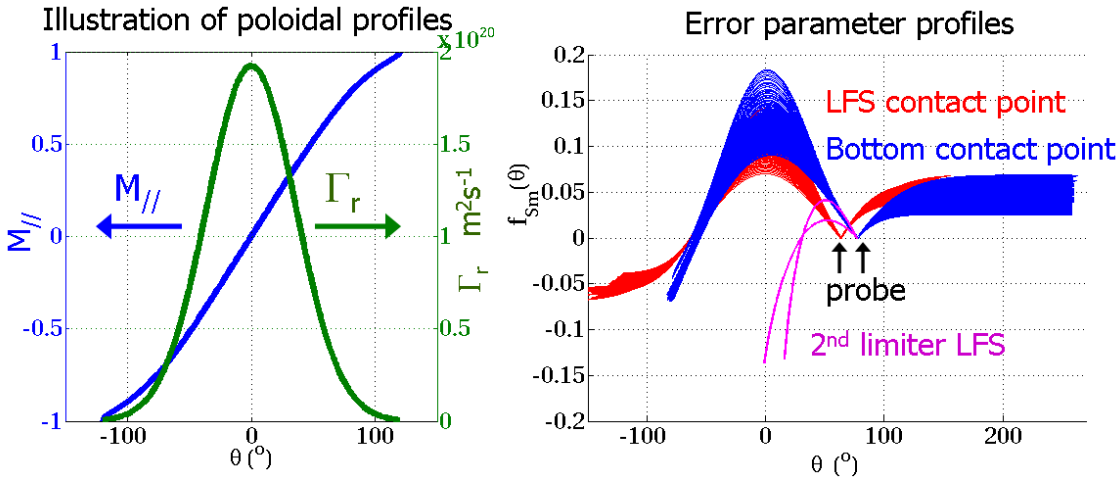

Figure 5.18: *Left : Illustration of a Gaussian profile of the radial particle flux and the related parallel Mach number along a field line. Right : Poloidal variation of the error function along the field line, for a variety of plasma conditions.*

Finally, validation of the pressure conservation assumption is performed *a posteriori* from the radial flux mapping. The parallel momentum transfer from the radial flux is not showing to play an important role in the onset of the parallel pressure equilibrium, that is likely since the pressure conservation was a major assumption leading our experimental approach of the SOL transport.

5.3.2 Numerical simulations of SOL shaping : SOLEDGE2D

The SOL tailoring experiment has received a great support from numerical simulations based on a 2D numerical code : SOLEDGE2D, that has been recently developed in terms of a collaboration between CEA and the M2P2 laboratory (Marseille) [1]. The model is fluid and describes in a (r,//) slab geometry the temporal evolution of the particle flux balance and the parallel momentum conservation in the confined region and the SOL. Except the viscous term present in the momentum equation and the imposed diffusive nature of the radial flux, the model - in steady-state - is identical to the one we used along the thesis. Despite the fact that the electrostatic turbulence has not yet been implemented, the originality of the numerical code stands in the possibility to add different limiters in the simulated domain by a penalisation

[1] G. Ciraolo, E. Serre, L. Isoardi, F. Schwander, H. Bufferand

technique [Serre].

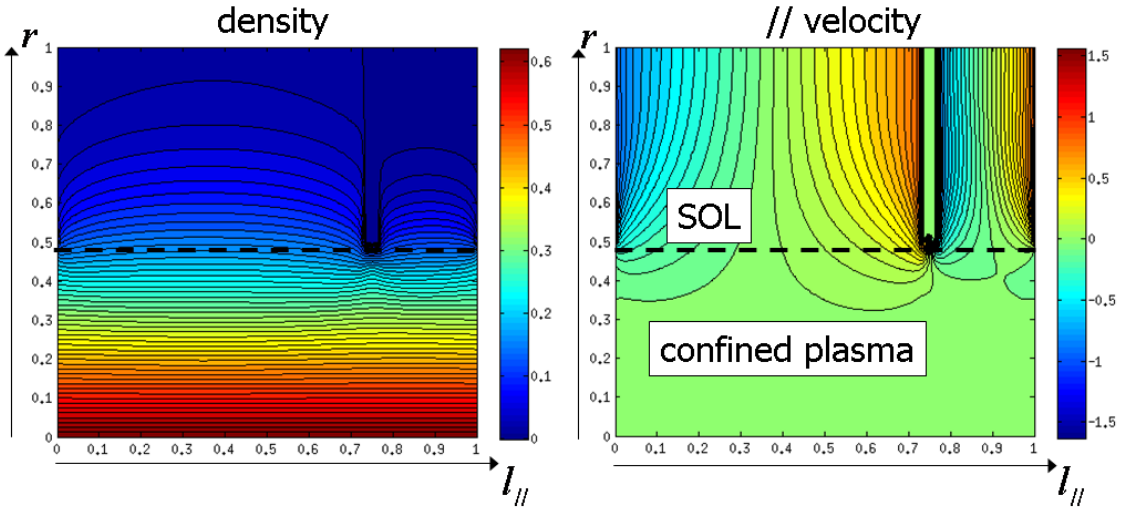

Figure 5.19: *Numerical simulation of a complex SOL (r,//) with SOLEDGE2D : limiters determines the // boundary conditions and a second limiter is inserted inside the SOL. Left : density map . Right : parallel velocity map.*

The tailoring experiment has been simulated by defining a spatially asymmetric diffusion coefficient enhanced at the outboard midplane - see firue 5.19. The first important result is that the pressure is effectively almost constant along field lines : the viscosity does not play a significant role in the establishment of the parallel pressure such that the parallel extrapolation of the local flow variables from a virtual the probe position to the limiters is correct within 10% of error. Therefore the line integrated radial flux calculation as we proposed in the thesis is found to be significantly close to the real value , within 10 % of error.
Secondly, the flux mapping built indirectly from the field line tailoring has been complied for different location of the second limiter along the field lines. It turns out that the numerical simulation suffers from a crucial issue : the diffusive nature of the flux implemented in the code implies that the sharp profiles taking place behind the second limiter modify the profiles *in front* of it - see firue 5.19: the assumption that the second limiter does not disturb the plasma (in front of it) is not verified. Anyhow the result of the numerical tailoring is in qualitative good agreement with the initial diffusion coefficient asymmetry, inferring the reliability of the experimental technique to describe the particle flux asymmetry [Ciraolo].

5.4 Mapping consistency with transport dedicated experiments

This section is devoted to the comparison of the previous steady-state flux mapping - described as a centered Gaussian - with different experiments dedicated to SOL transport. First of all, we start with comparison of density profiles measured at the outboard midplane using fixed Langmuir probes located on heated antenna. Then we perform a comparison of the model previsions with steady-state flows measured at the top when the plasma is rolled

on the outboard midplane. Finally, the local ExB turbulent transport measured at the top is compared to the poloidal mapping.

5.4.1 Density profiles at the outboard midplane

Most of the movable outboard limiters corresponds to heating antenna protection, and these antennae are equipped with fixed Langmuir probes lying on the antenna surface. One experiment [2] was consisting on defining a private region by two ICRH antennae separated by 120 degree toroidally 5.20 - the parallel connection length in the private region is $L_{//} = 6$m - and scan the radial position of a third antenna (LH) lying in between. The ICRH limiters are positioned 3 cm from the LCFS and the LH antenna position was stepwisely scanned radially from the ICRH limiter position to 1.5 cm behind. For each radial position, the plasma density in front of the LH antenna is collected by 3 fixed Langmuir probes during ohmic phases of the experiments. The confined plasma density is kept rigorously constant so that a radial profile of the density in the private region is obtained from all radial positions of the LH antenna. Actually, it is known by experience that these probe underestimate the local density that we

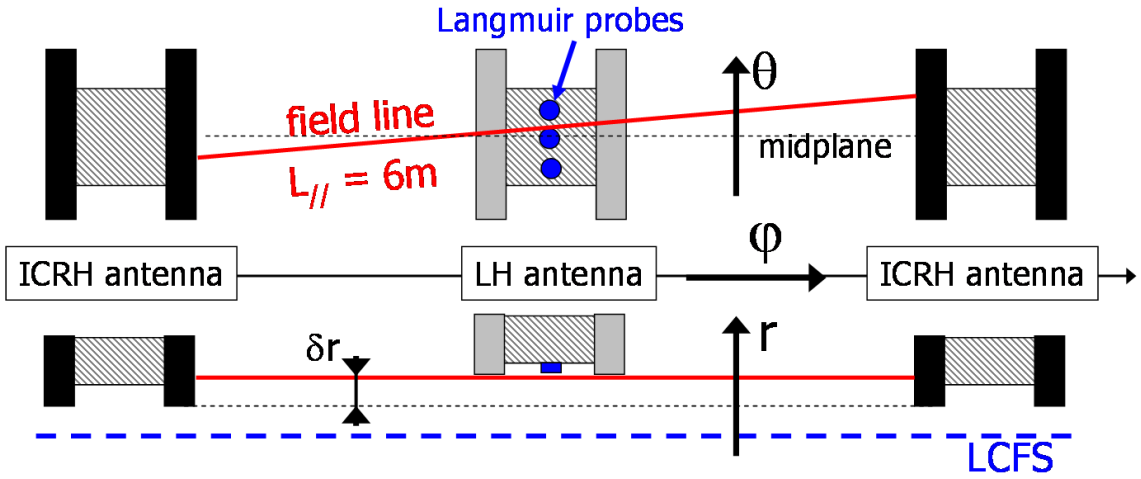

Figure 5.20: *antennae positions along the toroidal axis. The antenna of interest is placed in between two ICRH antennae. Top : Face view of the antennae configuration. The LH antenna is equipped with 3 fixed Langmuir probes . Bottom : Top view of the configuration. The two ICRH antennae are pushed radially upstream from the LH antenna so that the LH Langmuir probes measure a plasma density from short field lines ($L_{//} = 6$m) limited by the ICRH antennae.*

would measure with a Mach probe, and they even return different density value depending on the poloidal location on the antenna 5.21. On the other hand, we are not interested in the absolute amplitude of the density, but rather on the radial decay length measured in the private region. Indeed, the decay is similar for all measurements on the antenna and is about $\lambda_r \approx 1.1cm$. Combined with the length of the private region, we can build an effective dimensionless transport coefficient 3.20 $M_r = \frac{\lambda_r}{L_{//}}$ equal to $M_r \approx 1.8 \quad 10^{-3}$. This coefficient characterizes the radial transport filling the private region, thus at the outboard midplane -

[2] dedicated to the coupling efficiency of an LH antenna

the poloidal extend of the private region is $\Delta\theta = \pm 18^o$. Interestingly, the transport coefficient is almost two times higher than what is calculated from a probe reciprocation performed in a similar discharge but without second limiters inserted into the SOL. Indeed, the density profile measured at the top in a free SOL exhibits a radial decay length of 6cm for a parallel connection length of 65 m, corresponding to a transport coefficient of $M_r \approx 1 \quad 10^{-3}$. We have in that experiment a clear proof of the flux enhancement at the outboard midplane. A more

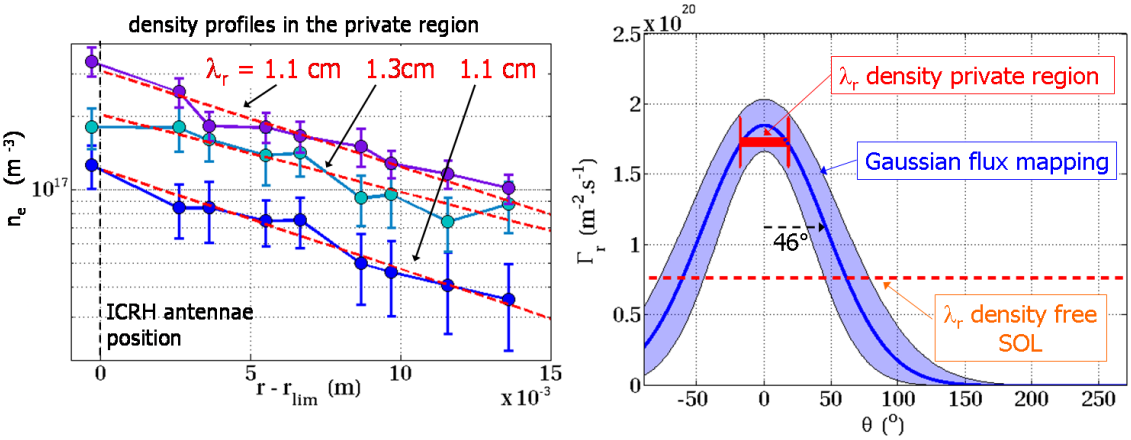

Figure 5.21: *Left : TS45199 to TS45209. Density profiles measured by 3 probes fixed on the moving antenna. The radial position is indexed from the extremity of the private region defined by the 2 ICRH antennae. Right : Poloidal mapping of the radial flux at the radial entrance of the private region. Is shown the poloidal Gaussian mapping calculated from a Mach probe reciprocation (TS44789), the local flux estimated from the density decay length in the private region (blue) and the line averaged flux estimated from the density profile in the free SOL.*

quantitative comparison is performed by evaluating the poloidal distribution of the radial flux from the Mach probe reciprocation in the free SOL. The poloidal distribution is compiled at the virtual private region entrance, and compared to the local flux at that position. This local flux is defined as the local saturation flux measured by the Mach probe $n_e c_S$ multiplied by the local effective transport coefficient M_r deduced in the private region $\Gamma_r = n_e v_r = n_e c_S M_r$. As seen on the figure 5.21, a quantitative good agreement is found between the local flux and the local enhancement deduced from the poloidal mapping. The effective radial flux deduced from the density profile in the free SOL is obviously lower than the maximum and corresponds more or less to a line average value.

This experiment shows that the local enhancement at the outboard midplane deduced from the Gaussian poloidal mapping is consistent with other indirect measurements at the midplane. Currently, this model of flux enhancement is considered for the modeling of wave propagations from the outboard midplane, since detailed density profiles in private regions are crucial for determining the wave propagation efficiency in front of wave launchers [Preynas 10].

5.4.2 Parallel flow reversal during plasma rolling

Now let us focus on the effect of flux enhancement on the drive of parallel flows. On standard configuration, we easily understand the quasi-sonic parallel flow measured at the top

as a pressure balance flow from the particle source located at the outboard midplane toward the inboard midplane. This simple understanding can be in fact applied to more complicated equilibrium as soon as the particle flux distribution is known with respect to limiters position. Thus let us consider the most interesting flow experiment done by rolling the plasma on the outboard midplane 5.22. Our purpose is to derive the flow amplitude at the probe position from the previous flux distribution, depending on the limiter position with respect to the outboard midplane. A simple approach to derive the Mach number from the flux distribution is to make

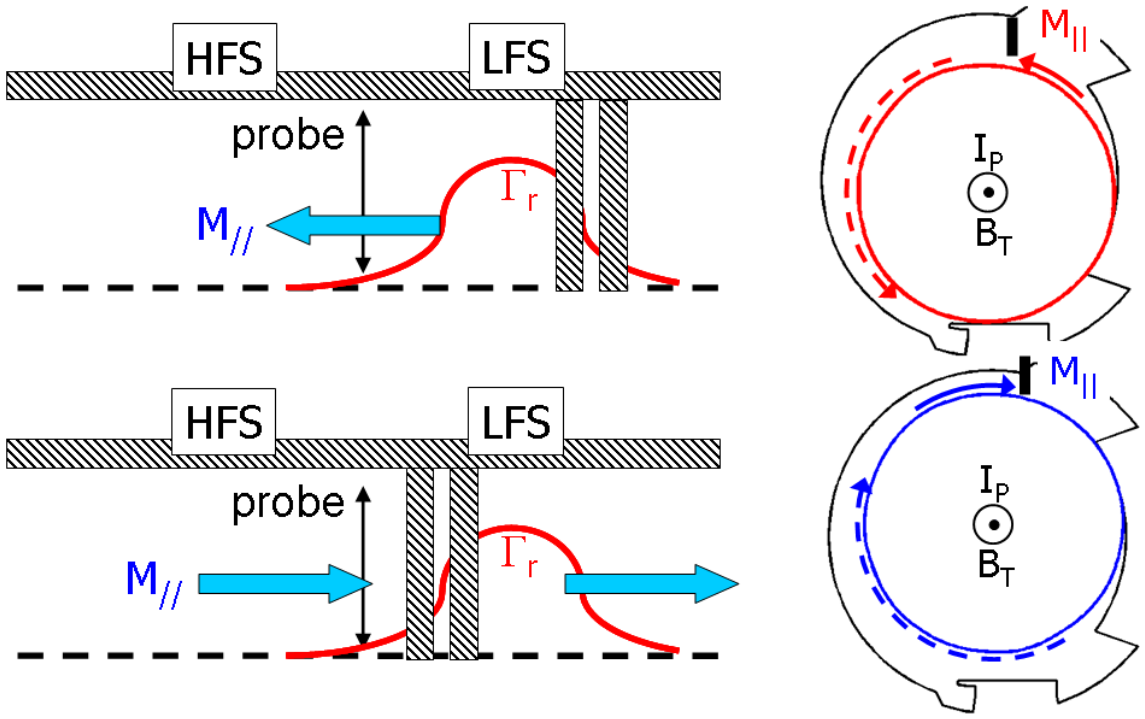

Figure 5.22: *SOL model for the rolling plasma experiment. Top : When the plasma is in contact with the bottom outboard limiters, the enhanced radial source force the parallel flow in the co-current direction. Bottom : When the plasma is in contact with the top outboard limiters, the flux forces the parallel flow in the co-current direction.*

use of the source line coordinate previously introduced 2.55 :

$$\frac{M_{||}}{1+M_{||}^2} = s - \frac{1}{2} \quad \text{with} \quad s(l_{||}) = \frac{\int_{-L/2}^{l_{||}} \nabla_r \Gamma_r dl_{||}}{\int_{-L/2}^{+L/2} \nabla_r \Gamma_r dl_{||}} \tag{5.1}$$

That is, the parallel Mach number is a direct consequence of the parallel distribution of the flux *gradient*, and not the flux direclty. On the other hand the radial decay length is considered not to vary strongly along the parallel coordinate since it is a consequence of line averaged phenomenon, such that the source coordinate s is calculated directly on the flux distribution. The parallel profile of the flow is easily deduced for any limiter configurations, in particular for the rolling experiment 5.22. In particular, the main bottom limiter has been considered when the plasma is on the *down* configuration. Surprisingly, we are able to reproduce almost perfectly the Mach number dependence with the plasma position 5.23. Only for the *up* configuration the model does not reproduce perfectly the flow behavior, and we consider the reason belongs

to a complicated experimental limiter pattern [3] that is not taken into account in the model. The key parameter of the flux distribution involved in that rolling experiment is its poloidal

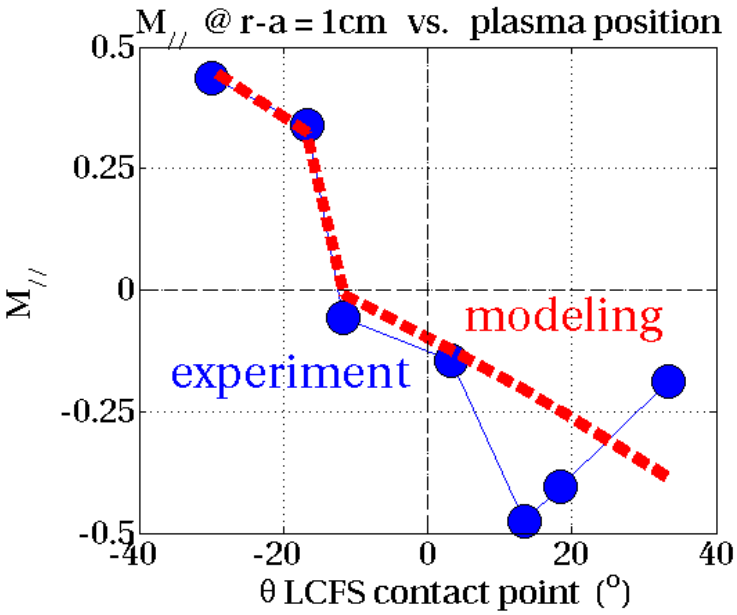

Figure 5.23: *Evolution of the Mach number measured at the top function of the position of the plasma along the outboard limiter, either from experiment or modeled from a a Gaussian shaped flux distribution centered at the midplane with a poloidal half opening of* 50^o.

opening. The reliability of our model to describe the experiment infer that this parameter, even defined as a Gaussian opening, describes correctly the flux asymmetry.

5.4.3 Comparison with local ExB turbulent flux

Up to now we have discussed the poloidal asymmetry of the radial flux without any assumption on its nature. The flux amplitude is anyhow in the turbulent scale compared to neoclassical predictions, and we inferred in the previous chapter the qualitative agreement between local turbulent transport - from ExB flux - with the density profile. Now, it is possible the compare in a quantitative approach the local ExB flux to the steady-state poloidal mapping within the Gaussian model 5.24. The comparison is made by selecting discharges during which both poloidal rake probe and Mach probe are plunging at the same time. At a given radial location, the poloidal mapping is extracted from the parallel flow data, and the local turbulent flux is calculated as the product of the local density measured by the Mach probe times the turbulent ExB transport coefficient measured by the poloidal rake probe. The agreement is remarkable between both quantities 5.24. The turbulent flux can be corrected by the error function related to the electric field under sampling 3.17, and shows an agreement in the error bar of the poloidal opening of the poloidal distribution.

In first sight the local ExB flux seems to overestimate the poloidal mapping even if it stays in a relatively good agreement for different plasma conditions 5.24, but we keep in mind that

[3] due to the low toroidal number of limiter and their low effective poloidal extent in that configuration, the effective toroidal uniformity is questionable

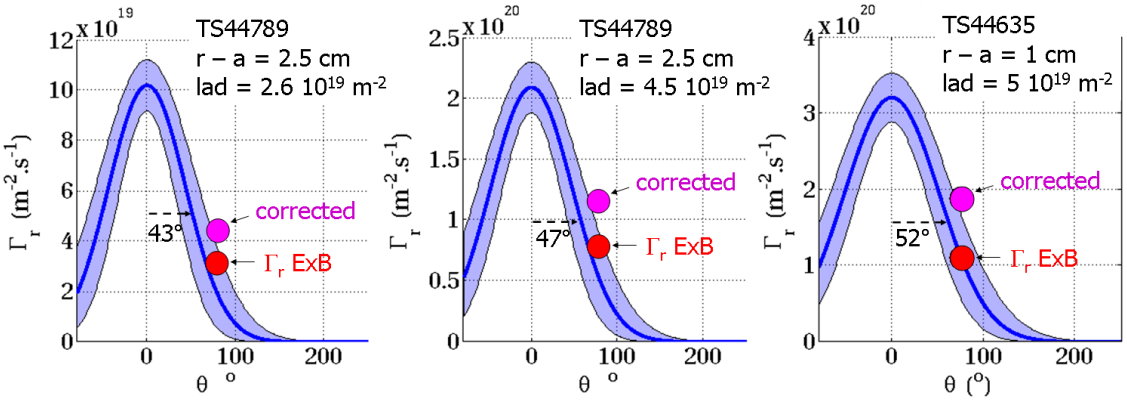

Figure 5.24: *Poloidal mapping of the radial flux measured with a Mach probe close to the LCFS (blue curve), with an error bar of 20% on the poloidal half width. The local turbulent flux measured with the poloidal rake probe is superimposed as well as the corrected term from electric field smapling. 3 different plasma conditions (density) are shown.*

the local value deduced from the line integrated flux interpreted as a Gaussian distribution is totally artificial. Indeed, when we compare the radial profile of the local flux calculated as presented above, we found a relatively good agreement close to the LCFS, whereas the local mapping strongly under estimate the local ExB flux in the far SOL 5.25. One of the possible reason is that the Gaussian opening deduced from the line integrated flux decreases to low values in the far SOL, that might put the Gaussian approximation questionable there.

More generally, we find that for a variety of plasma conditions and radial positions along the

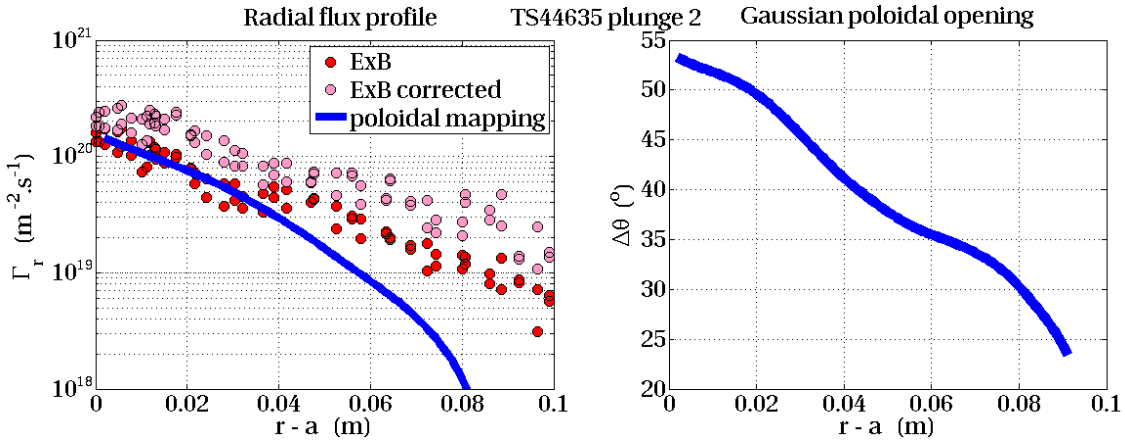

Figure 5.25: *TS44635 10s. Radial profile of the radial flux at the plasma top (probe position). The local flux deduced from the poloidal mapping is shown in blue, the local ExB flux is shown in red circles and its correction from electric field sampling is shown in coral. The fast decay of the local mapping might be due to the Gaussian definition of the flux asymmetry : on the right is shown the radial profile of the Gaussian half opening, that drops significantly in the far SOL.*

SOL, the local ExB flux is in relatively good agreement with the local steady-state mapping 5.26, although a large scatter is noticeable. For the lowest flux values -measured in the far SOL - the discrepancy is large but might be related to the latter remark.

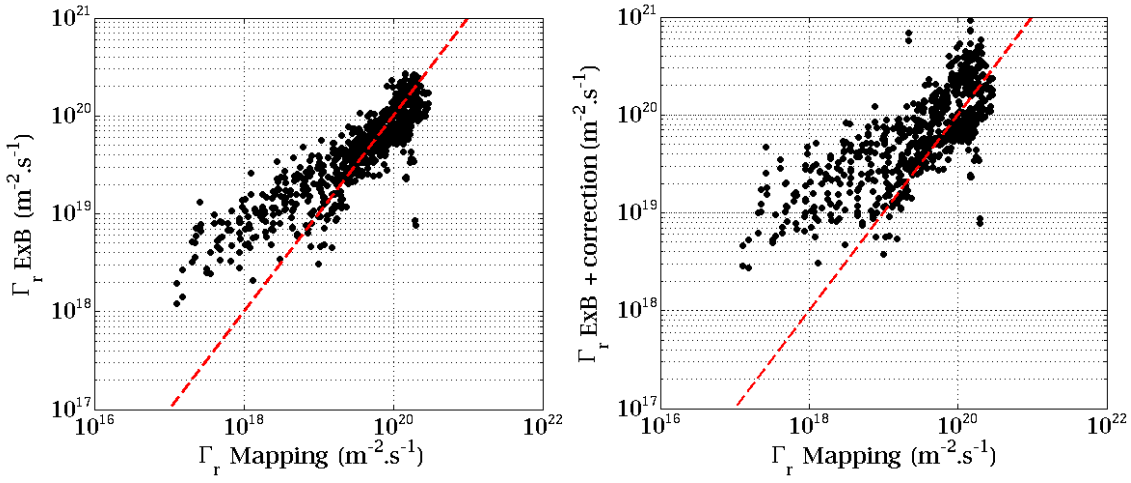

Figure 5.26: *Left : Comparison of the local radial flux from the mapping with the local ExB flux for a set of 10 plasma conditions . Data are collected along the radius of each plunges. Right : comparison with the ExB flux corrected with the electric field sampling error.*

5.5 Consistency between different diagnostics on Tore Supra

As a first experimental result, we found that the steady-state radial flux is highly localized around the outboard midplane. The distribution is described as a Gaussian with a poloidal width of about 50% depending mainly of the radial location in the SOL. Then, this steady-state mapping is compared to ExB fluctuating flux measurements performed at the plasma top, and a relatively good agreement is found. Finally, the fast visible imaging has shown that plasma filaments, aligned with magnetic field lines, exist and propagate radially mostly at the low field side poloidal section of the plasma. Noticing that fluctuations measured at the top can be straigforwardly interpreted as the signature of density filament convection, we infer that these fluctuations do correspond to the tail filaments observed at the outboard midplane by fast imaging. Indirecly but coherently, we infer that the steady-state flux enhancement at the outboard midplane is due to the poloidal asymmetry related to these plasma filaments, and thus to a poloidal asymmetry of the ExB radial flux, although any direct proof would need probe measurements at the outboard midplane.

5.6 Consistency with other tokamak experiments

5.6.1 Turbulent flux asymmetries

The ExB flux is often calculated at the outboard midplane of other tokamaks - TCV, DIII-D, Alcator C-mod. The intermittent nature of the flux is similar to what is observed at the Top of either Tore Supra or JET, shows an interchange like behavior with almost 0 phase shift between density and electric field fluctuations [Rudakov 02] [Garcia 07a] [Boedo 03], and the conclusion made from these experiments is that the transport at the midplane is dominated by the convection of density bursts. On the other hand, the local ExB flux at the outboard midplane is always found too high in amplitude to explain the density e-folding length [LaBombard 02]

[Fundamenski 07], and authors inferred a probable spatial asymmetry of the turbulent flux, enhanced at the outboard midplane. Similarly turbulent probe measurements performed at the inboard midplane of Alcator C-mod [Smick 10] have shown a robust zero turbulent flux, as well as fast imaging does not reveal any turbulent pattern [Terry 03] in that region proving directly that the ExB flux is asymmetrical. Thus experimental observations performed on different machines using different techniques come to the same qualitative conclusion. But still remains a skepticism in comparing divertor plasmas and limiter plasmas, sometimes due to apparent contradictions in the comparison of transport behavior. We would like to address an illustration of this disagreement and convince we can effectively resolve it in the scope of our transport model.

5.6.2 Radial dependence of the turbulent transport coefficient

.

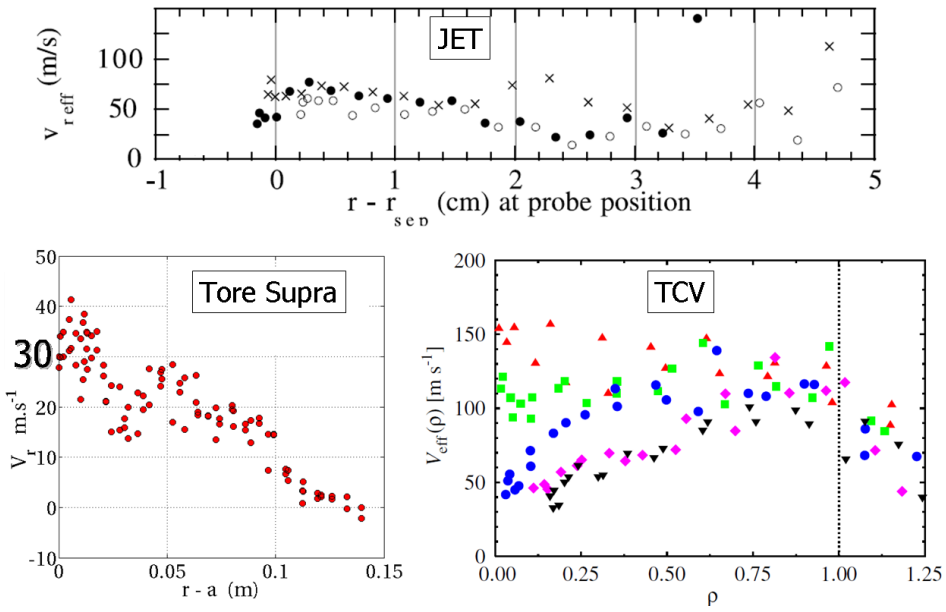

Figure 5.27: *Top : Effective convection velocity extracted from fluctuations measured at the top of JET (L-mode). Bottom left :transport coefficient at the top of Tore Supra. Bottom right : Same quantity at the outboard midplane of the TCV tokamak, for various density conditions.*

As observed on several tokamaks (TCV [Garcia 07a], DIII-D [Moyer 97], Alcator C-mod [Smick 10]), the ExB transport coefficient increases with radius from the LCFS, whereas a decay is usually found at the top of JET [Garcia-Cortes 01] or Tore Supra 5.27. Up to now, no consistent explanations were formulated for that unpleasant disagreement, but some arguments were preliminary formulated that circular and limited plasmas are not subject to the same transport dynamics. The matter is of crucial interest when considering transport modelings and extrapolations for larger scale fusion reactors like ITER : what are the physically relevant inputs in term of transport coefficients in the SOL? In fact, the disagreement can be resolved in the scope of understandings we have from Tore Supra experiments: As illustrated above

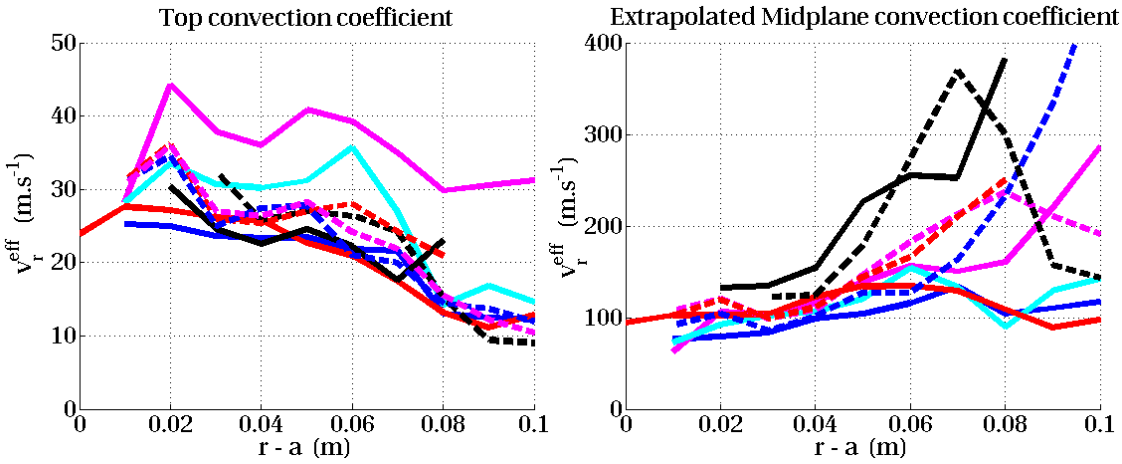

Figure 5.28: *Left : Set of convection coefficient profiles extracted at the top of Ohmic discharges on Tore Supra. Right, Extrapolated convection coefficients from the top to the outboard midplane assuming a Gaussian poloidal variation resolved by probe measurements.*

5.25, the poloidal extend of the radial flux is found to decrease with increasing distance from the LCFS. Although a Gaussian opening might not be the fully reliable parameter to describe the flux distribution, the statement does not depend on the nature of the distribution.
The poloidal peaking of the flux is an increasing function of the radius, inferring different behaviors for radial profiles of turbulent coefficients collected at the top or at the midplane. As a proof of principle, we try the following exercise : The flux asymmetry is in first order due to the transport coefficient asymmetry, assuming a constant density along field line. This assumption is not so brutal since in our model of SOL plasma equilibrium 2.55, the parallel profile of the density computed with a Gaussian like flux distribution shows a variation of only 30% from the outboard midplane to the probe position, whereas the flux drops by a factor of at least 2. Thus, the Gaussian poloidal mapping of the radial flux reflects the poloidal variation of the transport coefficient, that can be extrapolated from the top to the outboard midplane, along the SOL radial profile 5.28. As a result, we observe effectively that the extrapolated convection coefficient toward the outboard midplane is an increasing function of the radius, as really calculated for midplane measurements. Besides, amplitude of transport coefficients mapped at the midplane of Tore Supra are in ordering consistent with midplane measurements performed at TCV or Alcator C-mod. Of course, the top-to-midplane extrapolation is sensitive to the shape of the real distribution, but again the proof of principle made hereby is not senseless and shows that we are able to consiliate -more or less quantitatively - the measurements performed on different machines with the same transport model applied to either divertor or limiter plasmas.

5.7 3D properties of plasma fluctuations

In the scope of Tore Supra experimental findings and in coherence with other tokamak experiments, we claim that the turbulent ExB transport of particle is highly localized at the outboard midplane. Although filaments observed by fast imaging have a given extent along the

magnetic field, the previous conclusion infer that this extent is finite, such that these filaments are not flute modes at least concerning the particle flux carried by them. We can deduce an estimate of the parallel wave number of these filaments from the outboard midplane. A poloidal extend of $\pm 50^o$ is assumed, and reported in term of parallel length, giving $\lambda_{//}/L_{//} \approx 0.2$ at the outboard midplane. This finding is in apparent contradiction with what was observed on JET [Thomsen 02]. By looking at the cross-correlation between saturation current fluctuations measured along field lines at various parallel distance, a relatively good correlation was found ($> 40\%$) even when the fieldline was passing in the high field side and under the X-point. These observations were somehow the basement of considering flute modes $k_{//} \approx 0$) as the dominant parallel property of turbulence in the SOL. Consequently, a variety of interchange computationnal simulations are based on that approximation, like TOKAM2D [Sarazin 03]. For the simple reason that assumptions made in TOKAM2D are not consistent with experimental results of Tore Supra, we did not try to make a quantitative comparison between experiment and modelling, although experimental evidences support the interchange phenomena. In the following, we propose some elements of discussion on the parallel propetries of the filaments in the scope of experimental observations. Some elements are proposed as starting points for possible further analysis and should not be considered as accomplished works.

5.7.1 Parallel extent of interchange modes

The statistical properties of density and electric field fluctuations are good indicators of the nature of the related instability creating these plasma filaments. Adding to the picture the particle flux enhancement in the bad magnetic curvature region is considered enough to agree that interchange instability is the key mechanism for generating the SOL transport. A relatively simple picture of underlying mechanism is proposed 5.29:

- Let us consider an over-dense plasma structure in the plan transversal to the magnetic field, defining a centripetal pressure gradient all around the structure.
- Diamagnetic currents flow around the structure, scaling with $\propto 1/B$. Due to the magnetic field inhomogeneity, the transversal diamagnetic current is inhomogeneous, leading to effective charge accumulations that polarize the density structure.
- The electric field created by the potential eddies makes the over-dense structure to propagates along a direction opposite to the magnetic field gradient.

.

That simple mechanism explain why density structures are effectively convected radially outward at the outboard midplane and why hypothetic density structures born at the inboard midplane should be convected radially inward (stabilizing effect) thus rendering a spatial asymmetry of the transport. On the other hand we simply neglected the parallel extent of polarization. Indeed, a density structure exited at the outboard midplane necessarily extends along the field line with the reliable potential surrounding to propagate radially outward such that the

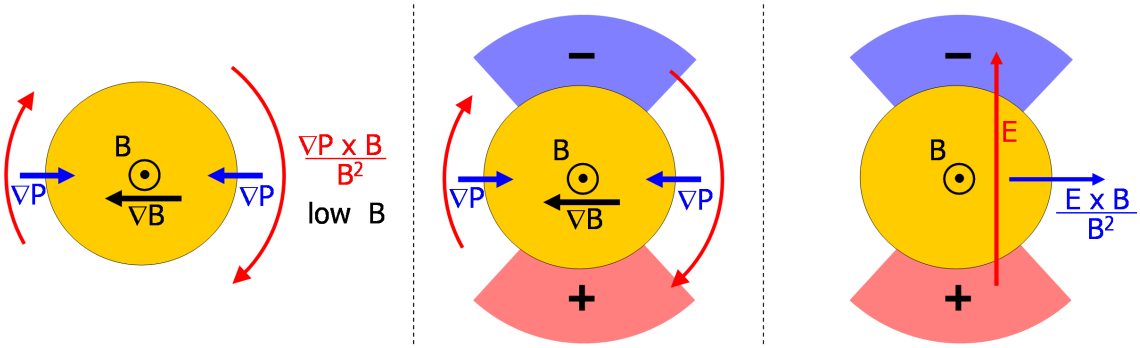

Figure 5.29: *Mechanism for self-propagation of an over-dense plasma structure*

entire filament elongated in the parallel direction propagates radially outward (flute approximation). Moreover, the parallel charge losses act as a regulating mechanism for the polarization growth that moderates the previous self-convection mechanism.
The exercise can be done to order the parallel extent of a density structure born at the outboard midplane. The simple model we propose is a balance between diamagnetic current and parallel charge losses :

$$\nabla \cdot \mathbf{j}_{dia} + \nabla_{||} j_{||} = 0$$

The diamagnetic current is expressed via the non-ambipolar diamagnetic drift velocity 2.39 and the parallel current is deduced from the ohm's law : $j_{||} = \sigma_{||} E_{||}$ where $\sigma_{||} \approx 3.610^7 [T_e($ keV$)]^{3/2}$ohm^{-1}.m^{-1} is the parallel conductivity in a collisional regime [Stangeby 00]. The previous equation is expanded and written :

$$\frac{-2\nabla P \cdot \mathbf{u}_Z}{R_p B} + \sigma_{||} \frac{T_e}{e} \nabla_{||}^2 \Phi = 0$$

Where u_Z is the vertical unit vector and Φ the normalized potential. The parallel gradient is simply replaced by a parallel scale length $l_{||}$ (assuming $\Phi \approx 1$) and the pressure gradient is replaced by a transversal scale length related to the over-density scale δ_b. As an ordering, the parallel scale length is expressed function of the other control parameters :

$$l_{||} \approx \sqrt{\frac{\sigma_{||} R_p B \delta_b}{2 e n_e}}$$

Using typical plasma parameters $R_p = 3$m, $B = 3$T, $T_e = 10$eV, $n_e = 10^{18}$m^{-3} and $\delta_b \approx 1$cm, the parallel scale length of the potential extent is about $l_{||} \approx 100$m, thus in the order of the field line length in Tore Supra SOL plasmas. To that point, the flute mode for potential is at least true, since the potential is mainly hold by electrons that move faster than ions. Therefore, we can evaluate an equilibrium time defined as the time taken by thermal electrons to expand along $l_{||}$, that is $\tau \approx 8.10^{-5}$s. On the other hand, the mass density can only extend in the parallel direction with the ion sound speed , leading to an effective parallel extent of the mass equal to $l_{||}^m = \tau c_S \approx 2.8$m corresponding to approximately 10% in the poloidal direction. By that time, the density structure has been radially advected with a velocity $v_r \approx \frac{T \nabla \Phi}{eB} \approx \frac{T}{\lambda_b e B} \approx 333$m - ordering in agreement with experiment observation, and thus over a radial distance of $\Delta_r \approx 2.5$

cm. Of course, the density structure can be initially extended in a region where the driving term -divergence of the diamagnetic current - acts in favor af the outward propagation. Considering in more detail the driving polarization term, we find that the poloidal pressure gradient acts as a charge accumulation term via the poloidal dependance :

$$\nabla \mathbf{j}_{dia} = -\frac{2\nabla_\theta P}{R_p B}\left[\cos\theta - \epsilon\left(\rho(1+\Lambda) - \frac{1}{q^2\rho^3}\right)\right]$$

Where the ϵ term is a correction due to the Shafranov shift 2.9. The geometrical term in the right hand side is defined as $\kappa(\theta)$, and its sign shows where the instability driver acts for an outward propagation of the plasma structure. As shown on the figure 5.30, the polarization growth leads to an outward propagation in a region localized on the low field side, but narrower than a simple trigonometric function due to the Shafranov shift. Strictly, the instability takes place in a region $-75^o < \theta < 75^o$, but the driving is efficient ($\kappa > 0.5$) in a narrower region, that is $-40^o < \theta < 40^o$.

To summarize, the density structures are effectively unstable with respect to an outward propagation in a region centered at the outboard midplane, having a poloidal extent of about $\pm 40^o$. The polarization driving the radial convection are effectively extended along the full field line, but the ions can only elongate a few poloidal degrees more while the structure propagates a few centimeters in the radial direction. Therefore this simple model is able to support the observation that the radial convection takes place mainly around the outboard midplane $\pm 50^o$. That said, the model does not include all the polarization term involved in the interchange instability like the polarization drifts, and should be only considered as a proof of principle.

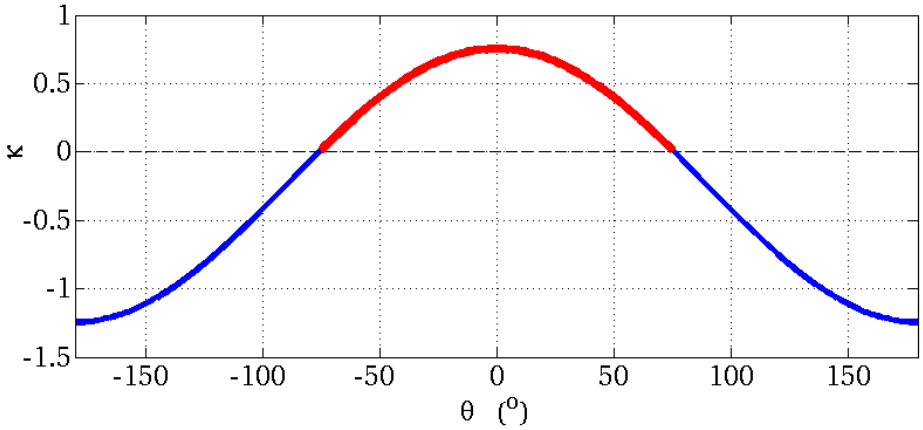

Figure 5.30: *Poloidal variation of the instability driver parameter. In red is shown where the instability leads to an outward propagation of the density structure*

More recently, a new paradigm was adopted in order to justify the strong localization of the flux at the outboard midplane : the flute mode is abandoned and let place to a picture of density structures strongly localized at the outboard midplane. The mass parallel expansion is done via parallel front expulsions [Havlickova 10] [Isoardi 09] [Chiavassa 10] whereas the overdensity is propagating across flux surfaces at the outboard midplane. Still under investigation and supporting the previous simple attempt, this possible mechanism could explain the highly localized nature of the radial flux in the SOL. Partial validations could be inferred by resolving

the fronts propagating in the parallel direction. Unfortunately, fast imaging is not able to capture events moving at the ion sound speed and fronts found on probe signals do mainly corresponds to radial motions of plasma filaments [Garcia 07a] that exhibits a long radial tail. Parallel fronts could exist on the signals but we do not have currently the way to extract them.

5.7.2 Effect of magnetic shear on the local filament shape

According to the interchange paradigm for plasma filament excitation, our experimental picture suggest that these filaments are predominantly born at the outboard midplane and extend along the magnetic field from that position. Thus the transversal shape of the structure along its flux tube is changed according to the magnetic shear, as illustrated on the figure 5.31. Starting with a transversally circular object at the outboard midplane, its parallel projection along the field lines gives a tilted and elongated structure at the top where the rake probes operate, and a strongly elongated structure at the inboard midplane. First of all, this simple geometric statement infer that a filament born at the outboard midplane is more subject to decorrelation phenomena at the inboard midplane where its transversal width is comparable to ion Larmor radius and transverse diffusion acts more efficiently. Indeed the transversal elongation means sharper transversal gradients at the structure periphery. Therefore we could expect an action of the magnetic shear on the capability of the structures to propagate radially in a coherent and thus efficient state, that would lead in principle to a poloidal asymmetry of the effective radial transport even in a flute mode approximation as soon as the instability occurs at the outboard midplane.

Secondly, the tilted shape of the structure at the plasma top is considered as a crucial filament

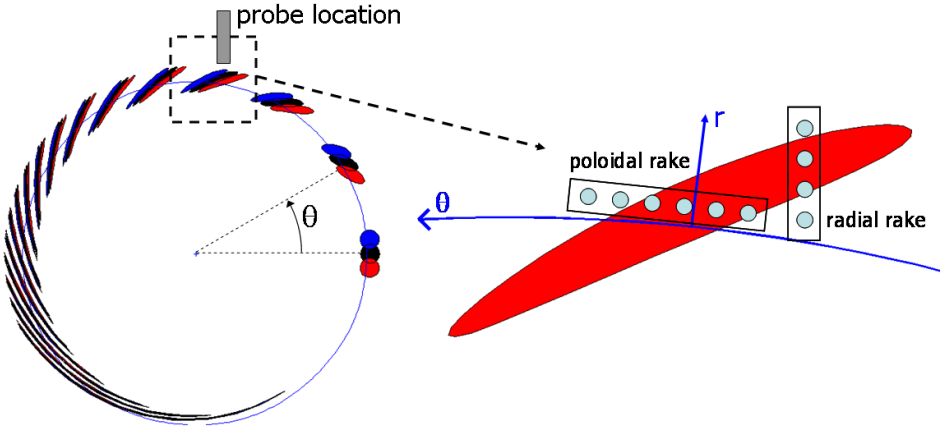

Figure 5.31: *Left : Poloidal cross section at a given toroidal location of a circular structure born at the outboard midplane and extended along the magnetic field to the high field side. Right : local shape of such structure at the probe position where are shown the geometry of the poloidal and radial rakes used to determine the phase velocity of fluctuations*

property in the scope of phase velocity extraction from multi-point analysis performed on rake probe signals. As we discussed a previous chapter 3.30, the time-lag evaluated by cross correlation between collectors of the radial rake probe was not consistent -on first sight- with an outward propagation of the over-dense structures. Now taking into account the magnetic

shear effect on the blob shape at the probe position 5.31 we have a consistent argument to explain the apparent inward blob propagation seen by the radial rake .

5.7.2.1 Re-visiting the phase velocity extraction

Now we have in our possession a new geometrical element to evaluate the phase velocity of fluctuations with the rake probes : the orientation of the structures in the poloidal cross section, fixed by the magnetic shear from the outboard midplane to the probe location. That is, we simply assume that the initial structure born at the outboard midplane is symmetric with respect to the midplane and that the shape at the top is assimilated to an ellipse. This ellipse is animated with a given velocity vector that we want to evaluate from the time lags calculated between spatially separated collectors. By looking carefully at this exercise, we realize that the shape of the structure as well as its orientation are directly involved in the onset of this time shift.

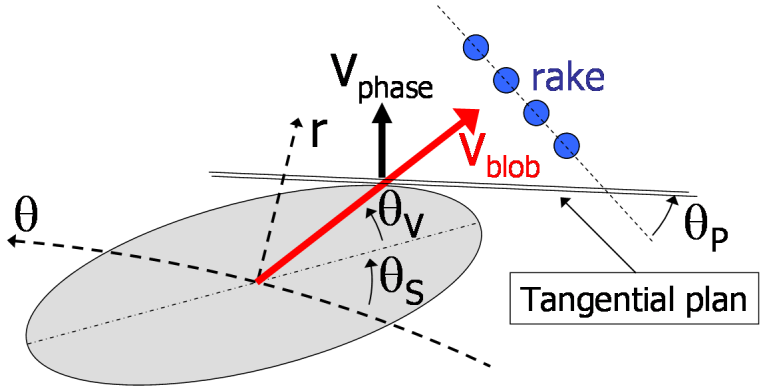

Figure 5.32: *Poloidal cross section of a filament at the probe location. The filament section is approximated as an ellipse tilted due to the magnetic shear θ_S with respect to the local cylindrical coordinates. The object is animated with a velocity V_{blob}. The phase velocity extraction by means of phase shift between spatially separated collectors is in fact related to the velocity V_{phase} of the* phase front *that is defined as the tangential plan on the ellipse at the intersection point with the velocity vector. Then, the temporal shift between collectors is related to the projection - with the angle θ_P - of the phase front velocity on the collector rake.*

As illustrated on the figure 5.32, the velocity effectively measured by the rake is not the structure velocity, but the effective velocity of the phase front defined by the assembly of similar structures crossing the probe. And this phase front orientation is a function of blob geometrical parameters that are initially unknown of the problem. Finally, we face a non-linear problem that has to be solved self-consistently by considering time lags and correlation length evaluated along both radial and poloidal rakes in order to decorrelate velocity field and shape of the blob. This technique has been applied to a set of plunges performed with the radial and the poloidal rake probe, unfortunately not at the same time but on almost identical plasmas 5.33. The evaluated velocitiy field is now more relevant in term of signs : we extract effectively a positive radial velocity of the order of a few hundreds of meter per seconds and a negative poloidal

velocity that is in the same order of magnitude. That said, the error related to the velocity field extraction is relatively high, first because the cross correlation amplitudes were not completely satisfactory and secondly because the algorithm is not fully optimized to take care of all informations given by the fluctuations, like all correlations length, auto-correlation times and time shifts.

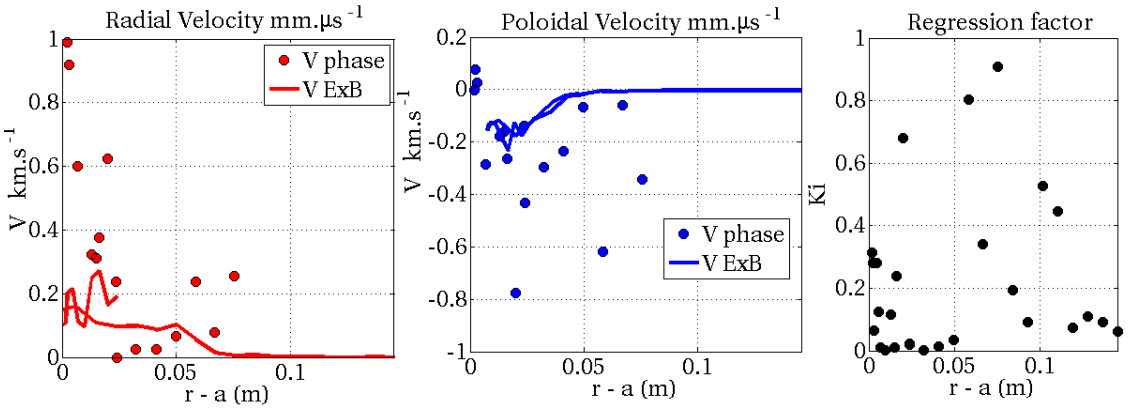

Figure 5.33: *TS45336 plunge 2 radial rake probe & TS45006 plunge 2 poloidal rake probe. Left : Radial velocity of the fluctuations along the SOL profile. Middle : Poloidal velocity of the fluctuations. The continuous curve corresponds to the averaged ExB velocity of density peaks whereas the circle are calculated with a time shifts process. Right: Regression factor on the time shift technique, calculated on the cross correlation amplitudes in between collectors. A value of 0 means a perfect correlation.*

5.7.2.2 ExB velocity field

On the other hand, the phase velocity extracted from cross-correlation is in the same ordering as the velocity given by the electric field fluctuations 5.33. In order to take care of the density fluctuations amplitude - that is a crucial parameter in the cross-correlation, the fluctuating electric field is averaged over the biggest positive density events. Again, the radial ExB velocity is positive as suggested by results presented earlier 3.39. And interestingly, the poloidal ExB velocity of the fluctuations is negative, as obtained with the time shift process forced by the magnetic shear elongation. This poloidal velocity has been calculated with the radial rake probe following the same approximations has done with the poloidal rake probe. In particular, the time averaged radial electric field has been forced to zeros, such that the poloidal ExB velocity does correspond to the fluctuations velocity in the frame of steady-state flows. That might give an additional argument justifying why the poloidal ExB blob velocity somehow underestimate the poloidal phase velocity component that is influenced by the steady-state flows. A brief discussion on the poloidal ExB transport is meaningful in the context of justifying the magnetic shear tilt of density filaments at the plasma top.

The fluctuations collected with the radial rake probe are subject to more ambiguity than those collected by the poloidal rake probe since the collectors suffer directly the probe head interaction with the plasma 3.17. But doing with available diagnostics, the probe configuration is able to measure the ExB poloidal flux. We simply note that radial rakes are mounted in a

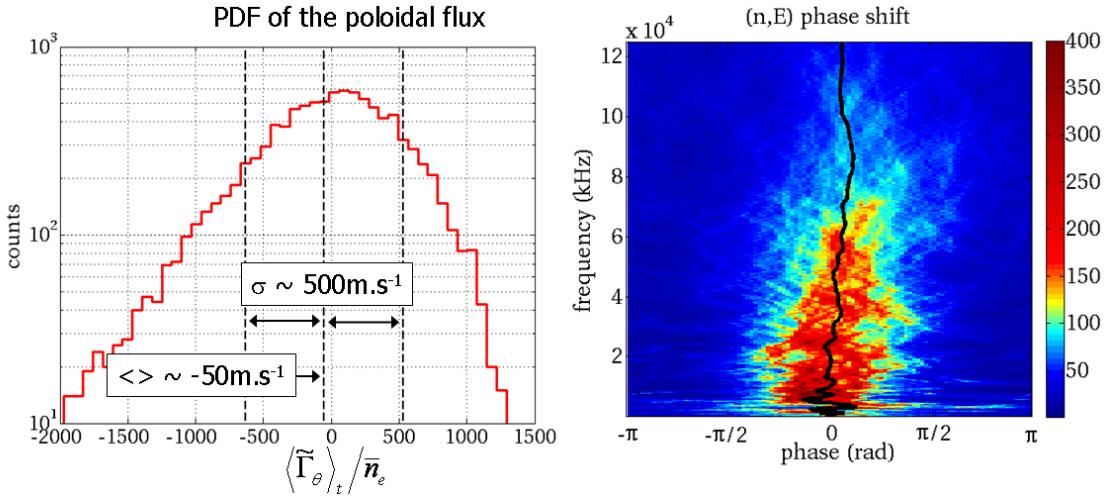

Figure 5.34: *TS45325 plunge 1 radial rake probe, data collected 2 cm from the LCFS. Left : Probability distribution function of the poloidal flux, expressed as a fluctuating effective velocity. We note the negatively skewed fluctuation behavior and the negative time averaged value. Right : phase shift between density fluctuations and poloidal electric field fluctuations. The black thick curves shows the time averaged phase shift for every frequency.*

Mach configuration and we only considered for that discussion the collectors facing the flow, i.e facing the low field side where the fluctuations are believed to be born. Indeed a strong difference in the electrostatic fluctuations is observed in term of transport amplitude or phase coupling, that might be considered as an argument that origins of fluctuations observed with the probe are not symmetric. Parenthesis closed, the poloidal flux is estimated as the coupling between inward electric field (giving a positive poloidal velocity) and the saturation current fluctuations. First of all, these fluctuations are again in phase 5.35 as for the radial flux, and the flux shows an intermittent behavior toward negative value. That is, the time averaged residual flux value is small compared to the standard deviation ($\frac{\sigma}{<>}$ 10) and is found to be negative and reproducible. Interestingly, we find that the poloidal flux has similar properties as the radial flux, and we infer that both correspond to the same transport process.

Thus, we now consider the two components of the effective velocity field carried by fluctuations *only*, namely without the contributions of steady-state flows. Data are collected with the poloidal and the radial rake probe during different but similar discharges. The finding is that at the plasma top, radial velocities are positive and poloidal velocities are negative 5.35 roughly in the same ordering, that is in a few tens of meter per seconds. In the assumption that geometrical aspects of fluctuations are on task in the link between the two velocity component, we compared the local velocity field orientation with the local orientation of filaments born at the outboard midplane and extended along field lines 5.35. As a first observation, the velocity orientation matches the filament orientation close to the LCFS although a divergence is noticeable 4 cm outward. And interestingly, the standard deviation of the velocity components follows the same orientation as the mean values. Our understanding of these observations is the following : plasma structures are born at the outboard midplane were they travel radially outward. Their parallel extent suffers the magnetic shear such that structures are tilted in the

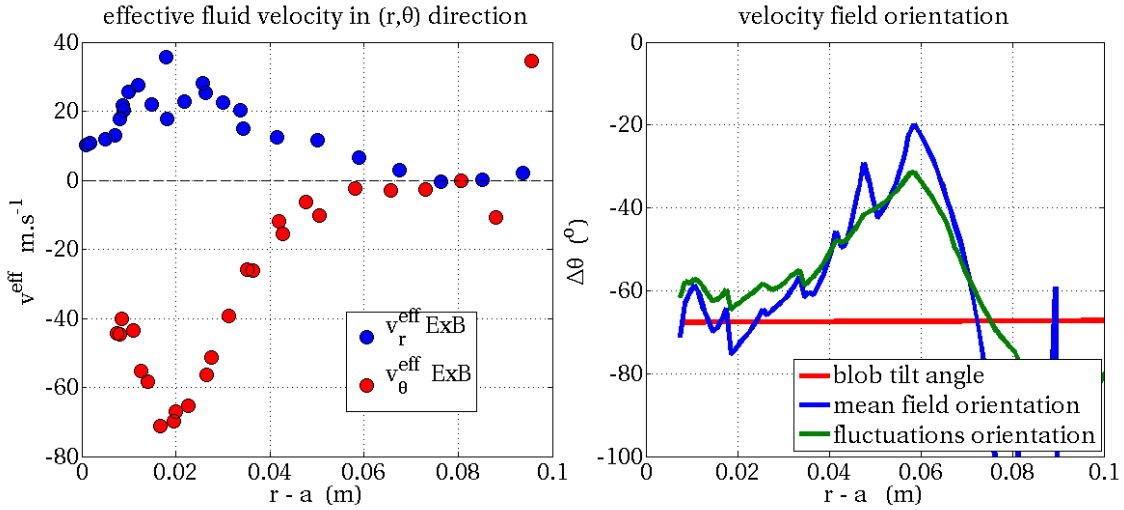

Figure 5.35: *TS45336 plunge 1 radial rake probe, TS45006 plunge 1 poloidal rake probe. Left : Radial profile of the effective radial and poloidal fluid velocity measured respectively with the poloidal and radial rake probe. The radial velocity is positive and the poloidal velocity is negative. Right : The local orientation of the velocity field (blue) is compared to the filament orientation (red) assuming it is born at the outboard midplane and is extended along the field lines in the circular magnetic field approximation. In green is shown the field orientation deduced from the fluctuation amplitudes -standard deviation- of the flux components*

poloidal plan. The local velocity is therefore not aligned with the local radial direction but is aligned with the local structure orientation such that a parallel extent along the magnetic field is kept during the filament travel across flux surfaces. The interpretation is subject to discussion and would need more attentions to draw consistent conclusions, but preliminary observations exposed there are going in the proposed direction. The issue is crucial to know whether the local velocity field expressed in a magnetic coordinate system is conserved along the parallel direction, otherwise the approximation of field aligned structures would be simply no relevant.

5.7.2.3 Perspectives on flows and core plasma rotation

Some experiments performed on Alcator C-mod [LaBombard 04] or Tore Supra [Hennequin 10] suggest that SOL flows influence the core edge rotation inside the LCFS. We would like to address this issue in the scope of our previous models.

As a summary of the previous chapter, we have shown that the near-sonic parallel flows are a direct consequence of the strong particle source enhancement at the outboard midplane. Thus, by resolving the particle source distribution, we are able to resolve in a first approximation the parallel flow distribution around the plasma 5.36. Besides, we have highlighted that the local radial turbulent flux is composed of a relatively important fraction of inward convections 3.39 although the time averaged value is positive. Thus a relatively important radial exchange occurs - even at the LCFS- between closed field lines and opened field lines. The exchange of momentum, described by the Reynold stress is worth to be considered following the latter

considerations : the parallel flows driven by the particle source asymmetry is radially transported inward due to the fluctuating ExB radial transport. A first approach would consist on considering the time averaged parallel flow value and couple it with the inward radial flux. That is, we are able to evaluate that component at the probe position -top- but nowhere else. Therefore, we make the approximation that the inward radial flux is just proportional to the time averaged radial flux value, along the whole field line. That said, the Reynold stress component counting for the inward radial source of parallel momentum can be compiled along the field line.

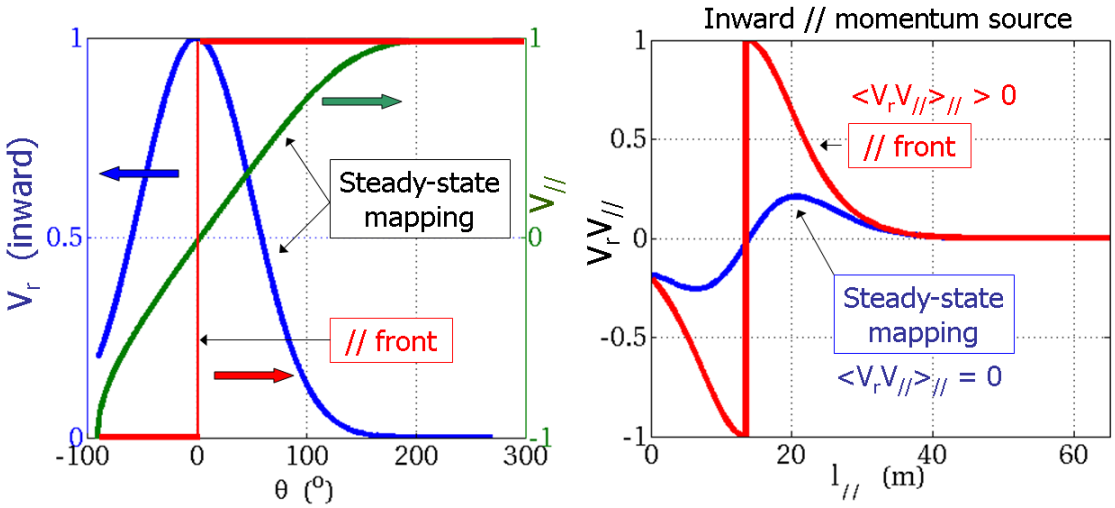

Figure 5.36: *Left : Illustration of the inward radial velocity (blue) function of the poloidal position. Is shown the parallel velocity (Mach number) variation (green) in the usual steady-state model and the parallel velocity field in the parallel front paradigm (red). Right : Parallel variation of the local radial source of parallel momentum, for the usual steady-state model (blue) and the parallel front assumption (red). The line averaged value is negative for the usual model and positive for the parallel fronts .*

The result is that although a momentum exchange effectively exist locally 5.36, the line integrated value counting for the global coupling between SOL flows and confined region is *zeros*. On the other hand, we could consider again the parallel front paradigm, for which the local Mach number is ± 1 along the whole field line. As a proof of principle, the edge plasma couples a positive parallel momentum to the plasma core, but of course we should consider more carefully the time coupling between parallel fronts and inward ExB fluctuations.
Last but not least, we highlighted previously that filaments have a net poloidal velocity due to the magnetic shear coupled with the parallel extent from the outboard midplane. Thus the SOL plasma could be a source of transversal momentum for the core plasma, that is suggested by experiments performed on Tore Supra [Hennequin 10]. But so far we are not able to explain the experimental observations.

5.8 Summary

This chapter was devoted to the alignment of all experimental properties of the particle transport obtained with our set of diagnostics. We focused our attention on the crucial issue of spatial transport asymmetries, and considered it as the leading phenomenon able to conciliate apparent inconsistencies found in between different experimental approaches of the edge transport.

First of all, we proposed an experiment dedicated to the poloidal mapping of the steady-state radial particle flux in the SOL. By tailoring the flux distribution along the field lines, we found that the flux is centered at the outboard midplane with a half poloidal opening of about 50^o, depending on the radial location in the SOL. We considered a synthetic Gaussian poloidal distribution as a relatively good extrapolation of the latter mapping. We verified that the iso-pressure field line assumption is relatively correct ether by showing *a posteriori* that the radial source of parallel momentum contribution is small or by means of numerical simulations (SOLEDGE2D).

Secondly we confronted our model with a variety of experimental evidences obtained on Tore Supra with different diagnostics and plasma configuration, and confirmed the validity of our mapping. In particular the mapping is consistent with the local $E \times B$ flux measured at the top.

In order to conciliate the visible evidences of filament asymmetries and the $E \times B$ flux enhancement at the outboard of other machines, we conclude that *the $E \times B$ flux is asymmetric and is mainly carried by the convection of plasma filaments that show a finite parallel extent*. The model is able to conciliate a variety of inconsistencies faced during limiter or divertor experiments on different machines.

Finally, we discussed on the underlying mechanism able to generate the observed asymmetries. The interchange is the reliable candidate as soon as non-flute modes are considered, in order to explain the radial flux asymmetry : plasma filaments are born at the outboard midplane and experience from that location a parallel extent along field lines. A relatively good consistency is found with the shape and the velocity orientation of density structures at the plasma top, suggesting that plasma filaments stay magnetically aligned during their transversal propagation.

Beyond these experimental evidences that filaments are born at the outboard midplane and extend along field lines, the mechanism explaining the strong flux asymmetry is not yet understood. Parallel fronts propagation could at work along field lines. Although we are not able to solve that parallel dynamic with currently operating diagnostics, these fronts could be crucial players on the turbulent coupling between SOL flows and internal rotation.

Conclusion

The transport of particles at the plasma edge has a determining influence on the fusion performances of a tokamak since it governs both the losses mechanisms from the confined region and the life time of plasma facing components by governing the heat fluxes they receive.
Although it is well established that turbulence is a major transport player, decades of experimental and theoretical investigations have hardly achieved a global understanding of turbulence effects at the edge. The reasons are obviously the complexity of transport processes involved in a magnetized plasma with respect to usual fluids, together with the difficulty to diagnose precisely an extreme medium. For instance the relative complexity of the magnetic field geometry in a tokamak is responsible for significant 3D effects on the edge transport. These crucial effects are usually not described by numerical simulations due to high computational demanding and hardly understood from experiments due to a critical lack of spatial resolution. Therefore the ITER project suffers from a crucial lack of prediction capabilities. Without a consistent transport model for the edge, we can not efficiently predict the heat load on plasma facing components, the power threshold for the H-mode transition, the spatial location of impurity accumulation, the coupling efficiency of heating wave launchers, or the efficiency of gas injection systems to fuel the plasma. On the other hand, the ITER design has been influenced by scaling laws built from experiments performed on a few relevant machines like JET, DIII-D , JT-60 or ASDEX-Upgrade although the physical meaning of these laws is missing for most of them.
In this thesis, we approach the subject of particle transport across the plasma boundary of Tore Supra, between the confined region and the plasma facing components. The objective is to progress in the experimental understanding of 3D effects that determine the particle flux balance around the confined plasma. In particular, this balance determines the scrape-off layer width and the parallel flows distribution around the confined region. These flows, aside of dragging impurities in the plasma chamber, are believe to influence the core rotation and hence the onset of the H-mode barrier. Although Tore Supra is a limiter machine and does not operate in H-modes, the circular plasma configuration is opportune to facilitate the experimental investigation of radial particle transport at the edge. The relevance of the highlighted results are justified by the capability of the model to explain the experimental observations done on ITER-relevant machines like Alcator C-mod, JET or DIII-D.

On a first part of our experimental investigations, we have been attached in proving the reliability of diagnostics and models to capture the plasma phenomena. We verified that the

steady-state Mach probe theory, leading interpretative tool for the measurement of parallel flows in edge plasmas, is correct in the scope of experimental evidences. Then we pointed out that probe geometry is of crucial importance to evaluate correctly the parallel flow strength: whereas the tunnel collectors do not suffer from significant uncertainty on the collection areas, the thin collectors are not reliable for determining the parallel Mach number. Hopefully Tore Supra is equipped with a tunnel Mach probe, but we pointed out that most of reciprocating probes used on other tokamaks are composed of thin collectors that prevent a reliable information about parallel flows.
Then we investigated the different mechanisms potentially involved in the drive of steady-state parallel flows. The ionization source has been computed with a Monte Carlo algorithm and was found to be almost negligible in the plasma SOL. Transversal flows due to electron temperature profiles are found to induce a small effects on parallel flows as well - due to the relatively flat temperature gradients in Tore Supra SOL. Finally only remains the radial particle flux distribution around the plasma as a parallel flow driver. From that statement, we could interpret the local parallel flow profile as a radial flux amplitude integrated along the field lines. The flux amplitude exceed by several order of magnitudes the neoclassical predictions. Moreover, the near sonic parallel flows measured at the plasma top are understood as a return flow from the main particle source location to balance the pressure along the field lines : $\approx \%85$ of the radial flux is located at the low field side of the plasma section. Thus the first conclusion drawn is that the turbulent radial flux - in opposition to neoclassical- is characterized by a strong amplitude and a strong spatial asymmetry driving the parallel flows around the plasma.

Secondly, we investigated the turbulent radial flux measured at the top by means of a poloidal array of small pins. Density fluctuations are characterized by a high degree of intermittency and coherency, as universally observed in all magnetically confined plasma devices. We first reconsidered the usual technique consisting on interpreting time lags between spatially separated points in term of fluctuations phase velocities. We pointed out that this technique should unambiguously include the spatial shapes of fluctuating structures, that can only be deduced from a 3D transport model that we proposed afterward. Then we considered carefully the usual technique that consist on evaluating the poloidal electric field from a simple spatial difference of potential. Inferring that the diagnostic size might be critical with respect to the size of electrostatic eddies, we investigated the electric field under-sampling effect on a turbulence simulation output. As a result, the under-evaluation of the electric field can be significant depending on the size of electrostatic eddies - up to a factor of 3 in the flux amplitude.
Finally we investigated the radial flux properties from the fluctuations of density and poloidal electric field. When the electric field under-sampling is negligible, we find that in most of the cases density and electric field fluctuate in phase : the positive density bursts are convected radially outward. The time averaged flux is found to be positive and reproducible and in good ordering with the flux amplitude needed to build the density profiles. But referred to the previous finding that the flux is spatially asymmetrical, we point out that comparing the density profile to the local radial flux value should be interpreted with precautions since density profiles

give informations only about the line averaged radial flux.

The third point about transport at the edge concerns the fast visible imaging. The relatively low sensitivity of the diagnostic imposes relatively narrow operational conditions for visualizing the plasma fluctuations at the edge. When the natural recycling on limiter was sufficient or during fully detached conditions, fluctuations could be resolves on the movies. Otherwise, we made use of gas injections either at the inboard or at the outboard midplane to increase the visible light emission. Although the diagnostic sensitivity could be pointed out as a mis-leading effect, the variety of plasma conditions return the following pictures of plasma fluctuations : field line elongated plasma filaments are observed. These filaments exist either in the confined plasma were they propagate poloidally in the electron diamagnetic direction - in a quantitative agreement with Doppler back-scattering measurements, or in the SOL where they propagate in the ion diamagnetic direction - confirmed with Doppler as well. Thus the phenomenon is not a consequence of the field line topology. Then, these filaments were rarely observed at the high field side of the plasma , and never at the inboard midplane. On the other hand they are found to propagate radially at the outboard midplane, with velocities coherent with probe measurements - at the top. Thus we conclude to a strong spatial asymmetry of these filaments : they exist mostly at the low field side and have a finite parallel extent from that location, either inside or outside of the LCFS.

Finally, these observation encouraged us to focus on the resolution of the spatial asymmetry of the turbulent flux : steady-state observations show that the radial flux is located at the low field side, filaments are observed to propagate radially only at the low field side and fluctuations measured at the top agree with the signature of filaments convection. In order to conciliate the local end global particle flux evaluation, we proposed and performed a dedicated experiment aiming at resolving the flux enhancement at the outboard midplane. As a result, the steady-state radial flux is found to be strongly enhanced at the outboard midplane, and the spatial distribution is consistent with a variety of dedicated evidences. Furthermore, the local turbulent flux is found to be in relatively good quantitative agreement with the mapping : *the revealed distribution, enhanced at the outboard midplane, is a property of the turbulent drift flux characterized by localized convection of filaments.*
Although the idea is not new, these results are the first quantitative resolution of the flux asymmetry. Immediate and strong implications are risen concerning the modeling efforts : a lot of models are based on the approximation that turbulent modes have an almost infinite parallel extent $k_{||}L_{||} \approx 0$ whereas our finding is that $k_{||}L_{//}$ 30. Thus 3D effects are significantly involved in the transport processes since the parallel uniformity criterion of filamentary structures does not hold. Instead, the model is consistent with the idea that plasma structures initially born at the outboard midplane where the interchange instability drives a density /electric field coupling favorable for an outward propagation. While the coupling builds up, the full electrostatic structure extends along field lines and propagates across the flux surfaces while keeping the field alignment. The magnetic shear has a direct influence on the local shape and orientation of

the structures, inferring a probable role of the filament propagation in the onset of asymmetric transversal drifts.

First of all, this work taken as a whole shows the importance of considering a set of diagnostics as large as possible in order to draw a *global* picture about transport phenomena. The model of flux enhancement due to an asymmetry of the turbulence has shown a relatively strong robustness faced to a variety of experimental evidences obtained during Tore Supra experiments. And the developed ideas are even robust in resolving apparent contradictions found between limiter & divertor experiments or between divertor & divertor experiments, inferring the universality of transport processes at the edge of tokamak plasmas.
In that frame work, the results presented along the theses show the importance of revisiting our approach of edge transport. The finite extent of plasma filaments and their implication on edge flux balance should be considered as a benchmark for the new generations of 3D numerical simulations since a global simulation of transport processes is required in the scope of understanding the H-mode transition or the density limit mechanisms.
This work initiated in Tore Supra is inserted in a broad experimental effort aiming understanding the precise mechanisms governing the plasma equilibrium at the edge. Further works should focus on the precise filament dynamics, both along the field lines and transversal to them in order to capture the mechanisms that could be involved in the coupling between SOL momentum fluxes and core rotation.

Bibliography

[ad S.J Zweben 04] J.L Terry ad S.J Zweben, B. Bose, O. Grulke, E.S. Marmar, J. Lowrence, V. Mastroola & G. Renda. *High-speed movies of turbulence in Alcator C-mod.* Review of scientific instruments, vol. 75, n° 10, 2004.

[Agency 09] International Energy Agency. *2009 report on energy balance.* 2009.

[Batishchev 97] O.V. Batishchev. *Kinetic effects in tokamak scrape-off layer plasmas.* Phys. Plasmas, vol. 4, n° 5, 1997.

[Boedo 03] J.A. Boedo, D.L. Rudakov, R.A. Moyer, G.R. McKee, R.J. Colchin, M.J. Schaffer, P.G. Stangeby, W.P. West, S.L. Allen, T.E. Evans, R.J. Fonck, E.M. Hollmann, S. Krasheninnikov, A.W. Leonard, W. Nevins, M.A. Mahdavi, G.D. Porter, G.R. Tynan, D.G. Whyte, & X. Xu. *Transport by intermittency in the boundary of the DIII-D tokamak.* Physics of Plasmas, vol. 10, n° 5, 2003.

[Braginskii 65] S.I. Braginskii. *transport processes in a plasma.* Reviews of Plasma Physics, vol. 1, page 055010, 1965.

[Brochard 09] F. Brochard, N. Fedorczak, G. Bonhomme, F. Clairet, M. Farge, P. Ghendrih, J. Gunn, P. Hennequin, S. Heuraux, N. Lemoine, P. Monier-Garbet, R. Nguyen van yen, S. Oldenbürger, K. Schneider, M. Schubert, & L. Vermare. *A first comparison between probes, fast imaging, and reflectometry synchronous measurements of edge turbulence in Tore Supra.* EPS Conference on Plasma Phys., vol. 33E, pages O–2.006, 2009.

[Caillé 07] A. Caillé, M. Al-Moneef, F.B. de Castro, A. Bundgaard-Jensen, N.F. de Medeiros, C.P. Jain, Y.D. Kim, M.J. Nadeau, C. Testa, J. Teyssen, E.V. Garcia, R. Wood, Z. Guobao & G. Doucet. *Deciding the Future:Energy Policy Scenarios to 2050.* World Energy Council, 2007.

[Carpentier 09] S. Carpentier. Etude des depots de chaleur dans le tokamak tore supra. These de doctorat de l Universite de Provence, 2009.

[Carreras 05] B.A. Carreras. *Plasma edge cross-field transport: experiment and theory.* Journal of Nuclear Materials, vol. 337-339, pages 315–321, 2005.

[Chen 03] F.F. Chen & J.P. Chang. *Lecture notes on principles of plasma processing.* Paperback, 2003.

[Chiavassa 10] G. Chiavassa, Ph. Ghendrih, G. Ciraolo, L. Isoardi, F. Schwander, E. Serre, Y. Sarazin, P. Tamain & H. Guillard. *Parallel Expansion of a Density Burst.* Journal of Nuclear Materials, 2010.

[Choruda] R. Choruda. *Plasma flow in the sheath and the presheath of a scrape-off layer.* MPI für plasmaphysik.

[Choruda 82] R. Choruda. *Plasma-Wall interaction in an oblique magnetic field.* Phys. Fluids, vol. 25, n° 9, 1982.

[Ciraolo] G. Ciraolo, G. Chiavassa, L. Isoardi, F. Schwander, E. Serre, N. Fedorczak, Ph. Ghendrih, J. Gunn, Y. Sarazin & P. Tamain.

[Clairet 03] F. Clairet, C. Bottereau, J. M. Chareau & R. Sabot. *Advances of the density profile reflectometry on TORE SUPRA.* Review of scientific instruments, vol. 74, n° 3, 2003.

[Connor 73] J.W. Connor & J.R. Hastie. Nuclear Fusion, vol. 13, page 221, 1973.

[de l'energie nucléaire 05] Direction de l'energie nucléaire. L'énergie nucléaire du futur : quelles recherches pour quelles objectifs? Commissariat à l'énergie atomique, 2005.

[Dejarnac 07] R. Dejarnac, J.P. gunn, J. Stöckel, J. Adámek, J. Brotánková & C. Ionipa. *Study of ion sheath expansion and anisotropy of the electron parallel energy distribution in the CASTOR tokamak.* Plasma Phys. Control. Fusion, vol. 49, pages 1791–1808, 2007.

[Dudson 08] B D Dudson, N Ben Ayed, A Kirk, H R Wilson, G Counsell, X Xu, M Umansky, P B Snyder, B LLoyd & the MAST team. *Experiments and simulation of edge turbulence and filaments in MAST.* Plasma Physics and Controlled Fusion, vol. 50, 2008.

[Erents 04] S.K Erents, R.A Pitts, W. Fundamenski, J.P Gunn & G F Matthews. *A comparison of experimental measurements and code results to determine flows in the JET SOL.* Plasma Physics and Controlled Fusion, vol. 46, n° 11, page 1757, 2004.

[F. Saint-Laurent 08] J.P. gunn F. Saint-Laurent. Field line reconstruction at the plasma edge. Private communication, 2008.

[Fedorczak 09] N. Fedorczak, J.P. Gunn, Ph. Ghendrih, P. Monier-Garbet & A. Pocheau. *Flow generation and intermittent transport in the Scrape-off-layer of the Tore Supra tokamak.* Journal of Nuclear Materials, vol. 390-391, pages 378–371, 2009.

[Fedorczak 10] N. Fedorczak, J.P. Gunn, Ph. Ghendrih, G. Ciraolo, H. Bufferand, L. Isoardi, P. Tamain & P. Monier-Garbet. *Experimental investigation on the poloidal extent of the turbulent radial flux in tokamak scrape-off layer.* Journal of Nuclear Materials, 2010.

[Fundamenski 07] W. Fundamenski, O.E. Garcia, V. Naulin, R.A. Pitts, A.H. Nielsen, J. Juul Rasmussen, J. Horacek, J.P. Graves & JET EFDA contributors. *Dissipative processes in interchange driven scrape-off layer turbulence.* Nuclear Fusion, vol. 47, pages 417–433, 2007.

[Garbet 07] X. Garbet. Equilibrium and mhd stability. Master Sciences de la Fusion, 2007.

[Garbet 09] X. Garbet, G. Dif-Pradalier, C. Nguyen, Y. Sarazin, V. Grandgirard & Ph. Ghendrih. *Neoclassical equilibrium in gyrokinetic simulations.* Physics of Plasmas, vol. 16, n° 6, page 062503, 2009.

[Garcia-Cortes 01] I. Garcia-Cortes, A. Loarte, R. Balbin, J. Bleuel, A. Chankin, S.J. Davies, M. Endler, S.K. Erents, C. Hidalgo, G.F. Matthiews & H. Thomsen. *Turbulent transport studies in JET edge plasmas in X-point configurations.* Journal of Nuclear Materials, vol. 290-293, pages 604–608, 2001.

[Garcia 07a] O.E. Garcia, J. Horacek, R.A. Pitts, A.H. Nielsen, W. Fundamenski, V. Naulin & J. Juul Rasmussen. *Fluctuations and transport in the TCV scrape-off layer.* Nuclear Fusion, vol. 47, pages 667–676, 2007.

[Garcia 07b] O.E. Garcia, R.A. Pitts, J. Horacek, J. Madsen, V. Naulin, A.H Nielsen & J. Juul Rasmussen. *Collisionality dependent transport in TCV SOL plasmas.* Plasma Physics and Controlled Fusion, vol. 49, pages B47–B57, 2007.

[Ghendrih 09] Ph. Ghendrih, G. Ciraolo, Y. Larmande, Y. Sarazin, P. Tamain, P. Beyer, G. Chiavassa, G. Darmet, X. Garbet & V. Grangirard. *Shearing effects on density burst propagation in SOL plasmas.* Journal of Nuclear Materials, vol. 390-391, pages 425–427, 2009.

[Grandgirard 06] V. Grandgirard, Y. Sarazin, X. Garbet, G. Dif-Praladier, Ph. Ghendrih, N. Crouseilles, G. Latu, E. Sonnendrucker, N. Besse & P. Bertrand. *GYSELA, a full-f global gyrokinetic Semi-Lagrangian*

code for ITG turbulence simulations. Proceedings of Theory of Fusion Plasmas, Varenna, 2006.

[Greenwald 01] M. Greenwald. *DENSITY LIMITS IN TOROIDAL PLASMAS.* 43rd Annual Meeting of the APS Division of Plasma Physics, 2001.

[Groebner 08] R.J. Groebner & R.A. Moyer. *Summary : Edge Working Group.* 21st US Transport Task Force Workshop, 2008.

[Gunn 01] J.P. Gunn. *Magnetized plasma flow through a small orifice.* Physics of Plasmas, vol. 8, n° 3, 2001.

[Gunn 02] J.P. Gunn, P. Devynck, J.Y. Pascal, J. Adámek, I. Duran, M. Hron & J. Stöckel et al. *A DC probe diagnostics for fast electron temperature measurements in tokamak edge plasmas.* Czechoslovak Journal of Physics, vol. 52, n° 10, pages 1107–1114, 2002.

[Gunn 07] J.P. Gunn, C. boucher, M. Dionne, I. Duran, V. fuchs, T. Loarer, I. Nanobashvili, R. Paneck, J.-Y. Pascal, F. Saint-Laurent, J. Stöckel, T. Van Rompuy, R. Zagorski, J. Adamek, J. Bucalossi, R. Dejarnac, P. Devynck, P. Hertout, M. Hron, G. Lebrun, P. Moreau, F. Rimini, A. Sarkissian & G. Van Oost. *Evidence for a poloidally localized enhancement of radial transport in the scrape-off layer of Tore Supra tokamak.* Journal of Nuclear Materials, vol. 363-365, pages 484–490, 2007.

[Havlickova 10] E. Havlickova, W. fundamenski, V. Naulin, A.H. Nielsen, S. Wiesen, J. Horacek & J. Seidl. *The effect of plasma fluctuations on parallel transport parameters in the scrape-off layer.* Journal of Nuclear Materials, 2010.

[Heidbrink 08] W.W. Heidbrink. *Basic physics of Alfvén instabilites driven by energetic particles in toroidally confined plasmas.* Physics of Plasmas, vol. 15, page 055501, 2008.

[Hennequin 10] P. Hennequin, L. Vermare, N. Fedorczak, J. Bernardo, Ö.D. Gürcan, E. Trier, N. Stuyck, C. Fenzi, J. Gunn, P. Monier-Garbet, C. Bourdelle, P. Ghendrih & X. Garbet. *The effect of SOL flows on edge and core radial electric field and rotation in Tore Supra.* Proceedings in European Physical Society, 2010.

[Hutchinson 88] I.H. Hutchinson. *Ion collection by probes in strong magnetic fields with plasma flow.* Physical Review A, vol. 37, n° 11, 1988.

[Isoardi 09] L. Isoardi, G; Ciraolo, G. Chiavassa, P. Haldenwang, E. serre, Ph. Ghendrih, Y. Sarazin, F. Schwander, X. Garbet & P. Tamain. *Mod-*

elling SOL flow pattern spreading in the edge plasma. Journal of Nuclear Materials, vol. 390-391, pages 388–391, 2009.

[Kocan 08] M Kocan, J P Gunn, J-Y Pascal, G Bonhomme, C Fenzi, E Gauthier & J-L Segui. *Edge ion-to-electron temperature ratio in the Tore Supra tokamak.* Plasma Physics and Controlled Fusion, vol. 50, n° 12, page 125009, 2008.

[Koch 07] B. Koch, A. Herrmann, A. Kirk, H. Meyer, J. Dowling, J. Harhausen, J. Neuhauser, H.W. Muller, W. Bohmeyer, G. Fussmann, AUG Team & MAST Team. *Observation of ELM structures in MAST and AUG using a fast camera.* Journal of Nuclear Materials, vol. 363-365, pages 1056–1060, 2007.

[Kumar 03] R. Kumar & S.K. Saha. *Temperature fluctuations and turbulent transport at the edge of the SINP tokamak.* Nuclear Fusion, vol. 43, pages 622–628, 2003.

[LaBombard 00] B. LaBombard, M.V. Umansky, R.L. Boivin, J.A. Goetz, J. Hughes, B. Lipschultz, D. Mossessian, C.S. Pitcher, J.L. Terry & Alcator Group. *Cross-field plasma transport and main-chamber recycling in diverted plasmas on Alcator C-Mod.* Nuclear Fusion, vol. 40, n° 12, page 2041, 2000.

[LaBombard 01] B. LaBombard, R.L. Boivin, M. Greenwald, J. Hughes, B. Lipschultz, D. Mossessian, C.S. Pitcher, J.L. Terry, S.J. Zweben & Alcator Group. *Particle transport in the scrape-off layer and its relationship to discharge density limit in Alcator.* Physics of Plasmas, 2001.

[LaBombard 02] B. LaBombard. *An interpretation of fluctuation induced transport derived from electrostatic probe measurements.* Physics of Plasmas, vol. 9, n° 4, 2002.

[LaBombard 04] B. LaBombard. *Transport-driven Scrape-Off-Layer flows and the boundary conditions imposed at the magnetic separatrix in a tokamak plasma.* Nucl. Fusion, vol. 44, pages 1047–1066, 2004.

[LaBombard 08] B. LaBombard, J.W. Hughes, N. Smick, A. Graf, K. Marr, R. McDermott, M. Reinke, M. greenwald, B. Lipschultz, J.L. Terry, D.G. Whyte, S.J. Zweben & Alcator C mod Team. *Critical gradients and plasma flows in the edge plasma of Alcator C-mod.* Physics of plasmas, vol. 15, 2008.

[Lipschultz 98] B. Lipschultz, J.L. Terry, C. Boswell, A. Hubbard, B. LaBombard & D.A. Pappas. *Ultrahigh Densities and Volume Recombination inside*

the Separatrix of the Alcator C-Mod Tokamak. Phys. Rev. Lett., vol. 81, n° 5, pages 1007–1010, 1998.

[Liu 10] H.Q. Liu, K. Hanaba, N. Nishino & QUEST group. *Study of Blob-like Strucutres in QUEST.* Journal of Nuclear Materials, vol. 0, n° 0, page 0, 2010.

[Müller 07] H.W. Müller, V. Bobkov, A. Herrmann, M. Maraschek, J. Neuhauser, V. Rohde, A. Schmid, M. Tsalas & ASDEX Upgrade Team. *Deuterium plasma flow in the scrape-off layer of ASDEX Upgrade.* Journal of nuclear materials, vol. 363-365, pages 605–610, 2007.

[Moyer 97] R.A. Moyer, J.W. Cuthbertson, T.E. Evans, G.D. Porter & J.G. Watkins. *The role of turbulent transport in DIII-D edge and divertor plasmas.* Journal of Nuclear Materials, vol. 241-243, pages 633–638, 1997.

[Naulin 07] V. Naulin. *Turbulent transport and plasma edge.* Journal of Nuclear Materials, vol. 363-365, pages 24–31, 2007.

[Oldenbürger 09] S. Oldenbürger. Eutde de la turbulence plasma dans une configuration magnétique linéaire. These de doctorat de l Universite de Nancy, 2009.

[Pitts 07] R.A. Pitts, K. Horacek, W. Fundamenski, O.E Garcia, A.H. Nielsen, M. Wischmeier, V. Naulin & J. Juul Rasmussen. *Parallel SOL flow on TCV.* Journal of nuclear materials, 2007.

[Preynas 10] Preynas. PPCF, vol. 0, page 0, 2010.

[Reux 10] C. Reux, J. Bucalossi, F. Saint-Laurent, C. Gil, P. Moreau & P. Maget. *Experimental study of disruption mitigation using massive injection of noble gases on Tore Supra.* Nuclear Fusion, 2010.

[R.H. Cohen 95] D.R Ryutov R.H. Cohen. *Plasma sheath in a tilted magnetic field: Closing of the diamagnetic currents; effect on plasma convection.* Phys. Plasmas, vol. 2, n° 6, 1995.

[Rienammn 91] K-U. Rienammn. *The Bohm criterion and sheath formation.* J. Phys. D: Appl. Phys., vol. 24, pages 493–518, 1991.

[Rompuy 08] T. Van Rompuy. *Influence of a Fast Electron Component on the Plasma Sheath Structure at the Inside of the Tunnel probe.* Contr. Plasma Phys., vol. 48, n° 5-7, pages 497–502, 2008.

[Rudakov 02] D.L Rudakov, J.A Boedo, R.A Moyer, S. Krasheninnikov, A.W. Leonard, M.A. Mahdavi, G.R. McKee, G.D. Porter, P.C. Stangeby, J.G. Watkins, W.P. West, D.G. Whyte & G. Antar. *Fluctuation-driven transport in the DIII-D boundary.* Plasma Physics and Controlled Fusion, vol. 44, n° 6, page 717, 2002.

[Sarazin 03] Y. Sarazin, Ph. Ghendrih ans G. Attuel, C. Clement, X. garbet, V. Grandgigard, M. Ottaviani, S. Benkada, P. Beyer, B. Bian & C. Figarella. *theoretical understanding of turbulent transport in the SOL.* Journal of Nuclear Materials, vol. 313-316, pages 796–803, 2003.

[Scott 02] B.D. Scott. *the nonlinear drift wave instability and its role in tokamak edge turbulence.* New Journal of Physics, vol. 4, pages 52.1–52.30, 2002.

[Serre] E. Serre, L. Isoardi, G. Chiavassa ang G. Ciraolo, F. Schwander, Ph. Ghendrih, Y. Sarazin & P. Tamain. *Boundary conditions at the limiter surface obtained in the modelling of plasma wall interaction with a penalisation technique.* Journal of Nuclear Materials.

[Silva 04] C. Silva, B. Gonçalves, C. Hidalgo, M. A. Pedros, K. Erents, G. Matthews & R. A. Pitts. *Fluctuation measurements using a five-pin triple probe in the Joint European Torus boundary plasma.* Review of Scientific Instruments, vol. 75, n° 10, 2004.

[Smick 10] N. Smick & B. Labombard. *Drift-driven and transport-driven plasma flow components in the Alcator C-Mod boundary layer.* Journal of Nuclear Materials, 2010.

[Spitzer 65] L. Spitzer. Physics of fully ionized gases. Interscience, New York, 1965.

[Stangeby 00] P.C. Stangeby. The plasma boundary of magnetic fusion devices. IoP, 2000.

[Stotler 03] D.P. Stotler, B. LaBombard, J.L. Terry & S.J. Zweben. *Neutral transport simulations of gas puff imaging experiments.* Journal of Nuclear Materials, vol. 313-316, pages 1066–1070, 2003.

[Tamain 07] P. Tamain. Etude des flux de matière dans le plasma de bord des tokamaks : Alimentation, transport et turbulence. These de doctorat de l Universite de Provence, 2007.

[Terry 03] J.L. Terry, S.J. Zweben, K. Hallatschek, B. LaBombard, R.J. Maqueda, B.Bai, C.J. Boswell, M. Greenwald, D. Kopon, W.M.

Nevins, C.S. Pitcher, B.N. Rogers, D.P. Stotler & X.Q. Xu. *Observations of the turbulence in the scrape-off-layer of Alcator C-Mod and comparisons with simulation.* Physics Of Plasmas, vol. 10, n° 5, 2003.

[Terry 05] J.L Terry, S.J. Zweben, O. Grulke, M.J. Greenwald & B. LaBombard. *Velocity fields of edge/Srape-Off-Layer turbulence in Alcator C-Mod.* Journal of Nuclear Materials, vol. 337-339, pages 322–326, 2005.

[Thomsen 02] H. Thomsen, M. Endler, J. Bleuel, A.V. Chankin, S.K. Erents, G.F. Matthews & Contributors to the EFDA-JET. *Parallel correlation measurements in the scrape-off layer of the Joint European Torus.* Physics of Plasmas, vol. 9, n° 4, 2002.

[van Houtte 04] D. van Houtte, G. Martin, A. Bécoulet, J. Bucalossi, G. Giruzzi, G.T. Hoang, Th. Loarer, B. Saoutic & the Tore Supra Team. *Recent fully non-inductive operation results in Tore Supra with 6 min, 1 GJ plasma discharges.* Nuclear Fusion, vol. 44, n° 5, page L11, 2004.

[Wagner 82] F. Wagner, G. Becker, K. Behringer, D. Campbell, A. Eberhagen, W. Engelhardt, G. Fussmann, O. Gehre, J. Gernhardt, G. v. Gierke, G. Haas, M. Huang, F. Karger, M. Keilhacker, O. Klüber, M. Kornherr, K. Lackner, G. Lisitano, G. G. Lister, H. M. Mayer, D. Meisel, E. R. Müller, H. Murmann, H. Niedermeyer, W. Poschenrieder, H. Rapp & H. Röhr. *Regime of Improved Confinement and High Beta in Neutral-Beam-Heated Divertor Discharges of the ASDEX Tokamak.* Phys. Rev. Lett., vol. 49, n° 19, pages 1408–1412, 1982.

[Ware 98] A.S. Ware, P.W. Terry, B.A. Carreras, & P.H. Diamond. *Turbulent heat and particle flux response to electric field shear.* Physics of Plasmas, vol. 5, n° 173, 1998.

[Watkins 97] J. G. Watkins, J. Hunter, B. Tafoya, M. Ulrickson, R.D. Watson, R.A. Moyer, J.W. Cuthbertson, G. Gunner, R. Lehmer, P. Luong, D.N. Hill, M. Mascaro, J.I. Robinson, R. Snider & R. Stambaugh. *Fast reciprocating Langmuir probe for the DIII-D divertor.* Review of Scientif Instruments, vol. 68, page 373, 1997.

[Wesson 04] J. Wesson. Tokamaks. Oxford science publications, 2004.

[Whiteford 09] Allan Whiteford, Martin O Mullane, Hugh Summers & dozens of others. *ADAS and Software issues.* ABS Workshop, Leiden, 2009.

[Yu 09] J.H. Yu, D.L. Rudakov, A.UY. Pigarov, R.D. Smirnov, N.H. Brooks, S.H. Muller & W.P. West. *Fast camera imaging of dust in the DIII-D*

tokamak. Journal of Nuclear Materials, vol. 390-391, pages 216–219, 2009.

[Zweben 02] S.J. Zweben, D.P. Stotloer, J.L. Terry ans B. LaBombard, M. Greenwald, M. Muterspaugh, D.S. Pitcher, K. Hallatschek ans R.J. Maqueda, B. Rogers, J.L. Lowrence, V.J. Mastrocola & G.F. Renda. *Edge turbulence imaging in the Alcator C-mod tokamak*. Physics of Plasmas, vol. 9, n° 5, 2002.

[Zweben 07] S.J. Zweben. *Edge turbulence measurements in toroidal fusion devices*. Plasma Phys. Control. fusion, vol. 49, pages S1–S23, 2007.